Centro Brasileiro de Pesquisas Físicas

Rafael Tourinho Aoude

A study of the doubly Cabibbo-suppressed decay $D^+ \to K^- K^+ K^+$

Rio de Janeiro - RJ
August 8, 2017

Rafael Tourinho Aoude

A study of the doubly Cabibbo-suppressed decay $D^+ \to K^- K^+ K^+$

Dissertação apresentada ao curso de Pós-Graduação em Física do Centro Brasileiro de Pesquisas Físicas, como requisito parcial para a obtenção do Título de mestre em Física.

Supervisor: Prof. Dr. Alberto Corrêa dos Reis

August 8, 2017

Resumo

Neste trabalho apresentamos a primeira análise de amplitude do decaimento $D^+ \to K^-K^+K^+$ duplamente suprimido por Cabibbo. A análise é baseada em dados coletados pelo experimento LHCb em colisões pp com 8 TeV de energia de centro de massa. O que corresponde à uma luminosidade integrada de $2\,\mathrm{fb}^{-1}$. A motivação desta dissertação é o estudo da amplitude de onda-$\mathcal{S}$ K^-K^+.

A análise do diagrama de Dalitz é feita usando duas abordagens. No primeiro, a amplitude de decaimento é parametrizada usando o Modelo Isobárico. Diferentes combinações de resonâncias intermediárias foram estudadas. Todas resultam em uma boa e equivalente descrição dos dados experimentais. O estudo com esse modelo permite mostrar que uma variação de fase na onda-$\mathcal{S}$, consistente com uma resonância, é necessária para descrever os dados nos dois limites do espectro de massa K^-K^+.

Alternativamente, os dados foram ajustados usando um modelo baseado Teoria de perturbacão quiral com resonâncias, em que as constantes de acoplamento da Lagrangeana são os parâmetros livres do modelo. O resultado mais importante desse modelo é o fato da interferência entre a onda-$\mathcal{S}$ e a onda-$\mathcal{P}$, que descrevem os dados experimentais, ser uma consequência direta da teoria.

Palavras-chave: Decaimentos de mésons; Espectroscopia de Hádrons; Diagrama de Dalitz.

Abstract

In this thesis, the first amplitude analysis of the doubly Cabibbo-suppressed $D^+ \to K^-K^+K^+$ nonleptonic three-body decay is presented. The analysis is based on an integrated luminosity of $2\,\text{fb}^{-1}$ of pp collisions data collected by the LHCb experiment at 8 TeV centre-of-mass energy. The main goal of this work is to study the K^-K^+ $\mathcal{S}$-wave amplitude.

The Dalitz plot analysis is performed using two approaches. In the first, the decay amplitude is parametrized using the Isobar Model. Different combinations of intermediate resonant states were studied, yielding an equally good description of the data. A phase variation of the $\mathcal{S}$-wave, consistent with a resonance, is required to describe the data at both ends of K^-K^+ spectrum.

Alternatively, the data was fit using a model based on Chiral Perturbation theory with Resonances, in which the Lagrangian coupling constants are the free parameters of the decay amplitude. The most striking feature of this model is that the interference between the $\mathcal{S}$- and $\mathcal{P}$-waves is directly derived from the theory.

Keywords: Heavy meson decays; Hadron spectroscopy; Dalitz Plot.

Contents

List of Figures

List of Tables

1 Introduction

> I have noticed that Dalitz plot are very popular with our colleagues in Rio de Janeiro. Having come here I understang why: the topography of Rio with its steeply rising mountain ranges crowned by spectacular peaks and separated by narrow valleys is a dramatic large scale model of a Dalitz plot.
>
> I.I. Bigi

The Standard Model (SM) has proven to be tremendously successful in describing particle physics. However, the source of CP violation in the SM - the irreducible complex phase in the Cabibbo-Kobayashi-Maskawa (CKM) matrix - cannot explain the baryon asymmetry of the Universe. In the quark sector, nonleptonic decays of flavoured mesons are the main processes for the study of CP violation, since flavour transitions probe the elements of the CKM matrix. Given the success of the SM, eventual new mechanisms of CP violation would play a subleading role in nonleptonic decays. CP violation phenomena are associated to phases. Therefore, controlling the strong phases in nonleptonic decays is critical for the identification of phases associated to physics beyond the SM (BSM).

Three-body nonleptonic weak decays of heavy mesons are of special interest for a number of reasons. These decays are sequential processes dominated by intermediate resonant states. This feature sheds light in two topics of flavour physics: (*i*) light mesons spectroscopy and (*ii*) direct CP violation. For the latter, the decay must proceed via at least two amplitudes with different weak and strong phases. In the case of multi-body decays, the strong phase difference is provided by the phase variation of the resonances.

The resonant structure in multi-body decays is determined by means of amplitude analysis. In such studies, one compares the distribution of events in the phase space with a model of the decay amplitude. The usual parametrization of the decay amplitude in three-body heavy meson decays is the Isobar model. It consists in a coherent sum of intermediate resonant amplitudes, $\mathcal{A} = \sum c_k A_k$. The decay contribution of a particular resonant state is determined by the complex coefficients c_k, which are the usual fit parameters.

The analysis of the decay amplitude is performed by fitting the Dalitz plot, a particular representation of the phase space. The Isobar model has been a successful effective description of Dalitz plot for data samples that are not very large. However, the amount of data produced by the LHCb in Run I and II requires a better description of B and D decays, since more subtle effects become visible.

In this thesis we analyse the doubly Cabibbo-suppressed decay $D^+ \to K^-K^+K^+$. This decay can proceed through two topologies, represented in Fig. 1. In the left diagram the heavy quark, c, emits a W and becomes an d-quark. The diagram on the right side represents an annihilation process, where the $\bar{d}$ belongs to the D meson.

Regarding the left diagram, a K^-K^+ pair can only be produced through rescattering. In order to the $d\bar{d}$ pair produce a K^-K^+ system, a $q\bar{q}$ pair should emerge from the QCD vacuum. These cases produce a $\bar{K}^0K^0$ or a $\pi\pi$ pair. This rescattering effect acts as a suppression on the amplitude.

Using this argument, we expect that the $D^+ \to K^-K^+K^+$ is dominated by the annihilation topology, which motivates and is the main assumption of an alternative

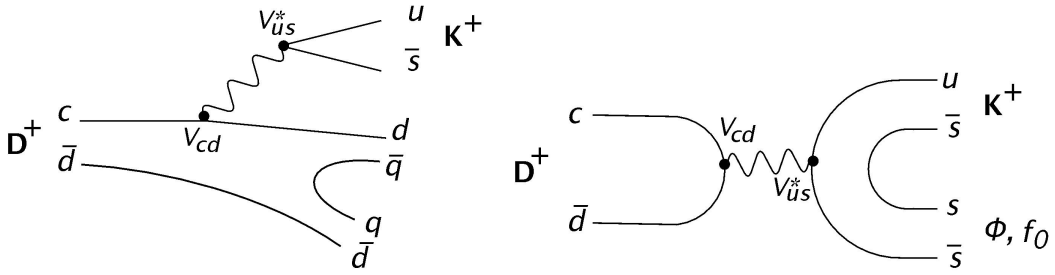

Figure 1: Annihilation diagram for $D^+ \to K^-K^+K^+$ via ϕ, a_0 and f_0 resonances (right); tree diagram for $D^+ \to f_0/a_0K^+$ (left).

model. Although it is not known how to calculate the left diagram, a full description would require both diagrams. In the case that this model does not give good and reliable results, this argument should be revisited.

In the specific topology of the annihilation diagram, the steps $D^+ \to W^+$ and $W^+ \to K^-K^+K^+$ can be factorized. As consequence, the decay amplitude may be written as

$$\mathcal{A} = \langle\, (KKK)^+|A_\mu|0\,\rangle\langle\, 0|A^\mu|D^+\,\rangle$$

where A_μ is the axial weak current. The second term in the right-hand side corresponds to the weak vertex and depends on the quark content of the initial meson D^+. The first term of the decay amplitude, $\langle\, (KKK)^+|A_\mu|0\,\rangle$, is the coupling between the W boson and the light mesons. In this thesis we present a model for this matrix element. We refer to this as the Multi-Meson model (MMM).

This model provides an alternative to the Isobar Model in order to parametrize the decay amplitude. In contrast to the pure phenomenological aspect of the Isobar model, the MMM is based on Chiral Perturbation Theory with Resonances (ChPTR) and provides improvements to some difficulties of the Isobar.

This thesis is organized as follows. In Section 2 the theoretical background required to understand the heavy-meson decays and the ChPTR is presented. This includes a brief overview of the Standard Model, chiral symmetries, Chiral Perturbation Theory (ChPT) up to leading order (LO) [1]. The next-to-leading order in ChPT will be included by Resonances coupling to the LO [2]. These two theories will be used in the construction of the Multi-Meson model.

The formalism for amplitude analysis will be explained in Section 4. This includes the description of the kinematics of a three-body decay and of the Dalitz plot. We describe the so called Isobar Model and its main difficulties. The fitting procedure and the limitations of the Isobar are also discussed.

The data used in this thesis correspond to approximately 2.0fb^{-1} of pp collisions at $\sqrt{s} = 8$ TeV collected by LHCb in 2012. The LHCb experiment is described in Section 3 The selection of the $D^+ \to K^-K^+K^+$ sample, the background estimation and modelling, and the determination of the efficiency variation across the phase space are described in Section 5. Results of fits to the data using the Isobar model are presented in Section 6.

Lastly, the Multi-meson model for the decay amplitude is proposed as an alternative to the Isobar model. Details of the calculation and results are given in Section 7. Since this is an ongoing work, it is presented the result of one fit and some studies of the importance of individual components of the MMM.

My contribution to this work was:

- The selection of the $D^+ \to K^-K^+K^+$ sample, the background modelling and estimation, and the determination of the efficiency variation across the Dalitz plot.
- Development of the `Rio+` software code [3].
- Fits to the LHCb data using the Isobar model.
- Calculations, simulations and fit with the MMM.

2 Theoretical background

> To be accepted as a paradigm, a theory must seem better than its competitors, but it need not, and in fact never does, explain all the facts with which it can be confronted.
>
> Thomas S. Kuhn, The Structure of Scientific Revolutions

Describing the basic elements of Nature has always been a tremendous task. Since the suggestion from Empedocles that earth, air, fire and water were the four basic elements, passing through the Mendeleev's periodic table, the Bohr atom model and finally arriving at General Relativity, Quantum Field Theory, etc. has been a long journey.

Nowadays, the way matter interacts and behaves is described by the Standard Model of Particle Physics, or just Standard Model (SM). The SM has one of its roots in 1928, when Dirac first proposed an equation to describe the electron dynamics. As a consequence a new particle, the positron, was predicted. In fact, a new concept, that of antimatter, was proposed.

Throughout the years, hundreds of particles of different kinds were discovered, creating a big zoo of particles. This recalls the same situation that Mendeleev encountered himself in 1869. In 1964, few years after Dirac equation, Gell-Mann and Zweig proposed, independently, a model to describe two sets of particles appearing in this zoo. These two sets are the mesons and baryons, known as hadrons. These particles are grouped in singlets, octets and decuplets with nearly degenerate masses. This approximate symmetry indicates a hidden structure of these particles. Their proposal postulates three basic constituents, called 'quarks' (due to Gell-Mann), which are the elementary representation of the SU(3) group[1] and could be compiled in a quark vector $\mathbf{q} = (u, d, s)^T$. Consequently, the mesons were bound states of $q\bar{q}$ and baryons qqq. This *quark model* describes the appearance of these multiplets but has three difficulties: *(i)* quarks have fractional electric charge, *(ii)* there were no evidences of multiplets from a different composition (such as qq, qqqq) and mainly *(iii)* the Δ^{++} particle seemed to violate the Pauli exclusion principle.

The solution for those difficulties emerged with the postulation of a new hidden degree of freedom proposed by Gell-Mann, called *colour*. Each type of quark can come in three different colours which form a triplet under $SU(3)_c$. Within this symmetry, mesons and baryons are colour singlets, the only configuration that can be seen as asymptotic degrees of freedom. It should be stressed that this SU(3) has nothing to do with the previous one.

Earlier, the understanding of the weak interaction started with the study of the β decay. The $n \to p + e^- + \bar{\nu}_e$ decay was discovered, as well as other similar decays, such as $\pi \to \mu + \bar{\nu}_\mu$ and $\mu \to e + \bar{\nu}_e + \nu_\mu$. The model proposed by Fermi to describe this decay was based on a four-point fermion interaction [4]:

$$\mathcal{L}_{\text{Fermi}} = \frac{G_F}{\sqrt{2}}[\bar{p}(x)\gamma_\mu n(x)][\bar{e}(x)\gamma^\mu \nu(x)] \tag{1}$$

The discovery of parity violation in weak interaction, due to Wu. [5], stimulated the research in this field and lead to the V-A theory [6], in which the weak boson only interacts

[1] This is a flavour SU(3) and should not be confused with the colour SU(3)

with left-handed fermions, and is described by an effective Lagrangian:

$$\mathcal{L}_{\text{eff}} = \frac{G_F}{\sqrt{2}} J^{\dagger}_{\lambda}(x) J^{\lambda}(x) + h.c. \tag{2}$$

The weak current $J_\lambda(x)$ has the V-A form. Therefore, *parity violation is maximal in weak interactions*. Also, the current could be separated in a leptonic and hadronic part:

$$J_\lambda(x) = J_{l,\lambda}(x) + J_{h,\lambda}(x) \tag{3}$$

which can be written as:

$$J_{l,\lambda}(x) = \bar{\nu}_e \gamma^\lambda (1-\gamma_5) e + \bar{\nu}_\mu \gamma^\lambda (1-\gamma_5)\mu \text{ and } J_{h,\lambda}(x) = \bar{u}\gamma^\lambda(1-\gamma_5)\tilde{d}. \tag{4}$$

The $\tilde{d}$ is a mixture of d and s quarks through the Cabibbo angle: $\tilde{d} = cos\theta_c\ d + sin\theta_c\ s$. The problem with this model is that it allows for a considerable amount of flavour changing neutral current (FCNC), which is highly suppressed. With that in mind, Glashow Illianopoulos and Maiani (GIM) suggested that this current should be generalized with the prediction of a new particle, called *charm* quark:

$$J_{h,\lambda}(x) = \bar{u}\gamma^\lambda(1-\gamma_5)\tilde{d} + \bar{c}\gamma^\lambda(1-\gamma_5)\tilde{s} \tag{5}$$

where $\tilde{s} = cos\theta_c s - sin\theta_c d$. With the inclusion of the charm quark, the induced FCNC is canceled out in tree-level, occurring only at loop level.

Although it is very consistent and predictive, this theory still presents two major problems: *Violation of unitarity* and the *lack of renormalizabilty*. The conservation of probability requires the $\mathcal{S}$-matrix to be unitary. The problem of unitarity will be an important issue in the models presented in this thesis.

The latter is more difficult because a non-renomalizible theory is not predictive. The term responsible for the lack of renomabilization is the quartic fermion coupling. These problems were solved with the proposal of Intermediate Vector Bosons (IVB) mediating the interaction: the $W^\pm$ boson. This avoids the use of nonrenormalizable quartic fermion couplings. This changes the Lagrangian to:

$$\mathcal{L} = g(J_\mu W^\mu + h.c.) \tag{6}$$

These bosons are massive (M_W) and in the low-energy limit ($M_W \to \infty$) one should recover the previous lagrangian.

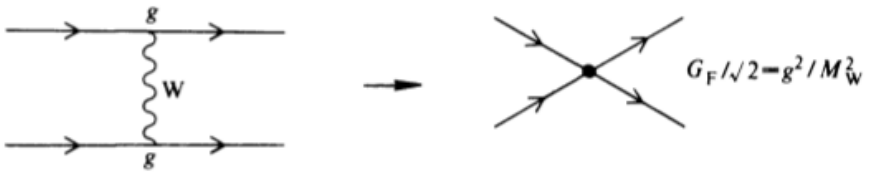

Figure 2: Effective four-fermion vertex after 'integrating-out' the W boson. Extracted from [4]

This idea of 'integrating-out' the heavy massive mediator will be used in the modelling of the $D^+ \to K^-K^+K^+$. In the annhilation diagram, the W boson will be treated in the same way as in the Fermi interaction.

Although the proposal of massive vector bosons solved the unitarity and renormalizabilty of the Fermi interaction, the mass of the boson spoils the renormalizabilty of the free vector boson Lagrangian. The solution of this problem came from the emergence of a spontaneously broken gauge theory. This gauge theory would not only solve the renormaliability but also unify electromagnetism and weak interaction, using the group $SU(2) \otimes U(1)$. This solution was given by Schwinger and Glashow [7–9]. But only in 1967-68, Weinberg and Salam proposed, independently, that the masses from IVB were generated by the so called Higgs mechanism [10, 11]. However, this result was not recognized until, in 1971, t'Hooft proved that non-Abelian gauge theories, with or without spontaneous symmetry breaking, were renormalizable [12].

In this solution, a scalar complex field forming a $SU(2)$ doublet ϕ is introduced, the non-zero vacuum expectation value of ϕ spontaneously breaks the symmetry implying in three of the original four gauge bosons becoming massive and one, which is identified as the photon, remaining massless. This is known as the ElectroWeak symmetry breaking (EWSB). After the EWSB, the system is still invariant under $U(1)_{EM}$. Another consequence of this mechanism is the appearance of a scalar degree of freedom, the Higgs boson.

All pieces of the SM were systematically confirmed until the last piece, the Higgs boson, was discovered in 2012 at the LHC. Although its great success, the Higgs boson has some theoretical complications, which arise from its scalar nature. This implies that quantum corrections to its mass diverge. In order to the Higgs mass has a finite value, all these divergent quantum corrections should fine-tune, which seems very unlikely. This is still a SM open problem.

2.1 The Standard Model of Particle Physics

The SM of particle physics is the Quantum Field Theory that describes the interactions of the fundamental constituents of matter. Its main ingredients are the quarks, leptons, photons, gluons, $W^{\pm}$, Z^0 and the Higgs boson. Throughout the years, its construction was based on successful and failed hypothesis, given by the precision and frontier physics experiments. As a consequence, nowadays we can define it in simple ingredients and a generic model of particle physics can be defined using three ingredients. [13]

- The **internal symmetries** of the Lagrangian : A QFT requires that the Lagrangian obeys the Lorentz symmetry. Due to that, fields have to be representations of the Lorentz group (*i.e.* scalar, vector, spinor, etc). However, internal symmetries can be accommodated in the Lagrangian. In the vast majority of the models, gauge symmetry is the internal symmetry. A gauge symmetry can be *global* or *local*, depending on whether the parameters vary or not with position in space-time. It can also be *Abelian* or *non-Abelian* depending on the algebra of the groups, which can be commutative or non-commutative.

  The internal gauge symmetry of the SM is local:

  $$G_{SM} = SU(3)_C \times SU(2)_L \times U(1)_Y \tag{7}$$

  The $SU(3)_C$ and $SU(2)_L$ are non-abelian local gauge groups and $U(1)_Y$ is abelian. The former is the symmetry group of Quantum Chromodynamics (QCD), which is the theory that describes the strong interaction. And the $SU(2)_L \times U(1)_Y$ is the theory describing Eletroweak interactions.

- The pattern of the **spontaneous symmetry breaking (SSB)** or the **vacuum symmetries**: In a QFT, the vacuum does not need to respect all the symmetries of the Lagrangian. It can be invariant under a subgroup of the gauge group. In such cases, we say that there is a *hidden* symmetry or that there is a *spontaneous symmetry breaking* (SSB). In the SM, the G_{SM} is broken by a non-zero vacuum expectation value (vev) of a single Higgs scalar, the subgroup is the $SU(3)_C \times U(1)_{EM}$, where the $U(1)_{EM}$ is the responsible for the Electromagnetic interactions.

$$\phi(1,2)_{+1/2} \quad (\langle \phi^0 \rangle = v/\sqrt{2}) \tag{8}$$

$$G_{SM} \to SU(3)_C \times U(1)_{EM} \quad | \quad Q_{EM} = 2T_3 + Y \tag{9}$$

  The relation $Q_{EM} = 2T_3 + Y$ is called the Gell-Mann Nishijima formula and relates the Hypercharge (Y), the Electromagnetic charge (Q_{EM}) and the third component of the weak-isospin. It was proposed independently by Murray Gell-Mann in 1956 [14] and Tadao Nakano and Kazuhiko Nishijima in 1955 [15]

- The **representations** of the fermions and scalars under G_{SM} : One has to define which representation (scalar, doublet, triplet, etc) the fields belong to. There are five fermionic representations in the SM, each consisting of three families, represented by the index $i = 1, 2, 3$.

$$Q_{Li}(3,2)_{+1/6} \quad U_{Ri}(3,1)_{+2/3} \quad D_{Ri}(3,1)_{-1/3} \quad L_{Li}(1,2)_{-1/2} \quad E_{Li}(1,1)_{-1} \tag{10}$$

  The first one, $Q_{Li}(3,2)_{+1/6}$, is the left-handed quarks.[2] It is a triplet under $SU(3)_C$, with each index representing the colour, a doublet under $SU(2)_L$ and the charge for the $U(1)_Y$ is set by the Gell-Mann Nishijima formula. The right-handed up and down quarks are still triplets for QCD but singlet under $SU(2)_L$, represented by $U_{Ri}(3,1)_{+2/3}$ and $D_{Ri}(3,1)_{-1/3}$, respectively. The leptonic fields behaves the same as the quarks with respects to $SU(2)_L \times U(1)_Y$. However they are $SU(3)_C$ singlets.

The Lagrangian is then constructed asking for the invariance of G_{SM} symmetry and expanding the fields around the vacuum, which is not invariant under G_{SM}. The non-zero vacuum expectation value will provide masses to the particles.

2.2 The SM Lagrangian

Respecting these requirements, the most general renormalizible Lagrangian can be decomposed in 3 parts: [3]

$$\mathcal{L}_{SM} = \mathcal{L}_{kin} + \mathcal{L}_Y + \mathcal{L}_\phi \tag{11}$$

- $\mathcal{L}_{kin}$: This piece contains all kinetic terms using the covariant derivative, including all the gauge interactions.

[2] In this notation, the numbers in the parentesis are the representation under $SU(3)_C$ and $SU(2)_L$, respectively and the lower index represent the fields charge for the $U(1)_Y$, given by the Gell-Mann Nishijima formula

[3] One can also include $\mathcal{L}_\psi$ (Dirac mass terms) and argue that should be zero due to chirality, i.e. Left and Right fermions are in a different representation

- $\mathcal{L}_Y$: Contains the Yukawa interactions between the fermions and the scalar field. All the quarks and leptons masses are derived from this term. It is the heart of flavour physics.
- $\mathcal{L}_\phi$: The scalar potential.

The local G_{SM} symmetry requires gauge boson degrees of freedom, which have the following representation:

$$G_a^\mu(8,1)_0 \quad W_a^\mu(1,3)_0 \quad B^\mu(1,1)_0 \tag{12}$$

The first is the gluon field and the W's and B represents the $W^\pm, Z^0$ and the photon. In this way, it is not clear which one is which. After the eletroweak symmetry breaking this will become clear. Each boson is a combination of W_a^μ and B^μ.

With these degrees of freedom, the corresponding field strengths describes the gauge boson dynamics:

$$\begin{aligned} G_a^{\mu\nu} &= \partial^\mu G_a^\nu - \partial^\nu G_a^\mu - g_s f_{abc} G_b^\mu G_c^\mu & (13)\\ W_a^{\mu\nu} &= \partial^\mu W_a^\nu - \partial^\nu W_a^\mu - g\epsilon_{abc} W_b^\mu W_c^\mu & (14)\\ B^{\mu\nu} &= \partial^\mu B^\nu - \partial^\nu B^\mu & (15)\\ & & (16) \end{aligned}$$

The first and the second are the $SU(3)_C$ and $SU(2)_L$ field strengths, where the non-commutative algebra can be seen clearly in the last term. In a non-abelian group, the generators do not commute, resulting in a gauge boson self-interaction. This comes with the interaction parameter and the gauge group structure factor. This will lead to vertices with three and four gluons. In the case of EW, things are only clear after the EW symmetry breaking, but there are WWZ and $WW\gamma$ vertices. In order to have a Lagrangian invariant under local G_{SM} one should substitute the regular derivative by a covariant derivative one:

$$D^\mu = \partial^\mu + ig_s G_a^\mu L_a + gW_b^\mu T_b + ig' B^\mu Y \tag{17}$$

In the above equation, Y represents the $U(1)_Y$ charge and L_a and T_b the $SU(3)_C$ and $SU(2)_L$ generators, which are the Gell-Mann and Pauli matrices for triplets and doublets, respectively, and 1 for singlets. The covariant derivatives acting on the fields are given by:

$$\begin{aligned} D^\mu U_{Ri} &= \left(\partial^\mu + \tfrac{i}{2} g_s G_a^\mu \lambda_a + \tfrac{2i}{3} g' B^\mu\right) U_{Li} & D^\mu D_{Ri} &= \left(\partial^\mu + \tfrac{i}{2} g_s G_a^\mu \lambda_a - \tfrac{i}{3} g' B^\mu\right) D_{Li}\\ D^\mu L_{Li} &= \left(\partial^\mu + \tfrac{i}{2} g W_b^\mu \tau_b\right) L_{Li} & D^\mu E_{Ri} &= \left(\partial^\mu - ig' B^\mu\right) E_{Li}\\ D^\mu Q_{Li} &= \left(\partial^\mu + \tfrac{i}{2} g_s G_a^\mu \lambda_a + \tfrac{i}{2} g W_b^\mu \tau_b + \tfrac{i}{6} g' B^\mu\right) Q_{Li} & D^\mu \phi &= \left(\partial^\mu + \tfrac{i}{2} g W_b^\mu \tau_b + \tfrac{i}{2} g' B^\mu\right) \phi \end{aligned} \tag{18}$$

Finally, the kinetic part of the SM Lagrangian is given by:

$$\begin{aligned} \mathcal{L}_{kin}^{SM} &= -\frac{1}{4} G_a^{\mu\nu} G_{\mu\nu}^a - \frac{1}{4} W_a^{\mu\nu} W_{\mu\nu}^a - \frac{1}{4} B^{\mu\nu} B_{\mu\nu} & (19)\\ &- i\bar{Q}_{Li} \not{D} Q_{Li} - i\bar{U}_{Ri} \not{D} U_{Ri} - i\bar{D}_{Ri} \not{D} D_{Ri} - i\bar{L}_{Li} \not{D} L_{Li} - i\bar{E}_{Ri} \not{D} E_{Ri} & (20)\\ &- (D^\mu \phi)^\dagger (D_\mu \phi), & (21) \end{aligned}$$

where $\not{D} = \gamma_\mu D^\mu$.

The Yukawa part of the SM Lagrangian, given by Eq. 22, contains all the relevant parameters to flavour physics. In the charged lepton sector one can diagonalize Y^e with a bi-unitary transformation such that the interaction basis and the mass basis are the same. The same type of transformation can be used to diagonalize either Y^d or Y^u, but not both at the same time. This renders a mass basis which is different from the interaction basis, where the changing basis matrix is the Cabibbo-Kobayashi-Maskawa (CKM) matrix. The redefinition of the fields leave four independent parameters: 3 mixing angles and 1 irreducible phase, which is responsible for the CP violation in weak interactions.

$$\mathcal{L}_Y^{SM} = Y_{ij}^d \bar{Q}_{Li} \phi D_{Ri} + Y_{ij}^u \bar{Q}_{Li} \bar{\phi} U_{Ri} + Y_{ij}^e \bar{L}_{Li} \phi E_{Ri} + h.c. \tag{22}$$

The last piece to this lagrangian is the $\mathcal{L}_\phi$ which is just the scalar potential:

$$\mathcal{L}_\phi^{SM} = -\mu^2 \phi^\dagger \phi - \lambda (\phi^\dagger \phi)^2 \tag{23}$$

Which is responsible for the Higgs couplings and also to give mass to the weak bosons $W^\pm$ and Z^0

2.3 Flavour Physics

In the SM there are three generations, or flavours, for the lepton and quark sectors, represented by the index $i = 1, 2, 3$ in the $\mathcal{L}_{SM}$. After the eletroweak symmetry breaking, the electromagnetic and the weak interaction separate, and since the vacuum is still invariant under the $SU(3)_C \times U(1)_{EM}$, both strong and electromagnetic interactions are *flavour universal*, *i.e* the interactions do not mix different flavours and have the same couplings. However, the weak interactions are different.

There are two types of weak currents: the neutral current (NC) and the charged current (CC). The first is mediated by the Z^0, which couples diagonally, in flavour space, to all fermions of the SM. Consequently, there are no flavour changing neutral currents (FCNC) at tree level. The lack of FCNC experimentally, due the suppresion of the $K^0 \to \mu\mu$ decay, lead to the GIM mechanism and the proposal of the charm quark.

The charged current is mediated by the $W^\pm$ and behaves differently for leptons and quarks. Since in lepton sector, the interaction and mass basis are the same, the CC couples each charged lepton to a single neutrino and vice-versa, so no generation changing occurs. Things are different for charged current in the quark sector. The interaction and mass basis are different, so non-diagonal terms appear in the Lagrangian and generation changing currents occurs. Basically, if a generation changing process is required, one should look to CC weak interactions.

In Eq. 22, the fields are written in the interaction basis. The physical states, the mass states, are obtained performing the bi-unitary transformation for $Y^{u,d}$, this requires four unitary matrices $V_{L,R}^{u,d}$, resulting in the mass matrix $M_{diag}^f = V_L^f Y^f V_R^{f\dagger}(v/\sqrt{2})$, where v is the vacuum expectation value and $f = u, d$.

$$\mathcal{L}_{SM} \supset -\frac{g}{\sqrt{2}} (\bar{u}_L, \bar{c}_L, \bar{t}_L) V_{CKM} \not{W}^+ \begin{bmatrix} d_L \\ s_L \\ b_L \end{bmatrix} + h.c. \qquad V_{CKM} \equiv V_L^u V_L^{d\dagger} = \begin{bmatrix} V_{ud} & V_{us} & V_{ub} \\ V_{cd} & V_{cs} & V_{cb} \\ V_{td} & V_{ts} & V_{tb} \end{bmatrix} \tag{24}$$

2.3.1 CKM matrix and CP Violation

The Cabibbo-Kobayashi-Maskawa matrix is a 3x3 unitary matrix. It is possible to show that the CKM matrix just depends on 4 parameters: 3 mixing angles and 1 irreducible phase. There are different parametrizations of the CKM matrix. The Particle Data Group [16] choice relies on the rotations angles with the complex phase in the 13 matrix element.

$$V_{CKM} = \begin{bmatrix} c_{12}c_{13} & s_{12}c_{13} & s_{13}e^{-i\delta_{13}} \\ -s_{12}c_{23} - c_{12}s_{23}s_{13}e^{i\delta_{13}} & c_{12}c_{23} - s_{12}s_{23}s_{13}e^{i\delta_{13}} & s_{23}c_{13} \\ s_{12}s_{23} - c_{12}c_{23}s_{13}e^{i\delta_{13}} & -c_{12}s_{23} - s_{12}c_{23}s_{13}e^{i\delta_{13}} & c_{23}c_{13} \end{bmatrix} \quad (25)$$

$$(26)$$

$$= \begin{bmatrix} 1 & 0 & 0 \\ 0 & c_{23} & s_{23} \\ 0 & -s_{23} & c_{23} \end{bmatrix} \begin{bmatrix} c_{13} & 0 & s_{13}e^{-i\delta_{13}} \\ 0 & 1 & 0 \\ -s_{13}e^{i\delta_{13}} & 0 & c_{13} \end{bmatrix} \begin{bmatrix} c_{12} & s_{12} & 0 \\ -s_{12} & c_{12} & 0 \\ 0 & 0 & 1 \end{bmatrix} \quad (27)$$

where, $c_{ij} = \cos\theta_{ij}$ and $s_{ij} = \sin\theta_{ij}$. The angle θ_{12} is also known as the Cabibbo angle, which is roughly 13^o. Experimentally, it is known that $s_{13} \ll s_{23} \ll s_{12} \ll 1$, the magnitudes of the CKM matrix are [16]:

$$V_{CKM} = \begin{bmatrix} 0.97427 \pm 0.00014 & 0.22536 \pm 0.00061 & 0.00355 \pm 0.00015 \\ 0.22522 \pm 0.00061 & 0.97343 \pm 0.00015 & 0.0414 \pm 0.0012 \\ 0.00886^{+0.00033}_{-0.00032} & 0.0405^{+0.0011}_{-0.0012} & 0.99914 \pm 0.00005 \end{bmatrix} \quad (28)$$

$$(29)$$

Due the size of the $\theta_{12} = 13.04 \pm 0.05^o$, the Cabibbo angle, different processes are classified by the power of $\lambda = \sin\theta_{12}$. Transitions for which the amplitude depends on $\sin\theta_{12}$ are called **Cabibbo-suppressed**. When the amplitude depends on $\sin^2\theta_{12}$ the transitions are referred to as **doubly Cabibbo-suppressed**. In the case that depends only on $\cos\theta_{12}$ then the process is **Cabibbo-favored**. The ampltude for the $D^+ \to K^-K^+K^+$ decay, subject of this thesis, is proportional to $V_{cd}V_{us}^*$, or, in other words, to $\sin^2\theta_{12}$. This explains the small branching fraction of this channel.

2.3.2 Heavy Flavour Physics

The six quarks of the SM can be organized with respect to their masses in the following order:

$$m_u < m_d < m_s \ll 1\text{GeV} \sim m_c < m_b \ll m_t \quad (30)$$

The masses of the first three quarks are below 1 GeV, the domain of non-perturbative QCD. The charm quark has mass of 1.27 GeV, which is close to the 1 GeV scale. The b-quark has mass of approximately 4 GeV [16]. The study of hadrons containing quarks b and c is called *Heavy Flavour Physics*. The heaviest quark, the top quark, has mass of 173 GeV, almost 10^5 times larger than the lightest quark. Due to its large mass, this quark decays too fast and there is not enough time to hadronize.

The behavior of QCD through scales tells us that at low energy it is impossible to treat it perturbatively. However at high scales this can be done. In this scope, we can divide the effects of QCD in low-energy (or long-distance) and high-energy (or short-distance)

effects. Then, to access the low-energy dynamics we use effective theories when hadronic bound states are the explicit degrees of freedom of theory.

In order to access the parameters of the CKM matrix, flavour changing currents are required. In the scope of hadronic bound states, flavour changing currents can be accessed through decays of heavy hadrons or through flavour oscillations (oscillations from particle to antiparticle). Table 1 summarized the main processes used for the determination of the magnitudes of the CKM elements.

Table 1: Processes used to determine the magnitude of the CKM matrix elements. Extracted from [16]

$\lvert V_{ij}\rvert$	process
$\lvert V_{ud}\rvert$	$0^+ \to 0^+$ nuclear beta decay
$\lvert V_{us}\rvert$	$K_L^0 \to \pi e \nu$
$\lvert V_{cd}\rvert$	semileptonic charm decays
$\lvert V_{cs}\rvert$	semileptonic D or leptonic D_s decays
$\lvert V_{cb}\rvert$	semileptonic decays of B mesons to charm
$\lvert V_{ub}\rvert$	inclusive $B \to X_u l \bar{\nu}$
$\lvert V_{td}\rvert$	$B - \bar{B}$ oscillations
$\lvert V_{ts}\rvert$	$B - \bar{B}$ oscillations
$\lvert V_{tb}\rvert$	top-quark-production

As said previously, the main difficulty in the study of heavy hadron decays is the different scales involved in the process. We have the W boson mass scale, the long- and short-distance QCD effects. The main theoretical issue is related to the long-distance QCD effects, with typical energies below $\Lambda_{QCD} = 1$GeV. The b-quark has mass of 4 GeV, which to some extent can be considered very large compared to the u-quark mass, so the Heavy Quark Effective Field Theory (HQEFT) can be applied. On the other hand, the three lightest quarks have mass below the Λ_{QCD}, and in the 'other' limit can be considered very small, which is the scope of Chiral Perturbation Theory. The problem of the charm quark, and therefore the charm mesons, is that its mass is exactly on the transition between ChPT and HQEFT, typically a energy scale of $\mathcal{O}(2\text{GeV})$. Due to that, what we have in the literature is an extension of one or the other.

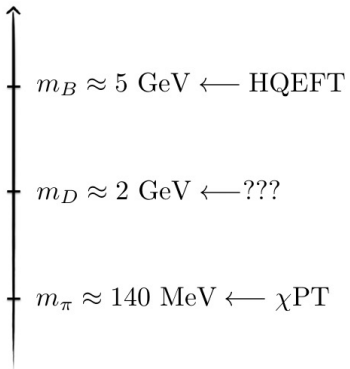

Figure 3: Flavour physics mesons scales

2.3.3 Nonleptonic decays

Nonleptonic decays provide insight in CP violation effects and give info on the CKM matrix. However, the difficulty to treat it from first principles leads to a description of the decay in a phenomenological framework, the quark-diagramatic approach introduced by Chau [17]. This is even harder in the charm regime, where effective theories are applied only in an extented version.

These decays are dominated by intermediate resonances, which makes it even harder to calculate the decay amplitude. Moreover, the presence of strong interactions in the final state, leading to the so called *final state interactions* (FSI), makes the scenario way more involved.

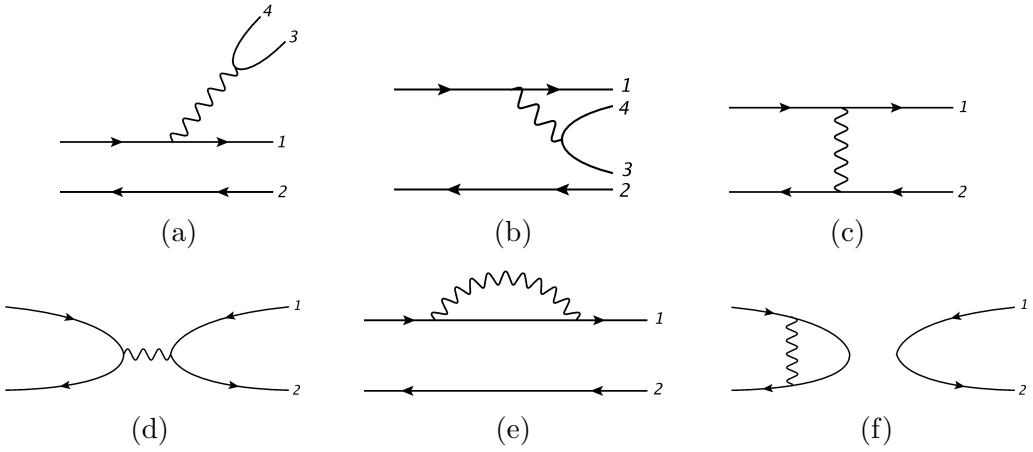

Figure 4: Chau quark-diagram approach for a heavy meson nonleptonic decay

In this approach, all topologies of nonleptonic decays of a D meson are contained in 6 diagrams, shown in Fig. 4 : Diagram *(a)* is called *external W emission* while the *(b)* is the *internal W emission*. The main difference between these diagrams is that the quarks in the external can be in any colour state, whereas in the internal emission, the quark pair must recombine with the other quaks forming colour singlets. The diagrams *(e)* and *(f)* are known as *penguin* and *side-way penguin*. They are really important for B-physics but highly suppressed in charm decays. The diagram *(c)* is called W-exchange diagram and only contribute for neutral mesons.

The last and most important diagram for the $D^+ \to K^-K^+K^+$ is the *(d)*, called *W-annihilation* diagram. In this diagram the quark and antiquark of the initial state meson annihilate producing a W boson, which couples to another quark antiquark pair. The process has two different energy scales. This is somehow a generalization of the Fermi interaction, because this is the only diagram which factorizes the weak interaction (short-distances effects) from the strong hadron interactions (long-distances effects).

2.3.4 $D^+ \to K^-K^+K^+$ using the quark-diagram approach

As shown by Chau [17], the quark diagram amplitude for inclusive decays of charm mesons is:

$$D^+ \to \text{hadrons} = V_{cq_1}V^*_{q_3q_4}[(a)+(b)] + V_{cd}V^*_{q_3q_4}[(d)+(e)] + V_{ci}V^*_{q_1i}[(e)], \quad i = d, c, b \quad (31)$$

Within this approach, in order to produce three particles in the final state, a pair of quarks should be produced from the QCD vacuum The two amplitudes that can contribute for the $D^+ \to K^- K^+ K^+$ are shown below:

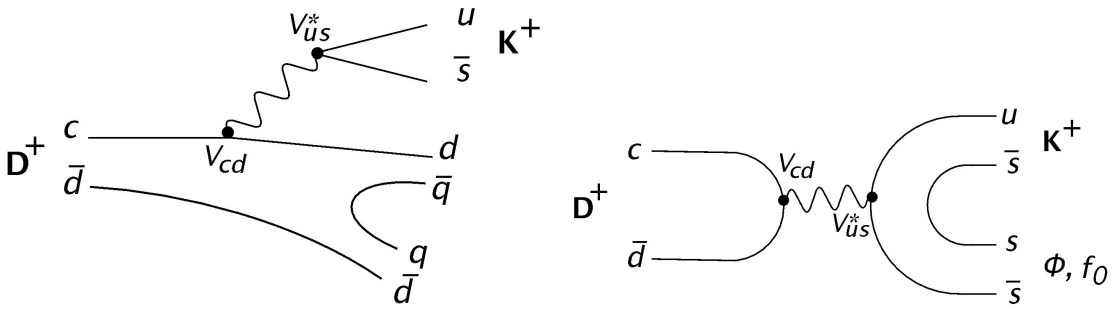

Figure 5: Annihilation diagram for $D^+ \to K^- K^+ K^+$ via ϕ, a_0 and f_0 resonances (left); tree diagram for $D^+ f_0/a_0 K+$ (right).

Inspecting the diagrams on Fig. 5, the first one is a W-external emission. As said in the introduction, the $K^- K^+$ pair can only be produced through rescattering, which suppresses this amplitude. The second diagram is a annihilation diagram and is expected to be the main contributor to the $D^+ \to K^- K^+ K^+$ decay. We are going to present a model to the matrix element $\langle\, (KKK)^+ | A_\mu | 0 \,\rangle$, based on ChPTR. The main elements of this theory will be presented in the following.

2.4 Strong Interaction and chiral symmetry

Using the Chau diagram approach, we inspected the overall CKM dependence of the decay amplitude. However, this does not tell us anything about the strong interactions. A phenomenological model, which we reffer to as Triple-M, was developed, in collaboration with P. C. Magalhães and M. R. Robillota, in order to describe the dynamics of the three kaon final state. The model will be described in detail in Sec. 7. Here we present the theoretical background of its construction.

If we restrict ourselves just to the QCD sector, the lagrangian can be written as [18]:

$$\mathcal{L}_{QCD} = -\frac{1}{2} \left\langle G^a_{\mu\nu} G^{a,\mu\nu} \right\rangle + \sum_f \bar{\psi} (i \not{D} - m_f) \psi \tag{32}$$

Where,

$$D_\mu = \partial_\mu + i g_s A^a_\mu \lambda^a / 2; \quad G^a_{\mu\nu} = \partial_\mu A^a_\nu - \partial_\nu A^a_\mu - g_s [A^b_\mu, A^c_\nu] \tag{33}$$

The main problem of the strong interaction is the running coupling constant $\alpha_s = g_s / 4\pi$ behavior. At low energies, the value of α_s prevents the use of the perturbative approach.

The non-pertubative regime of QCD is then a theoretically challenging problem. One way out to study this problem is Lattice QCD. In this scheme, the continuum space-time is replaced by a discrete statistical mechanical system on a four-dimensional Euclidean lattice. Calculations are then performed numerically with the aid of Monte Carlo methods.

The alternative approach to study non-perturbative QCD is the use of an effective field theory (EFT). An EFT relies on the fact that is not necessary to know the physics of

all scales to describe phenomena at one particular scale. This very intuitive idea allowed years of Newtonian Mechanics without knowing relativity and quantum mechanics. It is completely unnecessary to know the top mass to describe Mercury's orbit. In this sense, if we look to the quark mass spectrum, it spans from $m_u \sim 2$ MeV up to $m_t \sim 180$ GeV, roughly six orders of magnitude. In order to describe low-energy phenomena it should be possible to 'integrate-out' [4] the heavy quarks in the same way that the W boson is integrated out in the Fermi interaction. If the quarks with masses above 1 GeV are integrated out and the light quarks are considered massless, a new symmetry emerges.

2.4.1 Chiral Symmetry

The QCD lagrangian is Lorentz invariant by construction, parity (P), charge conjugation (C), time reversal (T) and $SU(3)_c$ gauge invariant. The masses m_f's for the fermions are given by the Yukawa coupling matrix. Before the EWSB, the left-handed and right-handed fermions belong to different representations of the gauge $SU(2)_L \times U(1)_Y$ group. But after, the left-handed mixes with the right-handed by the elements of Yukawa matrix and the *vev* of the scalar field. Considering this, decomposing the second term in $\mathcal{L}_{QCD}$ in left and right fields:

$$\psi = \frac{1}{2}(1-\gamma_5)\psi + \frac{1}{2}(1+\gamma_5)\psi = \psi_L + \psi_R \tag{34}$$

We obtain, for each fermion, exactly this mix given by the mass term:

$$\mathcal{L}[\psi_L, \psi_R] = i\bar{\psi}_L \not{D} \psi_L + i\bar{\psi}_R \not{D} \psi_R - m(\bar{\psi}_L \psi_R + \bar{\psi}_R \psi_L) \tag{35}$$

In the limit of massless fermions $m \to 0$, an additional symmetry is obtained, which is the concept of *naturalness*. Considering that we just want to study low energy physics, we can think of the other quarks c, b, t masses as heavy degree of freedom that can be integrated out of this theory

With the lightest quarks, the QCD lagrangian can be decomposed in the chiral limit $m_{u,d,s} = 0$, and the mass term becomes:

$$\mathcal{L}_{QCD} = \mathcal{L}^0_{QCD} - \bar{q}\mathcal{M}q, \quad q^T = (u, d, s), \quad \mathcal{M} = diag(m_u, m_d, m_s) \tag{36}$$

With,

$$\mathcal{L}^0_{QCD} = -\frac{1}{2}\langle G^a_{\mu\nu} G^{a,\mu\nu} \rangle + i\bar{q}_L \not{D} q_L + i\bar{q}_R \not{D} q_R \tag{37}$$

which is invariant under the chiral transformation of $U(3)_L \times U(3)_R$:

$$q_R \to R q_R, \quad q_L \to L q_L, \quad R, L \in U(3)_{R,L} \tag{38}$$

As in the case proposed by Gell-Mann, this is a flavour symmetry. Noether's theorem states that for a particular symmetry of the lagrangian, there is a conserved current. And, current conservation implies in charge time-independence and therefore this charge commutes with the Hamiltonian. If the vacuum is invariant under this group transformation, then various one-particle states of the fundamental representation multiplet have the same masses. This realization of a symmetry is called **Wigner-Weyl** mode.

[4] The jargon integrate out comes from the functional path formalism where the quarks are integrated out from the generating functions.

Due to the existence of different quark masses, it is clear that this symmetry is not exact, there is a explicit symmetry breaking. However, effects of a quasi-symmetry should still be seen in a multiplet with particles with the approximate same mass. The same arguments which we are using for $m_{u,d,s}$ could be also used to a more exact symmetry using just $m_{u,d}$ and integrating out also the $s-$quark, this would end up in a SU(2).

The chiral transformation can be rewritten as $U(3)_L \times U(3)_R = SU(3)_V \times SU(3)_A \times U(1)_V \times U(1)_A$, where $L + R = V, \quad L - R = A$. The $U(1)_V$ has the same phase transformation for all quarks and implies in the quark or baryon number conservation. The $U(1)_A$ is broken by quantum effects and is out of the scope of this dissertation (Chiral anomaly).

Following the Wigner-Weyl realization of a symmetry one should expect two multiplet of particles, one vectorial and one axial, for the symmetries $SU(3)_V \times SU(3)_A$. The well-known "eightfold way" appears for the $SU(3)_V$ [14]:

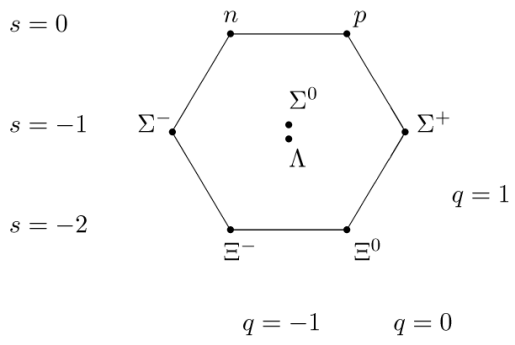

Figure 6: Baryon octet

This octet has nearly the same mass and is explicit broken due the m_s being greater than $m_{u,s}$, so it is an Wigner-Weyl realization of the $SU(3)_V$ symmetry. To look for the $SU(3)_A$ symmetry, we should look for parity partners of the baryon octet. However no axial multiplet appears in the particle spectrum. The alternative symmetry to a Wigner-Weyl is the Nambu-Goldstone mode.

In the **Nambu-Goldstone** realization of a symmetry, the vacuum is not invariant under the transformation and no multiplets of this symmetry appears in the mass spectrum. However, massless particles called Nambu-Goldstone bosons appears as a consequence of the non-zero vacuum expectation value. Strictly speaking, the Goldstone theorem states that [19]:

> Let G represent the symmetry of the Lagrangian, with n_G generators associated with this symmetry and H a subgroup of G, with n_H generators, that leaves the vacuum invariant. As consequence, a mass- and spinless particle, called Goldstone Boson, appears for each unbroken generator, *i.e.* $n_G - n_H$ goldstone bosons emerge due the spontaneous symmetry breaking $G \to H$.

The famous application of this theorem is the Higgs mechanism, where the G group is $SU(2)_L \otimes U(1)_Y$ broken to $H : U(1)_{EM}$. In this case, the Goldstone bosons that appear are 'eaten' by the vector boson in order to acquire mass.

Two empirical observations on the hadron spectrum indicate that a SSB happens in the chiral limit of QCD. First, the $SU(3)_V$ is approximately realized as a symmetry of

hadrons, suggested by the baryon octet. Second, the octet of pseudoscalars mesons have small masses compared to other multiples. These facts suggest that the this octet of pseudoscalars, $\pi^{\pm}, \pi^0, K^{\pm}, K^0, \bar{K}^0, \eta$, are good candidates for the goldstone bosons of a spontaneous symmetry breaking [19]

$$SU(3)_L \otimes SU(3)_R \to SU(3)_V \tag{39}$$

However, there are issues about our candidates. *(i)* How do they acquire mass? *(ii)* How to parametrize these fields, in order words, how to parametrize the goldstone boson from this symmetry breaking? To answer the second question we use a nonlinear parametrization, where we collect all the fields in a matrix U:

$$U = \exp\left(\frac{i\Phi}{F}\right), \quad \Phi = \sqrt{2}\begin{pmatrix} \frac{\pi^0}{\sqrt{2}} + \frac{\eta}{\sqrt{6}} & \pi^+ & K^+ \\ \pi^- & -\frac{\pi^0}{\sqrt{2}} + \frac{\eta}{\sqrt{6}} & K^0 \\ K^- & \bar{K}^0 & -\frac{2\eta}{\sqrt{6}} \end{pmatrix} \tag{40}$$

Where, the F is the pion decay constant and this matrix transform under $SU(3)_L \otimes SU(3)_R$ as:

$$U \to g_L U g_R^{\dagger}, \quad \text{where} \quad g_{L,R} \in SU(3)_{L,R} \tag{41}$$

2.4.2 Chiral Perturbation Theory (ChPT)

Up to now, we have been considering the chiral limit where $m_{u,d,s}$ have zero masses. But, in nature, we know that quarks have mass, small but non-zero. Therefore, the chiral symmetry is **explicitly** broken by the quark masses [18]. However, if the symmetry breaking parameters (quarks masses) are small, then one can do a perturbation expansion and this is ChPT.

The lagrangian that have been proposed, initially by Gasser and Leutwyler [1], models the pseudoscalar interactions and their interactions with external currents to this theory, which are the SM weak and electromagnetic currents. This effective lagrangian includes a mass dependent term that explicitly breaks the chiral symmetry, also implemented by external currents.

The chiral Lagrangian couples to external currents through the covariant derivative:

$$\mathcal{L}^{(2)} = \frac{F^2}{4}[\langle D_\mu U D^\mu U^\dagger \rangle + \langle \chi U^\dagger + \chi^\dagger U \rangle] \tag{42}$$

where,

$$D_\mu U = \partial_\mu U - i(v_\mu + a_\mu)U + iU(v_\mu - a_\mu), \quad \chi = 2B_0(s + ip) \tag{43}$$

At leading order, the lagrangian without the external currents reads:

$$\mathcal{L}^{(2)} = \frac{F^2}{4}[\langle \partial_\mu U \partial^\mu U^\dagger \rangle + 2B \langle \mathcal{M} U^\dagger + \mathcal{M}^\dagger U \rangle] \tag{44}$$

From this model, one can directly see the pseudoscalar masses, at order $\mathcal{O}((m_u - m_d))$:

$$M^2_{\pi^\pm} = B(m_u + m_d), \quad M^2_{\pi^0} = B(m_u + m_d) \tag{45}$$

$$M^2_{K^\pm} = B(m_u + m_s), \quad M^2_{K^0} = B(m_d + m_s) \tag{46}$$

$$M^2_\eta = \frac{B}{3}(m_u + m_d + 4m_s) \tag{47}$$

$$\tag{48}$$

The Gell-Mann-Okubo mass formula is directly extracted from these masses:

$$4M_K^2 = 3M_\eta^2 + M_\pi^2 \tag{49}$$

From this Lagrangian, the $\pi\pi$ scattering amplitude at leading order is given by:

$$A(s,t,u) = \frac{s - M_\pi^2}{F_\pi^2} \tag{50}$$

Although everything seems to work well, a fundamental problem arise from the fact that this amplitude is purely real and the unitarity of the S-matrix requires that (for partial waves t_l^I):

$$Im\ t_l^I = \sqrt{1 - \frac{4M_\pi^2}{s}}|t_l^I|^2 \tag{51}$$

Therefore, an amplitude that respects unitarity should have both imaginary and real parts, related by this formula. In order to correct the real amplitude predicted by the the leading order in ChPT, loops should be introduced in the scope. But with loops, always comes the divergences and renormalizations. In conclusion, in order to have a amplitude that satisfy unitarity, imaginary parts generated by loops should be introduced. In purely ChPT, the common approach is to unitarize the amplitude order-by-order in perturbation theory and NLO will be required.

However, here the unitarization will be done by means of the resummation of all diagrams, using the K-matrix approximation. This will be explained in detail in Sec. 7. The motivation to go beyond the LO is to extend the validity of the theory in energy scale and obtain the resonances as explicit degrees of freedom.

In order to produce a 4-point interaction, we need to expand the U matrix up to 4 powers in Φ:

$$U = 1 + i\Theta - \Theta^2/2! - i\Theta^3/3! + \Theta^4/4! \tag{52}$$

where $\Theta = \Phi/F$. Which results in (again, without external axial and vector currents):

$$\mathcal{L}^{(2)} = \frac{F^2}{4}\langle\, \partial_\mu\Theta\partial^\mu\Theta + \frac{1}{12}[\Theta,\partial_\mu\Theta][\Theta,\partial^\mu\Theta] + 4B\chi\left(1 - \frac{1}{2}\Theta^2 + \frac{1}{24}\Theta^4\right)\rangle \tag{53}$$

The mass term is included via a external s field, $\chi = 2Bs$, whereas $s = \lambda_a s_a$, where λ_a are the Gell-Mann matrices. The vacuum expectation value for this external fields are non zero for only three components: $\langle\, s_0\,\rangle = \sigma_0$, $\langle\, s_8\,\rangle = \sigma_8$ and $\langle\, s_3\,\rangle = \sigma_3$, then we can write the matrix as:

$$\sigma = \sigma_0 I + \sigma_3\lambda_3 + \sigma_8\lambda_8 \tag{54}$$

Taking the traces from all Gell-Mann matrices

$$\begin{aligned}
\mathcal{L}^{(2)} &= 3F^2B\sigma_0 && (55)\\
&+ \frac{1}{2}\partial_\mu\phi_i\partial^\mu\phi_i - B(\sigma_0\delta_{ij} + \sigma_8 d_{8ij})\phi_i\phi_j && (56)\\
&- \frac{1}{6F^2}f_{ijs}f_{kls}\phi_i\partial_m\phi_j\phi_k\partial^\mu\phi_l + \frac{B}{24F^2}\left(\sigma_0\frac{4}{3}\delta_{ij}\delta_{kl} + 2d_{ijs}d_{kls}\right) && (57)\\
&+ \sigma_8\left(\frac{4}{3}\delta_{ij}d_{kl8} + \frac{4}{3}d_{ij8}\delta_{kl} + 2d_{ijm}d_{kln}d_{8mn}\right)\phi_i\phi_j\phi_k\phi_l. && (58)
\end{aligned}$$

The first line corresponds to the vacuum term, the second line corresponds to the free lagrangian of the pseudoscalars and gives its masses, the four-point interaction corresponds to the LO pseudoscalars interactions and will gives us the $KK \to KK$ scattering amplitude, a crucial amplitude to our problem, which will be discussed in more details in Sec. 7

2.4.3 ChPT beyond Leading Order

In order to obtain the resonances as degrees of freedom and extend the validity of the theory, the following question arise: How do we go to higher order in PT? . But first, to add more and more terms, one should do this in a pragmatic way, adding the same relevant order. To classify which types of terms one should add in the lagrangian, we need to go through the Weinberg power counting argument. In this famous paper of phenomenological lagrangians [20], he argued that one should add terms in the expansion following the chiral dimension ν. Considering an arbitrary loop diagram based on an effective lagrangian:

$$\mathcal{L}_{eff} = \sum_d \mathcal{L}^{(d)} \tag{59}$$

then, the amplitude containing L loops, I internal lines, V_d vertices of order d will be:

$$\mathcal{A} \propto \int (d^4p)^L \frac{1}{(p^2)^I} \prod_d (p^d)^{V_d}. \tag{60}$$

After some algebra, the chiral dimension will be:

$$\nu = \sum_d V_d(d-2) + 2L + 2 \tag{61}$$

The chiral dimension is the power that we should introduce the effective Lagrangian. Up to now, we have been considering only tree level amplitude ($L = 0$) and $V_{d>2} = 0$, *i.e* $\nu = 2$. In order to unitarize our theory, we should add loops that correct the imaginary part of the lagrangian. So, going to $\nu = 4$ two types of diagrams will emerge to the amplitude: one-loop graphs with $\mathcal{L}^2$ and tree amplitude graphs from $\mathcal{L}^4$. Then the lagrangian at $\nu = 4$ is:

$$\begin{aligned}
\mathcal{L}^4 &= L_1\langle D_\mu U^\dagger D^\mu U\rangle^2 + L_2\langle D_\mu U^\dagger D_\nu U\rangle\langle D_\mu U^\dagger D_\nu U\rangle && (62)\\
&+ L_3\langle D_\mu U^\dagger D^\mu U D_\nu U^\dagger D^\nu U\rangle + L_4\langle D_\mu U^\dagger D^\mu U\rangle\langle \chi^\dagger U + \chi U^\dagger\rangle && (63)\\
&+ L_5\langle D_\mu U^\dagger D^\mu U(\chi^\dagger U + \chi U^\dagger)\rangle + L_6\langle \chi^\dagger U + \chi U^\dagger\rangle^2 + L_7\langle \chi^\dagger U - \chi U^\dagger\rangle^2 && (64)\\
&+ L_8\langle \chi^\dagger U\chi^\dagger U + \chi U^\dagger\chi U^\dagger\rangle - iL_9\langle F_R^{\mu\nu} D_\mu U D_\nu U^\dagger + F_L^{\mu\nu} D_\mu U^\dagger D_\nu U\rangle && (65)\\
&+ L_{10}\langle U^\dagger F_R^{\mu\nu} U F_{L\mu\nu}\rangle + H_1\langle F_{R,\mu\nu}F_R^{\mu\nu} + F_{L,\mu\nu}F_L^{\mu\nu}\rangle + H_2\langle \chi^\dagger\chi\rangle && (66)
\end{aligned}$$

where,

$$F_{R,L}^{\mu,\nu} = \partial^\mu(v^\nu \pm a^\nu) - \partial^\nu(v^m \pm a^\mu) - i[v^\nu \pm a^\nu, v^\nu \pm a^\nu]. \tag{67}$$

The $L_1, ..., L_{10}$ are the ten low energy couplings (LEC) of order $\nu = 4$, with F and B_0 of $\nu = 2$ fully determined by the theory. The LECs contribution to the amplitude is two-fold: renormalize the $\nu = 2$ lagrangian and add new interactions for the amplitude and the renormalized coupling constants can be written as:

$$L_i^r(\mu) = \sum_{R=V,A,S,P} L_i^R + \tilde{L}_i(\mu) \tag{68}$$

The first term is the renormalized LECs, whereas the second term are the counterterms, where the renormalization scale dependence is. This is the common approach to go beyong ChPT. However, to obtain the resonances, an alternative approach is more useful.

In 1989, G. Ecker, J. Gasser, A. Pich and E. de Rafael [2] shown that the first part of the LECs, *i.e.* the part that does not renormalize, is dominated by resonance contributions, in particular by Vector Meson contributions. To do so, they built a lagrangian of resonances that coupled with the pseudoscalar octet and calculated the contribution from this resonances to the LECs. This lagrangian has the resonances as degrees of freedom of the theory, in contrast with $\mathcal{L}^4$ where they were non-linear effects. In this lagrangian, the resonances are explicit degrees of freedom, which respect the given symmetries of the problem. In our problem, two types of resonances contribution will appear, the scalar and the vector. The former can be described by:

$$\mathcal{L}_S^{(2)} = \tilde{c}_d R_0 \langle\, u_\mu u^\mu \,\rangle + \tilde{c}_m R_0 \langle\, \chi_+ \,\rangle + c_d \langle\, R u_\mu u^\mu \,\rangle + c_m \langle\, R \chi_+ \,\rangle, \tag{69}$$

$$R = \lambda_k R_k \tag{70}$$

where,

$$\begin{aligned} u &= e^{i\Phi/2F} \to u^2 = U, \\ u_\mu &= i u^\dagger D_\mu U u^\dagger = u_\mu^\dagger, \\ \chi_+ &= u^\dagger \chi u^\dagger + u \chi^\dagger u. \end{aligned} \tag{71}$$

The fields S_i are associated with the scalar resonances. Using these definitions, the lagrangian in terms of the ϕ fields are:

$$\begin{aligned} \mathcal{L}_S^{(2)} &= \frac{2\tilde{c}_d}{F^2} R_0 \partial_\mu \phi_i \partial^\mu \phi_i - \frac{4\tilde{c}_m}{F^2} B R_0 (\sigma_0 \delta_{ij} + \sigma_8 d_{8ij}) \phi_i \phi_j \\ &+ \frac{2c_d}{\sqrt{2}F^2} d_{ijk} R_k \partial_\mu \phi_i \partial^\mu \phi_i - \frac{4Bc_m}{\sqrt{2}F^2} \left[\sigma_0 d_{ijk} + \sigma_8 \left(\frac{2}{3} \delta_{ik} \delta_{j8} + d_{i8s} d_{jsk} \right) \right] \phi_i \phi_j R_k; \end{aligned} \tag{72}$$

where $\tilde{c}_d, \tilde{c}_m, c_d$ and c_m are coupling constants of the interactions of the scalars resonances R_0, which is a singlet, and R_k, which belongs to the octet, with the pseudoscalars mesons. This coupling constants can be calculated in the limit of $N_c \to \infty$, given the following approximate relation $|\tilde{c}_d| = |c_d|/\sqrt{3}$ and $|\tilde{c}_m| = |c_m|/\sqrt{3}$. However, this coupling constants can be fixed experimentally and the authors from [2] have some prediction to c_d and c_m based on $a_0 \to \pi\eta$. The same authors found that the contribution of this scalar resonances lagrangian to the LECs, were given by:

$$\begin{aligned} \text{Octet:} \quad L_1^{S_o} &= -\frac{c_d^2}{6M_S^2}, \quad L_3^{S_o} = -3L_1^{S_o}, \quad L_4^{S_o} = -\frac{c_d c_m}{3M_S^2}, \quad L_5^{S_o} = -3L_4^{S_o}, \\ L_6^{S_o} &= -\frac{c_m^2}{6M_S^2}, \quad L_8^{S_o} = -3L_6^{S_o}, \quad H_2^{S_o} = -\frac{c_m^2}{M_S^2}. \\ \text{Singlet:} \quad L_1^{S_1} &= \frac{\tilde{c}_d^2}{2M_{S_1}^2}, \quad L_4^{S_1} = \frac{\tilde{c}_d \tilde{c}_m}{M_{S_1}^2}, \quad L_6^{S_1} = \frac{\tilde{c}_m^2}{2M_{S_1}^2}. \end{aligned} \tag{73}$$

Considering the chiral limit, the mass of the (octet) singlet is denoted by M_S (M_{S_1}). From this we can already suppose that the scalar contributions to the problem is more complicated by the number of contributions.

The resonances related to the vector fields can be given by:

$$\mathcal{L}_V^{(2)} = \frac{F_V}{2\sqrt{2}}\langle\, V_{\mu\nu} f_+^{\mu\nu}\,\rangle + \frac{iG_V}{\sqrt{2}}\langle\, V_{\mu\nu} u^\mu u^\nu\,\rangle \tag{74}$$

where

$$f_+^{\mu\nu} = u F_L^{\mu\nu} u^\dagger + u^\dagger F_R^{\mu\nu} u, \tag{75}$$

and

$$\langle\, V_{\mu\nu} u^\mu u^\nu\,\rangle = \frac{1}{F^2} V_a^{\mu\nu} \partial_\mu \phi_i \partial_\nu \phi_j (i f_{aij} + d_{aij}), \tag{76}$$

where $V_a^{\mu\nu}$ is an element of the vectorial octet. Considering again the chiral limit, where the masses of the vector octet is given by M_V, the following contribution of the LECs are:

$$\begin{aligned} L_1^V &= \frac{G_V^2}{8M_V^2}, \quad L_2^V = 2L_1^V, \quad L_3^V = -6L_1^V, \\ L_9^V &= \frac{F_V G_V}{2M_V^2}, \quad L_{10}^V = -\frac{F_V^2}{4M_V^2}, \quad H_1^V = -\frac{F_V^2}{8M_V^2}. \end{aligned} \tag{77}$$

The constant G_V is a universal coupling constant and, in the limit $N_c \to \infty$, can be approximated to $G_V = F_\pi/\sqrt{2} = 65.3$ MeV. However, these couplings F_V and G_V are well determined by the data in the $\rho^0 \to e^+e^-$ and $\rho \to 2\pi$ decays, giving :

$$|F_V| = 154 \text{ MeV} \quad \text{and} \quad |G_V| \quad 69 \text{ MeV}. \tag{78}$$

3 The LHCb experiment

> It doesn't matter how beautiful your theory is, it doesn't matter how smart you are. If it doesn't agree with experiment, it's wrong.
>
> Richard P. Feynman

The baryon asymmetry of the Universe cannot be explained by the CP violation mechanism of the SM. Therefore, new sources of CPV beyond the SM are required. Many extensions of the SM introduce new CP violating phases, which could manifest themselves via virtual loops processes, in rare decays of beauty and charm hadrons. As consequence, Heavy Flavour Physics is the perfect place to search for those new sources.

3.1 The Large Hadron Collider

The Large Hadron Collider (LHC) is, up to date, the most powerful particle accelerator for Physics Research. Located at CERN, Geneva, it is designed to collide two beams of protons with center-of-mass energy of 14 TeV, but it is also capable to collide heavy (Pb) ions with energy of 2.8 GeV per nucleon. The collider has 27 km of circumference and it is located 110 meters underground, in the same tunnel that once acommodated the Large Electron Positron Collider (LEP) [21].

The protons passes through a complex chain of accelerator before reaching the LHC. This chain consists of the LINAC2 - BOOSTER - PS - SPS - LHC, shown in Fig. 7. First, protons are created via ionization of hydrogen gas and accelerated by a linear accelerator (LINAC2) up to 50 MeV. And goes through the PSB (Proton Synchrotron Booster), which splits the beam in four bunches that are accelerated to an energy of 1.4 GeV. Protons are then injected in the PS (Proton Synchrotron), acquiring an energy of 25 GeV and in the Super Proton Synchrotron (SPS), the last step before the LHC, where the beam energy reaches 450 GeV. In the LHC storage ring, the beam is accelerated up to the desired energy.

The LHC has 4 interaction points, where the main experiments occurs: ATLAS (Point 1), CMS (Point 5), LHCb (Point 8) and ALICE (Point 2).

ATLAS The "A Toroidal LHC ApparatuS experiment" is a general purpose experiment dedicated to precision measurements of the SM and searches for New Physics. This experiment operates at full luminosity.

CMS The Compact Muon Solenoid has the same purpose of ATLAS experiment and, together, they were responsible for the Higgs discovery.

LHCb The LHC-beauty experiment is dedicated to the study of CPV and rare decays. In contrast with the previous one, it operates at a modest luminosity.

ALICE A Large Ion Collider Experiment is a dedicated experiment to study the Quark Gluon Plasma (QGP) colling heavy ions (Pb-Pb).

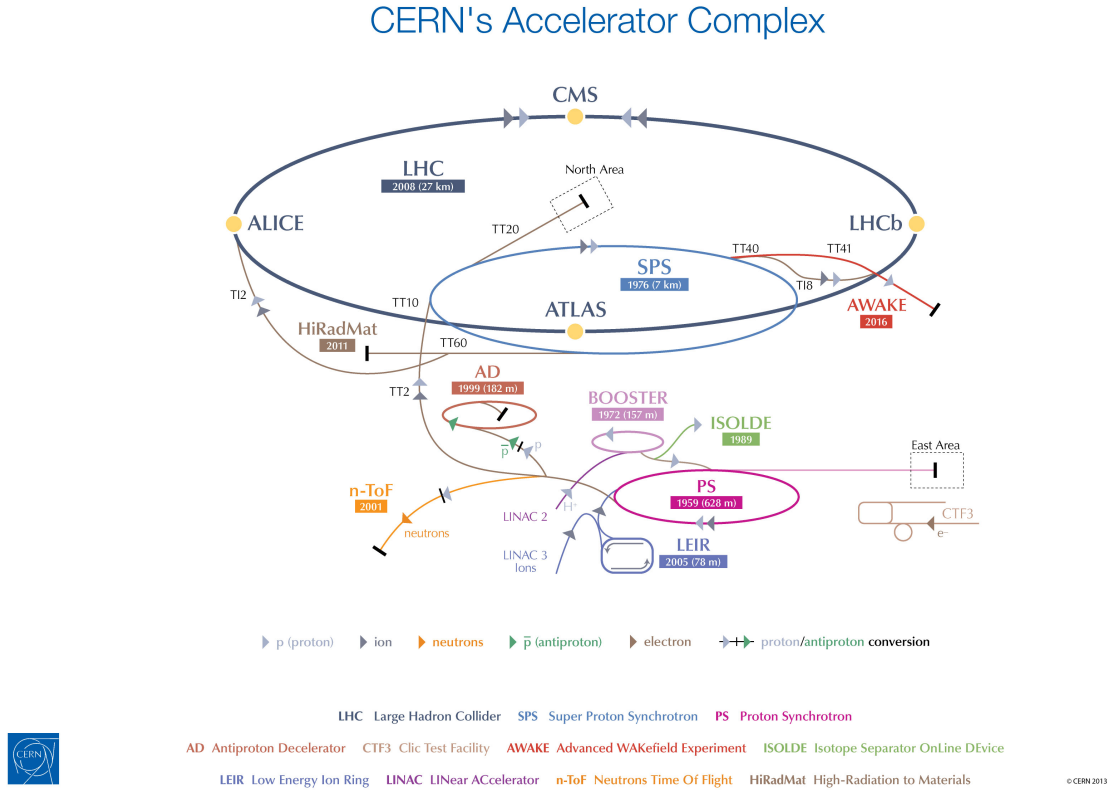

Figure 7: Schematic view of the CERN accelerator complex [22]. The four main experiments are also displayed.

3.1.1 Luminosity

The number of events for a particular process depends on the cross section σ and on the luminosity $\mathcal{L}$ via:

$$N_{\text{ev}} = \mathcal{L}\sigma_{\text{ev}} \tag{79}$$

Where, the luminosity is given by:

$$\mathcal{L} = \frac{N_b^2 n_b f_{rev} \gamma_r}{4\pi\epsilon_n \beta^*} F \tag{80}$$

Each term of this equation depends on the beam configuration: N_b and n_b are the number of particles per bunch and the number of bunches per beam, respectively. f_{rev} the revolution frequency, γ_r the relativistic gamma factor, ϵ_n the normalized transverse beam emittance, β^* the optic function at the collision point, and F the geometric luminosity reduction factor due to the crossing angle between the two beams at the interaction point (IP).

The LHC was designed to deliver an instantaneous luminosity up to $\mathcal{L} = 10^{34} cm^{-2} s^{-1}$. The peak luminosity value can be tuned by changing the beam focus at its IP, i.e. changing the F factor in Eq. 80, this can be done independently for each interaction point. The two high-luminosity experiments, ATLAS and CMS, exploit this value. However, the LHCb operates at a modest luminosity of $\mathcal{L} = 10^{32} cm^{-2} s^{-1}$.

The advantages of a reduced luminosity includes lower occupancy, lower radiation damage and, mainly, the fact that the events are dominated by single pp interaction per bunch, which facilitates the data analysis.

3.1.2 Heavy Flavour Physics

In Sec. 2, we have shown that Heavy flavour physics is a privileged field to understand Flavour physics open questions and the LHC is an unique place to study such problems. In order to produce Open Flavour states, one should first produce $b\bar{b}$ or $c\bar{c}$. The LHC production cross section for b and c quarks are enormous, making it a abundant source of these states. Fig 8 shows the relevant processes to $b\bar{b}$ and $c\bar{c}$ pair production,which are: $q\bar{q}$ annihilation, gluon separation and gluon fusion, respectively. These process are highly correlated in the polar angle because the two heavy quarks are produced in the foward direction.

Recently, LHCb has measured the $b\bar{b}$ and $c\bar{c}$ production cross-section at $\sqrt{s} = 7$ TeV and for $\sqrt{s} = 13$ TeV. In this thesis, we use data from Run I, collected in 2012, corresponding to a $\sqrt{s} = 7$ TeV. The results are shown in the table below. At this energy, the expected factor between $b\bar{b}$ and $c\bar{c}$ corresponds to roughly 20. However, the numbers for $\sqrt{s} = 13$ TeV corresponds to a factor of 2 compared to 7 TeV.

$\sigma(pp \to b\bar{b}X)$ at 7 TeV	$75.3 \pm 5.4(\text{stat}) \pm 13.0(\text{sys})\mu b$
$\sigma(pp \to c\bar{c}X)$ at 7 TeV	$1419 \pm 12(\text{stat}) \pm 116(\text{sys}) \pm (\text{frag})\mu b$

Table 2: Charm and beauty inclusive production cross section, from [23, 24]

Assuming the LHCb reduced luminosity of $\mathcal{L} = 4 \times 10^{32} cm^{-2} s^{-1}$ and the above cross-sections, the production rate of $c\bar{c}$ is around 600 kHz per second. In constrast, the $b\bar{c}$ production rate is roughly 30 kHz. This 20 factor between both explains why the main background contribution to b-hadrons analysis comes from the charm.

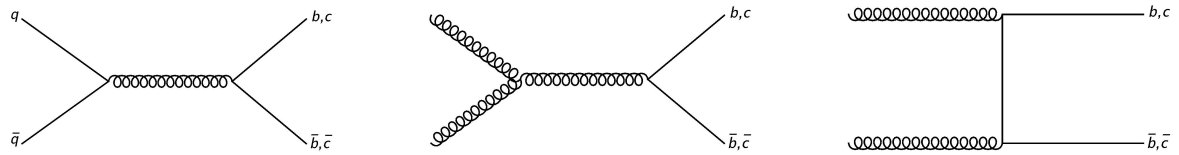

Figure 8: Dominant process to $b\bar{b}$ and $c\bar{c}$ pair production

Due this very large data samples, two interesting areas of heavy flavour *precision* spectroscopy emerges as a byproduct of the search for CP violation [25]:

- Hidden flavor states, i.e. $c\bar{c}$ and $b\bar{b}$ heavy quakonium states
- Open flavor states, i.e. $B^{\pm}$, B^0, B_s^0, $B_c^{\pm}$, $D_s^{\pm}$, D^0 and $D^{\pm}$ meson systems and charm and beauty baryons

In 25 August of 1995, the LHCb Letter of Intent was first published [25], proposing open geometry forward collider detector to study B-physics [5] that fully exploit this $b\bar{b}$ production rate and the $b\bar{b}$ angle correlation.

[5] At that time, the experiment name was LHC-B

3.2 Overview of the experimental setup

The LHCb detector is a single-arm spectrometer with a forward angular coverage from approximately 10 mrad to 300 (250) mrad in the bending (non-bending) plane, which corresponds of a pseudorapidity[6] range $2 < \eta < 5$. This geometry layout was chosen due the $b\bar{b}$ pair angle correlation, as shown in Fig 9.

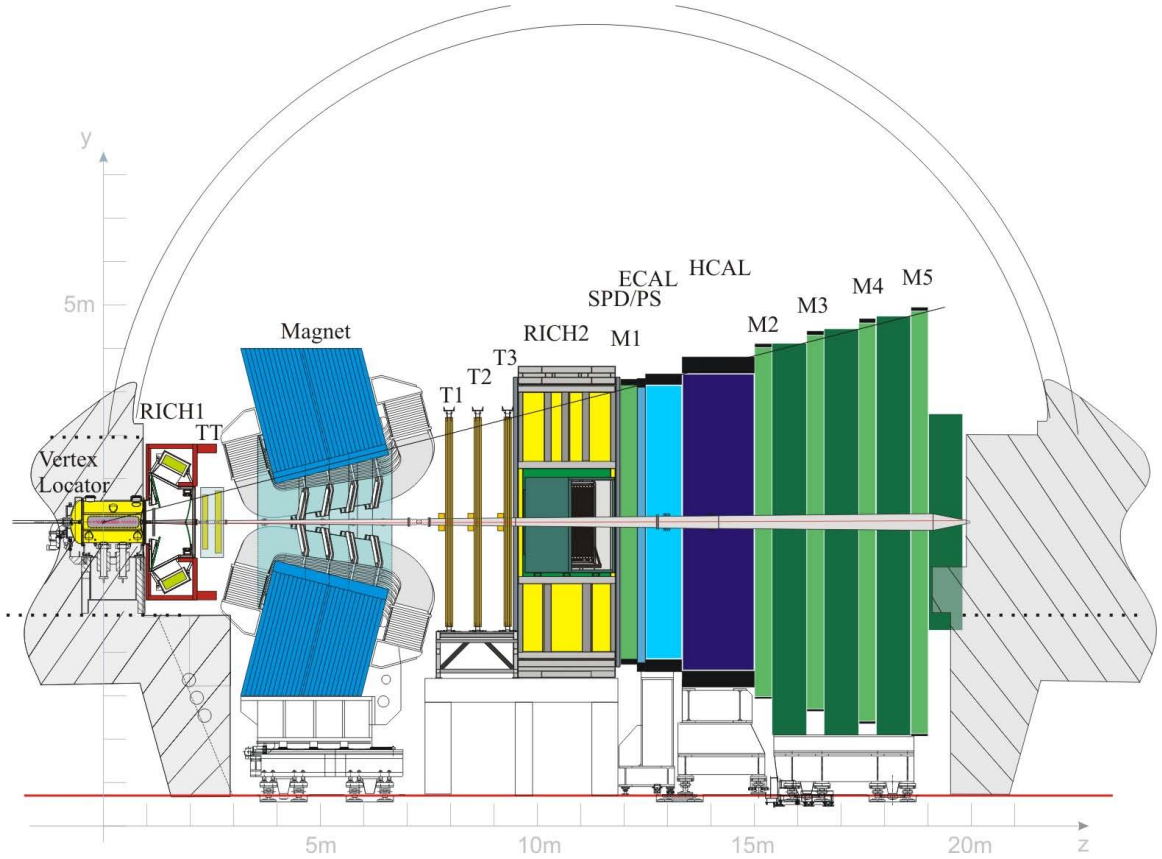

Figure 9: Schematic view of the LHCb layout [26]

The pp collisions occur inside the Vertex Locator (VELO) detector, which consists of a series of silicon modules measuring radial (r) and azimuthal(ϕ) coordinates, along the beam axis. After the collision, the particles goes through the first Ring Imaging Cerenkov (RICH) detector and the Tracker Turicensis (TT), these detectors are located upstream the LHCb Magnet. The LHCb magnet is a dipole magnet providing an magnet field of 4Tm bending power, which deflects the charged particles in the horizontal axis ($x - z$ plane), displayed in Fig. 9. Downstream the magnet, there are the T1-T3 tracking stations, another RICH detector (RICH2), the Electromagnetic and Hadron Calorimeter (ECAL and HCAL) and Muon system.

3.3 Tracking system

The LHCb Tracking system consists on VELO and the four planar tracking stations, two downstream the LHCb magnet and two upstream. The VELO is closest sub-detector

[6]Pseudorapidity is defined as $\eta \equiv -\ln\left[\tan\frac{\theta}{2}\right]$, where θ is the polar angle

to the LHC and is the main contributor to the excellent vertex reconstruction of LHCb. This tacking system gives an excellent measurement of the particle momentum p with a relative uncertainty varyng from 0.4% at low momentum up to 1% at 200 GeV/c.

3.3.1 Vertex Locator

The VELO detector is a series of 42 silicon modules, each one providing information about the radius r (R-sensors) and the azimutal angle ϕ (ϕ sensors) according to the reference axis in Fig. 9. A cylinder geometry was chosen to provide a faster reconstruction of tracks and vertices in the LHCb trigger. Two planes are located most upstream to the impact parameter and are called *pile-up veto system*, which is used to reject multiple pp interactions in the trigger.

A precise determination of particle trajectiories is a vital requirement for the LHCb detector. The VELO detector, which is the main contributor to this, is required to have excellents signal-to-noise ratio, efficiency and resolution. It has a primary vertex (PV) spatial resolution of $40\mu m$ along the z axis and plays a signification role in the trace reconstruction. The minimum distance between the PV and the track is called impact parameter (IP) and is measured with a resolution of $(15 + 29/p_T)$ μm, where p_T is the transverse momentum. Due to its proximity to the beam, another requirement is to be capable to operate in extreme radiation conditions, which degrade the sensors in the long-term, reducing its performance. To deal with this problem, a radiation tolerant technology had to be chosen.

The 42 silicon modules are divided into two retractable halves, which stay 4cm from the beam during the injection, when the beam is not stable, and 8mm when the beam is stable. This is done in order to avoid radiation damage to the sensors. Each module has three basic functions: assure that the sensors are in a fixed position relative to the module support, provide and connect the electrical readout to the sensors. and, for the modules operating in vacuum, it must enable thermal management. Each semicircular $R-$ and $\phi-$sensor are exposed to a high neutron fluence ($1.3 \times 10^{14} n_{eq}/cm^2$), which correspond to a year of operation at nominal luminosity. This environment influenced on the choice of a 300 μm thick n-implants in n-bulk technology (n^+-on-n). Using this technology, the minimum pitch, located at the innermost radius, is 38 μm increasing linearly to 101.6 μm at the outer radius of 41.9 mm. The readout of each of these sensors are done by 16 Analog ASICs chips a total of 32 Beetle chips for each module.

3.3.2 Silicon Tracker

The Silicon Tracker consists of two detectors. The first is the Tracker Turicensis (TT), located upstream the LHCb Magnet, and the second one, downstream the magnet, is the Inner Tracker (IT). The T1-T3 are separated in two parts (Inner and Outer) in order to cover the full detector acceptance. Following VELO's idea, both TT and IT use silicon microstrips with a strip pitch of 200 μm. The Silicion Trackers detectors design was chosen considering: Spatial resolution, Hit occupancy, Signal shaping time, Single-hit efficiency, Radiation damage, Material budget and Number of readout channels.

The TT, shown in Fig. 11, covers the full acceptance of the experiment and consists on a planar tracking station with 150 cm wide and 130 cm high. It has four layers disposed in a "x-u-v-x" layout, where the x is aligned with horizontal axis and u and v are rotated by

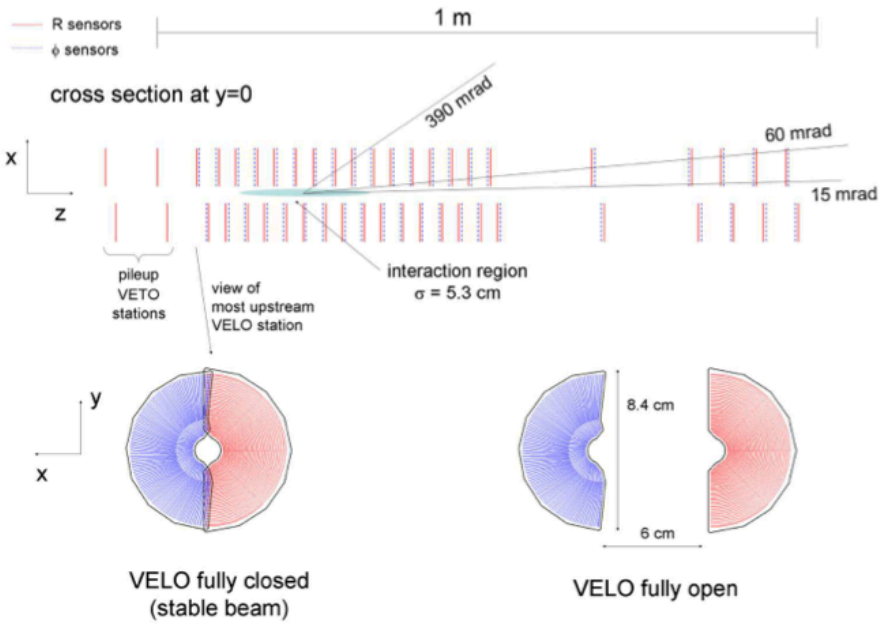

Figure 10: Schematic view of the VELO [27]

a stereo angle of $+5^o$ and -5^o, respectively. Such design provides a sufficient redundancy to resolve the particle trajectory. The TT detector is particularly important for decays occurring downstream to the VELO and with low momentum particles.

The IT, also shown in Fig. 11, consists on four boxes displayed around the LHC beam pipe. Each one of the boxes has four detection layers, each one with seven detectors modules. This cross-shaped detector is 120 *cm* wide and 40 *cm* and is located in the center of the three tracking stations.

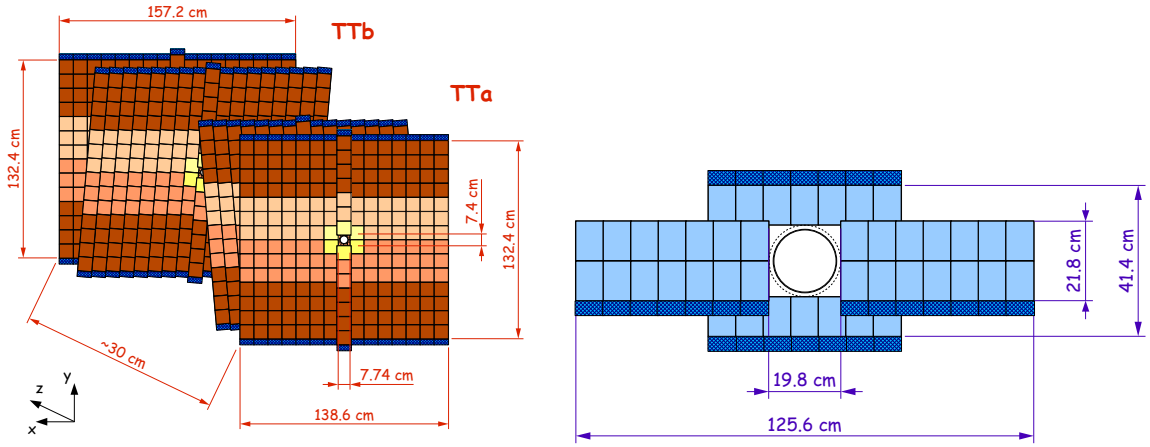

Figure 11: Schematic view of the TT (left) and IT (right) [28]

3.3.3 Outer Tracker

Also part of the three downstream tracking stations, the OT is a drift-time detector covering a large acceptance area. It consists on an array of individual, gas-tight straw-tube modules. The gas is a mixture of 70% of Argon an 30% of CO_2, this guarantees a fast drift time, essential for the tracking algorithm. Each one of these modules contains two layers of drift-tubes with inner diameters of 4.9 mm.

3.3.4 Tracking reconstruction

The tracking reconstruction exploits the information of all trackers in order to reconstruct the particle trajectory. The reconstruction strategy aims at an optimal momentum resolution and reconstruction efficiency and it occurs in a two stage process. The first step is to search for a track seed, straight lines joining clusters, in the VELO detector. A cluster is defined as set of three R-sensor and ϕ-sensors measurements. This information is then extrapolated with the z coordinate of the module to reconstruct the complete track. Secondly, this cluster is fitted using a Kalman filter [29] method, which is an recursive method (refreshing the information from the fit to the seed) giving a final three-dimensional track.

There are five types of tracks in the LHCb depending on which detectors are hit, as illustrated in Fig. 12. The first type is the VELO track. As the name says, it is the track which hits only the VELO detector. Secondly, the upstream tracks have hits only in the VELO and in the two upstream trackers; T tracks, have hits only in the T stations; downstream tracks hits not only the T stations but also the TT. And finally, the long tracks have hits in the VELO and the T stations, but can additionally have hits in TT.

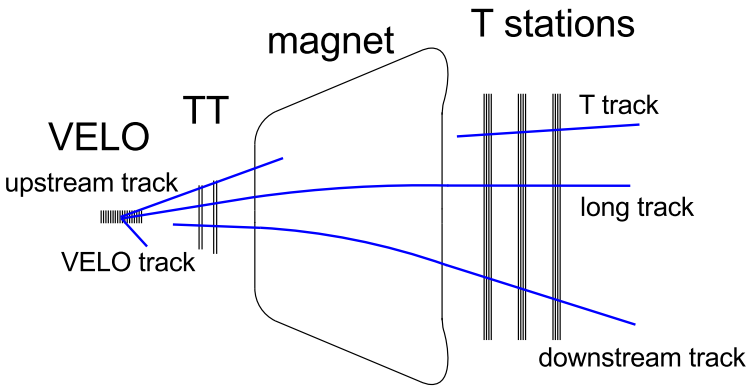

Figure 12: Tracking detectors and track types reconstructed by the track finding algorithms at LHCb. [30]

3.4 Particle identification

3.4.1 RICH

RICH detectors are based on Cherenkov radiation. When a charged particle transverse a medium with a velocity greater than the speed of light *in that medium*, radiation is

emitted in a cone with aperture θ_c with respect to the particle trajectory. This angle, called Cherenkov angle, can be related to the particle velocity with the following formula:

$$cos\ \theta_c = \frac{1}{n\beta}, \tag{81}$$

where n is the refraction index of the medium and $\beta = \gamma c$, being γ the Lorentz factor and c the speed of light. Through this formula one may determine the the particle rest mass, once the momentum is measured (obtained using TT trackers information).

The RICH1, located upstream the TT stations, uses aerogel SO_2 ($n = 1.03$) and C_4F_{10} ($n = 1.0014$) and it is optimized to measure low and intermediate momentum tracks from $[2, 60]$ GeV and covering the full angular LHCb acceptance of $25 - 300$ mrad. In contrast, RICH2 is optimal for the high momentum tracks from $[15, 100]$ GeV but it only covers the acceptance near the beam pipe of $15 - 120$ mrad, with the use of CF_4 ($n = 1.0005$).

The use of two RICH detectors is fundamental to obtain full momentum coverage. Both detectors uses similar optical system, with a primary spherical mirror focusing on the secondary flat mirror, which allows the photon detectors to be placed outside the acceptance coverage. The photons are detected using an Hybrid Photon Detectors (HPDs), measuring the position of the photon.

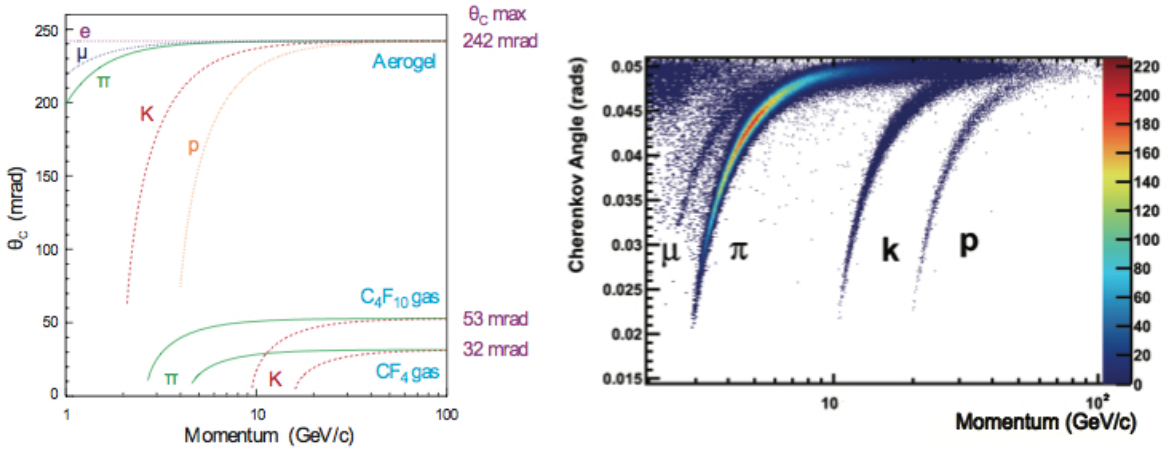

Figure 13: RICH performance at LHCb. [31]

3.4.2 Calorimeters

The importance of the Calorimeter system is twofold: The first is to provide the identification of electrons, photons and neutral hadrons and the measurement of their energies and positions. Secondly, it selects the transverse energy hadron, electron and photon candidates for the L0. The calorimeter system has four sub-detectors. The first two are the Scintillating Pad Detector (SPD) and the Preshower (PS), followed by the classical structure of an Electromagnetic and a Hadron Calorimeter (ECAL and HCAL, respectively). When a particle transverse a medium, it loses energy accoding to the Bethe-Bloch

equation [16]. In other words, the energy loss is inversely proportional to the radiation length, X_0. This particle can interact with the medium and produce secondary particles, which can also interact, leading to a particle shower. The calorimeter philosophy is to absorb all of the energy of the incident particles. In order to do this, a high Z material is interleaved with scintillating material. The showers generate photons in scintillators and this light is transmitted to photomultipliers (PMT) by wavelength-shifting (WLS) fibers.

The ECAL measures the energy deposit of electrons and photons and reconstruct neutral pions. It consists of 66 alternating layers of 2 mm thick lead, 4 mm thick scintillator tiles and 120 μm white reflecting paper. Due the occupancy the ECAL is separated in three regions: Inner, Middle and Outer section, which varies in cell size. This scheme is also adopted in the SPD/PS. The detector layout was designed to achieve an energy resolution of $\sigma_E/E = 10\%/\sqrt{(E)} \oplus 1\%$, where the Energy is in GeV.

The HCAL measures the energy deposit of hadrons and, in contrast with the SPD/PS and ECAL, has only 2 sections (Inner and Outer); alternating layers of 16 mm thick of iron and 4 mm of scintillator plates, which are oriented parallel to the beam pipe. With this design and energy resolution of $\sigma_E/E = 69\%/\sqrt{(E)} \oplus 0.9\%$ can be achieved.

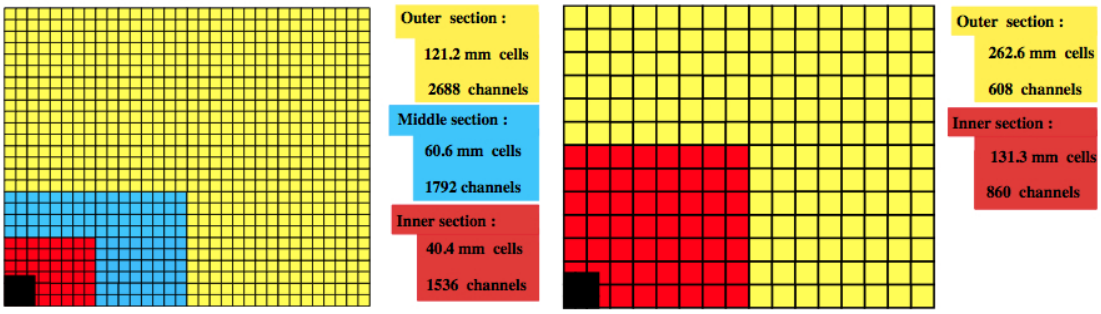

Figure 14: CALO SPD/PS, ECAL (left) and HCAL (right). [27]

3.4.3 Muon system

The muon system is responsible for identification of muons, and is one of the main components of the hardware-based trigger . It consists of five stations (M1-M5), the first one located upstream the Calorimeter and the others downstream, as shown in Fig. 15. These are the most downstream detectors of the LHCb. The M2-M5 stations are interleaved with iron absorbers of 80 cm thick in order to avoid hadron background. Each of the M-stations is divided into four regions, called R1-R4. The size of these regions increase as one moves away from the beam axis,with segmentation scale using the ratio 1:2:4:8. This geometry is used in order to achieve the same occupancy over the four regions. All the downstream stations are instrumented with Multi Wire Proportional Chamber (MWPC), except the R1 region of the M1-stations, which uses Gas Electron Multiplier (GEM) detectors.

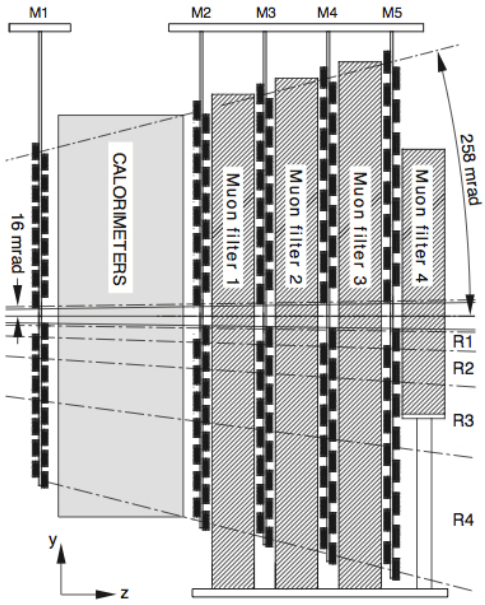

Figure 15: Schematic view of the Muon Stations. [27]

3.5 Trigger system

The bunch cross rate at the LHC is 40 MHz (1 event bunch cross each 25 ns). This enormous rate is well beyonf the LHCb capability of data storage. The trigger system is responsible for reducing this high rate selecting only the interesting events in an effective way. This process is separated in two stages. Firstly the hardware stage, which requires a fast decision, reducing the rate from from 40 MHz to 1 MHz. Secondly, the High Level Trigger, software-based reducing from 1MHz to 5kHz. This final rate allows the storage for offline analysis.

3.5.1 First Level Trigger (L0)

The L0 is the first stage of the trigger and is hardware-based. Since one of the requirement is to reduce the rate from 40 MHz to 1 MHz, a decision has to be made each $4\mu s$ (which defines the trigger latency) syncronized with the LHC clock. The philosophy in the L0 is to exploit the fact that $b-$hadrons decays products have large momentum and transverse energy E_T. Using the information from the *pile-up system* at the VELO, the Calorimeter and the Muon system, a L0 Decision Unit (LDU) evaluates a final boolean decision.

3.5.2 High Level Trigger (HLT)

After the hardware decision, a more elaborated trigger decision is performed [32]. The HLT is a C++ application running in the CPU of an Event Filter Farm (EFF). This full software implementation enables a great flexibility that evolves with the real data knowledge and physics priorities of the experiments. The first task of the HLT is to confirm the L0 decision and afterwards reject the great amount of uninterested events using only part of the event data information, due the CPU and time limitations. This

process is divided in two stages: HLT1 and HLT2. The HLT1 performs a partial event reconstruction and an inclusive selection of signal candidates, reducing the rate from 1MHz to 80 kHz. This rate allows a full pattern reconstrucion by the HLT2, with a set of inclusive and exclusive selections. The HLT2 reduces the tigger rate to 5 kHz, and the remaing events are saved for more offline selections. Differents triggers lines are relevants for each specific channel, here is discussed only the relevant for this analysis.

The HLT1 reconstructs the tracks segments in the VELO. Track segments with high IP tracks and track segments that can be matched with hits in the muon chambers are then extrapolated into the main tracker. The `Hlt1TrackAllL0` trigger line, used for inclusive beauty and charm, aim for good displacement from the PV and quality track candidates based on their p_T ($p_T > 1.6$ GeV).

The HLT2 performs a full event reconstuction for all tracks with $p_T > 300$ MeV, reducing the rate to 5 kHz. The relevant exclusive selection for prompt charm is the hadronic three body trigger line `Hlt2CharmHadD2HHH`. Both trigger line cuts are better described in Sec. 5.

An essential event feature for this analysis is its association with the trigger. A particular event signal track can fire or not the trigger. If the signal track fires the trigger it is classified as TOS (Trigger On Signal), otherwise is classified as TIS (Trigger Independent of Signal). This feature will be studied in the analysis at Sec. 5. The trigger efficiency can be obtained for non-exclusive classification of TOS and TIS, obtained through:

$$\epsilon^{TOS(TIS)} = \frac{N^{TIS\&\&TOS}}{N^{TIS(TOS)}} \tag{82}$$

4 Amplitude Analysis and kinematics

I visualize geometry better than numbers.

Richard Dalitz

In experimental particle physics, the common approach to study any process is to prepare a given state with a definite particle content in an asymptotic time $t \to -\infty$ and measure the final state in the limit $t \to +\infty$. Both states in initial and final limits are described by means of a free theory, where the particles do not interact. Between these limits, the phenomena is described by a interacting theory, in which calculations are done using perturbative approaches.

The transition amplitude between an initial state $|i\rangle$ and a final state $|f\rangle$ is written using the $\mathcal{S}$-matrix:

$$\mathcal{S}_{fi} = \langle f|\mathcal{S}|i\rangle = \langle f|i\rangle - 2\pi i\langle f|\mathcal{M}|i\rangle. \tag{83}$$

The first term represents the scenario where nothing happens, *i.e,* the particles do not interact. The second term represents the interaction, where $2\pi i$ is just a normalization factor. Lorentz invariance requires the $\mathcal{S}$-matrix to be an unitary operator. Although this matrix represents the amplitude for a given process, it is not the measured quantity in the experiment. The observables are rates and cross-sections. The *decay rate* gives the number of decays per unit of time divided by the number of initial state particles present [33]. A generic differential decay rate, $d\Gamma$, where a particle M, with momenta p, decays into n-particles in the final state f is given by:

$$d\Gamma = \frac{1}{2M}\left(\prod_{i=1}^{n}\frac{d^3p_i}{(2\pi)^3}\frac{1}{2E_i}\right)|\mathcal{M}|^2(2\pi)^4\delta^{(4)}(P - \sum_{i=1}^{n}p_i). \tag{84}$$

Momentum and energy conservation are ensured by the delta function. The term between parentesis is the Lorentz invariant phase space element. In this work, we deal with a three-body decay, particularizing for $n = 3$ particles in the final state and considering them on-shell ($p^2 = E^2 - |\mathbf{p}|^\mathbf{2}$):

$$d\Gamma = \frac{(2\pi)^4}{2M}|\mathcal{M}|^2\delta^4(P - \sum_{i=1}^{3}p_i)\prod_{i=1}^{3}\frac{d^4p_i}{2\pi^3}\delta(p_i^2 - m_i^2) \tag{85}$$

4.1 Kinematics of three-body decays

In a three-body decay, the decay rate only depends on two variables, this can be argued counting the degrees of freedom (d.o.f). We start with 12 of them (3 four-momenta vectors) and imposing momentum conservation between final and inital state, 4 constraints, and considering these particles on-shell, 3 constraints, which decreases for 5 of them. Since this decay is a pseudoscalar into pseudoscalares we have 3 angle invariance constraints, ending up with only two variables.

In 1953, Richard Dalitz used a particular choice of Lorentz invariant variables to analyze the decay $\tau^+ \to \pi^+\pi^+\pi^-$ [34]. The chosen variables, $s_{ij} = (p_i + p_j)^2$, provides a constant phase space element, a fundamental feature for the analysis. This allows us to identify any deviation as a dynamical effect. This work was a relevant contribution

for the $\theta - \tau$ puzzle. The θ^+ and the τ^+ particles had equal masses, but the θ^+ decayed into a positive parity state ($\pi^+\pi^0$) and τ^0 to a negative parity state ($\pi^+\pi^+\pi^-$). The discovery that weak interactions does not conserve parity allowed the identification of θ and τ mesons as the same particle, called nowadays the K^+ meson.

In the rest frame of the decaying particle, the initial 4-momentum is $P^\mu = (M, 0, 0, 0)$ and the 4-momentum of the decay products are $p_i^\mu = (E_i, \vec{p}_i)$. Energy and momentum conservation imply $P^\mu = p_1^\mu + p_2^\mu + p_3^\mu$. One can construct the following Lorentz invariants:

$$\begin{aligned} s_{ij} &= (p_i + p_j)^2 = m_i^2 + m_j^2 + 2E_iE_j - 2\vec{p}_i\vec{p}_j & (86)\\ &= (P - p_k)^2 = M^2 + m_k^2 - 2ME_k. & (87)\end{aligned}$$

From this equation the maximum and minimum value of s_{ij} are given by:

$$(m_i + m_j)^2 \leq s_{ij} \leq (M - m_k)^2, \tag{88}$$

and from the 3 invariants only two are linear independent. The third is given by

$$s_{12} + s_{13} + s_{23} = M^2 + m_1^2 + m_2^2 + m_3^2. \tag{89}$$

Using properties of the Dirac delta function, one can show that the differential decay rate is proportional to the matrix element squared.

$$\frac{d\Gamma}{ds_{ij}ds_{jk}} = \frac{1}{(2\pi)^3}\frac{1}{32M^3}|\mathcal{M}|^2 \tag{90}$$

One immediately sees that if $|\mathcal{A}|^2$ is constant, the Dalitz plot (DP) will be uniformly populated. Any observed structure reflects the dynamics of the decay. A representation of the Dalitz plot can be seen below.

The minimum of s_{12}, $(s_{12})_{\min} = (m_1+m_2)^2$, represents the configuration where particles 1 and 2 are collinear and with opposite direction to the particle 3. The maximum of s_{12}, $(s_{12})_{\max} = (M - m_3)^2$ occurs when particles 1 and 2 are emitted back-to-back, with particle 3 at rest. A similar reasoning holds for θ_{13} and θ_{23}

A comment should be made here about the choice of variables s_{ij}. It is clear that any choice of two variables from the s_{12}, s_{13} or s_{23} set can be made. In this thesis, the final-state particle ordering is such that particle 1 is always the one with opposite charge. Mesonic resonances decaying into two pseudoscalars are neutral states, so it is natural to choose combination of particles with negative and positive charge. In this case will be s_{12} and s_{13}, so the resonance appear as vertical and horizontal bands. The subtlety in the $D^+ \to K^-K^+K^+$ is that two of the final-state particles are identical. As consequence, the amplitude should be symmetric with respect to s_{12} and s_{13}. In such cases, a possible choice of variables takes into account the K^+ momentum, forming the invariants $s_{high}(s_{low})$ combining the K^- with the K^+ with the highest (lowest) momentum. In a similar way, one also construct the s_{low} variable. The Dalitz plot as a function of s_{high} and s_{low} is a folded version of the previous one.

Hereafter, the choice will be s_{12} and s_{13} for the Dalitz Plot. Although, some of them can also be shown in the $s_{high} \times s_{low}$ version.

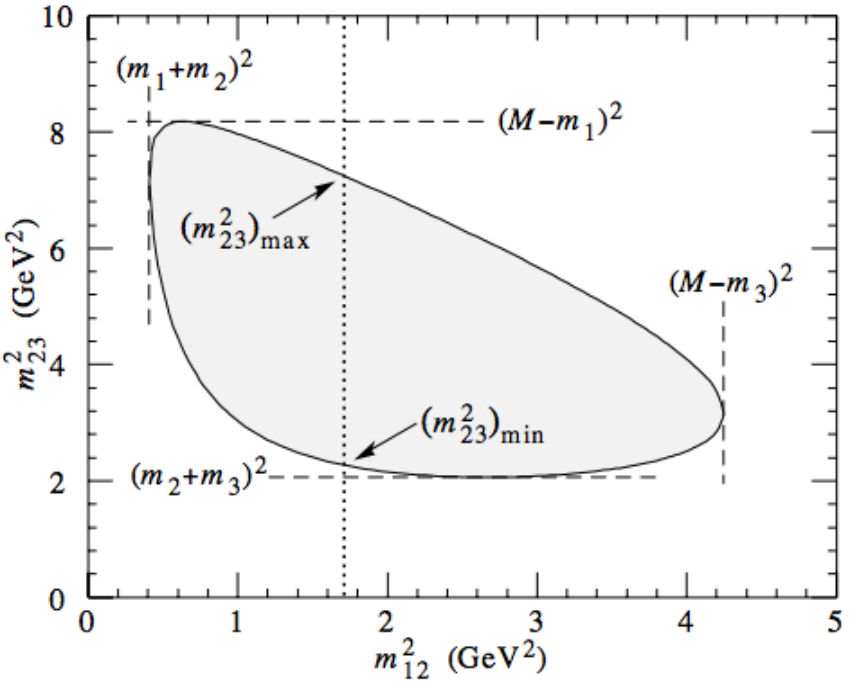

Figure 16: A DP of the $M \to m_1 + m_2 + m_3$ decay. Minimum and maximum values of the invariants are shown. Figure from [16]

4.2 Isobar model

The most common approach for the description of the decay amplitude in the Daliz plot is the Isobar model [35]. It consists of a coherent sum of resonant amplitudes, describing sequential process dominated by intermediate resonant states. In the case of three-body decays,the mother particle decays into a resonance plus a pseudoscalar. The resonance then decays into two pseudoscalars: $D \to Rc$, $R \to ab$. In addition to the resonance states, the mother particle may decay directy into the final-state particles, a process which is referred to as nonresonant (NR) decay. This nonresonant contribution is usually modelled by a constant amplitude across the phase space. This constant behavior will be revisited in the 3M model.

The total Lorentz invariant amplitude, $\mathcal{M}$, is then written as a coherent sum of a nonresonant and resonant amplitudes [16]:

$$\mathcal{M} = c_{NR}A_{NR} + \sum c_k A_k. \tag{91}$$

The nonresonant amplitude is parametrized by a complex constant c_{NR} ($A_{NR} = 1$). The resonant complex coefficients $c_k = a_k e^{i\delta_k}$ are unkown parameters to be determined by a fit to the data. One of the c_k coefficients is fixed, determining the scale and the phase convention for the other coefficients. In some cases, besides the c_k's fit parameters, the amplitude A_k may also have some additional free parameters, such as masses and widths of resonances.

The general form of A_k in the Isobar model is a product of form factors, F_D and F_R, representing the D^+ and resonance decay vertices, respectively, angular distributions, $\mathcal{S}$, which takes into account the angular momentum conservation in the decay between

the resonance and the other particle, and a dynamical function M_k, representing the resonance propagator, or the 2-body lineshape (a Breit-Wigner function in almost all cases). Considering that the resonant state is the $K_1^- K_2^+$ system, the amplitude is given by:

$$A_k(s_{12}, s_{13}) = \underbrace{F_D^L F_R^L}_{\text{Form Factors}} \times \underbrace{\mathcal{S}(\theta_{13}^{R12})}_{\text{Angular distributions}} \times \underbrace{M_k(s_{12})}_{\text{Resonance propagator}} \tag{92}$$

Form Factors

The form factors F_D^L and F_R^L are parametrized by the Blatt-Weisskopf penetration factors [36]. These factors are responsible for the suppression of states with angular momentum greater than zero close to the threshold. The D^+ meson is a pseudoscalar particle, *i.e.* spin-0. The resonance spin, J, is, therefore, equal to the orbital angular momentum L in the decay $D^+ \to RK^+$, and also to the orbital angular momentum l in the resonance decay $R \to K^- K^+$. From now on, the label L will be used to specify any angular momentum in the decay amplitude. Since for spin > 0 an angular dependence is required, a reference frame should be chosen: In the rest frame of the resonance, $\mathcal{R}12$, we define q as the momentum of either the K^- or the K^+, and q_0 the value of q when $s_{12} = m_R^2$. The parameter d is related to the decaying mesons radius. Defining $z = (qd)^2$ and $z_0 = (q_0 d)^2$, both form factors can be written in different formulations, given in the table below:

L	B_L	B'_L
0	1	1
1	$\sqrt{\frac{2z}{1+z}}$	$\sqrt{\frac{1+z_0}{1+z}}$
2	$\sqrt{\frac{13z^2}{1+z}}$	$\sqrt{\frac{(z_0-3)^2+9z_0}{(z-3)^2+9z}}$

Table 3: Blatt-Weisskopf form factors for angular momentum $L = 0, 1, 2$ with two distinct formulations.

In this thesis, the formulation chosen is the B'_L, with the momenta in F_D^L and F_R^L always computed in the rest frame of the decaying particle.

Angular distributions

In order to describe the angular dependence of A_k, we use the Zemach formalism described in [37] for the angular distribution $\mathcal{S}$. This function is defined using the angle $\theta_{13}^{R12} = \theta_{13}^{R12}(s_{12}, s_{13})$, which is the angle between the K_1^- and the K_3^+ momenta measured in the rest frame of $K_1^- K_2^+$ system, $\mathcal{R}12$:

$$\mathcal{S} = (-2|p_1||p_3|)^L P_L(\cos\theta_{13}^{R12}), \tag{93}$$

where P_L is the Legendre polynomial of order L. Although it seems that $\mathcal{S}$ is reference dependent, it only depends on the two invariants s_{12} and s_{13}, making it also Lorentz invariant. For scalar resonances, this term is constant and 1.0 across all the Dalitz Plot. However, for vector resonances, it has zeros where the helicity angle is either 90^o or 180^o.

Lineshapes

In atomic physics, an unstable state appears as a *resonance* and near the resonance energy the scattering amplitude is given by the non-relativistic Breit-Wigner formula, which was created to describe resonant transitions in capture of slow neutrons. [33]:

$$f(E) \propto \frac{1}{E - E_o + i\Gamma/2}. \tag{94}$$

This is an approximation valid for narrow and isolated resonances. The relativistic formulation of the Breit-Wigner formula is written as

$$\frac{1}{p^2 - m^2 + im\Gamma}. \tag{95}$$

Since the Isobar model assumes that one particle is the spectator, the resonance occurs in a given channel, *e.g.* s_{12}, and the formula for the Isobar model is:

$$\mathrm{BW}(s_{12}) = \frac{1}{m_R^2 - s_{12} - im_R\Gamma(s_{12})}, \tag{96}$$

where m_R is the mass of the resonances and $\Gamma(s_{12})$ is the mass-dependent width:

$$\Gamma(s_{12}) = \Gamma_R \left(\frac{q}{q_0}\right)^{2L+1} \frac{m_R}{\sqrt{s_{12}}} \left(\frac{F_R^L(z)}{F_R^L(z_0)}\right)^2, \tag{97}$$

where Γ_R is the resonance width.

Another lineshape commonly used for resonances that couple to different channels is the Flatté [38]. This formulation will be used in this work to represent a resonance with mass close to a threshold, such as an $f_0(980)$:

$$\mathcal{F}(s_{12}) = \frac{1}{m_R^2 - s_{12} - im_R(\rho_{\pi\pi}g_\pi^2 + \rho_{KK}g_K^2)}, \tag{98}$$

where g_π and g_K are dimensionless coupling constants to the $K\bar{K}$ and $\pi\pi$ channels, respectively, and $\rho_{\pi\pi}$ and ρ_{KK} are the corresponding phase space factors,

$$\rho_{\pi\pi} = \sqrt{\left(\frac{s_{12}}{4} - m_\pi^2\right)} + \sqrt{\left(\frac{s_{12}}{4} - m_{\pi^0}^2\right)} \tag{99}$$

$$\rho_{KK} = \sqrt{\left(\frac{s_{12}}{4} - m_K^2\right)} + \sqrt{\left(\frac{s_{12}}{4} - m_{K^0}^2\right)}. \tag{100}$$

4.3 Fitting procedure

The optimum values of the $c_k's$ parameters are obtained using the *Maximum Likelihood Method*, taking in account the efficiency variation across the Dalitz plot and the background distribution. The fit is performed in the `Rio+` software.

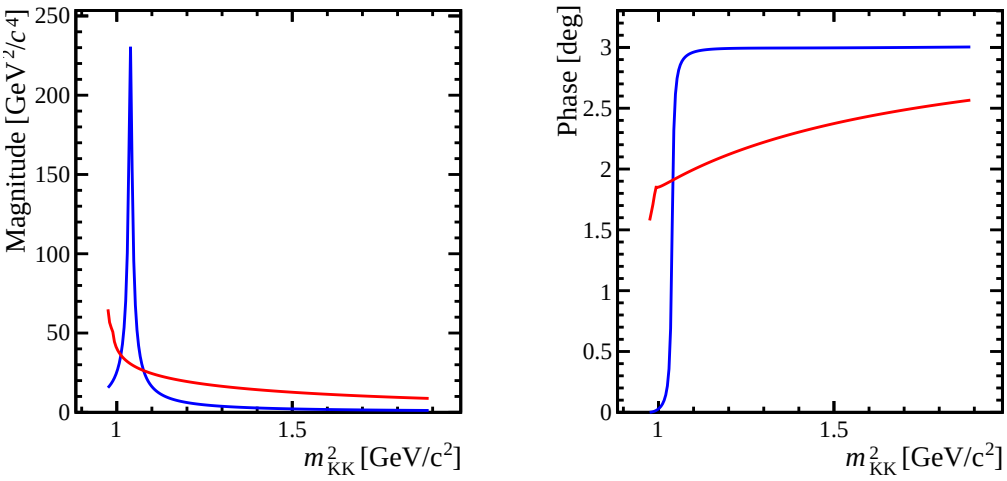

Figure 17: Lineshapes for the $\phi(1020)$ and the Flatté $f_0(980)$

Maximum Likelihood method

The maximum likelihood method (MLM) is a method for parameter estimation, given set of data points $x : x_1, ..., x_N$. The model to describe the distribution of these data points is called probability density function (PDF) $f(x;\theta)$, which depends on a set of parameters $\theta : \theta_1, ..., \theta_{N_{par}}$.
The task of the MLL is to determine the optimum set of θ's values based on the data x's. This is also called *statistical inference*. To perform this inference, one need to define the likelihood function:

$$\mathcal{L}(x;\theta) = \prod_{i=1}^{N} f(x_i;\theta) \tag{101}$$

The optimum set of θ's values is the one that maximizes the $\mathcal{L}(x;\theta)$ function, *i.e.* solve the equation $\frac{\partial \mathcal{L}}{\partial \theta_k} = 0$. Alternatively, one can instead of maximizing $\mathcal{L}(x;\theta)$, minimize the quantity $-2\log\mathcal{L}$, the negative log likelihood (NLL). In this way, a sum is performed instead of a product:

$$-\frac{\partial}{\partial\theta}\ln\mathcal{L} = -\frac{\partial}{\partial\theta}\sum_{i=1}^{N}\ln f(x_i;\theta) = 0 \tag{102}$$

Amplitude analysis

The goal of an amplitude analyses is to determine the resonant structure in multi-body decays. In addition to the model for the decay amplitude $\mathcal{M}$, one has to consider the variation of the detection efficiency and the background distribution across the phase space. Efficiency and background will be described in the next section. The likelihood function is a sum of two terms, the signal PDF ($S_{\rm pdf}$) and the background PDF, ($B_{\rm pdf}$). Each of these terms comes with a multiplicative factor which is the fraction of signal f_S^i, depending on the $K^-K^+K^+$ invariant mass of the event and described in the next Section, and the background fraction $(1 - f_S^i)$

$$\mathcal{L} = \prod_{events} f_S^i \times S_{\rm pdf}(s_{12}^i, s_{13}^i) + (1 - f_S^i) \times B_{\rm pdf}(s_{12}^i, s_{13}^i), \tag{103}$$

To ensure the convergence of the fit, a likelihood function normalization is required. This is done independently for the signal and the background. The normalized signal PDF is

$$S_{\rm pdf}(s_{12}, s_{13}) = \frac{1}{N_S}|\mathcal{M}(s_{12}, s_{13})|^2\varepsilon(s_{12}, s_{13}) = \frac{1}{N_S}\left|\sum_k c_k A_k(s_{12}, s_{13})\right|^2 \varepsilon(s_{12}, s_{13}). \quad (104)$$

Where, $\varepsilon(s_{12}, s_{13})$ is the efficiency function. The normalization factor, N_S, is given by

$$N_S = \int {\rm d}s_{12}{\rm d}s_{13}\left|\sum_k c_k A_k(s_{12}, s_{13})\right|^2 \varepsilon(s_{13}, s_{13}). \quad (105)$$

The optimum set of parameters is determined by minimizing the quantity $-2\log\mathcal{L}$, using the `MINUIT` package. Once determined, one can define the *fit fraction* for each decay channel, FF_k, and the interference fit fractions FF_{ij}, which defines a rate for a single channel and interference between channels, respectively. The sum of fit fractions and interference fit fractions is, by construction, 100%. The fit fraction of a given channel is calculated by the formula:

$$\mathrm{FF}_k = \frac{\int |c_k A_k(s_{12}, s_{13})|^2 {\rm d}s_{12}{\rm d}s_{13}}{\int \left|\sum_i c_i A_i(s_{12}, s_{13})\right|^2 {\rm d}s_{12}{\rm d}s_{13}}. \quad (106)$$

In general, the sum of the fit fractions is different from 100% due to interferences. If it is greater than 100%, this indicates the presence of a constructive interference between different channels and a value less than 100% a destructive. The difference is due the interference fit fractions, that can be defined as:

$$\mathrm{FF}_{ij} = \frac{\int 2\mathrm{Re}|c_i c_j^* A_i A_j^*|^2 {\rm d}s_{12}{\rm d}s_{13}}{\int \left|\sum_k c_k A_k(s_{12}, s_{13})\right|^2 {\rm d}s_{12}{\rm d}s_{13}}. \quad (107)$$

4.4 Isobar Model approach limitations

The Isobar model is widely used in amplitude analyses in almost all experiments but it has its own limitations. The main issue with the isobar model is the three-body unitarity and final state interactions. In 2015, the LHCb and the CBPF organized a workshop on multi-body decays of B and D mesons [39], with experimentalist and theorists, in order to trigger a discussion on new tools for amplitude analysis. One of the question asked is about the **rescattering**. How does one describe it in D and B decays? And what happens with the inclusion of multiple channels?

The rescattering is a final state interaction effect and can be divided into two different mechanisms. The first is the two-body rescattering. This problem has been extensively studied with the aid of ChPT and dispersion relations. This should include all possible effects in a two-body system, *i.e.* all possible interactions, resonances and coupled channels. These effects are embebbed in the width of a resonance state. The second mechanism is the three-body rescattering. All the considered models work in the (2+1) approximation, where one final state particle are considered to be the spectator and does not interact.

The Isobar model considers the first type of rescattering in the width of the resonance states. However, it is not clear which effects are included in the two-body rescattering

since instead of the interaction, the width of the resonances are included as an input. On top of that, it is also not clear the rôle of rescattering in nonresonant states, commonly parametrized as a constant . The second effect is ignored in the Isobar model. But, this effect could be relevant in some regions of the phase space. The problem is the difficulty of parametrizing interactions with hadron loops involving all three final state particles.

These two issues are commonly called three- and two-body unitarization and were the most discussed topics in the workshop.

In this scope, the limitations of the Isobar Model also include [40]:

- poles of BW are in general not identical to the true poles of the $\mathcal{S}$-matrix
- BW do not reproduce the analytical properties of reaction amplitudes
- sum of BWs violates unitary

Despite all this complication, they work. Sebastian Neubert has shown in a LHCb Amplitude Analysis Group presentation, called "Why Amplitude Models are Garbage and why they work nevertheless", that a sum of BWs represent wrong analytical properties but the coefficients c_k's are flexible enough to accommodate some of its problems.

Lastly, the importance of a parametrization of the non-resonant amplitude that, in the Isobar model, is just a constant function all across the phase space, interfering with all other resonances. However, the problem is that a constant amplitude does not assume any dynamics for the system going from a D meson directly to 3K and some interaction, due to rescattering, are expected.

Aiming to understand these problems, the Multi-meson model was proposed and will be discussed in Sec. 7

5 Data selection, background and efficiency

In God we trust, all others must bring data

W. Edwards Deming

In this section, we describe the selection of the final samle, the determination of the efficiency variation across the Dalitz plot and the model for the background. The online event selection is performed by a trigger [27], which consists of a hardware stage, based on information from the calorimeter and muon systems, followed by a software stage, which applies a full event reconstruction. The offline selection is performed in two stages. The first stage - stripping - is based on general features of the decay topology and on loose PID requirements. In the second stage, or final selection, a multivariate analysis is employed to further reduce the combinatorial background and tight PID requirements are used to eliminate peaking background structures. These selection requirements introduce variations across the DP phase space, which are corrected by MC simulations. Therefore, the final efficiency is combined using simulations and data-driven methods. Even after the selection, a remaining noise - or *background* - always stays in the sample. This remaining contamination has to be modeled so the final PDF does not overestimate (or underestimate) the signal.

5.1 Definition of variables

Before we proceed to the data selection criteria it is necessary to define the relevant variables to the problem. These variables are used both in the stripping and final selection. The vast majority of B and D mesons are produced in the pp collision point, called Primary Vertex (PV), and decay after traversing distances of order of 1 cm, due to its relatively short lifetime ($c\tau_D = 311.8\mu m$). The D meson decay point is called Secondary Vertex (SV) and the *flight distance* (FD) is, as the name suggests, the distance between the production, PV, and the decay point, SV. The FD information is given by the VELO detector with excellent precision.

The main variables considered in this analysis are:

D Mass (`D_MM`) The invariant mass of the three kaons, $\texttt{D\_MM} = \sqrt{(p_1^\mu + p_2^\mu + p_3^\mu)^2}$.

D transverse momentum (`D_PT`) The absolute value of the transverse component of the D momentum relative to the beam axis.

Flight distance χ^2 (`FD` χ^2) It is defined as the ratio between the FD squared and the fit uncertainty of PV and SV.

D Impact parameter (D_IP) Defined as the minimum distance between the D^+ reconstructed trajectory and the PV.

D Impact parameter χ^2 ($\texttt{IP}_{\chi^2}$) It is defined as the χ^2 fit difference with and without the D^+ reconstructed trace, which is defined as the diference in the vertex-fit χ^2 the PV reconstructed with and without the D^0 candidate trajectory

Cosine of the direction angle (`DIRA`) The direction angle is defined and the angle between the PV-SV vector and the D^+ tri-momentum vector.

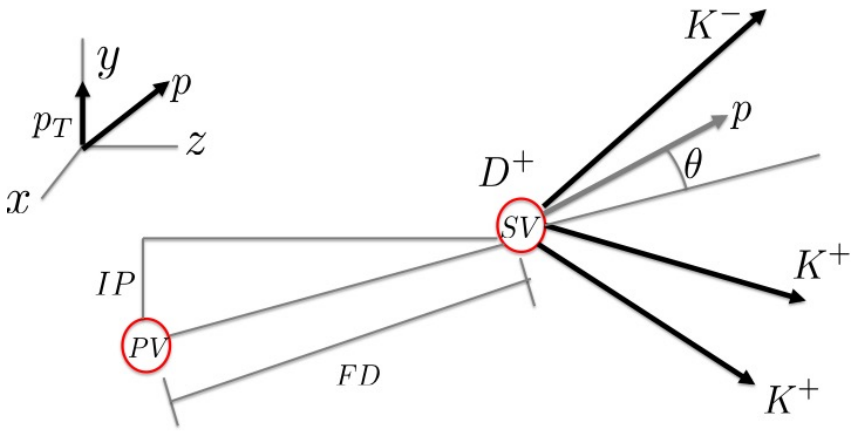

Figure 18: Topology of the production process of the meson D and its decay $D^+ \to K^-K^+K^+$. The D^+ tri-momentum, which defines its trajectory, is represent by p.

Secondary Vertex χ^2 (`Vertex` χ^2) It is the χ^2 of the secondary vertex fit. Vertex χ^2 requires that the daughter trace forms a good vertex.

Daughters IP w.r.t PV (p_i $\texttt{IP}_{\chi^2}$)

Daughter transverse momentum (P_T^i) The absolute value of the transverse component of the i-th daughter momentum relative to the beam axis.

`PTsum` Sum of the three daughters transverse momentum P_T^i.

$\texttt{doca}_{ij}$ Distance of closest approach between the tracks i and j.

Particle Identification (p_i `PID`) Using the RICH information, for each track it is calculated the likelihood to be one of the possible particles: pion, kaon, protons, electrons and muons. The p_i `PID` is the likelihood separation. In our case, we are going to use the p_i `PIDK`, which is $\ln \mathcal{L}(K) - \ln \mathcal{L}(\pi)$ for the i particle. It belongs to the class of variables called Combined Delta LogLikelihood (DLL).

Particle Identification NN (p_i `ProbNN`) The ProbNN is a multivariate Particle Identification, is the response of an Artificial Neural Network, called PIDANN. This algorithm is tuned on simulated signal and background samples. The DLL and the ProbNN method has a better perfomance depending on the particle momentum. The best performance is achieved combining both techniques.

`logIP` Defined as the logarithm of the ratio between the product of the daughter's χ^2_{IP} and the D^+ χ^2_{IP},
$\texttt{logIP} = \frac{\prod_i p_i\texttt{\_IP}_{\chi^2}}{\texttt{D\_IP}_{\chi^2}}$

`POINTING` It is a weighted comparison of transverse momenta of the mother and its daughters. The transverse momentum of the mother is defined w.r.t its flight direction, whereas for the daughters the transverse momentum is defined w.r.t the z-axis:

$$\text{POINTING} = \frac{p \sin\theta}{p \sin\theta + \sum p_{\text{T}i}}, \tag{108}$$

5.2 Selection

In 2012, the LHCb collected a data sample of approximately $2.0\,\text{fb}^{-1}$ of pp collisions at $\sqrt{s} = 8$ TeV. In order to avoid some bias in the sample due to the magnet polarity, $1.000 \pm 0.012\,\text{fb}^{-1}$ were taken with magnet polarity up (MagUp) and $0.988 \pm 0.012\,\text{fb}^{-1}$ with magnet polarity down (MagDown). During the data taking, the magnet polarity was reversed several times, in order to cancel systematic effects due to small left-right differences in the detector performance.

5.2.1 Online selection: trigger requirements

The trigger [41] consists of a hardware stage, based on information from the calorimeter and muon systems, followed by a software stage, in which all charged particles with $p_T > 300$ MeV are reconstructed for 2012 data. For triggers that require neutral particles, energy deposits in the electromagnetic calorimeter are analysed to reconstruct π^0 and γ candidates.

At the hardware trigger stage, events are required to have a muon with high p_T or a hadron, photon or electron with high transverse energy in the calorimeters. For hadrons, the transverse energy threshold is 3.5 GeV. The software trigger requires a two-, three- or four-track secondary vertex with a significant displacement from any primary pp interaction vertex. At least one charged particle must have a transverse momentum $p_T > 1.6$ GeV/c and be inconsistent with originating from a PV. A multivariate algorithm is used for the identification of secondary vertices consistent with the decay of a b hadron

In the offline selection, trigger signals are associated with reconstructed particles. Selection requirements can therefore be made on the trigger selection itself and on whether the decision was due to the signal candidate, other particles produced in the pp collision, or a combination of both.

For the first hardware trigger selection, the data set should be divided into two independent samples, in order to correct by the trigger efficiency lately. These two subsets are `L0_TOS` or `L0_TIS&&!L0_TOS`. The ratio between `L0_TOS` and `L0_TIS&&!L0_TOS` is 2:1 with an overlap of 15%. A schematic diagram of the independent samples is shown in Fig. 19.

In this analysis, it is required either `L0Hadron_TOS` or `TIS` on the `L0` for `Hadrons, Electrons, Photons` and `Muons`.

The second stage in the trigger selection is the *software* trigger, performed using the accepted events by the `L0`. For the first level software trigger, the inclusive line `Hlt1TrackAllL0` selects good quality track candidates based on their p_T and displacement from the primary vertex [42]. For the second software trigger level, HLT2, we use a dedicated line designed by the Rio Charm Group aiming the selection of three-body decays of $D^+_{(s)}$ into light mesons.

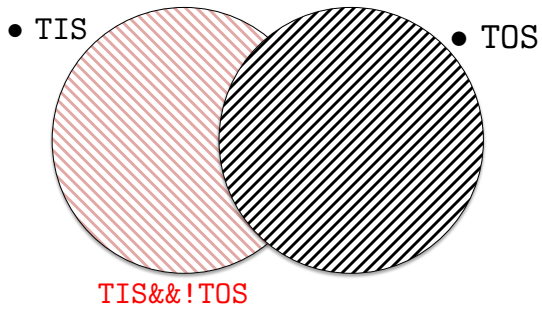

Figure 19: The two excludent subsets of the L0 trigger.

Cuts	Value	
Global Event Cut	N. Long Tracks $<$	180
final state particles	Track χ^2 $<$	3
	p_T(MeV/c) $>$	300
	p (MeV/c) $>$	3000
	IP χ^2 $>$	6
hhh combination	$\sum p_T$ (MeV/c) $>$	2800
	min DOCA (mm) $<$	0.08
$D^{\pm}$	FD χ^2 $>$	175
	Vertex χ^2/ndf $<$	15
	IP χ^2 $<$	12
	Mass (MeV/c^2)	1800–2040
TOS in any `Hlt1Track` Line		

Table 4: Selection criteria for `HLT2CharmHadD2HHH`.

After all the stripping and trigger requirements, the $K^-K^+K^+$ invariant mass distributions are shown in Fig. 21.

5.2.2 Offline selection: stripping

The first stage of the offline selection, the `Stripping`, was done at CERN. The goal of this stage was to split the data into the different categories (inclusive and exclusive selections), applying loose cuts (whenever possible) in order to reduce the combinatorial background, yielding a manageable data set for each specific analysis.

We are going to use data selected by a the exclusive line named `StrippingD2hhh_KKKLine`. The cuts applied in this line are listed in Table 6.

Track $IP\chi^2 > 16$
Track $p_T > 1.6$ GeV/c
Track $P > 3$ GeV/c
Track χ^2/ndf < 2
Track IP > 0.1 mm
Number of VELO hits/Track > 9
Number of missed VELO hits/Track < 3
Number of OT + IT hits/Track > 16
Number of Velo hits < 6000
Number of IT hits < 3000
Number of OT hits < 15000
`L0_Decision_Physics`

Table 5: `Hlt1TrackAllL0` requirements on at least one track.

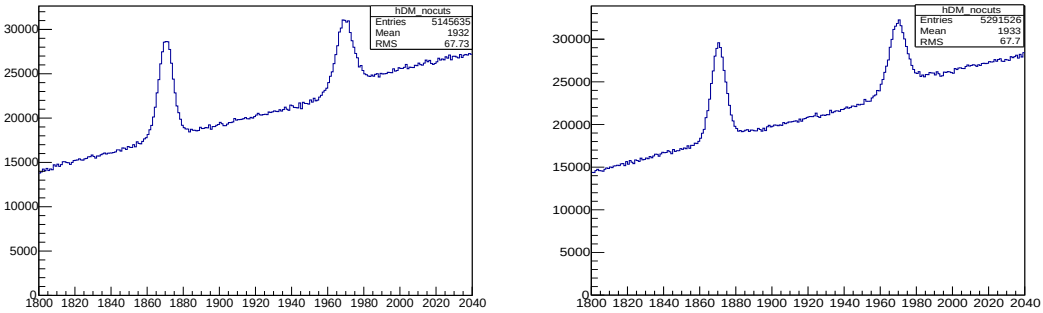

Figure 20: $K^-K^+K^+$ invariant mass distribution for MagDown (left) and MagUp (right) data as they come out of the Stripping 20. We can see the two peaks corresponding to the DCS decay $D^+ \to K^-K^+K^+$ and the Cabibbo suppressed decay $D_s \to K^-K^+K^+$.

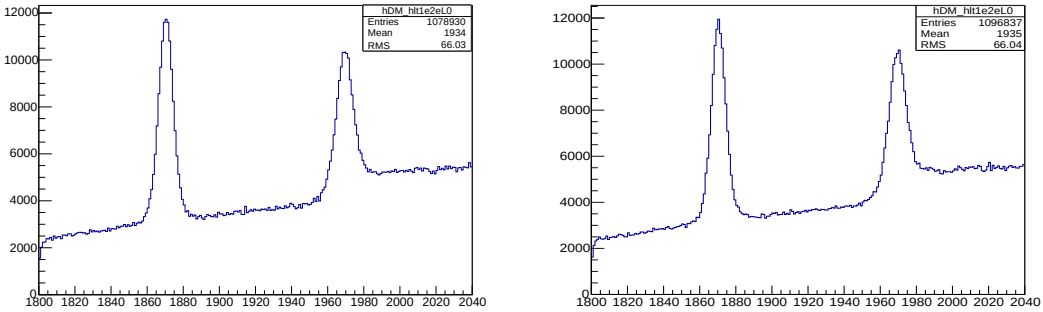

Figure 21: $K^-K^+K^+$ invariant mass distribution for MagDown (left) and MagUp (right) after trigger requirements. The largest reduction is due to the requirements on the HLT2.

Table 6: Stripping 20 cuts for `StrippingD2hhh_KKKLine`.

Variable	Selection requirement
Final state particles	
P_T	> 250 MeV/c (*)
p	> 2000 MeV/c (*)
$\sum P_T$	> 2800 MeV/c
`doca` max	< 0.5 mm
p IP χ^2	> 4
p_i`PID` > 7 for all tracks	
Combination cuts	
D (P_T)	> 1000 MeV/c
D Vertex χ^2	< 30
DIRA	> 0.98
D IP χ^2	< 12
D FD χ^2	> 125
Mass	1800 MeV/c^2 $< m_D <$ 2040 MeV/c^2

Table 7: The `doca`max variable is the maximum on the set `doca`$_{ij}$.

5.3 Monte Carlo (MC) samples

Full LHCb Monte Carlo (MC) simulation of the $D^+ \to K^-K^+K^+$ decay is used to guide the selection criteria and to determine the efficiency across the Dalitz plot. This simulation includes all the sub-systems steps, the selection requirements and the background of the decay. All the MC samples were generated with constant matrix element, using LHCb MC 2012 generation configuration, and is processed through the same stages as the data. The determination of the PID efficiency receives a special treatment. Due to some disagreement between the simulation of the response of the RICH detectors, a data driven method is used, using calibration data. This will be described later. The MC events are processed through the inclusive line of the stripping, in which no PID requirements are made. The MC sample generated for this analysis has a number of events for Magnet Polarity Down/Up of 184905 and 184865, respectively.

About 9% of this sample corresponds to D^+ mesons originated from b-hadron decays. In order to ensure that the efficiencies computed from the prompt MC samples are well defined, we process the signal sample with a filter that retains only events that contain a promptly produced signal decay. The filter traces the ancestry of the generated signal D^+ . If any of its ancestors has a mean lifetime longer than 0.1 fs it is classified as non-prompt.

5.4 Final selection

The final selection consists of multivariate analysis in order to extract a high purity sample keeping the efficiency across the Dalitz plot as uniform as possible. Typically, variables related to the daughter particles cause distortions of the phase space, we therefore avoid

them. The only exception made is for a particle identification variable. In this analysis, two kinds of backgrounds are taken into account.

Firstly, the reconstruction algorithm can combine three random tracks combinations of three uncorrelated tracks may pass the selection algorithms. Usually, this type of background, called **combinatorial**, does not introduce any DP structure and has a broad distribution over the 3 kaon invariant mass. Secondly, partially reconstructed charm decays can appear in the Dalitz plot as a structure, called **peaking background**, especially those decays with a ϕ. To deal with the combinatorial and the peaking background, two techniques are performed.

Multivariate Analysis

Multivariate analysis consists on a processing (or trainning), evaluation and application of multivariate classification technique. The framework used in this work is called Toolkit for Multivariate Analysis (TMVA), where all the techniques are "supervised learning" algorithms. In this class of algorithms, the desired output is known and training events are used to describe a decision boundary in a multivariate space. Essentially, these techniques consist in a two-stage process. The *training* (learning) phase, where the decision boundary is chosen from signal/background (yes/no) samples, and the *application* phase, where the algorithm is applied to data and a discriminating variable is assigned to each event. [43]

Widely used in LHCb Collaboration, the multivariate method chosen in this analysis is the *Boosted Decision Tree* (BDT). A decision tree is a binary tree structure classifier, which repeatedly make left/right (yes/no) decisions on one variable at a time until the criterion is achieved. The boosting of a decision tree extends the idea of a one tree to several, forming a *forest*. All the single trees are derived from the same training ensemble by reweighting events. Then, they are combined in a single classifier (which will be called `valBDT`), which is the average of the individual trees. This boosting process accounts for stabilization in the decision tree response w.r.t fluctuations in training samples and enhance the overall performance compared with a single tree. A schematic representation of a single tree is shown in Fig. 22.

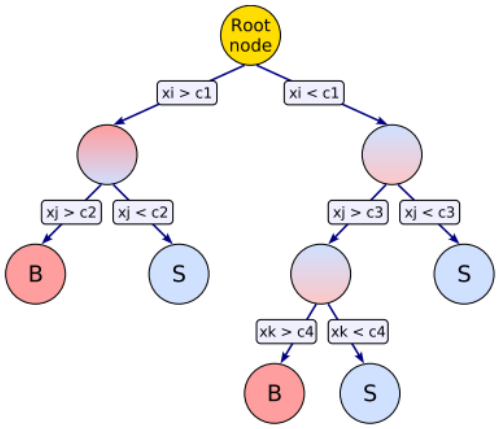

Figure 22: The schematic view of a decision tree single node. The boolean output is signal/background, with a given probability.

The BDT is aimed at reducing the combinatorial background. A MC sample represents the signal in the trainning phase. Events in his sample are weighted by the PIDCalib efficiency. For the background, data from the left $[1820, 1840]$ and right $[1900, 1920]$ MeV/c^2 sidebands are used.

The set of variables, shown in the Table 8, is chosen due their discriminating power and because they do not cause strong distortions in the DP. The measurement of each discriminating power of each variable is illustrated in Fig. 23 is done comparing the sidebands projection, into the desired variable, with the, so called, sideband-subtracted projection (also called background-subtracted).

Since we are using a multivariate algorithm, the correlation between variables are extremely useful to get a good performance. If the there were no such correlations, a linear cut-based algorithm would have a similar performance.

Table 8: Training Variables for the BDT classifier.

D_IP	D_IP$_{\chi^2}$	logIP = log $\left(\frac{\prod_i p_i\text{\_IP}_{\chi^2}}{\text{D\_IP}_{\chi^2}}\right)$
D_FD	D_FD$_{\chi^2}$	DOCAhi = max DOCA among pairs
D_ENDVX$_{\chi^2}$	PTsum	D_BPVTRGPOINTING

Additionally, the background subtracted projection can be compared to the LHCb simulation, which will tell if everything is well simulated and, consequently, if the Monte Carlo is well suited to use in MVA analysis. For this subtraction, we consider the signal region as 1870 ± 7.5 and the sidebands as 1850 ± 3.75 and 1910 ± 3.75. These numbers are chosen in order to the signal and background mass window are the same size.

After initializing the TMVA routine, a ranking of the BDT input variable can be derived by counting how often the variables are used to split decision tree nodes, shown in Table 9 for a single tree, and by weighting each split occurrence by the separation gain-squared it has achieved and by the number of events in the node. This rank can be used also for a forest.

The output of the BDT classification is shown in Figs. 24a and 24b, and used as a selection variable. In the first, the signal/background yield, for each valBDT cut, is

Table 9: Ranking result (top variable is best ranked)

Rank	Variable	Variable Importance
1	D_FD_OWNPV	0.1557
2	PTsum	0.1409
3	D_BPVTRGPOINTING	0.1401
4	logIP	0.1347
5	D_IPCHI2_OWNPV	0.1317
6	D_FDCHI2_OWNPV	0.1088
7	D_ENDVERTEX_CHI2	0.09357
8	docahi	0.06380
9	D_IP_OWNPV	0.03080
	sum	1.000

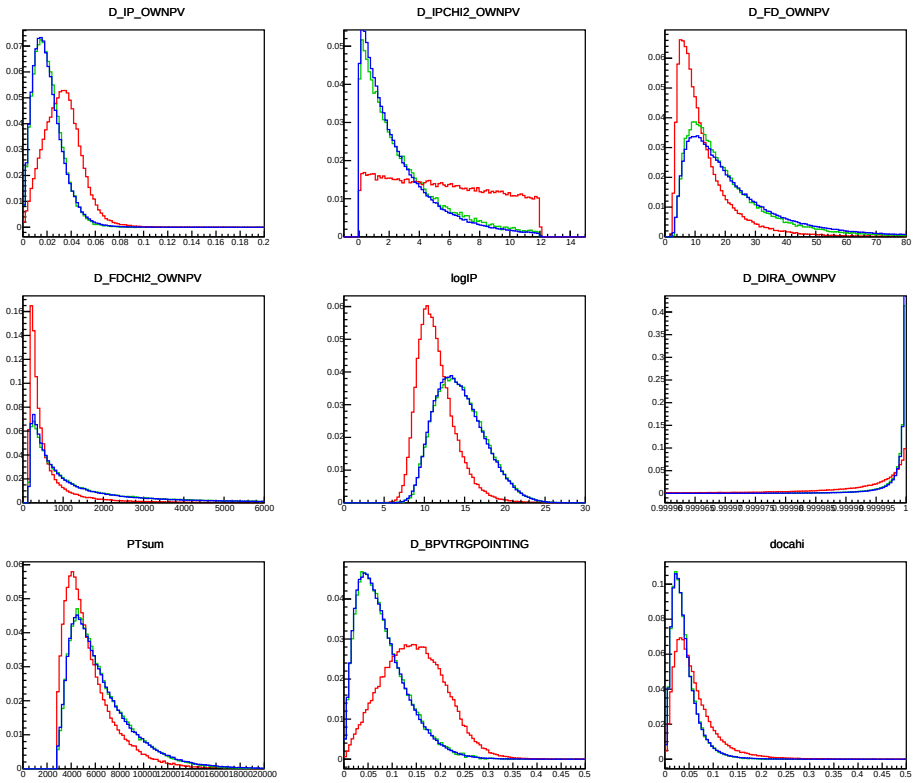

Figure 23: Blue, green and red lines are data sideband-subtracted, Monte Carlo and background, respectively.

extracted from a $K^-K^+K^+$ invariant mass fit, described in the next section. Using these yields, one can calculate the purity as $S/(S+B)$ and the signal efficiency, which is the ratio between number of signal events with/without the `valBDT` cut.

The final cut of `valBDT` > 0 is chosen as a compromise between efficiency and purity. Higher purity can be obtained with a strong cut, but at a high cost in efficiency and this can also distorce the DP. With this cut, an efficiency of 70% is obtained with a 83% purity.

Specific Backgrounds

The Dalitz plot of events from the sidebands reveals peaking structures. In top plots of Fig. 26, it is shown the folded DP of $K^-K^+K^+$ of events in the mass range $[1820, 1840]\,\mathrm{MeV}/c^2$, on the left, and $[1900, 1920]\,\mathrm{MeV}/c^2$, on the right. These events are shown using only the stripping selection. On top of a nearly uniform distribution, there are two peaking structures: a band corresponding to the ϕ resonance and a peak at the opposite edge of the Dalitz plot. The band in the ϕ region has two structure: one arises from uncorrelated ϕ, with o angular distribution, which accounts for the most of the structure and a contribution from ϕ's coming from other D decays. The latter is mostly due to $D \to KK\pi\pi^0$ decays, where the π^0 is not constructed and the π is misidentified as a kaon. In this case, the KK can form a ϕ resonance.

For kaons, `ProbNN` has shown to be a better discriminating variable than `PID`. A loose cut of `ProbNNk`> 0.15 it is applied to all particles. This removes the peaking structure at

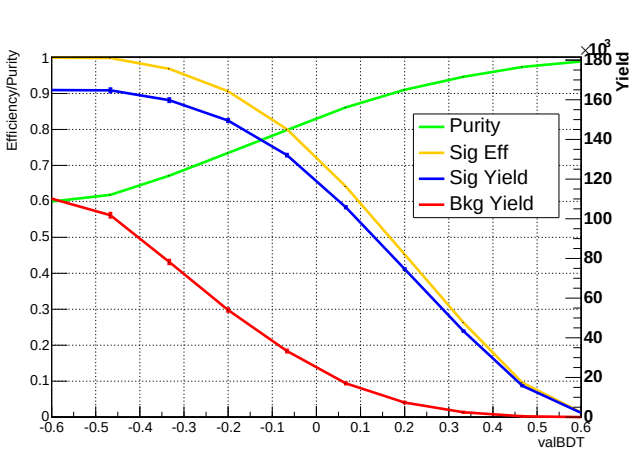

(a) MVA BDT Performance

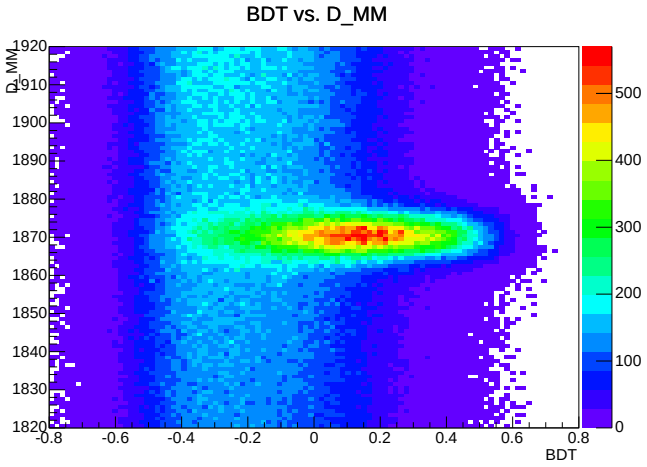

(b) $K^-K^+K^+$ invariant mass vs. `valBDT`.

Figure 24: BDT Performance

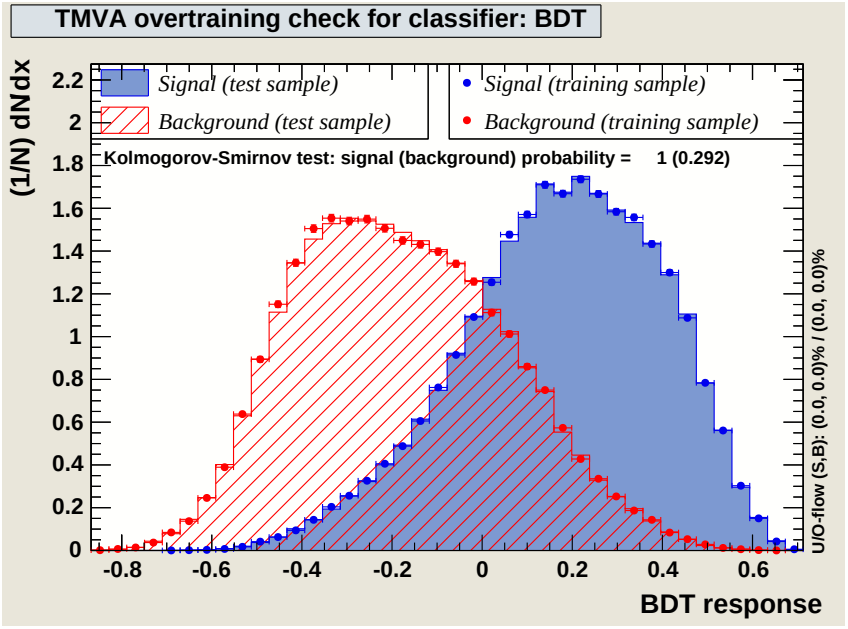

Figure 25: BDT overtraining check

high s_{KK}, but is not enough to remove the ϕ band in the background. The center plots of Fig. 26 shows the result of such cut.

Due to the particular kinematics of the $D^+ \to K^-K^+K^+$ decay, the ϕ band always appears in the lowest $s_{K^-K^+}$ projection. We call "bachelor" kaon the like-charged one which is not forming the resonance: particle 3 if $s_{12} < s_{13}$, particle 2 if $s_{13} < s_{12}$. Then, a stronger cut, `ProbNNk`> 0.6, is applied to this bachelor kaon, removing most of the $D \to KK\pi\pi^0$ background (bottom plots of Fig. 26), but also removes a great part of the uncorrelated ϕ. This last removal can be seen noticing that the peak was around ≈ 200 and, after the tight cut, is around≈ 100. This will be a crucial issue in the DP fit, since we need to separate the ϕ in the background from those in the signal. Therefore a

accurate background modelling is required.

The final set of cuts are summarized in the table below.

p_i ProbNNk > 0.15	$\forall i = 1, 2, 3.$
p_2 ProbNNk > 0.6	if $s_{12} \geq s_{13}$
p_3 ProbNNk > 0.6	if $s_{12} < s_{13}$
valBDT > 0.0	

Table 10: Final BDT and PID selections.

An additional issue is the that, in the final sample, a fraction of events has more than one candidate. This fraction accounts for 0.5% and, in this analysis, we keep all of the candidates. A precise estimate of the fraction of D's originated from B decays cannot be made due to the requirement on the impact parameter of the D candidate in both `StrippingD2hhh_KKKLine` and `HLT2CharmHadD2HHH` lines. The IP_{χ^2} variable is used to determine the fraction of secondary D's in the prompt charm cross-section paper [32]. At 7 TeV the fraction of $D^+ \to K^-\pi^+\pi^+$ decays from $b-$hadron decays is 4%.We assume the same fraction for the 8 TeV data. In the BDT selection of the $D^+ \to K^-K^+K^+$ candidates the IP_{χ^2} is one of the discriminating variables. After the `valBDT`> 0 requirement, only 3% of events have $IP_{\chi^2} > 7$. In Fig. 27 a comparison between the final distribution of the IP_{χ^2} of selected, sideband subtracted $D^+ \to K^-K^+K^+$ candidates (right) and that from the cross-section paper (left) is presented. From these plots we estimate that the fraction of secondary D's in the $D^+ \to K^-K^+K^+$ sample is of the order of 2% or less.

5.5 $K^-K^+K^+$ invariant mass fit

In order to determine the signal and yield of the sample, one need to fit the $K^-K^+K^+$ invariant mass spectrum, after the final cuts. This fit will also define the region, 2σ, where the DP fit will be performed. The chosen signal model is a weighted sum of two gaussian, with different widths but common mean.The background is parametrized by a exponential function, with the number of background events and the slope as free parameters. The fit function is the sum of the signal and background model, with the respective yields.

$$\mathcal{P}_{sig}(x; \mu_D, \sigma_1, \sigma_2) = fG(x; \mu_D, \sigma_1) + (1 - f)G(x; \mu_D, \sigma_2) \tag{109}$$

$$\mathcal{P}(x; \mu_D, \sigma_1, \sigma_2, \lambda) = \mathcal{N}_{\text{sig}}\mathcal{P}_{\text{sig}}(x; \mu_D, \sigma_1, \sigma_2) + \mathcal{N}_{\text{bkg}}\mathcal{P}_{\text{bkg}}(x; \lambda) \tag{110}$$

Tables 11 and 12 show a summary of the one dimensional fit results. The shared mean value is in agreement with the PDG [16]. For the Dalitz plot analysis, only candidates within $2\sigma_{\text{eff}}$ around the peak position are considered, where $\sigma_{\texttt{eff}} = (4.52 \pm 0.24)$. In this range, there are 111,464 events, where 90.45% are expected to be signal and 9.55% background.

Selecting events within the $2\sigma_{\text{eff}}$ window and projecting into the Dalitz plot result in the plots of Fig. 29. In the Dalitz plot analysis the invariantes $s_{12} \equiv s_{K_1^-K_2^+}$ and $s_{13} \equiv s_{K_1^-K_3^+}$

Table 11: Mass Fit Parameters

Parameter	Fitted Value
μ_D (MeV/c^2)	1870.45 ± 0.02
σ_1 (MeV/c^2)	3.80 ± 0.07
σ_2 (MeV/c^2)	6.5 ± 0.5
signal yield	$106,061 \pm 393$
f	0.78 ± 0.05
λ	$(2.59 \pm 0.14) \times 10^{-3}$
bkg yield	$59,028 \pm 327$

Table 12: Component Yields in $\pm 2\sigma$.

Component	$\pm 2\sigma$ Yield
total	111,464
signal	$(90.45 \pm 0.07)\%$
background	$(9.55 \pm 0.07)\%$

are computed constraining the invariant mass of the candidate to the nominal D mass. The goal of this constrained invariants is to improve their resolution.

The `DecayTreeFitter` (DTF) algorithm is used, with the requirement that the method converge, *i.e.* $\chi^2 > 0$. In Fig. 29, on top of a nearly constant distribution, the ϕ band is visible. Attention should be called here to the asymmetry between the upper and lower ϕ lobes, which is a direct effect of the interference between the $\mathcal{P}$-wave (a priori, just the ϕ) and the $\mathcal{S}$-wave.

The mass fit is also performed separating the `L0_TOS` and `L0_TIS&&!L0_TOS` samples. The yields, within $\mu_D \pm 2\sigma_{\text{eff}}$, are 36892±338 events for `L0_TOS` and 64291±308 for `L0_TIS&&!L0_TOS`. These values are used as weights for the final efficiency.

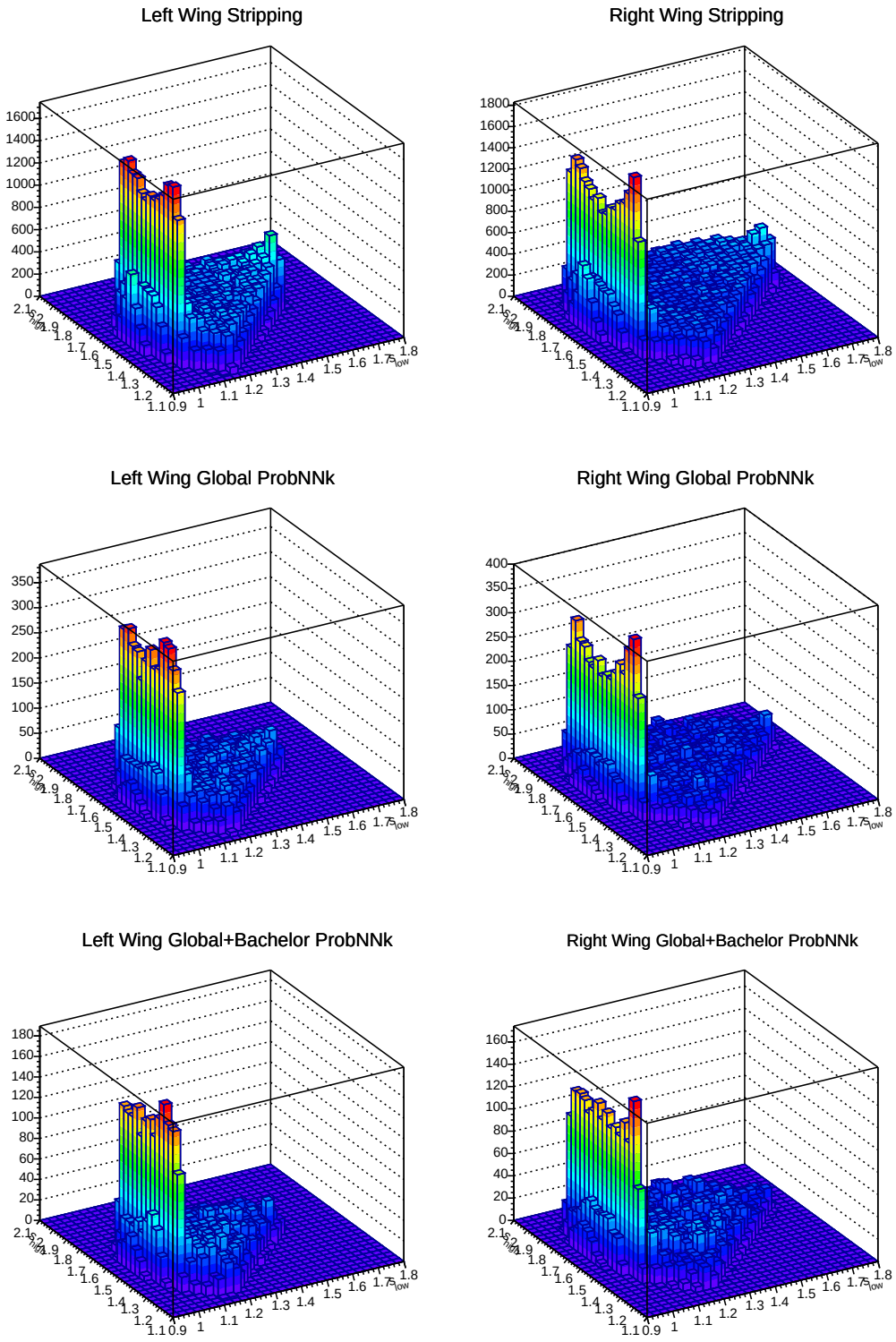

Figure 26: Dalitz plot distribution of events from the sidebands. On the left are the DP for the left sideband, whereas the DP from the right sidebands are shown in the plots on the right. Top plots: DP with stripping cuts; middle: DP with stripping cuts plus `ProbNNk`>0.15 applied to all kaons; bottom: DP with stripping cuts a further `ProbNNk`>0.6 requirement applied to the bachelor kaon.

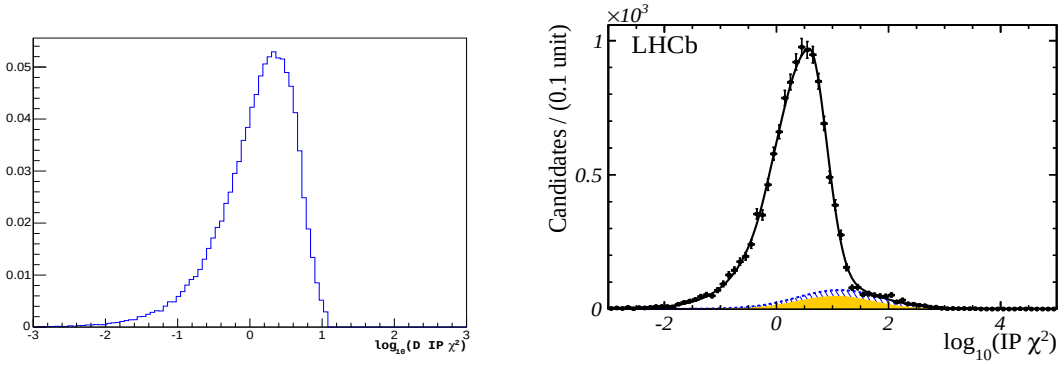

Figure 27: Distribution of IP_{χ^2} for sideband subtracted $D^+ \to K^-K^+K^+$ candidates (left) and for $D^+ \to K^-\pi^+\pi^+$ decays, reproduced from [32]. The contribution of $D^+ \to K^-\pi^+\pi^+$ from $b-$hadron decays is represented by the blue-dotted line in the right panel.

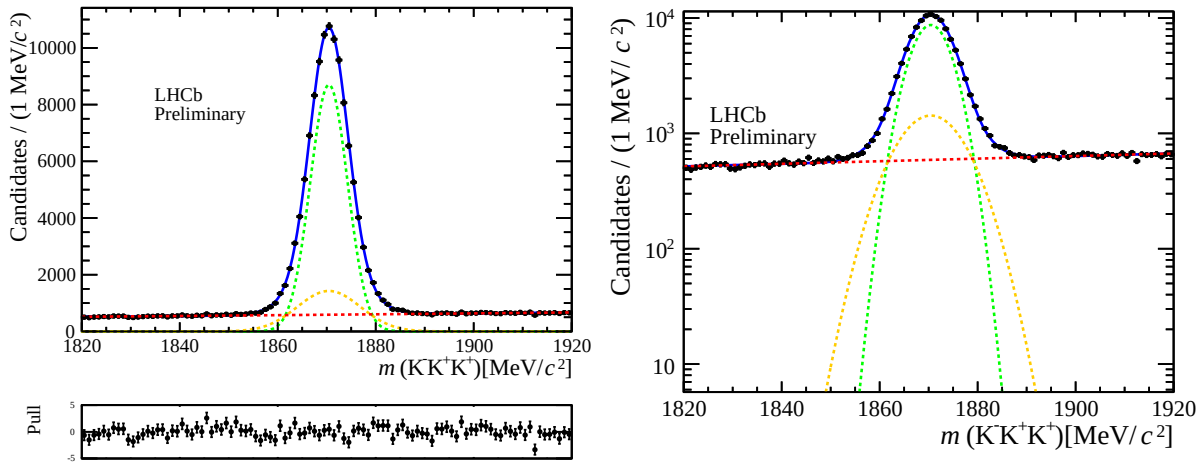

Figure 28: Result of the fit to the KKK Mass spectrum after final cuts in linear (left) and log (right) scales. The dashed lines indicate the two Gaussian functions representing the signal.

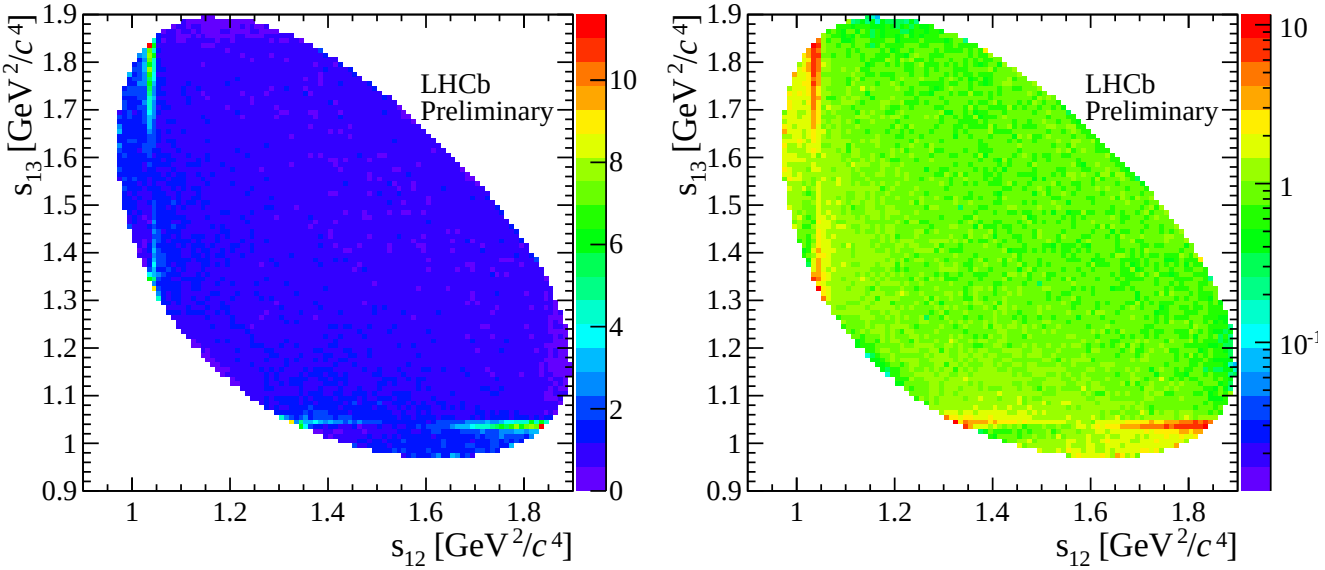

Figure 29: Dalitz plot of the final sample, in linear (left) and log scale (right).

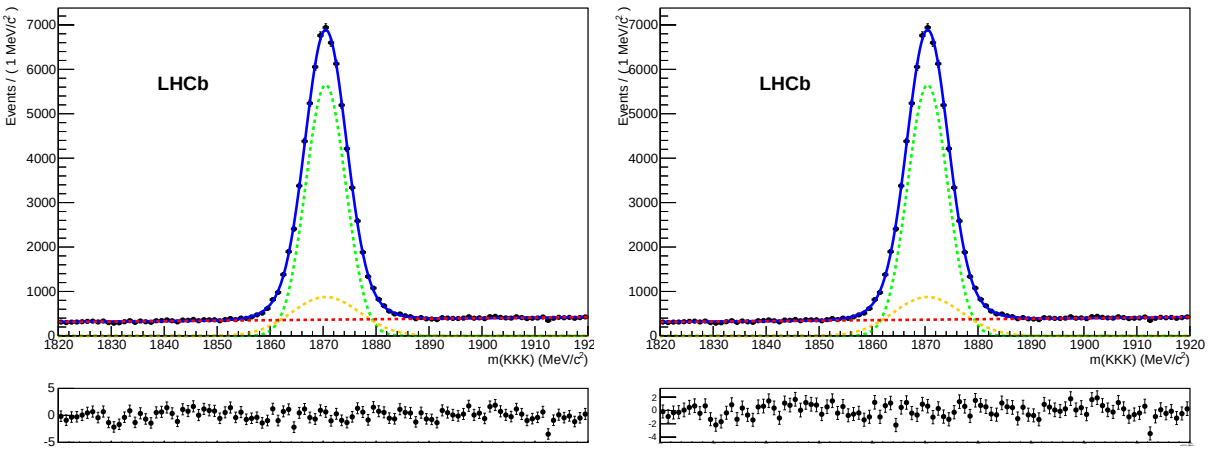

Figure 30: Result of the fit to the $K^-K^+K^+$ invariant mass spectrum after final cuts for the `L0_TOS` sample on the right and `L0_TIS&&!L0_TOS` on the left.

5.6 Efficiency

The efficiency as a function of the Dalitz plot variables is determined from the LHCb simulation. The $D^+ \to K^-K^+K^+$ MC sample is generated with a constant matrix element, resulting on an uniform Dalitz plot distribution.

The MC events are then passed through the same stages as the data - geometrical acceptance, reconstruction, stripping, full (`L0`, `Hlt1` and `Hlt2`) trigger requirement and MV selection - but **no PID** requirements are made, since the response of the RICH is not well modeled in the MC. Since the `StrippingD2hhh_KKKLine` stripping line has a PID cut on all kaons, the inclusive stripping is used instead.

There are known differences between the `L0` simulation and the data. However, given that the $D^+ \to K^-K^+K^+$ candidates are selected by the `Hlt2CharmHadD2HHH` line, which in turn has a requirement on the `Hlt1TrackAllL0`, the `L0` trigger requirement needs to be made in the MC. Data-driven methods are applied to account for PID efficiency and to correct for the `L0` trigger simulation. While the `PIDCalib` tool is used to determine the PID absolute efficiency, the `L0` trigger correction is determined from the efficiency tables, following same procedure of the $B_s^0 \to \bar{D}^0 K^-\pi^+$ analysis [44].

The number of MC events surviving the selection are summarized in Table 13.

Table 13: MC statistics after all cuts, except for the PID.

MC	UP	DOWN	UP+DOWN
TOS	54,539	55,055	109,594
TIS!TOS	78,775	78,599	157,374
ALL	133,314	133,654	266,968

In the Dalitz plot fit, events that are either `L0_TOS` or `L0_TIS` are combined into a single data set. Since these two `L0` requirements have different impact on the Dalitz plot, it is necessary to treat each separately when computing the efficiency map for the combined sample. The MC events are, therefore, divided into two exclusive samples, `L0_TOS` and `L0_TIS&&!L0_TOS`. The appropriate `L0` correction factor is applied to each exclusive sample, which are then combined into a single histogram, according to the relative fractions of `L0_TOS` and `L0_TIS&&!L0_TOS` signal events observed in data.

A histogram is filled with the weighted MC events. Since the sample of full MC was generated with a phase space distribution, the efficiency at a given position in the Dalitz plot is simply the height of the bin the event belongs to (the absolute scale of the efficiency is irrelevant in Dalitz plot analysis). Bins near the border of the Dalitz plot may be only partially contained in the phase space, causing the efficiency in these bins to be artificially lower. This effect is accounted for by dividing the MC weighted histogram by a histogram from a very large ToyMC sample with uniform distribution. All of this manipulation is done with, typically, a 10x10 bins histograms, but not all of the bins are occupied. In order to reduce the effect of the coarser binning of the original histogram, a smoothing process is required. A 2D cubic spline is then used to produce a high-resolution smoothed histogram, which is used in the fit. The spline procedure is based on the code LauCubicSpline from the Laura++ project [45].

5.6.1 Geometrical Acceptance, Reconstruction and Selection Efficiencies

The efficiency map, ϵ_0, as a function of the Dalitz plot variables (s_{12}, s_{13}) and prior to the PID and trigger corrections is shown in Fig. 31 (`L0_TOS` on the left, `L0_TIS&&!L0_TOS` on the right). The effects of PID are not considered at this stage. The histograms containing the selected LHCb MC events are divided by a histogram made from a very large ToyMC sample generated with constant matrix element. This division accounts for the bins not entirely contained in the phase space.

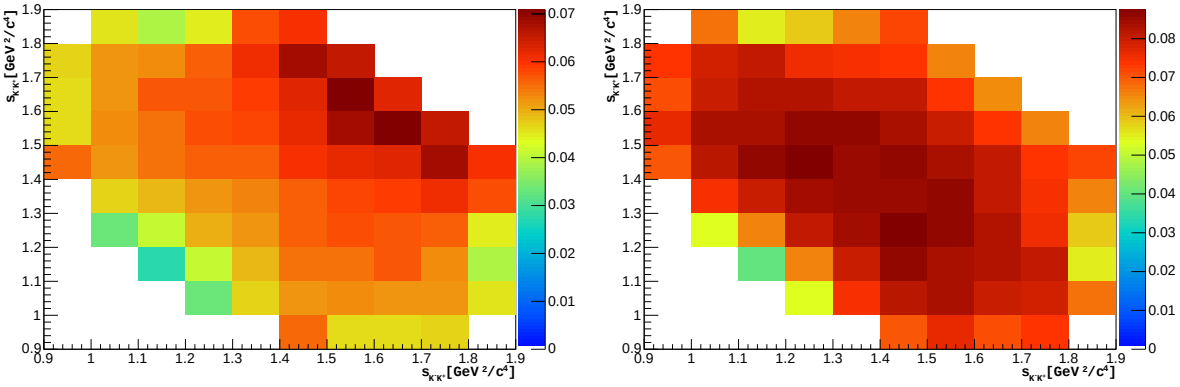

Figure 31: Efficiency histograms including geometrical acceptance, reconstruction and selection efficiency. Neither the effects of PID nor the `L0` efficiency correction are considered at this stage. On the left panel, events that are `L0_TOS`; on the right, `L0_TIS&&!L0_TOS`.

5.6.2 PID Efficiency

The efficiency of particle identification is computed from calibration sample using the `PIDCalib` tool. For a given cut value - or combination of values, if both `DLL` and `ANNPID` algorithms are used, as in the case of this analysis - the `PIDCalib` tool provide efficiency tables obtained from a calibration sample $(D^{*+} \to D^0(K^-\pi^+)\pi^+)$.

PID efficiency tables are produced corresponding to the stripping plus offline requirements. The tables are two-dimensional histograms, obtained by dividing the calibration data into bins of kaon momentum and pseudo-rapidity, using the `PIDCalib` default binning.

The PID efficiency for each track is determined from these tables, with the associated error. The MC events from each `L0` sample are weighted in an event-by-event basis, where the event weight is the product of the PID efficiency for each of the three kaons. The resulting efficiency maps, $\varepsilon_{\text{sel+PID}}$, are shown in Fig. 32. The histograms include all stages of the selection but one last step: the `L0` trigger efficiency correction.

5.6.3 `L0` trigger correction

There is a well known discrepancy between the data and the simulation of the `L0` trigger response in LHCb MC. Like the `PIDCalib` tool, the CALO group provides efficiency tables from calibration data.

The CALO tables give the probability for a single track to fire the `L0` hadron trigger, depending on the particle type, magnet polarity, which part of the calorimeter the track

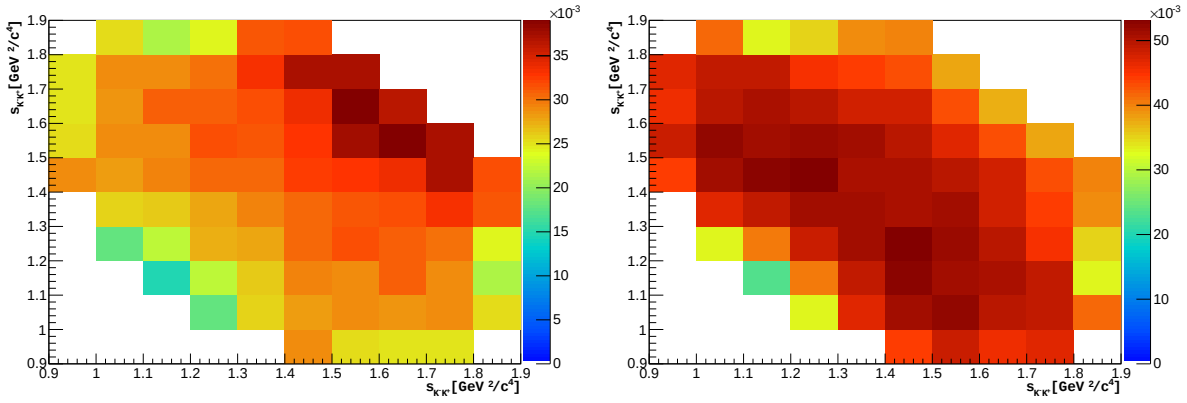

Figure 32: Efficiency histogram including geometrical acceptance, reconstruction, selection and PID efficiency. On the left panel, events that are `L0_TOS`; on the right, `L0_TIS&&!L0_TOS`. No `L0` trigger correction is applied at this stage.

hits and the transverse energy deposited. The probability increases when two tracks from the signal hit the calorimeter close enough together, depositing energy in the same cells. The probability that any of the signal tracks fires the trigger is obtained adding the probabilities for the individual tracks and considering all possible configurations for two-tracks superposition, following the recipe from [44].

Since the `L0` requirement is applied to the MC events, a correction factor is needed, rather than the absolute efficiency. Different corrections factors are determined for `L0_TOS` and `L0_TIS&&!L0_TOS` events.

The `L0_TOS` efficiency is determined, as usual, with respect to the unbiased TIS sample. In each bin of the Dalitz plot of MC events that are `L0_TIS`, the number of events that are also `L0_TOS` is computed. The `L0_TOS` efficiency in each bin is given by the ratio between the number of `TIS&&TOS` events and the number of `TIS` events in that bin,

$$\varepsilon^{\rm MC}_{\rm TOS} = \frac{\rm TIS\&\&TOS}{\rm TIS}. \tag{111}$$

The MC `L0_TIS&&!L0_TOS` efficiency is the complement of that of the `L0_TOS` sample,

$$\varepsilon^{\rm MC}_{\rm TIS\&\&!TOS} = \frac{\rm TIS\&\&!TOS}{\rm TIS}. \tag{112}$$

The efficiency for each `L0` category is also determined directly from the CALO tables. For each `L0_TIS` MC candidate, the probability, $p_{\rm TOS}$, that any of the three tracks fires the trigger is computed. The `L0_TOS` efficiency is a histogram of `L0_TIS` MC candidates weighted by $p_{\rm TOS}$. The `TIS&&!L0_TOS` efficiency is a histogram of `L0_TIS` MC candidates weighted by $1 - p_{\rm TOS}$.

Having computed the histograms for the `L0_TOS` and `TIS&&!L0_TOS` efficiency from MC and from the CALO tables, the histograms containing the trigger correction are determined as:

$$f^{\rm corr}_{\rm TOS} = \frac{\varepsilon^{\rm CALO}_{\rm TOS}}{\varepsilon^{\rm MC}_{\rm TOS}}, \tag{113}$$

$$f^{\rm corr}_{\rm TIS\&\&!TOS} = \frac{\varepsilon^{\rm CALO}_{\rm TIS\&\&!\mathit{TOS}}}{\varepsilon^{\rm MC}_{\rm TIS\&\&!\mathit{TOS}}}. \tag{114}$$

The final efficiency map for each L0 sample is obtained multiplying $\varepsilon_{\text{sel+PID}}$ by the corresponding trigger correction,

$$\varepsilon^{\text{TOS}}_{\text{sel+PID}} = \varepsilon_{\text{sel+PID}} \times f^{\text{corr}}_{\text{TOS}}, \tag{115}$$

$$\varepsilon^{\text{TIS\&\&!TOS}}_{\text{sel+PID}} = \varepsilon_{\text{sel+PID}} \times f^{\text{corr}}_{\text{TIS\&\&!TOS}}. \tag{116}$$

The final efficiency maps for each L0 sample are shown in Fig. 33.

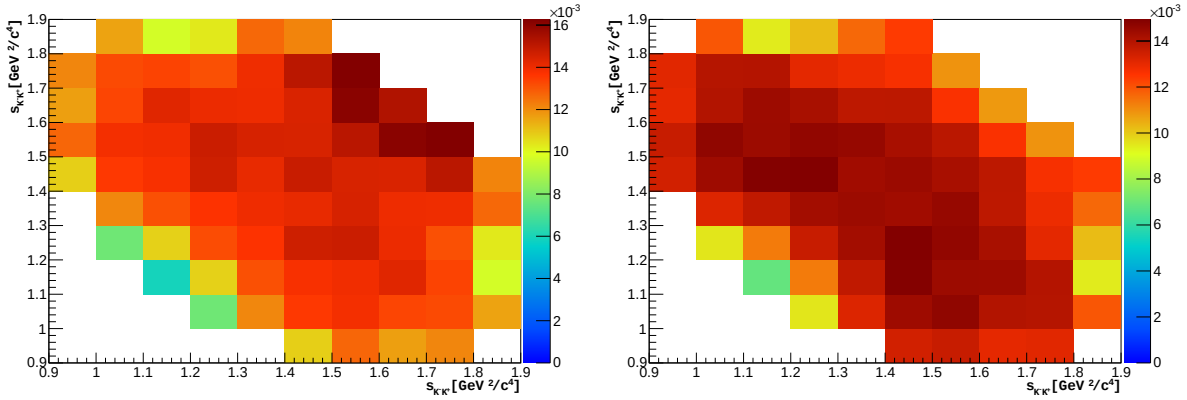

Figure 33: Final efficiency maps with geometrical acceptance, reconstruction, selection and PID efficiency, and L0 trigger corrections. On the left panel, events that are L0_TOS; on the right, L0_TIS&&!L0_TOS.

5.6.4 Final efficiency

The final efficiency is obtained combining the efficiency maps for the L0_TOS and L0_TIS&&!L0_TOS samples, shown in Fig. 33. The histograms of Fig. 33 are normalized to unity and weighted by the relative fractions of the L0_TOS and L0_TIS&&!L0_TOS samples observed in data, $g^{\text{data}}_{\text{TOS}}$ and $(1 - g^{\text{data}}_{\text{TOS}})$,

$$\varepsilon_{\text{TIS||TOS}} = g^{\text{data}}_{\text{TOS}} \times \varepsilon^{\text{TOS}}_{\text{sel+PID}} + (1 - g^{\text{data}}_{\text{TOS}}) \times \varepsilon^{\text{TIS\&\&!TOS}}_{\text{sel+PID}}. \tag{117}$$

A single, high resolution histogram is made combining the two independent trigger subsamples, weighted according to their relative fractions observed in data. The combined efficiency distribution is fitted with a two-dimensional cubic spline to smooth out statistical fluctuations due to limited size of the simulated sample. This fit is performed using the Laura++ libraries [45]. The histogram is shown in Fig. 34.

5.7 Background Model

From Fig. 26 we conclude that after the final selection, the background from the side bands to the left and to the right of the signal region have two components, namely the combinatorial and a peaking background at the ϕ mass.

The background model for the Dalitz plot fit is built as follows. The left and right side bands are divided into 10 MeV/c^2 slices. In each slice the amount of ϕ is determined

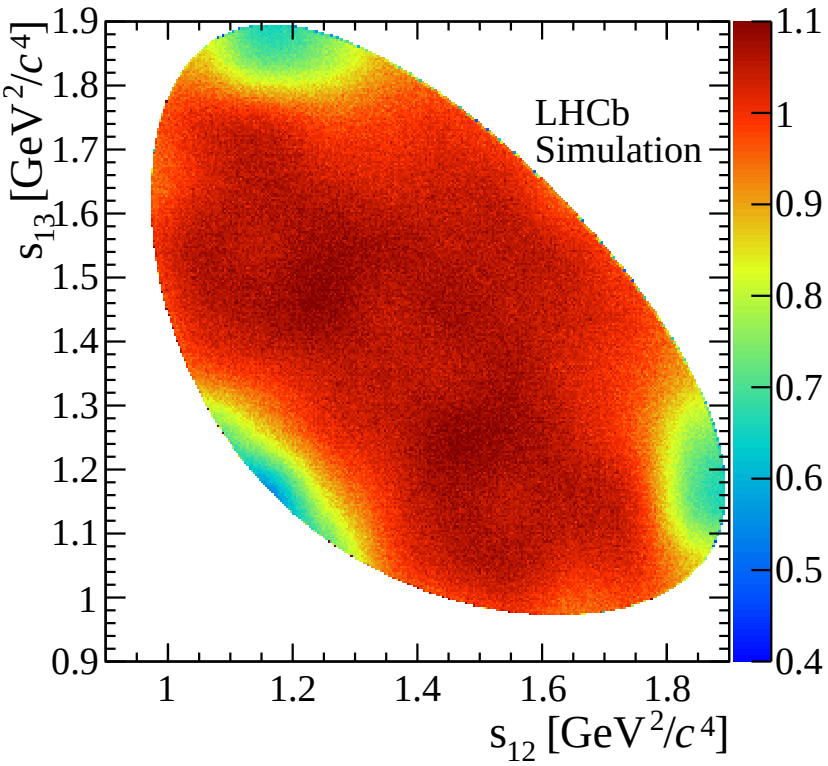

Figure 34: High resolution histogram of the final efficiency for the $D^+ \to K^-K^+K^+$ decay, including geometrical acceptance, reconstruction and selection, trigger and PID.

through a fit to the projections of the Dalitz plot onto each of the s_{KK} axes (s_{12}, s_{13}). Recall that the phase space is such that the ϕ band in s_{12} does not overlap with that in s_{13}. In each slice the data is fitted with a relativistic Breit-Wigner for the ϕ peak, with floating mass and width (these parameters vary with the $K^-K^+K^+$ mass due to DTF), and a phase space shape to model the combinatorial component of the background. Note that in each of the K^+K^- mass squared projections the ϕ signal from the crossed channel is embedded into the combinatorial. However, this does not prevent from extracting the contribution from the ϕ peak in each projection. This is illustrated in Fig. 35a, for the interval $1820 < m_{KKK} < 1830$ MeV/c^2. The contribution from the ϕ component of the background is given by the sum of the yields from the fits to each K^+K^- mass squared projection.

In Fig. 35b the relative fraction of each component of the background is displayed for each of the m_{KKK} slices. The relative proportion of each component, 80% for the combinatorial and 20% for the ϕ component, is very stable in both side bands, so it is safe to assume that it is the same in the signal region.

The background model is built from a large toy MC with a 20% of ϕ and 80% of an uniform amplitude. Since it is a difficult task to estimate the efficiency for the background,the resulting distribution is weighted by the acceptance map and rescaled to the number of background events in the signal region. The resulting histogram is smoothed by a 2D cubic spline, and is shown in Fig. 36.

As a systematic check, the background is modelled directly from the data. The effect

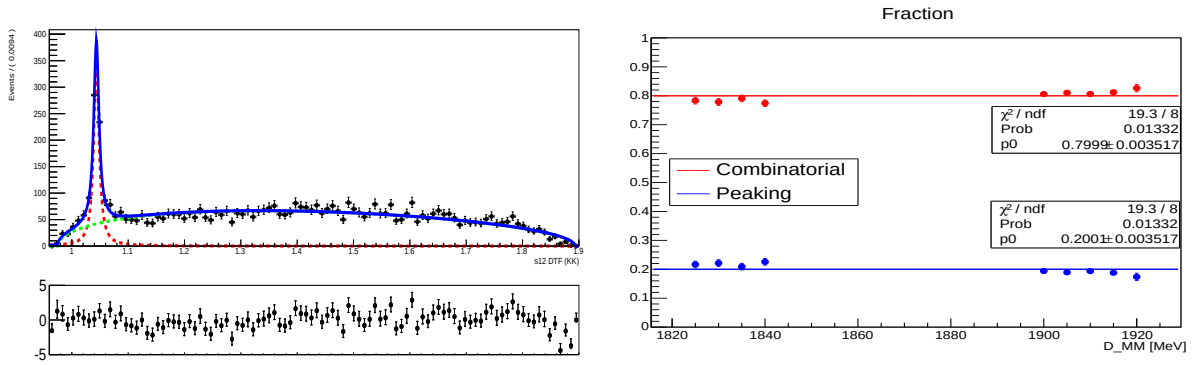

Figure 35: Left:s_{12} projection of KKK mass within 1840–1850 MeV/c^2; right: Relative contribution of ϕ and combinatorial backgrounds as a function of KKK mass.

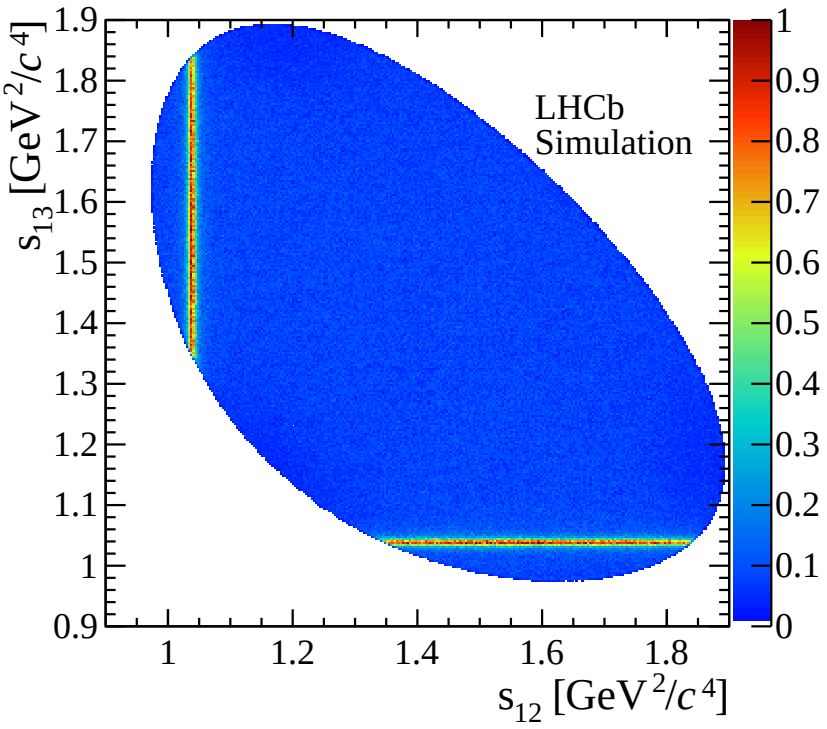

Figure 36: Background Dalitz plot model (z axis in arbitrary units).

of the mass constraint (DTF) on signal events is to improve the mass resolution across the Dalitz plot. But for background events, where the mass constraint is ill-defined, the effect goes in opposite direction. The ϕ peak from background becomes slightly broader with DTF momenta. As one moves away from the D mass in the $K^-K^+K^+$ spectrum, the peak position of background ϕ's is shifted from the true position. Thanks to the very good $K^-K^+K^+$ mass resolution ($\sigma_{\text{eff}} = 4.52 \pm 0.24$ MeV/c^2), one can define two background regions (one to the left and the other to the right of the signal region) not too far from the signal peak position. Two histograms with the Dalitz plot distribution of these background events are added to form the alternative representation of the background under the D^+

signal.

The effective width of the background ϕ's can be measured as a function of the $K^-K^+K^+$ mass in both side bands, so the value of the width in the signal region can be determined with an interpolation and compared to what is obtained when the histograms from the left and right side bands are added. This allows a fine tuning of the two background regions.

6 Isobar Model Results

> You don't need something more to get something more. That's what emergence means.
>
> Murray Gell-Mann

In this section, the first amplitude analysis of the doubly Cabibbo-suppressed $D^+ \to K^-K^+K^+$ decay is presented. The analysis is performed using the Isobar Model. As anticipated in the Introduction, the main focus of this analysis is an investigation of the K^-K^+ $\mathcal{S}$-wave, *i.e.* the scalar contribution to the $D^+ \to K^-K^+K^+$ decay. Possible contributions to the $\mathcal{S}$-wave are the resonant states $f_0(980)$, $a_0(980)$, $f_0(1370)$ and $a_0(1450)$ and a non-resonant amplitude.

From the Dalitz plot in Figure 29, two leading contributions are clear. The ϕ resonance, which is a visible structure and contributes to a $\mathcal{P}$-wave. The rest of the Dalitz plot has a nearly uniform distribution, except for the mass threshold. This is a broad scalar contribution, an $\mathcal{S}$-wave. To investigate this structure we are going to use moments of angular distribution in the mass range of $m(K^-K^+) < 1.05$ GeV/c^2, where there is no cross-channel contribution. This will be the guideline for our analysis.

All the results are obtained using the `Rio+` package, developed by the Rio Charm Group.Tests for validation of the algorithm are shown in Appendix B.

6.1 Moments of the angular distribution

The moments of the angular distribution can be used not only as a tool for accessing the goodness of fit but also as a guide in the determination of the decay model. As discussed above, one is limited to the very low part of the spectrum, $m(K^-K^+) < 1.05$ GeV/c^2, since this region is free from the interference from the crossed channel.

The distribution of events across the Dalitz plot is given by

$$\frac{d\Gamma}{ds_{12}ds_{13}} = \frac{1}{(2\pi)^3 32 M_D^3} \, |\mathcal{M}(s_{12}, s_{13})|^2. \tag{118}$$

The angular distribution is a function of the helicity angle $\theta(K^-K^+)$, which is the angle between the K^- momentum vector and the momentum vector of bachelor kaon, measured in the rest frame of the resonant K^-K^+ pair. Defining the $\cos\theta(K^-K^+) \equiv z$, $s = s_{12}$ and performing the transformation of variable $s_{13} \to z$ one has

$$\frac{d\Gamma}{ds_{12}ds_{13}} \longrightarrow \frac{d\Gamma}{dsdz} \propto pq|\mathcal{M}(s,z)|^2, \tag{119}$$

where q and p are the momenta of the K^- and of the bachelor kaon, respectively, evaluated in the resonance rest frame.

With the angular part of the spin (up to $j = 2$) amplitudes given by the Legendre polynomials, $P_l(z)$, the Lorentz invariant amplitude is

$$\mathcal{M}(s,z) = \sum_{l=0}^{2} A_l(s) P_l(z). \tag{120}$$

Defining $A_0 \equiv S$, $A_1 \equiv P$ and $A_2 \equiv D$, and taking the P-wave as reference, we have:

$$\mathcal{M}(s,z) = S(s)e^{i\phi_S} + P(s)P_1(z) + D(s)P_2(z)e^{i\phi_D}, \tag{121}$$

where ϕ_S and ϕ_D are the global phases between different waves.

The K^+K^- spectrum ($s = m^2_{KK}$) is divided into narrow bins, so that in each bin $s \sim$ constant. We then perform a multipole expansion of the angular distribution for each mass bin assuming $s \sim \text{const} = s_i$,

$$\left.\frac{d\Gamma}{dsdz}\right|_{s=s_i} = f^i(z) = \sum_{L=0}^{2l_{\max}} \sum_{mm'} \left(\frac{2L+1}{4\pi}\right) \; t_L^{M,i} \; D^L_{mm'}(z), \tag{122}$$

where $D^L_{mm'}(z)$ are the Wigner D-matrices and $f^i(z)$ is the efficiency-corrected, background-subtracted distribution of events in i-bin of the DP.

The moments $t_L^{M,i}$ are given by

$$t_L^{M,i} = \int_{-1}^{1} dz \; f^i(z) \; D^L_{mm'}(z). \tag{123}$$

Since the initial and final state particles are spinless, $m = m' = 0$, so we can write

$$t_L^{M,i} \to t_L^{0,i} \equiv t_L^i, \qquad D^L_{00}(z) = d^L_{00}(z) = P_L(z), \qquad t_L^i = \int_{-1}^{1} dz \; f^i(z) \; P_L(z). \tag{124}$$

The moments t_L^i are computed directly from data (no fitting). The integral is approximated by a sum over background subtracted events in the i-th mass bin,

$$t_L^i = \int_{-1}^{1} dz \; f^i(z) \; P_L(z) \sim \sum_j P_L(z_j) \; \frac{f^i_{\rm PS}}{\varepsilon_j}, \tag{125}$$

where ε_j is the efficiency for the j-th event and $f^i_{\rm PS}$ is a phase space correction factor depending on the position of the i-th mass bin.

If one substitutes $f^i(z)$ in the definition of t^i_k by the phenomenological expression of $\mathcal{M}(s,z)$, one can compare the model predictions with the observed moments. For that we need these useful relations:

$$\int_{-1}^{1} dz \; P_j(z)P_k(z) = \delta_{jk}, \tag{126}$$

$$D^{j_1}_{m_1\mu_1}(z)D^{j_2}_{m_2\mu_2}(z) = \sum_{j_3m_3\mu_3} (j_1m_1j_2m_2|j_3m_3)(j_1\mu_1j_2\mu_2|j_3\mu_3) \; D^{j_3}_{m_3\mu_3}(z). \tag{127}$$

In the $D^+ \to K^-K^+K^+$ decay we have $m_1 = \mu_1 = m_2 = \mu_2 = j_3 = m_3 = \mu_3 = 0$, so

$$D^{j_1}_{00}(z)D^{j_2}_{00}(z) = \sum_{j_3m_3\mu_3} (j_10j_20|j_30)^2 \; D^{j_3}_{00}(z) = \sum_{j_3m_3\mu_3} (j_10j_20|j_30)^2 \; P_{j_3}(z). \tag{128}$$

In terms of the decay model we have, for each mass bin,

$$t^i_L = \int_{-1}^{1} dz \; f^i(z) \; P_L(z) = \int_{-1}^{1} dz \; |S^iP^1_0(z)e^{i\phi_S} + P^iP_1(z) + D^iP_2(z)e^{i\phi_D}|^2 \; P_L(z). \tag{129}$$

The moments t^i_k, up to 4-th, order are then computed in terms of S^i, P^i and D^i. Products of 3 Legendre polynomials are reduced using the above relations. With the corresponding Clebsh-Gordan coefficients, the results are:

- $t_0 = S^2 + P^2 + D^2$
- $t_1 = \frac{2}{3}\ SP\cos\phi_S + \frac{4}{5}\ PD\cos\phi_D$
- $t_2 = \frac{2}{5}\ P^2 + \frac{2}{3}\ D^2 + \frac{2}{5}\ SD\cos(\phi_S - \phi_D)$
- $t_3 = \frac{6}{5}\ PD\cos\phi_D$
- $t_4 = \frac{36}{35}\ D^2$

In the limited region close to threshold where there is no $\mathcal{D}$-wave contribution, the above expressions become very simple. Inverting the above equations one has

$$S^2 = t_0 - \frac{5}{2}\ t_2, \tag{130}$$

$$P^2 = \frac{5}{2}\ t_2. \tag{131}$$

In Fig. 37 the first 5 moments are shown as a function of the K^+K^- mass. Near threshold, higher waves are highly suppressed. Indeed, the distribution of t_4^0 is consistent with zero for $m(K^-K^+) < 1.05$ GeV/c^2.

The contributions from $\mathcal{S}$- and $\mathcal{P}$-waves near threshold are shown in Fig. 38. The background is not subtracted, but the efficiency and phase space corrections are applied. There is a clear ϕ peak in the P-wave, whereas the S-wave rises as one approaches the K^-K^+ threshold, as expected for a $f_0(980)$ contribution. Small peak in the $\mathcal{S}$-wave is due to the ϕ from the background.

The $a_0(980)$, with mass and width similar to that of the $f_0(980)$, can also contribute. The differences in the line shapes of these two states are clearly visible in the $\pi\pi$ spectrum, while in the $K\bar{K}$ they can hardly by distinguished.

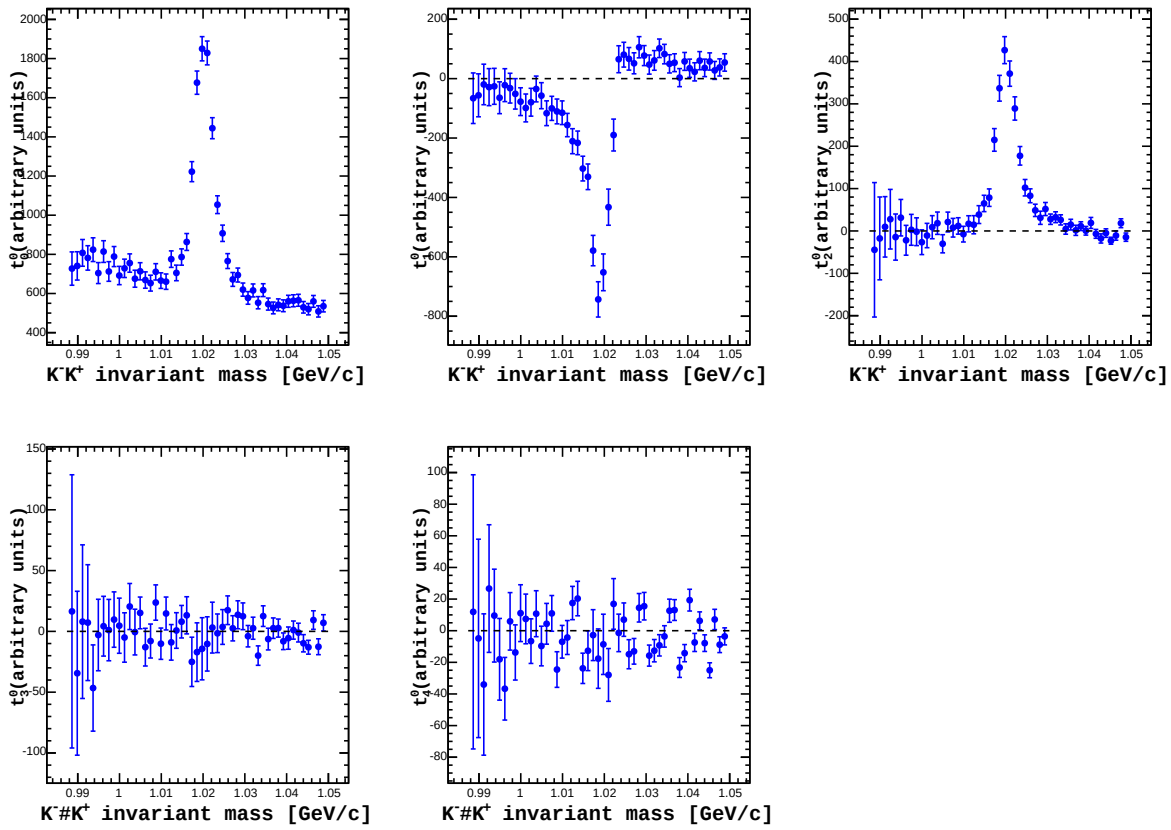

Figure 37: The first 5 Legendre polynomial weighted moments **NOT** background subtracted but efficiency corrected for $D^+ \to K^-K^+K^+$

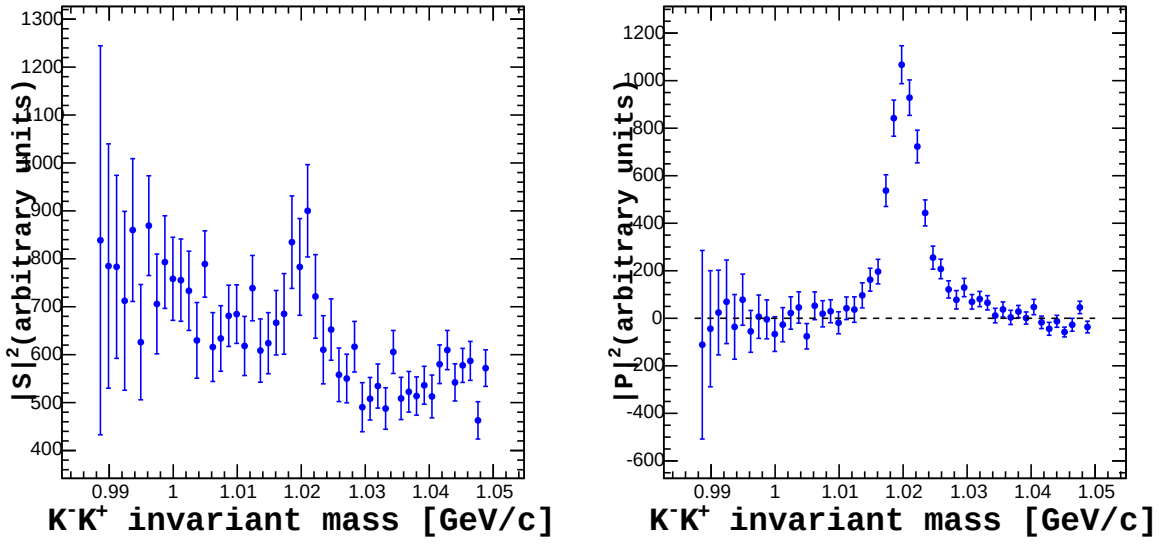

Figure 38: The S and P wave contributions calculated from eq. 130 and 131.

6.2 Signal Model

The available phase space for the $D^+ \to K^-K^+K^+$ is very limited due to the presence of three kaons. The KK spectrum runs from threshold up to $m_D - m_K = 1.370$ GeV/c^2. There aren't many resonances that couple to $K\bar{K}$ within these limits. In the K^-K^+ system the possible contributions include: the scalars $f_0(980)$, $a_0(980)$, $f_0(1370)$, $a_0(1450)$ and, perhaps, the $f_0(1500)$, the vector $\phi(1020)$, the tensor $f_2(1270)$. From the above resonances, only the $f_0(1370)$ is not well established. There is a large uncertainty in the values of its mass and width.

As was seen in the analysis of the moments of the angular distribution, the P-wave is very simple: there is only the $\phi(1020)$, which is the most prominent structure observed in the $D^+ \to K^-K^+K^+$ Dalitz plot. The remaining of it is divided into the S- and D-waves.

For the D-wave the only possible contribution is from $f_2(1270)$, which is easily distinguishable by the characteristic angular distribution. However, given the limited phase space and the small branching fraction for $f_2(1270) \to K\bar{K}$, the contribution of this spin-2 resonance is expected to be marginal.

The parametrization of the S-waves are always problematic. There is a long-standing debate about the nature of the scalar states, and which of them form the scalar nonet predicted by the Quark Model. Above 1 GeV there are three members of f_0 family, including the $f_0(1710)$, which does not contribute do the $D^+ \to K^-K^+K^+$ decay, because is way out of the phase space.

All f_0 states couple to $\pi\pi$ and to $K\bar{K}$. Having different combinations of $n\bar{n} = u\bar{u} + s\bar{s}$, the couplings to $\pi\pi$ and $K\bar{K}$ are expected to be different. In principle one should look also at the $\pi\pi$ channels in order to understand the role of the f_0 states in the $K\bar{K}$ system. In $D^+_{(s)} \to \pi^-\pi^+\pi^+$ [46–49] and $B^- \to K^-\pi^+\pi^-$ [50] decays a scalar state is required to fit the data. However, in these analyses the measured values of the mass and width of this scalar state are not consistent with any member of the f_0 family.

One possible interpretation is that in these decays what is observed is actually a combination of the $f_0(1370)$ and $f_0(1500)$. In this analysis we represent a possible superposition of the $f_0(1370)$ and $f_0(1500)$ by a single amplitude labeled as "$f_0(X)$". A single Breit-Wigner amplitude would be, in this case, just an effective representation of a superposition of nearby states. In the case of the $D^+ \to K^-K^+K^+$ decay, the scalar resonance $a_0(1450)$ ($m_0 = 1.474\,\text{GeV}/c^2$, $\Gamma_0 = 0.265$ GeV/c^2) [51] may also contribute. In some fits where the $a_0(1450)$ is not included, the parameters of the $f_0(X)$ amplitude may also include the effect of this state.

We therefore build the fit models in the following way. The $K\bar{K}$ system always include the $f_0(980)$ and $\phi(1020)$. For the $f_0(980)$ we use the values of the Flatté parameters from BES [52], $m_0 = 965 \pm 10\,\text{MeV}/c^2$, $g_\pi = 165 \pm 18$ MeV/c^2 and $g_K/g_\pi = 4.21 \pm 0.33$. (given the little sensiticvity for these parameters in the $K\bar{K}$ spectrum, we do not attempt to determine them parameters from the fit). In the K^-K^+ spectrum there is little sensitivity to the details of the line shape of the $f_0(980)$, though. Besides the $f_0(980)$, we also include a broad amplitude that occupies all the phase space. In the first fit, this amplitude is a non-resonant that returns a poor description of the data. Therefore, we tested using a amplitude with high-mass phase variation, a $f_0(X)$ and a $a_0(1250)$, which improve the fit quality.

This lack of sensitivity is illustrated in Fig. 39. In the left panel the Flatté formula is plotted in the $\pi\pi$ spectrum with two different sets of constants. The line in red is drawn

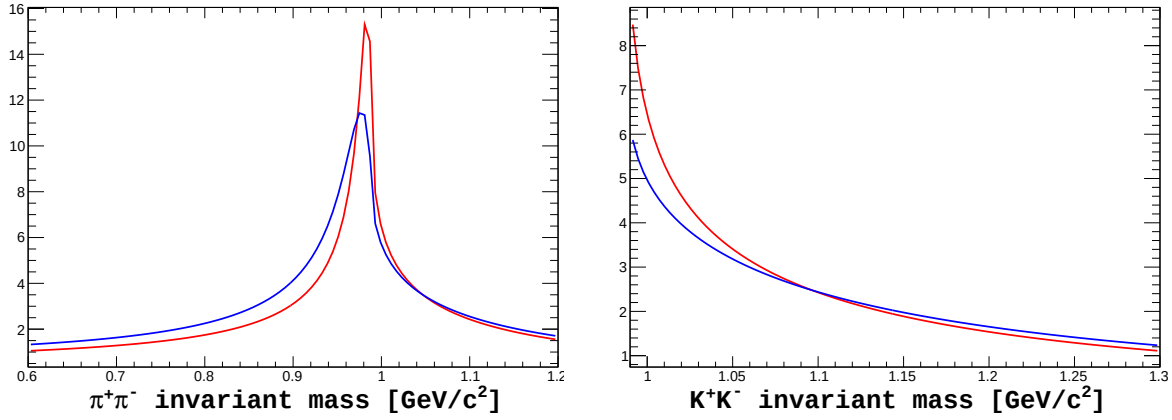

Figure 39: Left: two different parameterizations of the $f0(980)$ yield rather distinct line shapes below 1 GeV, but very similar ones above this limit. Right: the $f0(980)$ (red) and $a_0(980)$ (blue) line shapes in the $K\bar{K}$ spectrum.

using the values from BES, whereas the line in blue has is drawn changing the couplings by 50% and with $m_0 = 935\,\mathrm{MeV}/c^2$. These are arbitrary values, intended just to produce quite different line shapes in the $\pi\pi$ spectrum. We see that the line shapes are indeed very different below 1 GeV, but almost indistinguishable above the $K\bar{K}$ threshold.

The line shapes of the $f_0(980)$ and the $a_0(980)$ are very similar above 1 GeV, as shown in Fig. 39, so it is virtually impossible to disentangle these two states. This means that the state labeled as "$f_0(980)$" may be a combination of these two scalars.

Further combinations of the $K\bar{K}$ scalar resonances are tested. In some models the D-wave is also included. A summary of the relevant models is shown in Table 14.

Table 14: Summary of all Isobar Models considered in this analysis.

Model ID	$f_0(980)$	ϕ	NR	$f_0(X)$	$a_0(1450)$	$f_2(1270)$
1	✓	✓	✓			
2	✓	✓		✓		
3	✓	✓			✓	
4	✓	✓	✓			✓
5	✓	✓		✓		✓
6	✓	✓			✓	✓

6.3 Results

We now present the results of the $D^+ \to K^-K^+K^+$ Dalitz plot fits using the Isobar Model. The fits are performed on 111,464 candidates with $K^-K^+K^+$ mass within $2\sigma_{\mathrm{eff}}$ of fitted D mass, from which 90.45% we expect to be signal

The goodness-of-fit is estimated using as figure of merit the χ^2 per degree of freedom, χ^2/ndof, defined as

$$\chi^2 = \sum_{i=1}^{N\,\mathrm{bins}} \chi_i^2 = \sum_{i=0}^{N\,\mathrm{bins}} (N_{\mathrm{pdf_i}} - N_{\mathrm{data_i}})^2 / N_{\mathrm{data_i}}. \tag{132}$$

In the above definition, $N_{\mathrm{pdf_i}}$ is the expected number of events in the i^{th} bin and $N_{\mathrm{data_i}}$ is the observed bin population. The number of degrees of freedom, ndof, is the number of bins minus the number of free parameters minus one, $\mathrm{ndof} = N_{\,\mathrm{pars}} - N_{\,\mathrm{bins}} - 1$. Since there are two identical kaons in the final state, the χ^2/ ndof is computed using the folded Dalitz plot.

The Dalitz plot is divided into 500 bins of equal population (approximately 200 events per bin). The expected number of events is computed using a large MC simulation sample generated with phase space distribution. The MC simulation events are weighted by the full PDF, with the optimum set of parameters given by the fit. The MC simulation sample includes background and is weighted by the same efficiency function used in the signal fit. After weighting, the MC simulation sample is then scaled down to the number of events from data (signal and background) used in the fit to the data.

In this analysis, a signed χ_i^2 distribution over the Dalitz plot is also displayed. The positive values of χ_i^2 indicate an excess of predicted events. This plot has the information on how the discrepancies between the model and the data are distributed.

Another figure of merit are the moments of angular distribution. Described in Section 6.1, the moments are displayed here in two regions separately. Firstly, around the ϕ region, which is from the KK threshold up to 1.05 GeV/c^2 invariant mass. And, secondly from 1.05 GeV/c^2 until the KK kinematic limit.

A reference $\mathrm{FCN} = -2\log\mathcal{L}$ is calculated for the first model. For all other models, only the variation of FCN is quoted. In contrast with the χ^2/ ndof, the FCN is independent of the binning scheme.

As discussed in the previous section, all models include two components, namely the ϕK and $f_0(980)K$ amplitudes, plus one broad structure. The fits are repeated adding a fourth component, the $f_2(1270)K$. This procedure is based on our experience after trying many models.

In all fits the ϕK mode is chosen as reference, fixing the magnitude of its complex coefficient to 1 and its phase to zero degrees. All other coefficients are relative to this reference one.

6.3.1 Model 1

The first model (Model 1) is composed by a $f_0(980)$, $\phi(1020)$ and a nonresonant (NR) amplitude. The resulting magnitudes, phases and fit fractions are shown in Table 15. In Figs. 40 and 41 we see the projections of the Dalitz plot onto the three axes, $s^{\mathrm{hi}}_{K^+K^-} = s_{\mathrm{hi}}$, $s^{\mathrm{lo}}_{K^+K^-} = s_{\,\mathrm{lo}}$ and $s_{K^+K^+} = s_{23}$, with the fit result superimposed (blue line). The moments of angular distribution t^0_{0-4} are shown in Figs. 42 to 46

Although the fit projections appears to be in reasonable agreement with th data, the fit quality is poor. Model 1 is only in qualitative agreement with the data. The $f_0(980)K$ component has the largest fit fractions, almost twice the fraction of the NR. There is a good agreement in the ϕ region. A clear correlation between the NR and $f_0(980)K$

Table 15: Magnitudes, phases and fit fractions from the Dalitz plot fit using Model 1.

Resonance	**Magnitude**	**Phase[°]**	**Fraction (%)**
$f_0(980)$	4.48±0.15	-89.0±1.1	57.0±3.7
NR	10.47±0.25	124.0±3.3	29.4±1.3
ϕ	1[fix]	0[fix]	7.16±0.13
sum			93.6±4.0

FCN = -144193
χ^2/ndof = 844.49/495 = 1.71

Table 16: Interference fit fractions (%) for Model 1

	$f_0(980)$	NR	ϕ
$f_0(980)$	57.0	4.5	1.9
NR		29.4	0
ϕ			7.2

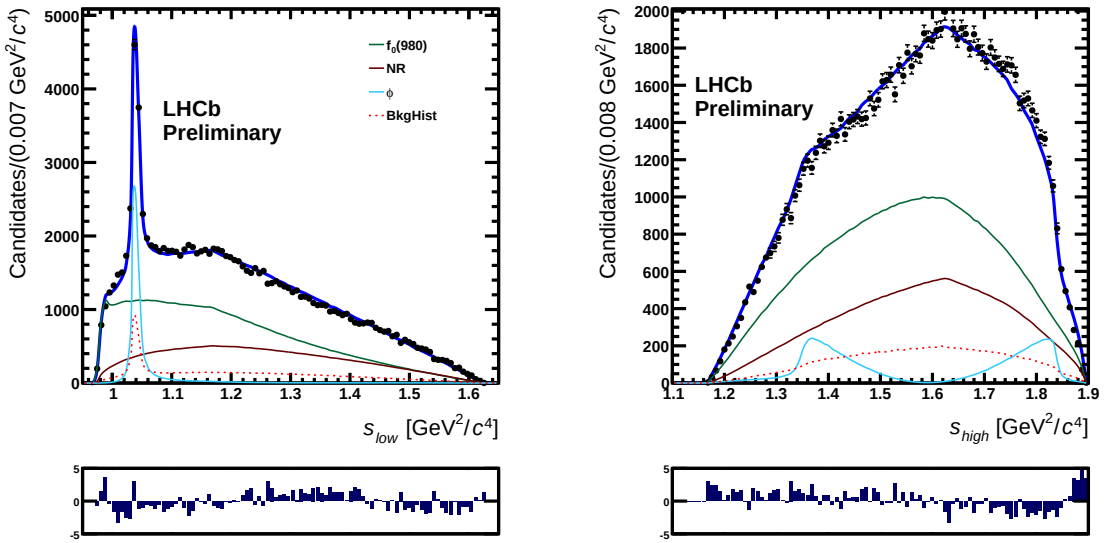

Figure 40: Projections of the data onto $s_{\rm hi}$ (left) and $s_{\rm lo}$ axes (right). The fit result (blue line) for Model 1 is superimposed. The contribution from the different amplitudes are also shown.

components can be observed in the interference fit fractions, shown in Table 16. To some extent, this is expected since these amplitudes populate the whole Dalitz plot. The phase of the Flatté function representing the $f_0(980)$ has a small variation above the ϕ peak, so the NR and $f_0(980)K$ have similar behaviour. The ϕK amplitude has a small interference with the other components.

In Fig. 41 we see three regions where the model is in clear disagreement with the data. The structures observed at $s_{\rm hi} \sim 1.8$ GeV$^2/c^4$ and $1.15 < s_{\rm lo} < 1.35$ GeV$^2/c^4$, and at the bottom of the Dalitz plot, $s_{\rm hi} < 1.3$ GeV$^2/c^4$ will appear in all fits. The former is due to a

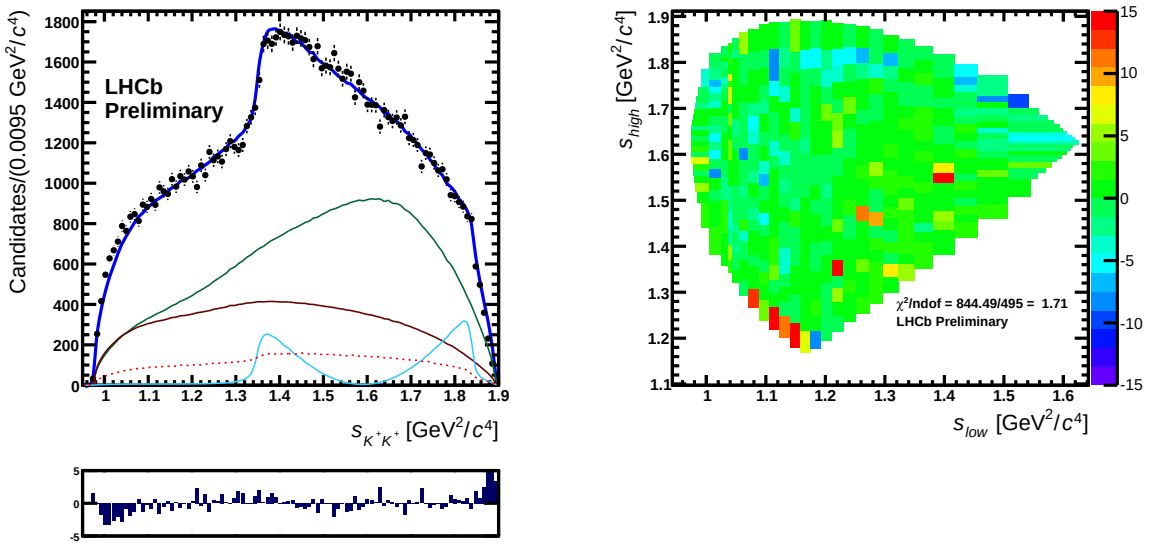

Figure 41: Left: projection of the data onto s_{23} axis, with the fit result for Model 1 superimposed. Right: the distribution of the signed χ^2 over the Dalitz plot.

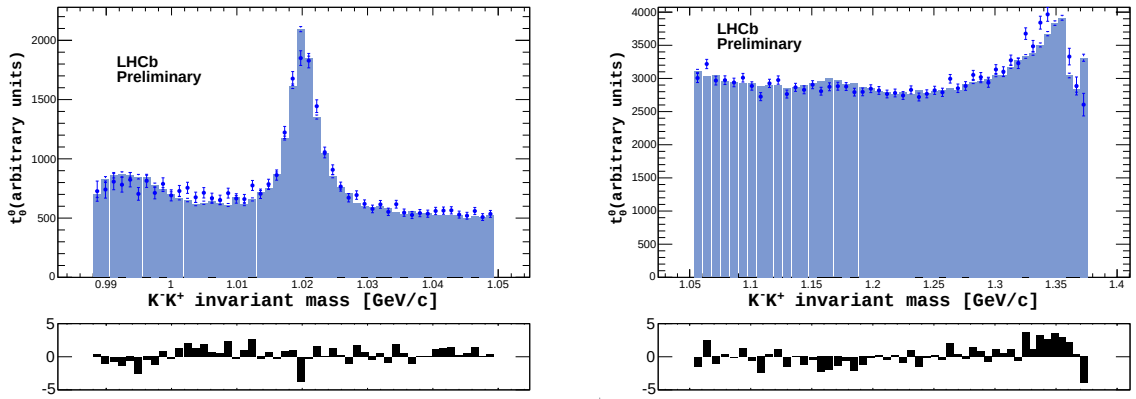

Figure 42: Moment t_0^0 of angular distribution for data (blue dots with error bars) and ToyMC of Model1 (solid histogram). From 0.9–1.05 GeV/c^2, on left panel, and from 1.05 GeV/c^2 up to 1.9 GeV/c^2 on right panel.

statistical fluctuation in the MC sample used for computing the efficiency, whereas the latter is in the region where the efficiency drops very rapidly. Both structures accounts for a discrepancy in the t_0^0 moments at $1.0 < m_{\rm KK} < 1.01$ GeV/c^2. The third region with large discrepancy is the large $s_{\rm hi}$, large $s_{\rm lo}$. This can be interpreted as a limitation of the model. As we will see in the following, a phase variation in this region is required to explain the data.

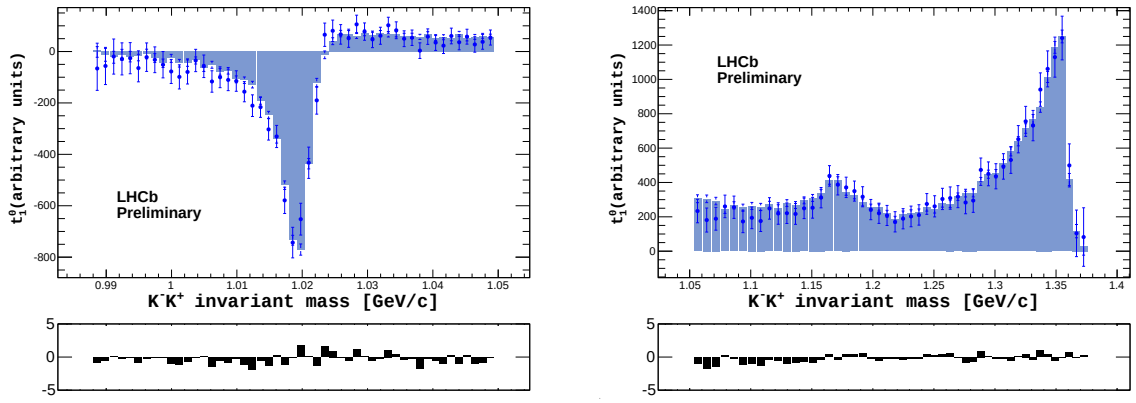

Figure 43: Moment t_1^0 of angular distribution for data (blue dots with error bars) and ToyMC of Model1 (solid histogram). From 0.9–1.05 GeV/c^2, on left panel, and from 1.05 GeV/c^2 up to 1.9 GeV/c^2 on right panel.

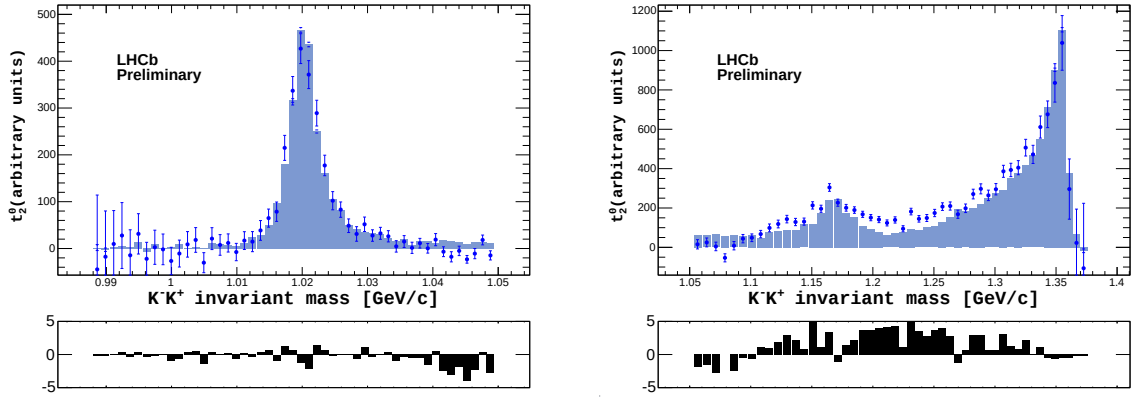

Figure 44: Moment t_2^0 of angular distribution for data (blue dots with error bars) and ToyMC of Model1 (solid histogram). From 0.9–1.05 GeV/c^2, on left panel, and from 1.05 GeV/c^2 up to 1.9 GeV/c^2 on right panel.

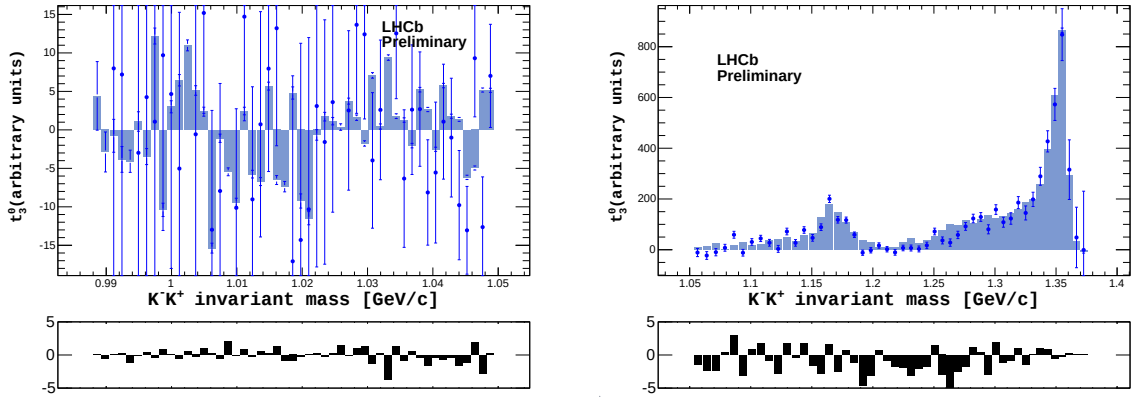

Figure 45: Moment t_3^0 of angular distribution for data (blue dots with error bars) and ToyMC of Model1 (solid histogram). From 0.9–1.05 GeV/c^2, on left panel, and from 1.05 GeV/c^2 up to 1.9 GeV/c^2 on right panel.

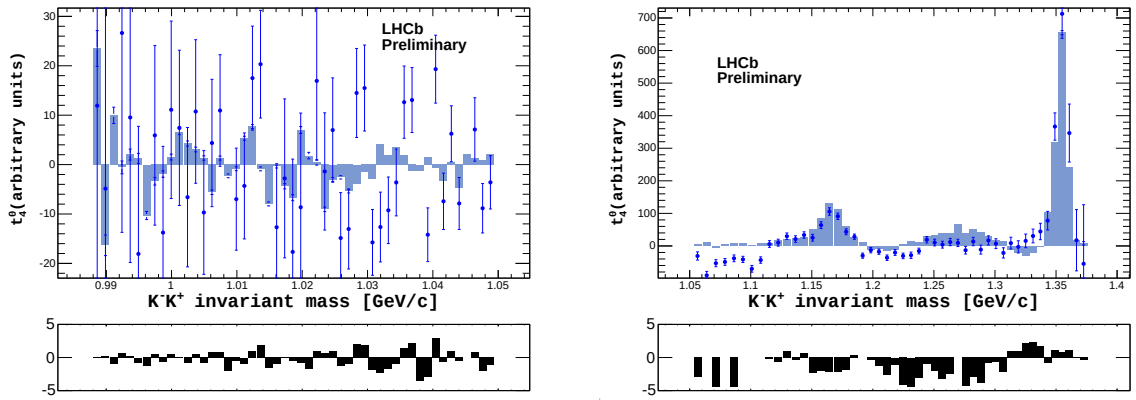

Figure 46: Moment t_4^0 of angular distribution for data (blue dots with error bars) and ToyMC of Model1 (solid histogram). From 0.9–1.05 GeV/c^2, on left panel, and from 1.05 GeV/c^2 up to 1.9 GeV/c^2 on right panel.

6.3.2 Model 2

Table 17: Magnitudes, phases and fit fractions from the Dalitz plot fit using Model 2.

Resonance	**Magnitude**	**Phase**[°]	**Fraction (%)**
$f_0(980)$	3.20±0.12	-59.3±5.1	26.5±1.5
$f_0(X)$	3.52±0.58	13.8±8.1	22.1±3.2
ϕ	1[fix]	0[fix]	6.5±0.12
sum			55.1±3.5

$\mathbf{\Delta}$ FCN $= \mathbf{-206}$
$\boldsymbol{\chi^2}$/ ndof $= \mathbf{635.66/493 = 1.29}$
$\boldsymbol{f_0(X):\ m_0 = 1429.8 \pm 19}$, $\boldsymbol{\Gamma_0 = 347.8 \pm 49\ MeV/c^2}$

Table 18: Interference fit fractions (%) for Model 2

	$f_0(980)$	$f_0(X)$	ϕ
$f_0(980)$	26.5	43.1	0.8
$f_0(X)$		22.1	1.0
ϕ			6.5

An attempt for a better description of the K^-K^+ S-wave consists in changing the NR amplitude by the $f_0(X)K$, which has a phase variation across the Dalitz plot.

The fit results are shown in Table 17 and in Figs. 47 to 53. A significant improvement on the fit quality is observed, in particular at the rightmost region of the Dalitz plot. The two S-wave components now have equivalent fit fractions, but the sum of all contributions is only 54%. The correlation between the S-wave components persists, since both amplitudes are broad and populate the whole phase space. The superposition of similar amplitudes is reflected in the large errors of the fit fractions. The interference fit fractions are very large, since the relative phase between the two S-wave components is $\sim 80°$. The ϕK fit fraction is nearly unchanged, reflecting the limited interference with the S-wave.

In this fit the mass and width of the $f_0(X)$ are free parameters. The fit yields $m_0 = 1415.4 \pm 14\,\mathrm{MeV}/c^2$ and $\Gamma_0 = 304 \pm 42$ MeV/c^2.

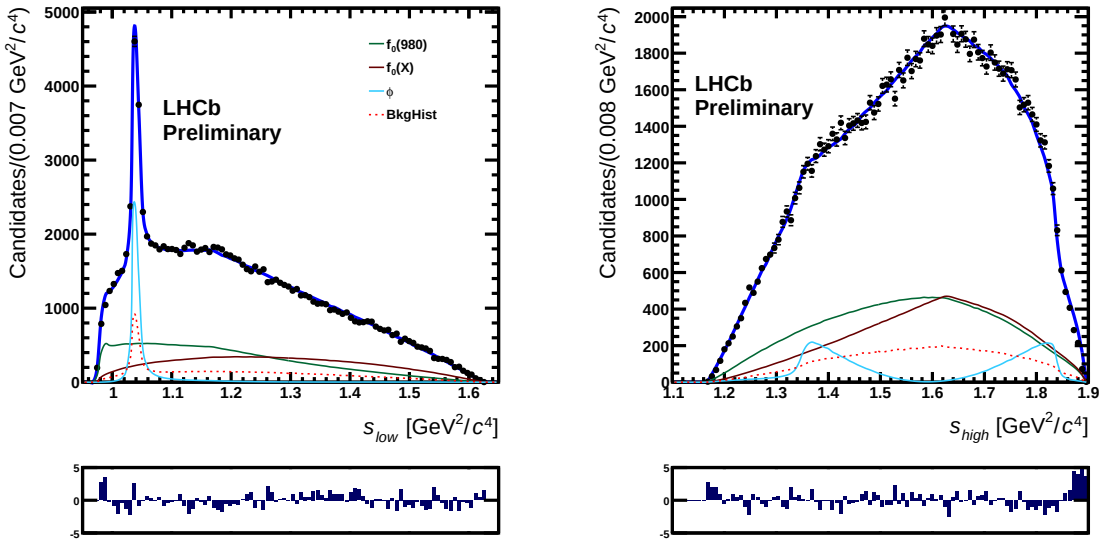

Figure 47: Projections of the data onto s_{hi} (left) and s_{lo} axes (right). The fit result (blue line) for Model 2 is superimposed. The contribution from the different amplitudes are also shown.

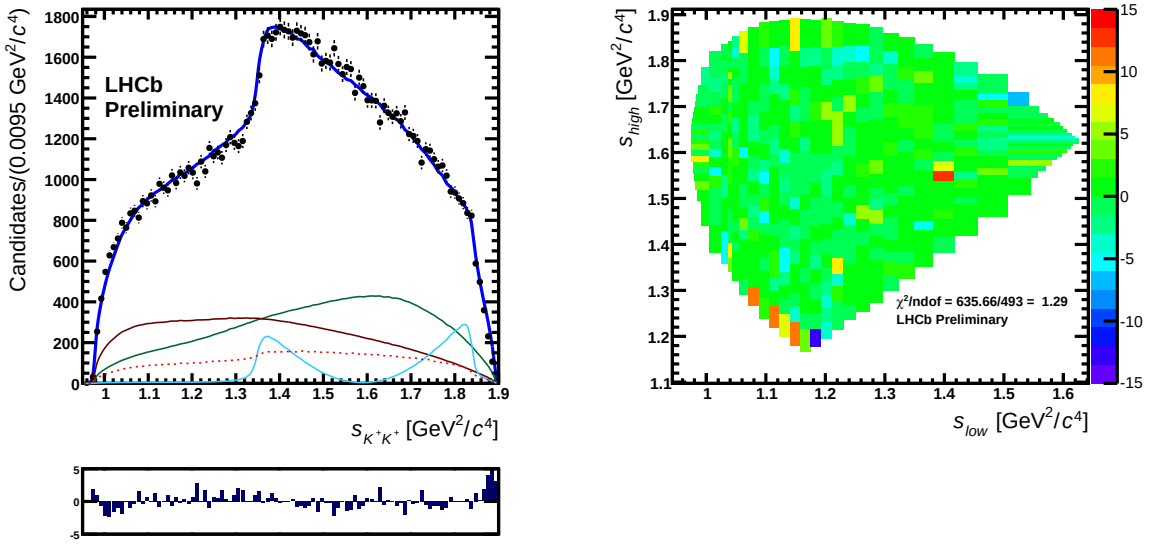

Figure 48: Left: projection of the data onto s_{23} axis, with the fit result for Model 2 superimposed. Right: the distribution of the signed χ^2 over the Dalitz plot.

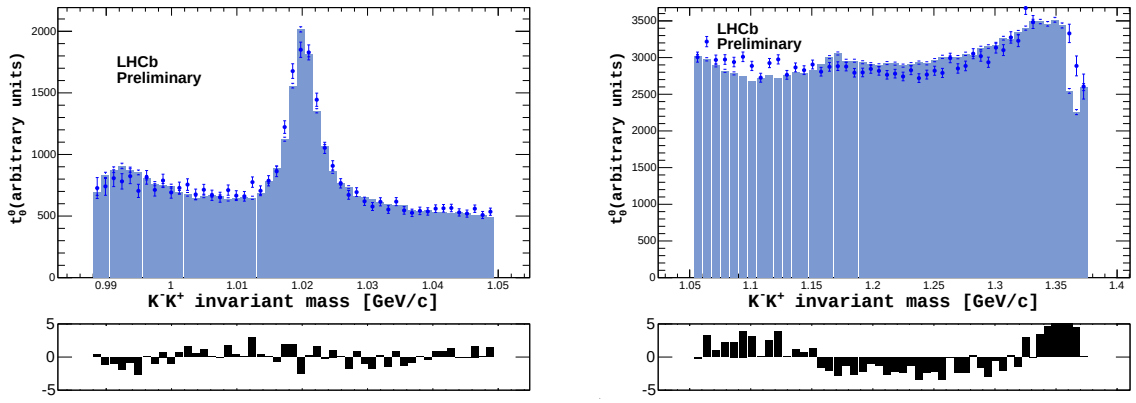

Figure 49: Moment t_0^0 of angular distribution for data (blue dots with error bars) and ToyMC of Model2 (solid histogram). From 0.9–1.05 GeV/c^2, on left panel, and from 1.05 GeV/c^2 up to 1.9 GeV/c^2 on right panel.

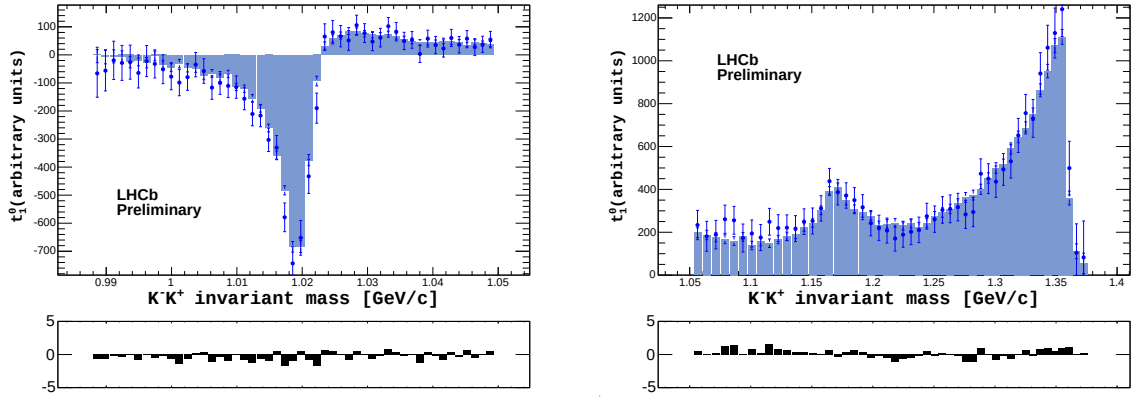

Figure 50: Moment t_1^0 of angular distribution for data (blue dots with error bars) and ToyMC of Model2 (solid histogram). From 0.9–1.05 GeV/c^2, on left panel, and from 1.05 GeV/c^2 up to 1.9 GeV/c^2 on right panel.

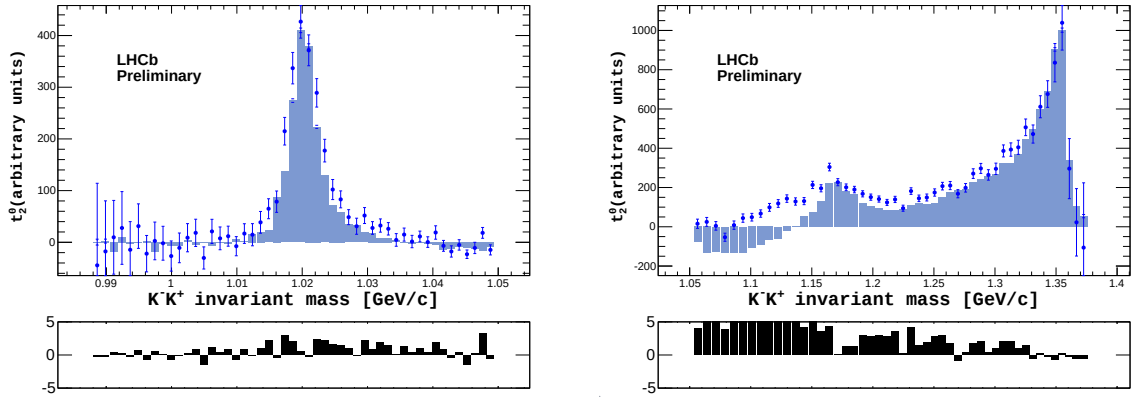

Figure 51: Moment t_2^0 of angular distribution for data (blue dots with error bars) and ToyMC of Model2 (solid histogram). From 0.9–1.05 GeV/c^2, on left panel, and from 1.05 GeV/c^2 up to 1.9 GeV/c^2 on right panel.

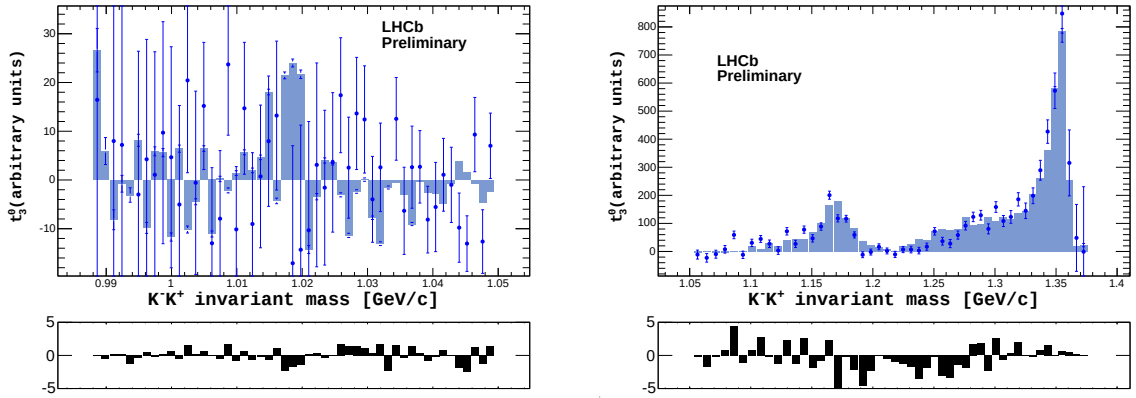

Figure 52: Moment t_3^0 of angular distribution for data (blue dots with error bars) and ToyMC of Model2 (solid histogram). From 0.9–1.05 GeV/c^2, on left panel, and from 1.05 GeV/c^2 up to 1.9 GeV/c^2 on right panel.

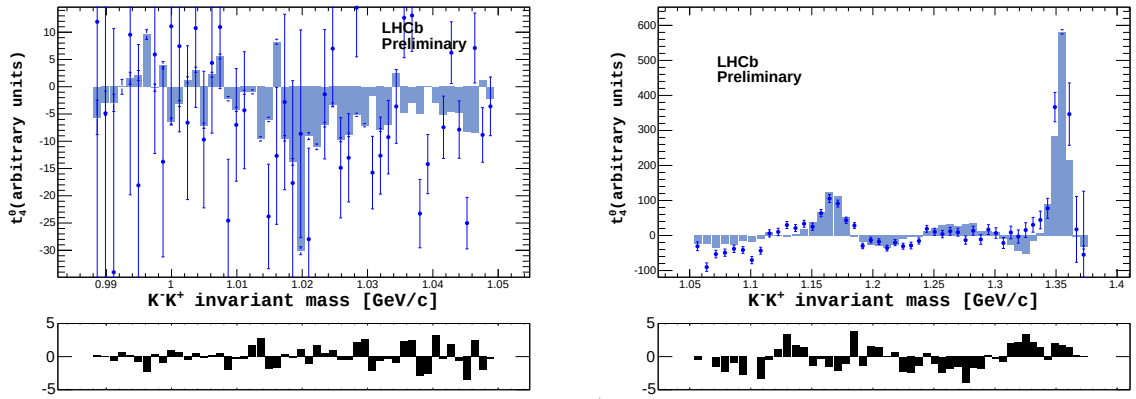

Figure 53: Moment t_4^0 of angular distribution for data (blue dots with error bars) and ToyMC of Model2 (solid histogram). From 0.9–1.05 GeV/c^2, on left panel, and from 1.05 GeV/c^2 up to 1.9 GeV/c^2 on right panel.

6.3.3 Model 3

Table 19: Magnitudes, phases and fit fractions from the Dalitz plot fit using Model 3.

Resonance	**Magnitude**	**Phase[°]**	**Fraction (%)**
$a_0(1450)$	3.417±0.064	44.6±3.4	18.56±0.57
$f_0(980)$	3.404±0.061	-71.8±1.3	29.86±0.96
ϕ	1[fix]	0[fix]	6.49±0.12
sum			54.91±1.12
$\mathbf{\Delta}$ FCN $= \mathbf{-183}$			
$\boldsymbol{\chi^2}$/ ndof $= \mathbf{652.15/495 = 1.32}$			

Table 20: Interference fit fractions (%) for Model 3

	$a_0(1450)$	$f_0(980)$	ϕ
$a_0(1450)$	18.6	43.1	1.0
$f_0(980)$		29.9	1.0
ϕ			6.5

In Model 3 the NR amplitude is replaced by the $a_0(1450)K$. This resonance has nominal mass above the kinematic limit ($m_D - m_K = 1.376$ GeV/c^2) but it still contributes due to its large width (265 ± 13 MeV/c^2). The fit results are shown in Table 19 and in Figs. 54 to 60.

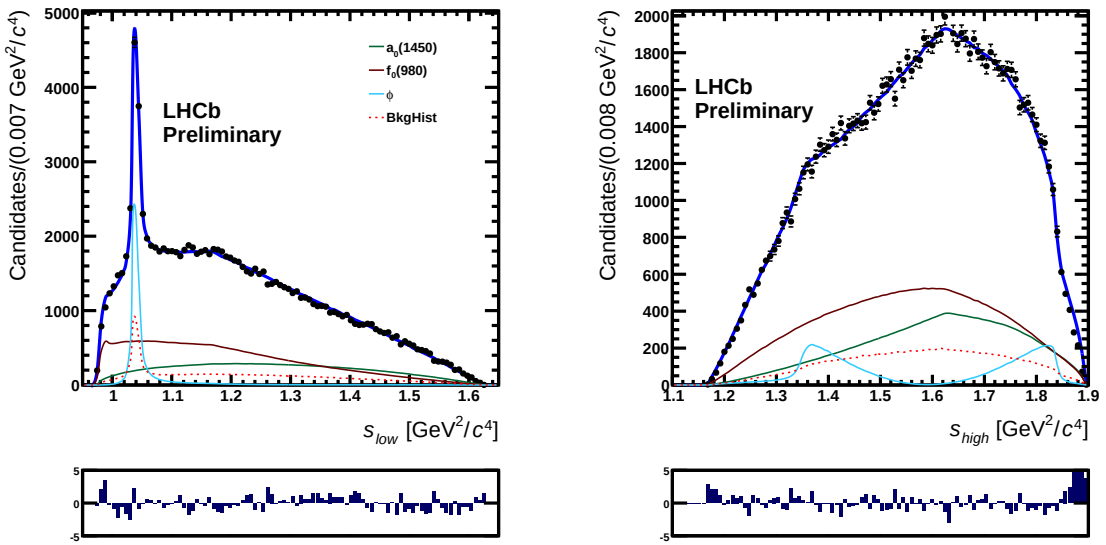

Figure 54: Projections of the data onto s_{hi} (left) and s_{lo} axes (right). The fit result (blue line) for Model 3 is superimposed. The contribution from the different amplitudes are also shown.

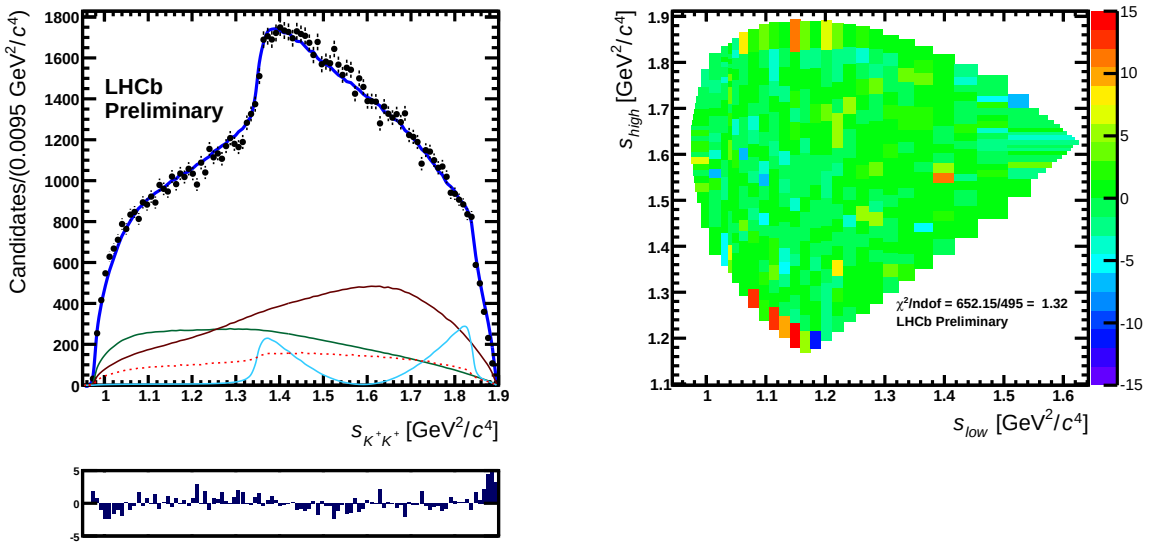

Figure 55: Left: projection of the data onto s_{23} axis, with the fit result for Model 3 superimposed. Right: the distribution of the signed χ^2 over the Dalitz plot.

The result is somewhat similar to that of Model 2, with a big correlation between the two S-wave components. The relative phase between the two amplitudes is $\sim 120°$, yielding a larger interference fit fraction, shown in Table 20, compared to Model 2. The sum of fit fractions is also small in Model 3, but with much smaller statistical error.

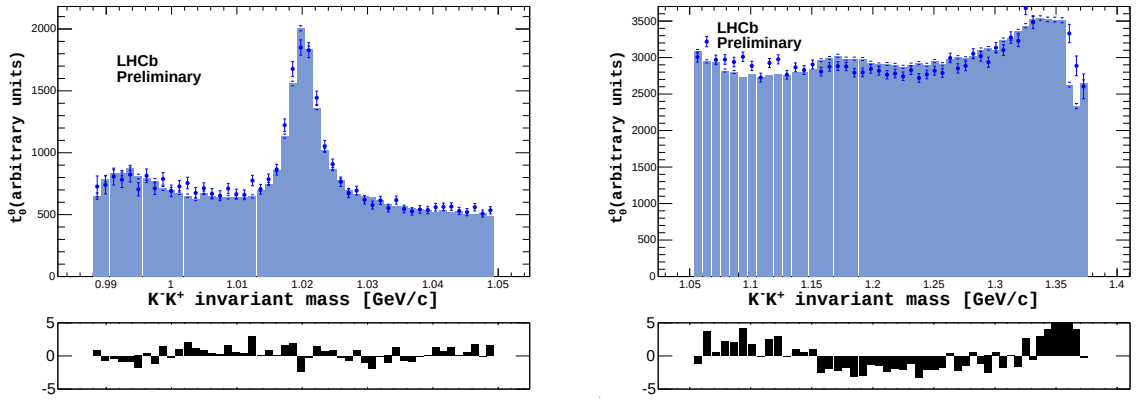

Figure 56: Moment t_0^0 of angular distribution for data (blue dots with error bars) and ToyMC of Model3 (solid histogram). From 0.9–1.05 GeV/c^2, on left panel, and from 1.05 GeV/c^2 up to 1.9 GeV/c^2 on right panel.

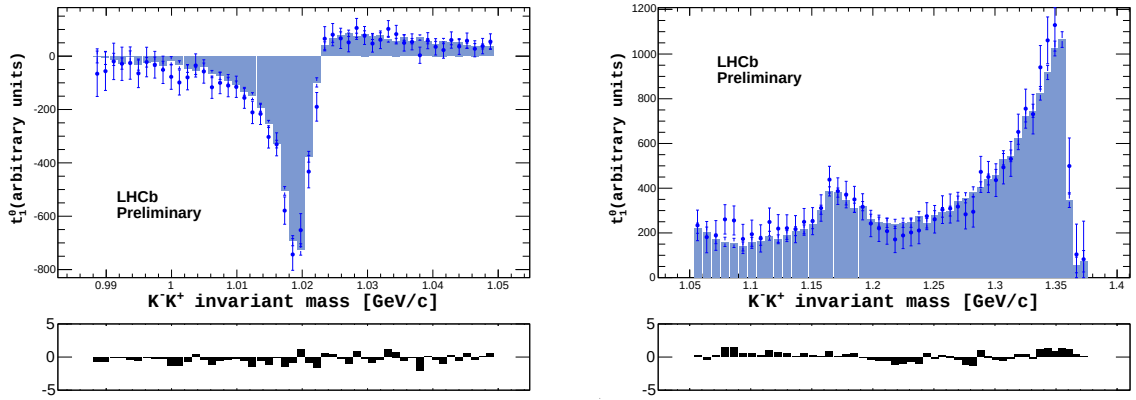

Figure 57: Moment t_1^0 of angular distribution for data (blue dots with error bars) and ToyMC of Model3 (solid histogram). From 0.9–1.05 GeV/c^2, on left panel, and from 1.05 GeV/c^2 up to 1.9 GeV/c^2 on right panel.

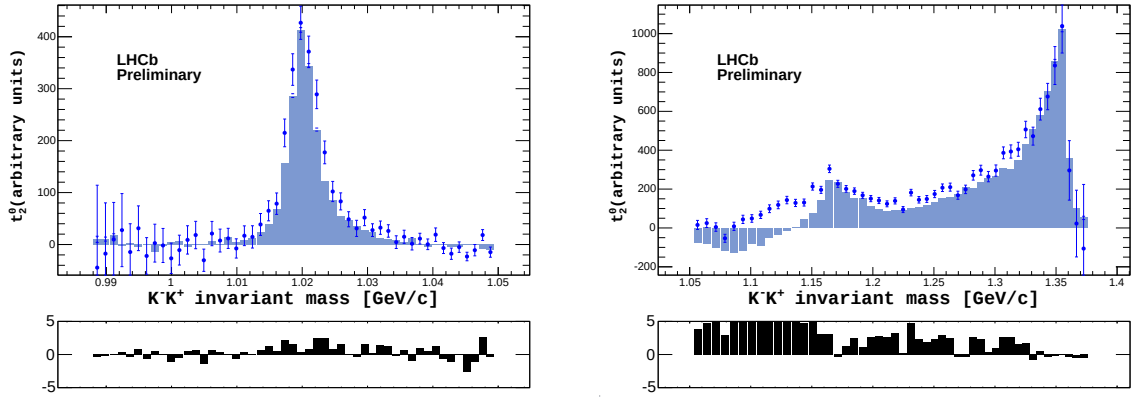

Figure 58: Moment t_2^0 of angular distribution for data (blue dots with error bars) and ToyMC of Model3 (solid histogram). From 0.9–1.05 GeV/c^2, on left panel, and from 1.05 GeV/c^2 up to 1.9 GeV/c^2 on right panel.

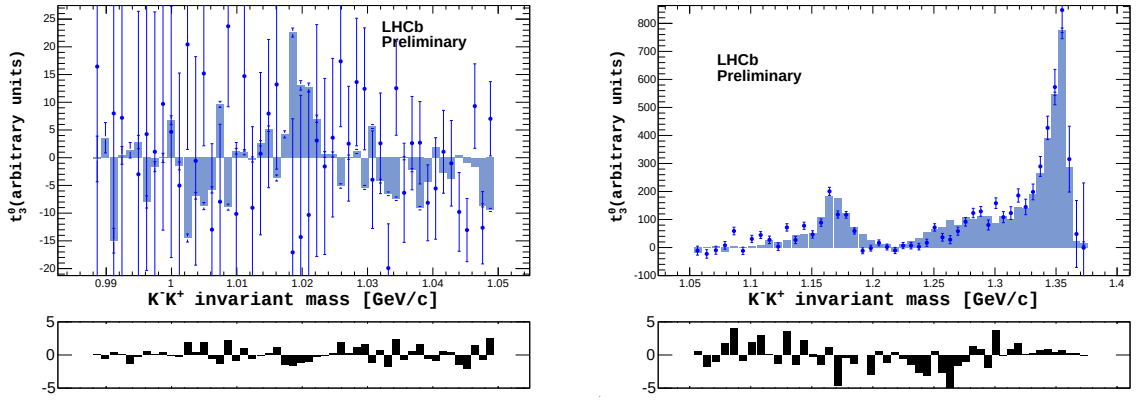

Figure 59: Moment t_3^0 of angular distribution for data (blue dots with error bars) and ToyMC of Model3 (solid histogram). From 0.9–1.05 GeV/c^2, on left panel, and from 1.05 GeV/c^2 up to 1.9 GeV/c^2 on right panel.

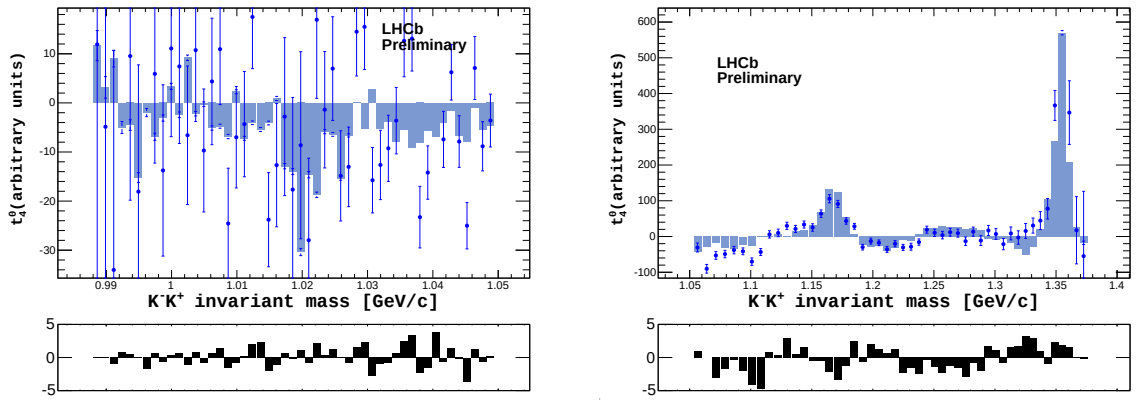

Figure 60: Moment t_4^0 of angular distribution for data (blue dots with error bars) and ToyMC of Model3 (solid histogram). From 0.9–1.05 GeV/c^2, on left panel, and from 1.05 GeV/c^2 up to 1.9 GeV/c^2 on right panel.

6.3.4 Model 4

Table 21: Magnitudes, phases and fit fractions from the Dalitz plot fit using Model 4.

Resonance	**Magnitude**	**Phase**[°]	**Fraction (%)**
$f_0(980)$	3.38±0.27	-85.8±2.1	31.7±10.3
$f_2(1270)$	1.98±0.27	-8.6±7.9	0.080±0.043
NR	10.48±0.20	98.5±6.5	28.8±1.8
ϕ	1[fix]	0[fix]	6.99±0.25
sum			67.5±10.4

$\mathbf{\Delta}$ FCN $= \mathbf{-114}$
$\boldsymbol{\chi^2}$**/** ndof $=$ **728.58/493 = 1.48**

Table 22: Interference fit fractions (%) for Model 4

	$f_0(980)$	$f_2(1270)$	NR	ϕ
$f_0(980)$	31.7	0.2	30.9	1.4
$f_2(1270)$	0	0.1	0	0
NR	0	0	28.8	0
ϕ	0	0	0	7.0

In Models 4, 5 and 6 the tensor resonance $f_2(1270)$ is added to Models 1, 2 and 3, respectively.

The results from Model 4 are shown in Table 21 and in Figs. 61 to 67. The contribution from the additional resonance is very small, as expected for a spin-2 state with so little phase space, but it is still significant. The inclusion of the $f_2(1270)$ causes a significant improvement in the fit quality of Model 1, reducing the fraction of the $f_0(980)$ component. An improvement is observed at the rightmost edge of the Dalitz plot, as shown in Fig. 62.

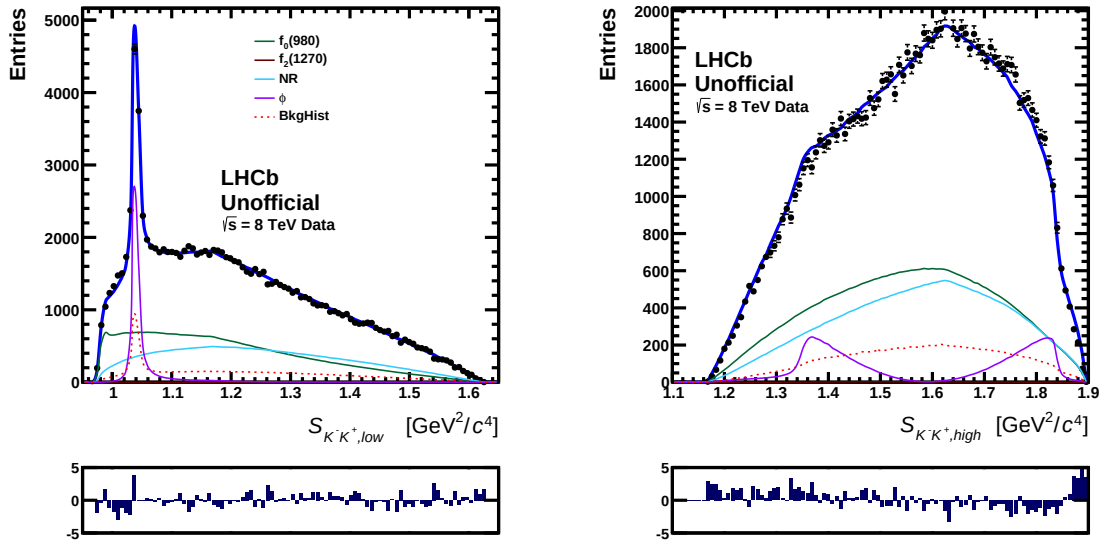

Figure 61: Projections of the data onto $s_{\rm hi}$ (left) and $s_{\rm lo}$ axes (right). The fit result (blue line) for Model 4 is superimposed. The contribution from the different amplitudes are also shown.

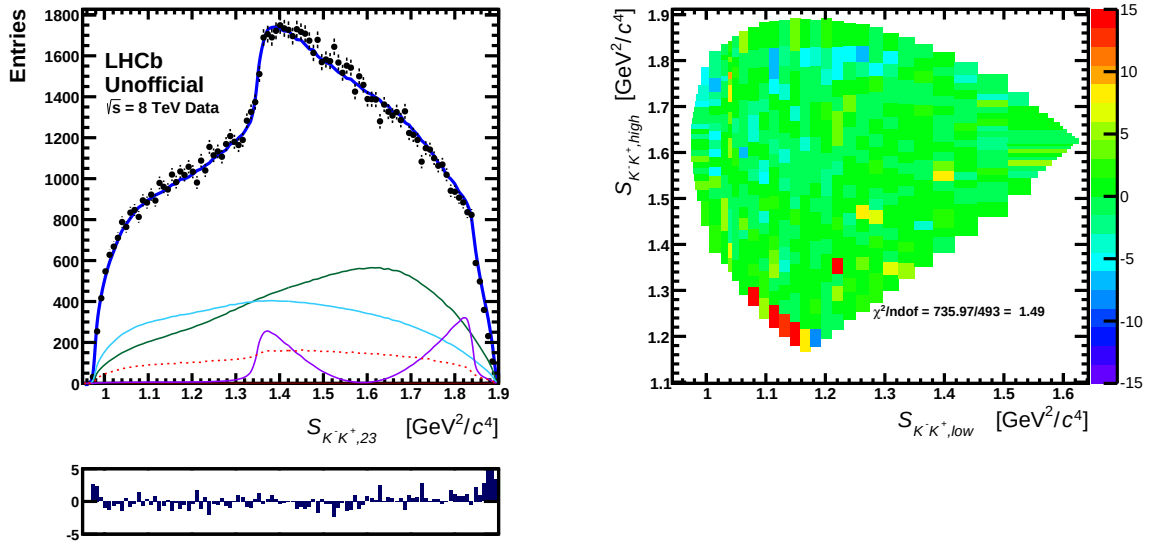

Figure 62: Left: projection of the data onto s_{23} axis, with the fit result for Model 4 superimposed. Right: the distribution of the signed χ^2 over the Dalitz plot.

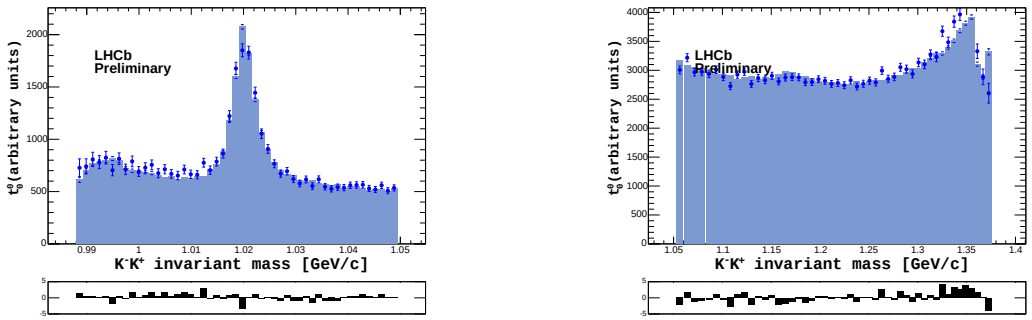

Figure 63: Moment t_0^0 of angular distribution for data (blue dots with error bars) and ToyMC of Model4 (solid histogram). From 0.9–1.05 GeV/c^2, on left panel, and from 1.05 GeV/c^2 up to 1.9 GeV/c^2 on right panel.

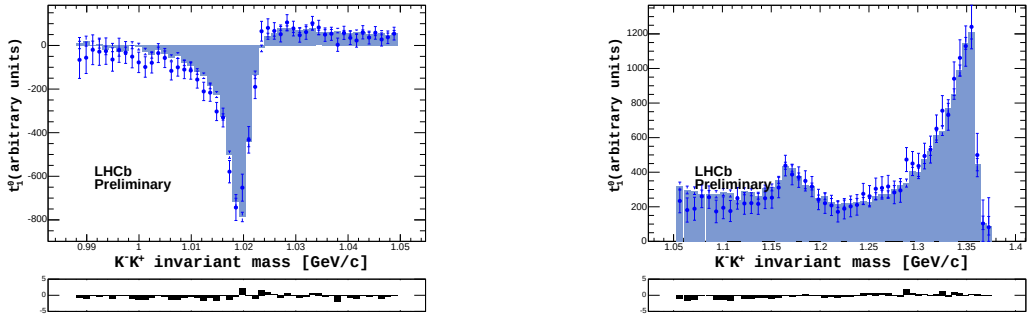

Figure 64: Moment t_1^0 of angular distribution for data (blue dots with error bars) and ToyMC of Model4 (solid histogram). From 0.9–1.05 GeV/c^2, on left panel, and from 1.05 GeV/c^2 up to 1.9 GeV/c^2 on right panel.

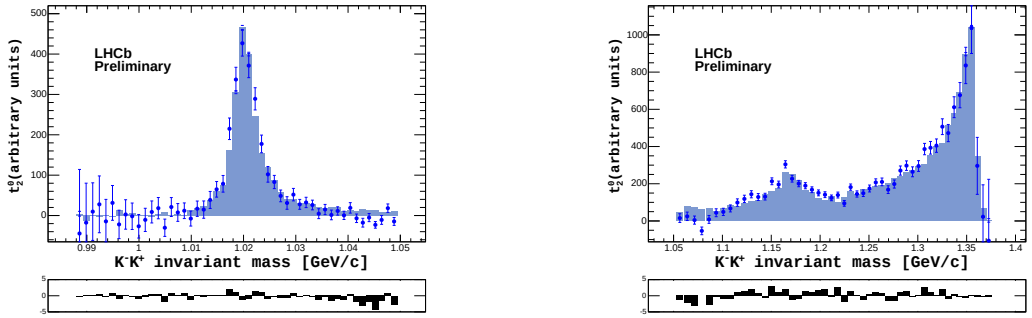

Figure 65: Moment t_2^0 of angular distribution for data (blue dots with error bars) and ToyMC of Model4 (solid histogram). From 0.9–1.05 GeV/c^2, on left panel, and from 1.05 GeV/c^2 up to 1.9 GeV/c^2 on right panel.

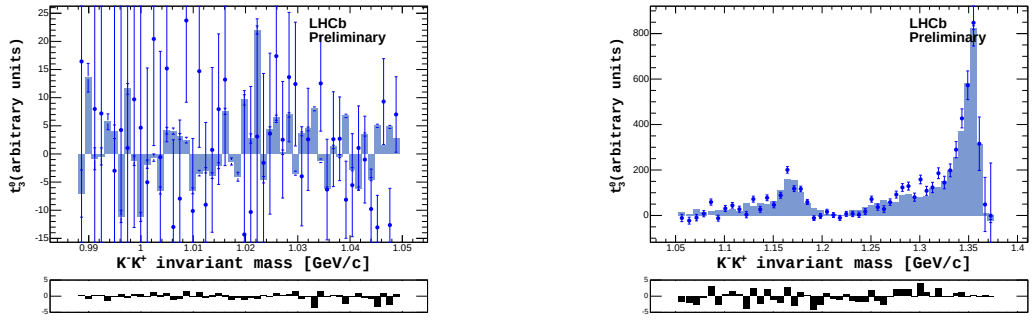

Figure 66: Moment t_3^0 of angular distribution for data (blue dots with error bars) and ToyMC of Model4 (solid histogram). From 0.9–1.05 GeV/c^2, on left panel, and from 1.05 GeV/c^2 up to 1.9 GeV/c^2 on right panel.

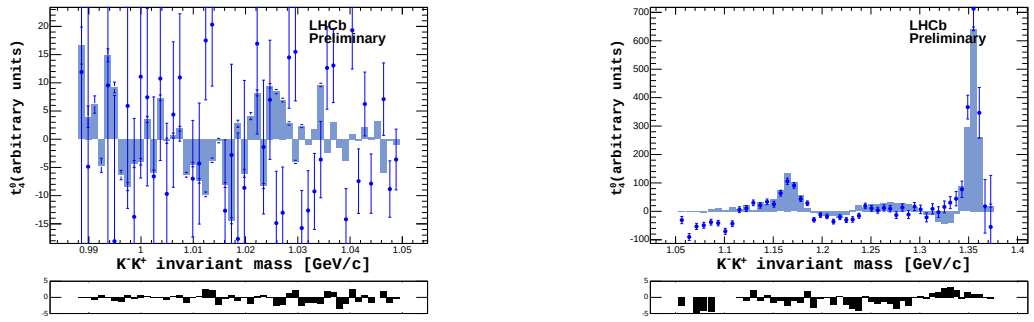

Figure 67: Moment t_4^0 of angular distribution for data (blue dots with error bars) and ToyMC of Model4 (solid histogram). From 0.9–1.05 GeV/c^2, on left panel, and from 1.05 GeV/c^2 up to 1.9 GeV/c^2 on right panel.

6.3.5 Model 5

Table 23: Magnitudes, phases and fit fractions from the Dalitz plot fit using Model 5.

Resonance	**Magnitude**	**Phase**[°]	**Fraction (%)**
$f_0(980)$	2.263±0.068	-37.7±9.9	13.6±5.3
$f_2(1270)$	1.79±0.25	-37.9±7.4	0.063±0.036
$f_0(X)$	14.7±2.9	36.3±7.7	48±22
ϕ	1[fix]	0[fix]	6.7±2.2
sum			68±23

$\boldsymbol{\Delta}$ FCN $= \boldsymbol{-257}$
$\boldsymbol{\chi^2}$/ ndof $= \boldsymbol{577.9/491 = 1.18}$
$\boldsymbol{f_0(X) : m_0 = 1.886 \pm 0.085,\ \Gamma_0 = 0.050 \pm 0.810}$ GeV/$\boldsymbol{c^2}$

Table 24: Interference fit fractions (%) for Model 5

	$f_0(980)$	$f_2(1270)$	$f_0(X)$	ϕ
$f_0(980)$	13.6	0.1	31.9	0.2
$f_2(1270)$	0	0.1	0	0.1
$f_0(X)$	0	0	47.6	-0.2
ϕ	0	0	0	6.7

In Table 23 and in Figs. 68 to 74 we have the fit results of Model 5, which is Model 2 plus the $f_2(1270)$.

As for Model 4, a small contribution from the tensor resonance in Model 5 causes an improvement on the fit quality when compared to Model 2.

There is a second solution in which the phases and fit fractions of the S-wave, as well as the $f_0(X)$ parameters are significantly different from those obtained with Model 2 (see Section B). In this solution the mass of the $f_0(X)$, $m_0 = 1.873 \pm 0.065$ GeV/c^2, is way out of the phase space limits, whereas the width, $\Gamma_0 = 0.264 \pm 0.297$ GeV/c^2 is much narrower than the one given by the fit without the $f_2(1270)K$ amplitude. This solution has a better FCN, but is discarded because of the unphysical values of the $f_0(X)$ parameters.

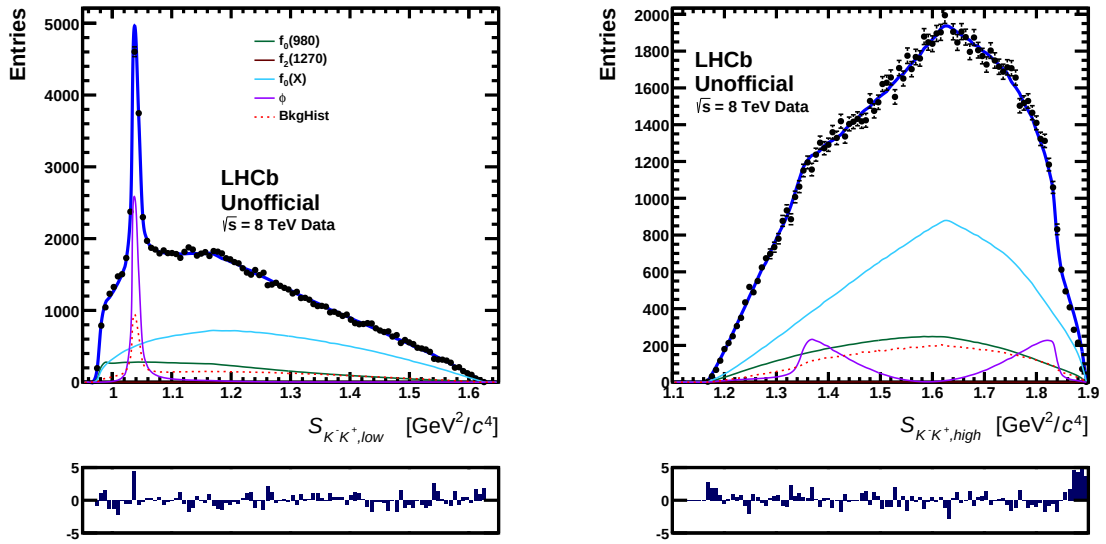

Figure 68: Projections of the data onto $s_{\rm hi}$ (left) and $s_{\rm lo}$ axes (right). The fit result (blue line) for Model 5 is superimposed. The contribution from the different amplitudes are also shown.

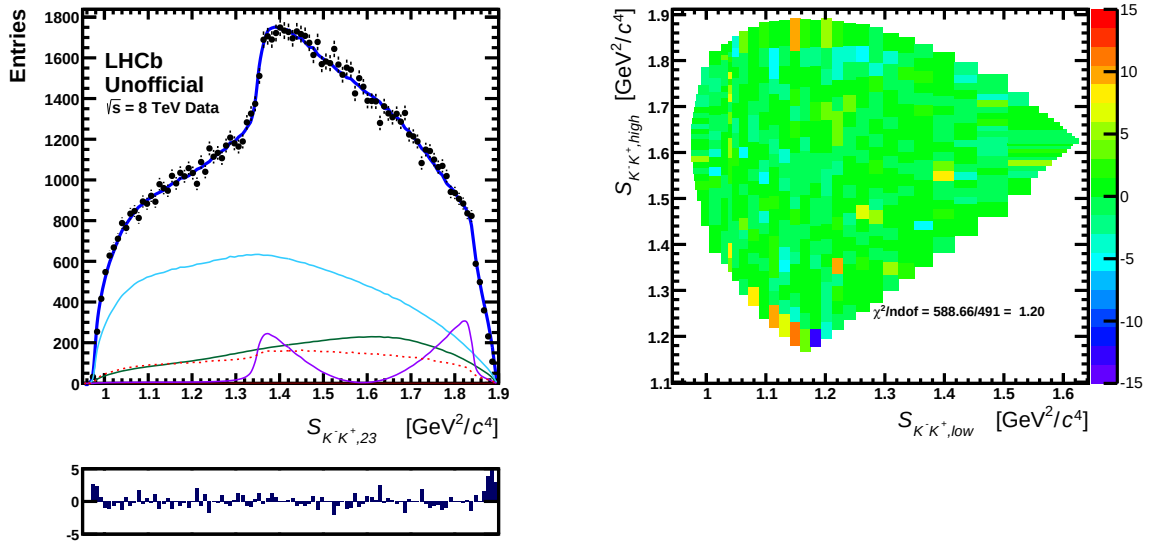

Figure 69: Left: projection of the data onto s_{23} axis, with the fit result for Model 5 superimposed. Right: the distribution of the signed χ^2 over the Dalitz plot.

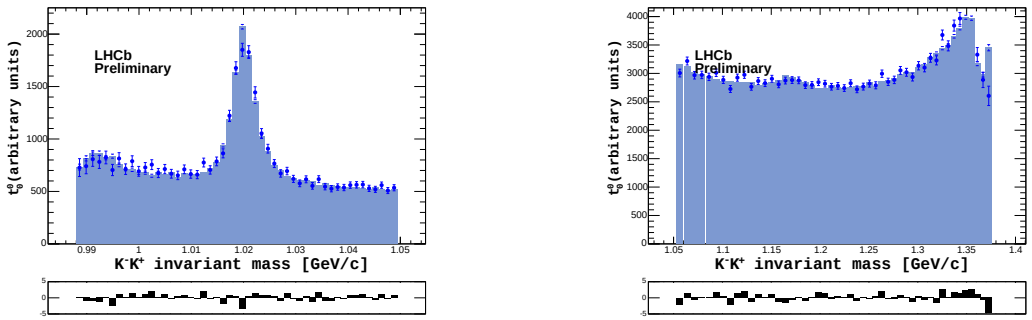

Figure 70: Moment t_0^0 of angular distribution for data (blue dots with error bars) and ToyMC of Model5 (solid histogram). From 0.9–1.05 GeV/c^2, on left panel, and from 1.05 GeV/c^2 up to 1.9 GeV/c^2 on right panel.

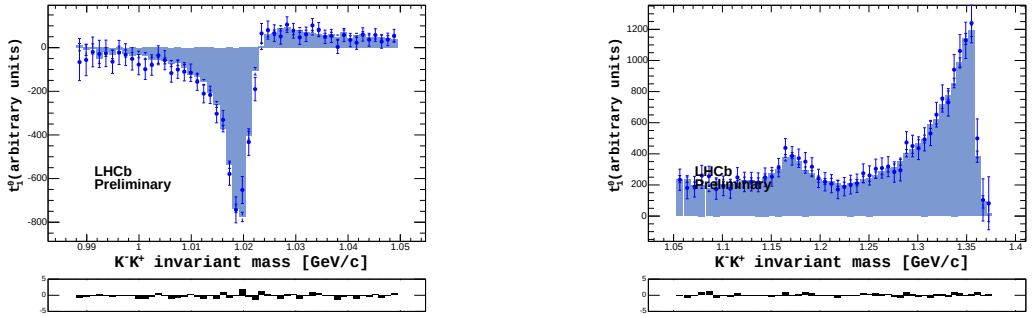

Figure 71: Moment t_1^0 of angular distribution for data (blue dots with error bars) and ToyMC of Model5 (solid histogram). From 0.9–1.05 GeV/c^2, on left panel, and from 1.05 GeV/c^2 up to 1.9 GeV/c^2 on right panel.

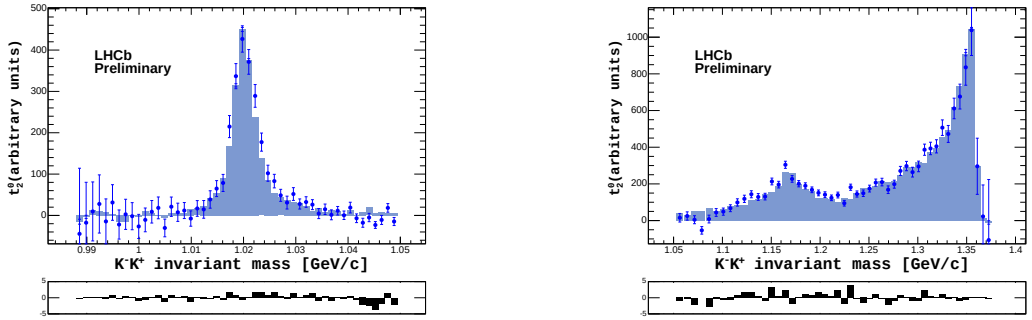

Figure 72: Moment t_2^0 of angular distribution for data (blue dots with error bars) and ToyMC of Model5 (solid histogram). From 0.9–1.05 GeV/c^2, on left panel, and from 1.05 GeV/c^2 up to 1.9 GeV/c^2 on right panel.

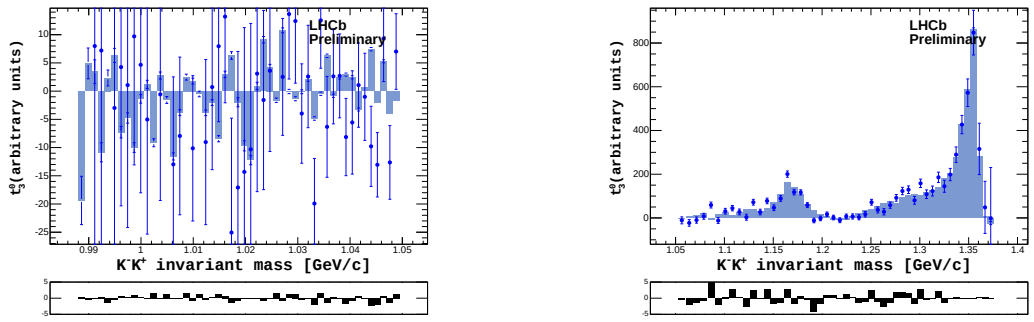

Figure 73: Moment t_3^0 of angular distribution for data (blue dots with error bars) and ToyMC of Model5 (solid histogram). From 0.9–1.05 GeV/c^2, on left panel, and from 1.05 GeV/c^2 up to 1.9 GeV/c^2 on right panel.

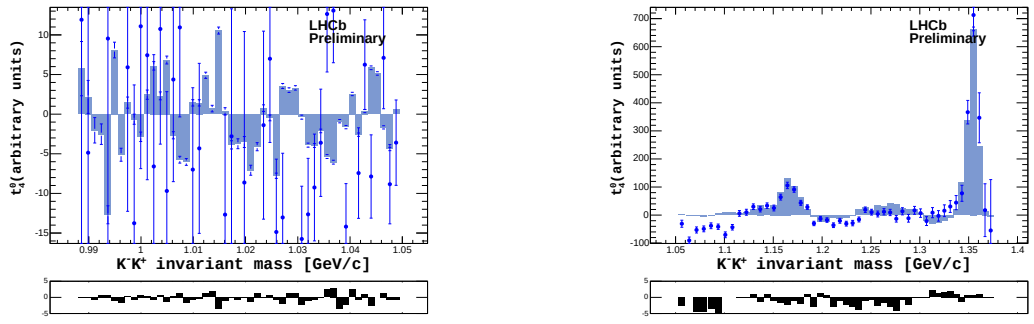

Figure 74: Moment t_4^0 of angular distribution for data (blue dots with error bars) and ToyMC of Model5 (solid histogram). From 0.9–1.05 GeV/c^2, on left panel, and from 1.05 GeV/c^2 up to 1.9 GeV/c^2 on right panel.

6.3.6 Model 6

Table 25: Magnitudes, phases and fit fractions from the Dalitz plot fit using Model 6.

Resonance	**Magnitude**	**Phase**[°]	**Fraction (%)**
$a_0(1450)$	3.51±0.07	44.5±3.3	19.4±1.2
$f_0(980)$	3.36±0.06	-71.7±1.4	28.7±1.9
$f_2(1270)$	1.143±0.32	-54.4±8.3	0.025±0.028
ϕ	1[fix]	0[fix]	6.43±0.24
sum			54.6±2.3

$\mathbf{\Delta}$ FCN $= \mathbf{-200}$
$\boldsymbol{\chi^2}$**/** ndof $= \mathbf{631.08/493 = 1.28}$

Table 26: Interference fit fractions (%) for Model 6

	$a_0(1450)$	$f_0(980)$	$f_2(1270)$	ϕ
$a_0(1450)$	19.4	43.2	0.0	1.0
$f_0(980)$	0	28.8	0.1	1.0
$f_2(1270)$	0	0	0.0	0.1
ϕ	0	0	0	6.4

The final model is Model6, which is Model 3 plus the $f_2(1270)K$ amplitude. The results of this model are shown in Table 25 and in Figs. 75 to 81.

The magnitude of the $f_2(1270)K$ amplitude is just at the 3σ level. The addition of this amplitude causes very little impact in the fit quality and leaves the phases and fit fractions nearly unchanged.

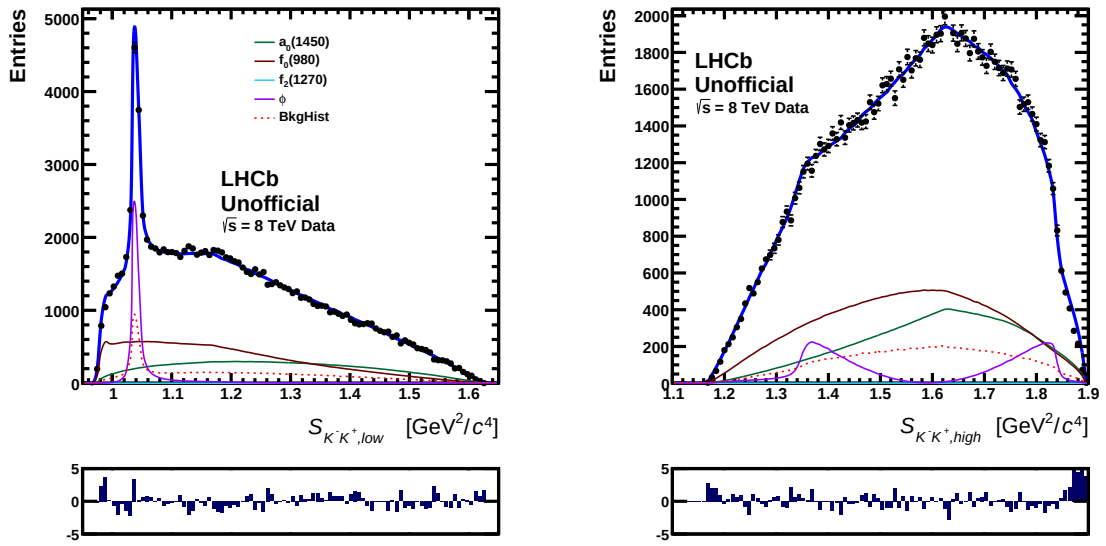

Figure 75: Projections of the data onto s_{hi} (left) and s_{lo} axes (right). The fit result (blue line) for Model 6 is superimposed. The contribution from the different amplitudes are also shown.

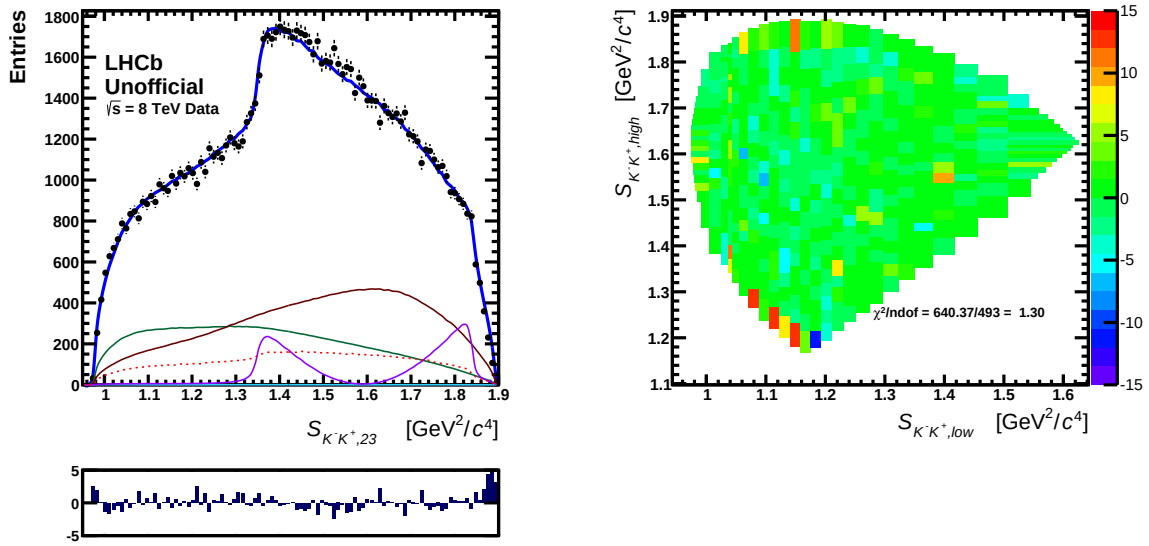

Figure 76: Left: projection of the data onto s_{23} axis, with the fit result for Model 6 superimposed. Right: the distribution of the signed χ^2 over the Dalitz plot.

6.4 Systematic uncertainties

Systematic uncertainties are split into two categories. The first category gathers the impact on the fit results from experimental aspects, such as background parameterization, efficiency correction, finite detector resolution, selection, trigger requirements, PIDCalib weighting, etc. The second category is related to the uncertainties in the resonance parameters – masses, widths and couplings. These systematic uncertainties are referred to as model systematics. The two categories are estimated and quoted separately and are evaluated for models 2 and 3.

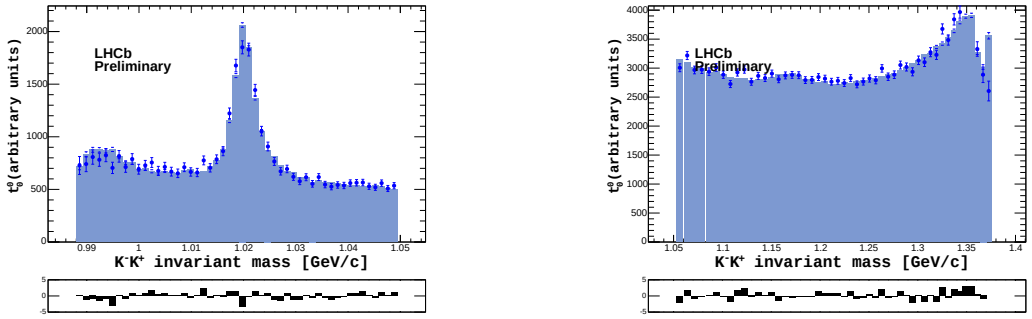

Figure 77: Moment t_0^0 of angular distribution for data (blue dots with error bars) and ToyMC of Model6 (solid histogram). From 0.9–1.05 GeV/c^2, on left panel, and from 1.05 GeV/c^2 up to 1.9 GeV/c^2 on right panel.

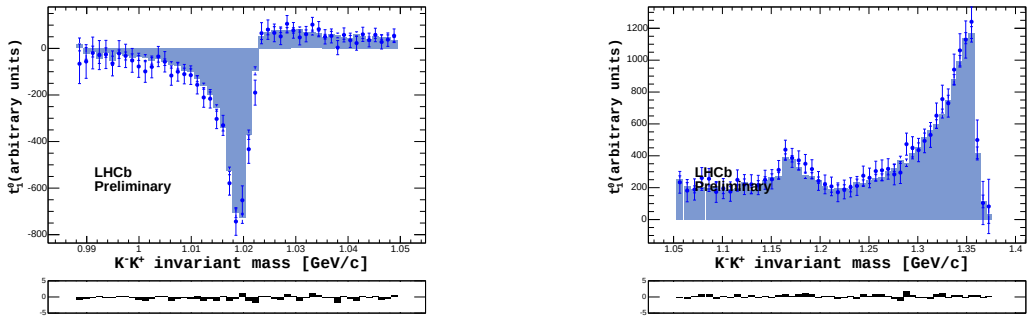

Figure 78: Moment t_1^0 of angular distribution for data (blue dots with error bars) and ToyMC of Model6 (solid histogram). From 0.9–1.05 GeV/c^2, on left panel, and from 1.05 GeV/c^2 up to 1.9 GeV/c^2 on right panel.

6.4.1 Experimental systematics

The main sources of experimental systematic uncertainties are the efficiency correction and the background parameterization.

Efficiency

The efficiency correction is performed using a 2D histogram of MC candidates, weighted according to efficiency numbers extracted from look-up tables provided by the CALO and PIDCalib groups, as explained in details in Section 5. The weighted histogram is smoothed using a 2D cubic spline. Different effects are considered.

- Different binning schemes result in slightly different smoothed histograms. We repeat the fit using smoothed histograms made with 12x12 and 11x11 binnings, alternatively to the nominal 10x10 binning. The difference in magnitude and phase of the a_0 (f_0), with respect to the nominal result of Model 3 (Table 19), are -0.041

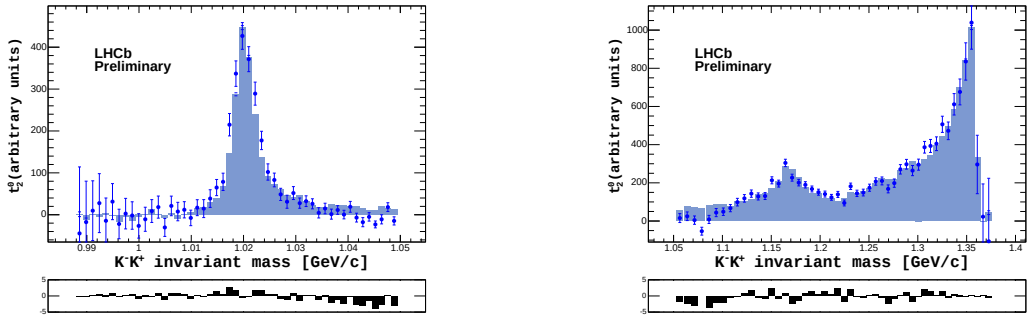

Figure 79: Moment t_2^0 of angular distribution for data (blue dots with error bars) and ToyMC of Model6 (solid histogram). From 0.9–1.05 GeV/c^2, on left panel, and from 1.05 GeV/c^2 up to 1.9 GeV/c^2 on right panel.

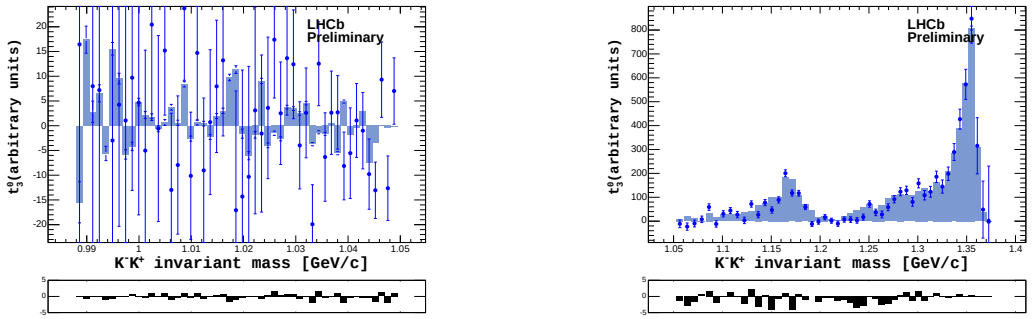

Figure 80: Moment t_3^0 of angular distribution for data (blue dots with error bars) and ToyMC of Model6 (solid histogram). From 0.9–1.05 GeV/c^2, on left panel, and from 1.05 GeV/c^2 up to 1.9 GeV/c^2 on right panel.

and 0.41° (0.14 and 0.18°), respectively, for the 12x12 binning, and 0.060 and 1.05° (0.002 and -0.096°), for the 11x11 binning. The greatest difference is taken as systematic uncertainty and presented as "acc binning" on Tables 28 and 29.

- Uncertainties in the `L0` trigger and PID efficiencies from the look-up tables are propagated to the final acceptance histogram. The fits are repeated varying the `L0` trigger and PID efficiencies according to the uncertainties provided by the CALO and PIDCalib tables. The difference is negligible, so no systematic uncertainty is assigned to this effect.

- the acceptance histogram is subject to statistical fluctuations due to the finite size of the MC sample. To estimate the impact of these fluctuations we generated 30 ToyMC histograms of acceptance from the original LHCb MC histogram. These ToyMC histograms are then smoothed and used for 30 fits to a Dalits plot generated according to the fits results of each model. The systematic uncertainties are defined as the RMS of the distributions of the differences from the fitted parameters to their

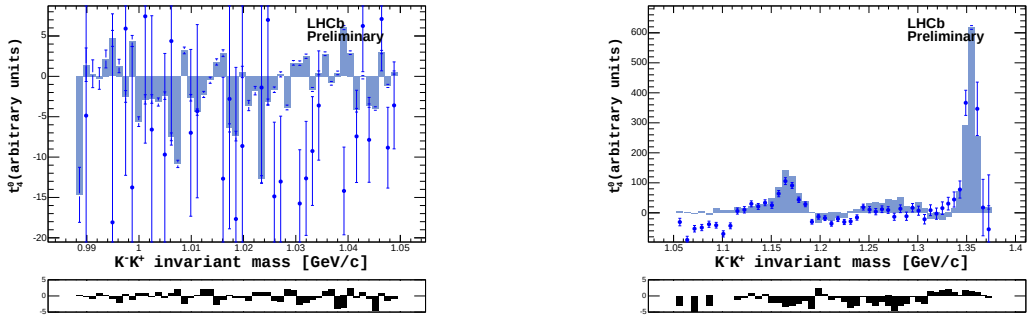

Figure 81: Moment t_4^0 of angular distribution for data (blue dots with error bars) and ToyMC of Model6 (solid histogram). From 0.9–1.05 GeV/c^2, on left panel, and from 1.05 GeV/c^2 up to 1.9 GeV/c^2 on right panel.

nominal values and are presented as "MC stats" on Tables 28 and 29. The mean values of these distributions are compatible with zero.

Background

The background corresponds to approximately 10% of the total number of candidates within the selected mass interval. There are uncertainties related to the background shape and level. Four sources of systematic effects are estimated, as described below.

The first potential source is based on the results in Table 12. We vary the relative background fraction by $\pm 1\sigma$, by fixing it in the Dalitz fit respectively to 9.48% and to 9.62%. We check the direct shift of the central values. For all parameters, these are negligible compared to the statistical uncertainty. No systematic uncertainties are assigned.

The second variation maintains the total background fraction to its central value, but changes the relative amount of peaking to combinatorial components. From Fig. 35b, the peaking background corresponds to $20.01 \pm 0.35\%$. We vary this fraction conservatively by $\pm 1\%$, so we perform two alternative fits using 19% and 21% as the fixed relative amount of the peaking background. This is shown in Tables 28- 29 under entry "peaking bkg fraction".

The third source deals with the effective width of the ϕ in the peaking background. As discussed in Section 5, the background model is built from inspection of the sidebands. The invariants are computed from the momenta given by the D mass constrained fit (DTF). The DTF variables improve the two-body mass resolution for signal events, but distorts the shape of the peaking background components obtained from the sidebands, causing two different effects: a shift on the peak position of the ϕ; a small increase in the width. Those effects are shown in Figure 82.

Extrapolating the sidebands points to the D mass, we obtain $\Gamma_\phi = 0.00512\,\mathrm{GeV}/c^2$. In order to compute the systematics due to this effect, we repeat the DP fit, generating the toyMC to describe the background using this value for Γ_ϕ instead of the value of Γ_ϕ from the PDG. The systematics errors for this test are obtained from the direct difference between the parameters and are summarized as "bkg ϕ width" on Tables 28 and 29.

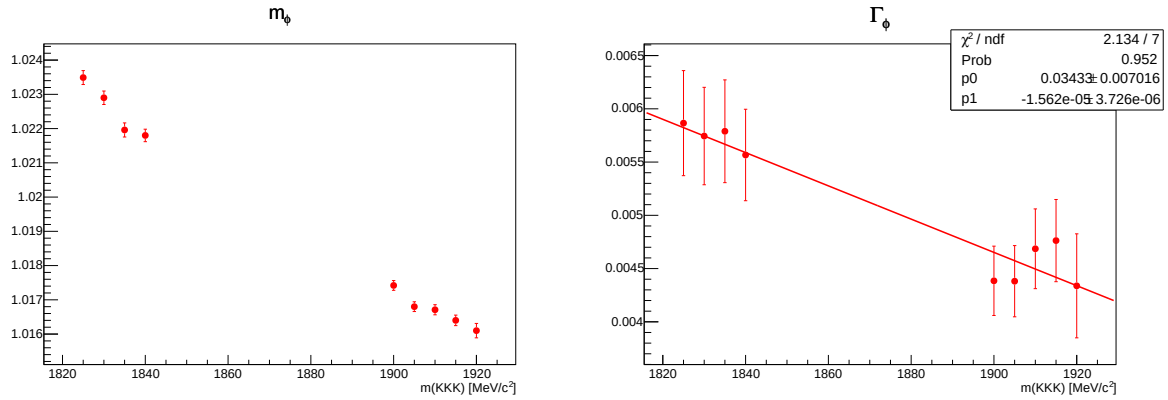

Figure 82: Peaking background parameters extracted from sideband fits shown in the $3K$ mass spectrum.

Table 27: Systematic uncertainties on the mass and width of $f_0(X)$ in Model 2. Total systematic uncertainty is calculated from the quadrature of all sources. The statistical uncertainty is also shown for comparison.

Uncertainty	$m_{f_0(X)}$	$\Gamma_{f_0(X)}$
acc binning	0.0042	0.029
MC stats	0.014	0.029
total bkg fraction	0.0	0.0
peaking bkg fraction	0.003	0.004
bkg ϕ width	0.003	0.006
total syst.	0.015	0.042
statistical	0.019	0.049

Table 28: Systematic uncertainties on magnitudes, phases and fractions of Model 2, from the various sources described in the text. The total systematic uncertainty is calculated adding all components in quadrature. The statistical uncertainty is also shown for comparison.

Uncertainty	$a_{f_0(X)}$	$\delta_{f_0(X)}$	a_{f_0}	$\delta_{(f_0)}$	FF(ϕ)%	FF($f_0(X)$)%	FF(f_0)%
eff. binning	0.28	5.3	0.10	2.9	0.07	1.9	1.3
MC stats	0.38	3.7	0.08	2.9	0.07	1.8	1.1
total bkg fraction	0.0	0.0	0.01	0.0	0.00	0.0	0.0
peaking bkg fraction	0.07	0.1	0.00	0.0	0.05	0.2	0.2
bkg ϕ width	0.08	0.3	0.02	0.5	0.06	0.0	0.1
total syst.	0.48	6.5	0.13	4.1	0.13	2.6	1.7
statistical	0.58	8.1	0.12	5.1	0.12	3.2	1.5

6.5 Summary of Isobar fits

A reasonable description of the $D^+ \to K^-K^+K^+$ Dalitz plot is obtained with simple isobar models. Two components are present in all models: the $f_0(980)$ and the $\phi(1020)$. While the presence of the $\phi(1020)$ is obvious in the Dalitz plot, the contribution from a near threshold resonance is suggested by the enhancement observed at low K^-K^+ mass in Fig. 38. Above the $\phi(1020)$ region the $D^+ \to K^-K^+K^+$ events have a nearly uniform

Table 29: Systematic uncertainties on magnitudes, phases and fractions for Model 3 from the various sources described in the text. The total systematic uncertainty is calculated adding the various components in quadrature. The statistical uncertainty is also shown for comparison.

Uncertainty	$a_{(a_0)}$	$\delta_{(a_0)}$	$a_{(f_0)}$	$\delta_{(f_0)}$	FF(ϕ)%	FF(a_0)%	FF(f_0)%
eff. binning	0.015	1.0	0.035	0.2	0.05	0.3	0.4
MC stats	0.035	1.0	0.028	0.8	0.07	0.3	0.4
total bkg fraction	0.0005	0.02	0.002	0.0	0.003	0.006	0.007
peaking bkg fraction	0.022	0.15	0.015	0.19	0.06	0.07	0.02
bkg ϕ width	0.005	0.7	0.04	0.3	0.07	0.3	0.4
total syst.	0.044	1.6	0.062	0.9	0.13	0.5	0.7
statistical	0.064	3.4	0.061	1.3	0.12	0.57	0.96

distribution in the Dalitz plot. A third component is added to the decay model to account for this nearly uniform distribution.

In the first model we tested the third component as a constant amplitude. The poor fit quality indicates that an amplitude with an energy-dependent phase is required.

In the second test a spin-0 relativistic Breit-Wigner function replaced the constant amplitude. This is the simplest way to introduce a phase variation and is motivated by the observation of the $f_0(1370)$ in other reactions ($p\bar{p}$ annihilation, $J/\psi \to \phi K^+K^+$, $\pi\pi \to KK$, etc.). The $f_0(1370)$ mass and width are poorly known, so in this fit these Breit-Wigner parameters are free. A significant improvement in the fit is observed. The fitted values of the mass and width are within the range quoted by PDG. A very large correlation with the $f_0(980)$ is observed, though.

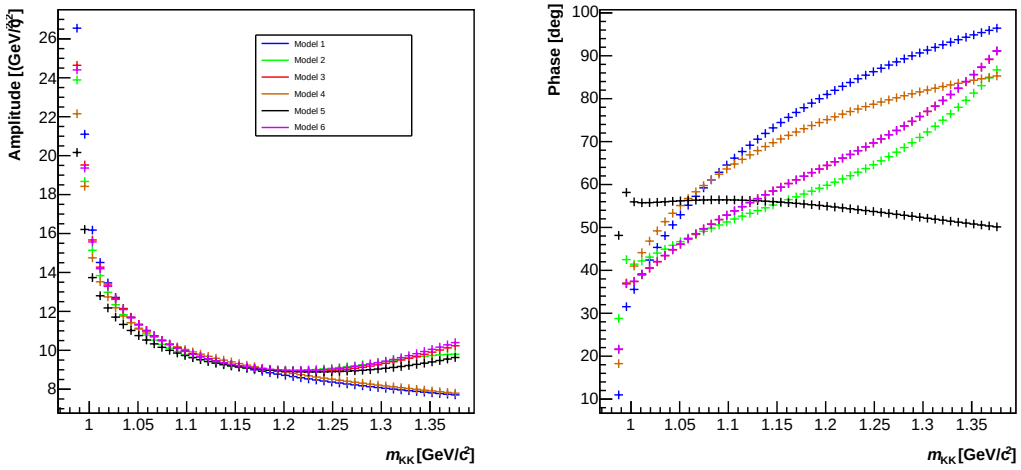

Figure 83: All Models magnitude and phase variation

A third alternative is tested, replacing the $f_0(X)$ by the known $a_0(1450)$. This resonance couples to $K\bar{K}$, but the branching fraction is not known. This model yields a fit with comparable quality. This is not surprising, since the mass and the width of the $a_0(1450)$ are not so different from those of the $f_0(X)$. It is likely that both states are present in this region, but their individual contribution cannot be disentangled with the

isobar model.

A possible contribution from the $f_2(1270)$ resonance is tested. This amplitude is suppressed by the angular momentum barrier. This suppression is indeed observed in the fit results. The contribution from $f_2(1270)$ is very small in all models.

The magnitude and phase of the $\mathcal{S}$-wave amplitude, as a function of the K^-K^+ mass, are shown in Figure 83 for all models. The $\mathcal{P}$-wave is rather stable in all models.

7 Multi-Meson Model (MMM)

Everything not forbidden is compulsory.

Murray Gell-Mann (borrowed from T. H. White's, The Once and Future King)

The central assumption of this model is that the $D^+ \to K^- K^+ K^+$ decay is dominated by the annihilation diagram, where the initial quarks, c and $\bar{s}$ in the D^+, annihilate into a W^+, which hadronizes in the vacuum. Within this topology, the steps $D^+ \to W^+$ and $W^+ \to K^- K^+ K^+$ can be factorized as $\mathcal{A} = \langle (KKK)^+ | A_\mu | 0 \rangle \langle 0 | A^\mu | D^+ \rangle$, where the former matrix element in the right-hand side can be determined by means of chiral effective theories. We are going to use Chiral Perturbation Theory with Resonances, introduced in Sec. 2 and also used in previous works of the $D \to K\pi\pi$ [53, 54].

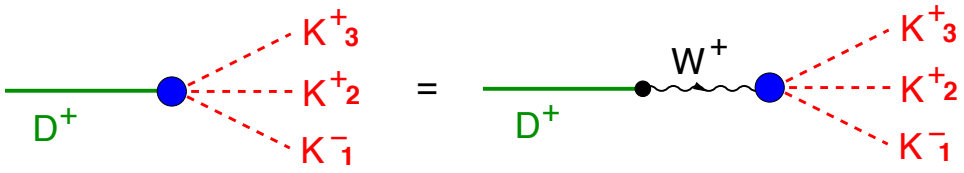

Figure 84: The decay $D^+ \to K^- K^+ K^+$ (left) is assumed to proceed through quark-annihilation topology in the steps $D^+ \to W^+$ and $W^+ \to K^- K^+ K^+$ (right).

The theoretical description of Heavy meson decays deals with two scales. The first, is the primary weak vertex, in which the heavy quark, either b or c, emits a W and becomes a light quark. Sequentially, the quarks hadronize and the final state interacts purely hadronic, the produced mesons rescatter in the final state.

The energy scale of ChPT is valid up to the SU(3) flavour symmetry scale. One way to extend the theory up to the D mass energy is to include resonances as explicit degrees of freedom (ChPTR) and unitarize the amplitudes. The different energy scales are shown in Fig. 85.

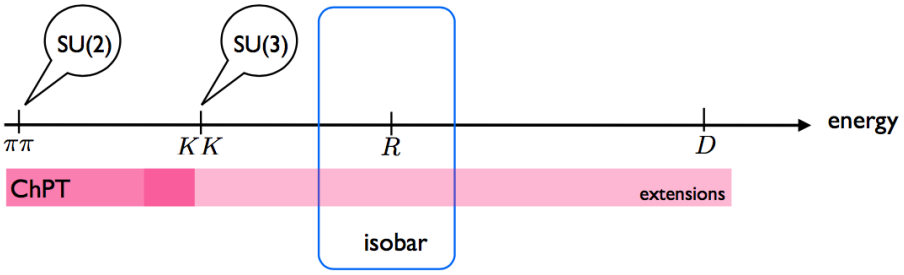

Figure 85: Different energy scales involved in a heavy meson decay. Credits to P. C. Magalhães

The MMM can also be extended to other heavy mesons, such as D_s, B and B_s. The model dynamics and its results will be described in detail in the following.

7.1 Model dynamics

Based on this factorization assumption, the decay $D^+(P) \to K^-(p_1)\,K^+(p_2)\,K^+(p_3)$ amplitude can be written as:

$$T = -\left[\frac{G_F}{\sqrt{2}}\sin^2\theta_C\right]\langle\, K^-(p_1)K^+(p_2)K^+(p_3)|A^\mu|0\,\rangle\langle\, 0|A_\mu D^+(P)\,\rangle \tag{133}$$

where G_F is the Fermi decay constant, θ_C is the Cabibbo angle and the A^μ are axial currents. If we denote the D^+ decay constant as F_D, we can write

$$\langle\, 0\,|A^\mu|\,D^+(P)\,\rangle \;=\; -i\sqrt{2}\,F_D\,P^\mu\;, \tag{134}$$

and find that

$$T = i\left[\frac{G_F}{\sqrt{2}}\sin^2\theta_C\right]\sqrt{2}F_D\left[P_\mu\langle\, K^-(p_1)K^+(p_2)K^+(p_3)|A^\mu|0\,\rangle\right]. \tag{135}$$

This matrix element will be the one described by means of ChPTR. Weak interactions vertices have a V-A form. However, the coupling of a W^+ boson with an odd number of pseudoscalars has to conserve parity and, as a consequence, only the axial current takes part in the interaction. Moreover, in the ChPT, all the couplings of the W^+ to the $K^-K^+K^+$ system always involve a direct interaction associated with a kaon pole, and only both contributions are compatible with the chiral symmetry predictions. This is represented in Fig. 86 by the diagrams (A) and (B), respectively.

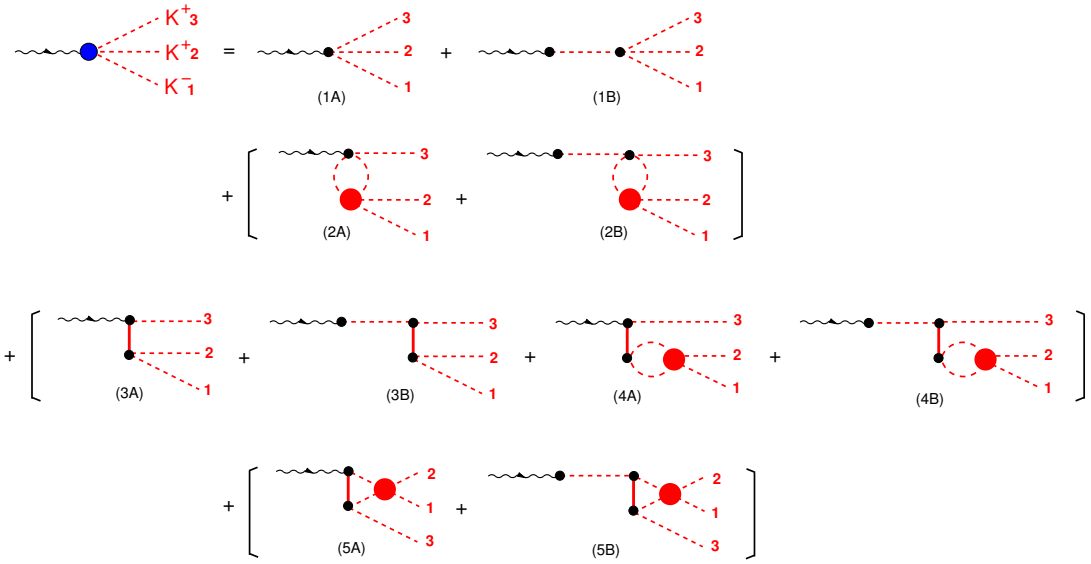

Figure 86: Dynamical structure of the blue blob in Fig. 84; the wavy line is the W^+, dashed lines are mesons, continuous lines are resonances and the red blob is the meson-meson scattering amplitude, described in Fig. 87; all diagrams within square brackets should be symmetrized, by making 2↔3.

(1A) + (1B) LO diagrams describing a non-resonant contribution, a proper three-body interactions. This is a great improvement of the Isobar model, since goes beyond the (2+1) approximation.

(2A) + (2B) After produced in the weak vertex, the two kaon system of the nonresonant contribution can rescatter. The two-meson rescattering unitarized amplitude is represented by the red blob.

(3A) + (3B) NLO contribution describing the production of a bare resonance at the weak vertex.

(4A) + (4B) After decaying, the two-meson produced from the resonance can also rescatter.

(5A) + (5B) NLO contribution describing resonance exchanges in the $t + u$ channels.

Both (4A)+(4B) and (5A)+(5B) diagrams contributes for the full-width of each resonance included in the problem. All vertices in these diagrams are derived from chiral Lagrangian and correspond to real functions.

7.2 $\bar{K}K$ scattering amplitude

The two-meson system plays a fundamental role in the $D^+ \to K^-K^+K^+$ final state interactions. Before proceeding to the production amplitudes, we are going to define the kernels, denoted by $\mathcal{K}_{ab\to cd}$.

At tree level, the scattering amplitude, represented by the empty red blob in figure 87, has three contributions. The first diagram represents a resonance exchange in the s-channel, this is a NLO contribution and proportional to $1/F^4$. The second is a four-meson contact term and is a LO contribution, proportional to $1/F^2$. The third diagram is a resonance exchange in the t and u channel, this is also a NLO contribution, and will become a polynomial term once projected in the s-channel.

In order to obtain the full unitarized scattering amplitude, represented by a full red blob, a resummation of all diagrams should be done. Representing the two-meson propagator function by $\Omega(s)$, the bottom equation in Fig. 87 can be written as:

$$\begin{aligned} T &= \mathcal{K} + \mathcal{K}\,(-\Omega)\,\mathcal{K} + \mathcal{K}\,(-\Omega)\,\mathcal{K}\,(-\Omega)\,\mathcal{K} + ... \\ &= \mathcal{K}\,\left[1 + (-\Omega)\,\mathcal{K} + (-\Omega)\,\mathcal{K}\,(-\Omega)\,\mathcal{K} + ..\right] \\ &= \frac{\mathcal{K}}{1 + \Omega\,\mathcal{K}} \end{aligned} \tag{136}$$

The two-meson propagator function have a unwanted ultraviolet divergence. This can be solved regulating this function, *i.e* subtracting the divergence

$$\bar{\Omega}(s) = \Omega(s) - \Omega(0) \tag{137}$$

This $\Omega(0)$ is real and the function $\bar{\Omega} = \bar{\Omega}_R + i\bar{\Omega}_I$ will have an arbitrary constant in the real part. Here, we are going to use the K-matrix approximation, where the real part of the loop is ignored. Within this approximation, there is no need for renormalization and the particles running inside the loops are considered on-shell. Therefore, the unitarized amplitude can be written as:

$$T = \frac{\mathcal{K}}{1 + i\bar{\Omega}_I\,\mathcal{K}} \tag{138}$$

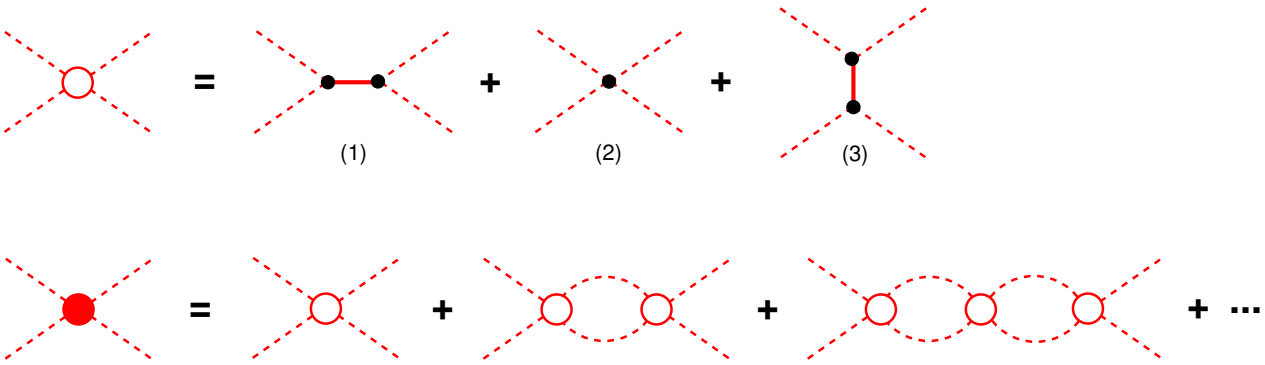

Figure 87: Top: tree-level structure for the two-body interaction kernel $\mathcal{K}_{ab\to cd}$ matrix element: the last two processes represent respectively LO and NLO polynomial terms, whereas the first involves an explicit s-channel resonance and is also NLO. Bottom: unitarized scattering amplitude.

As K^-K^+ interactions are attractive, we consider all the relevant channels in this subsystem with spin $J = 0, 1$ and isospin $I = 0, 1$ and therefore the resonances included in the calculations are the ρ, ϕ, a_0 and two scalar states, allowed by the ChPTR. These scalars are denoted hereafter as S_1 and S_o, which correspond to a singlet and to a member of an octet of $SU(3)$, with the same quantum numbers. The physical scalar state $f_0(980)$ could then be a linear combination of S_1 and S_o.

Kernel

The kernel matrix elements for the four channels considered can be written as $\langle ab|K^{J,I}|cd\rangle$, where the initial and final states are defined by the spin and isospin nature of the fields in flavour SU(3) symmetry, described in App. E. One needs the following set of matrix elements:

$$\begin{aligned}
\langle\, V_3^{ab} \,|\, \mathcal{K}^{(1,1)} \,|\, V_3^{cd} \,\rangle &\to \ \rho \text{ channel,} \\
\langle\, V_8^{ab} \,|\, \mathcal{K}^{(1,0)} \,|\, V_8^{cd} \,\rangle &\to \ \phi \text{ channel,} \\
\langle\, U_3^{ab} \,|\, \mathcal{K}^{(0,1)} \,|\, U_3^{cd} \,\rangle &\to \ a_0 \text{ channel,} \\
\langle\, S^{ab} \,|\, \mathcal{K}^{(0,0)} \,|\, S^{cd} \,\rangle &\to \ f_0 \text{ channel.}
\end{aligned}$$

As far as dynamics is concerned, each kernel receives contributions from resonances R, leading order contact chiral polynomials $A_{(2)}$ and next-to-leading order resonance polynomials $A_{(4)}$. The last term is written as $A_{(4)} = A_{(4,V)} + A_{(4,S1)} + A_{(4,So)}$, where V, $S1$, and So stand for $SU(3)$ vector, scalar singlet and scalar octet intermediate states. Since there are too many kernels involved, we are going to show some representative contributions, which are the direct channel $\bar{K}K \to \bar{K}K$, for the ϕ and f_0 channel and comment t main characteristics. All the contributions can be found in Appendix G.

Kernel J=1, I=0. ϕ channel

$$[J, I = 1, 0] \to \langle\, V_8^{ab} \,|\, \mathcal{K}^{(1,0)} \,|\, V_8^{cd} \,\rangle = (t-u)\; \mathcal{K}^{(1,0)}_{(ab|cd)} \tag{139}$$

$$\mathcal{K}^{(1,0)}_{(KK|KK)} = -3 \left[\frac{G_V^2\, \sin^2\theta}{F^4}\right] \frac{s}{D_\phi^{\pi\rho}} + P^{(1,0)}_{(KK|KK)} \tag{140}$$

$$P^{(1,0)}_{(KK|KK)} = \left[\frac{3}{2\,F^2}\right] + \left[\frac{3\,G_V^2\; s}{2\,F^4 M_V^2}\right] + \left[\frac{4}{F^4\, M_{S_1}^2}\right] \left[-\tilde{c}_d^{\,2}\, s + 4\,\tilde{c}_d\,\tilde{c}_m\, M_K^2\right]$$

$$+ \left[\frac{5}{3F^4\, M_{So}^2}\right] \left[-c_d^2\, s + 4\, c_d\, c_m\, M_K^2\right] \tag{141}$$

The first thing to notice in this amplitude is the angular dependence signature $(t-u)$. This appear as a consequence of angular momentum $J = 1$ of this channel. This dependece is, up to a constant factor, the same Isobar angular distributions and will lead to a node in the Dalitz Plot.

The decay of a $\phi \to \pi\rho$ accounts for 15% of its branching fractions. The inclusion of this decay channel is explained in detail in Appendix D of the previous work of the 3M [55] and is represented here by the propagator $D_\phi^{\pi\rho}$.

In Eq. 222, we can immediately notice that LO are proportional to $1/F^2$ and NLO to $1/F^4$. The parameters M_S and M_V represents the approximate masses, in the chiral limit, of the scalar and vectorial octet and will be fixed in 1 GeV.

The singlet contributions $(4, S1)$ will always comes with the parameters $\tilde{c}_d$ and $\tilde{c}_m$, whereas the octet $(4, S_o)$ with c_d and c_m. These will be free parameters in the fit.

Kernel J=0, I=0. f_0 channel

$$[J, I = 0, 0] \to \langle\, S^{ab} \,|\, \mathcal{K}^{(0,0)} \,|\, S^{cd} \,\rangle = \mathcal{K}^{(0,0)}_{(ab|cd)} \tag{142}$$

$$\mathcal{K}^{(0,0)}_{(KK|KK)} = -\frac{1}{s - m_{S1}^2} \left[\frac{16}{F^4}\right] \left[\tilde{c}_d\, s - (\tilde{c}_d - \tilde{c}_m)\, 2M_K^2\right]^2$$

$$-\frac{1}{s - m_{So}^2} \left[\frac{2}{3\,F^4}\right] \left[c_d\, s - (c_d - c_m)\, 2M_K^2\right]^2 + P^{(0,0)}_{(KK|KK)} \tag{143}$$

$$P^{(0,0)}_{(KK|KK)} = \left[\frac{3s}{2F^2}\right] - \left[\frac{G_V^2}{F^4\, M_V^2}\right] \left[2\, s^2 - 10\, s\, M_K^2 + 8\, M_K^4\right]$$

$$+ \left[\frac{4}{F^4\, M_{S_1}^2}\right] \left[\frac{2}{3}\, \tilde{c}_d^{\,2} \left[s - 4\, M_K^2\right]^2 + 4\, \tilde{c}_d\, (\tilde{c}_d - \tilde{c}_m)\, s\, M_K^2 - 8\, (\tilde{c}_d^{\,2} - \tilde{c}_m^{\,2})\, M_K^4\right]$$

$$+ \left[\frac{5}{3\,F^4\, M_{So}^2}\right] \left[\frac{2}{3}\, c_d^2 \left[s - 4\, M_K^2\right]^2 + 4\, c_d\, (c_d - c_m)\, s\, M_K^2 - 8(c_d^2 - c_m^2)\, M_K^4\right] \tag{144}$$

$$\tag{145}$$

The f_0 channel is the more involved of all contributions. Although the presence of two scalars makes the calculation a cumbersome, the same characteristics presented in the ϕ channel applies here, but in presence of two poles.

A substantial difference from the Isobar model appears as a consequence of two poles. The Isobar is referred as the sum of Breit-Wigner, whose lineshapes has mass and width. A width of a resonance is consequence of the resummation of all interactions that this resonance can have, which includes loops. In the Isobar scope, this is done separately for each resonance. In this way, an amplitude has a single pole with a definite width.

However, in the MMM, as a consequence of considering the f_0 as an octet and a singlet, we have two poles. In the processes of resummation, the considered poles mix between themselves. The resulting poles will contribute to more than one resonant state. Though, it is not clear the direct connection between these poles and the f_0's.

7.3 Production Amplitude

The full production amplitude for the process $D^+ \to K^- K^+ K^+$ can also be decomposed in the four channel considering the allowed $J = 0, 1;\ I = 0, 1$ combinations and the nonresonant contribution

$$\begin{aligned}
\langle K_1^- K_2^+ K_3^+ | \, T \, | \, D \rangle &= \langle K_1^- K_2^+ K_3^+ | \, T_c \, | \, D \rangle \\
&+ \big[\langle K_1^- K_2^+ (K_3^+) | \, T^{(1,1)} \, | \, D \rangle + \langle K_1^- K_2^+ (K_3^+) | \, T^{(1,0)} \, | \, D \rangle \\
&+ \langle K_1^- K_2^+ (K_3^+) | \, T^{(0,1)} \, | \, D \rangle + \langle K_1^- K_2^+ (K_3^+) | \, T^{(0,0)} \, | \, D \rangle \\
&+ (2 \leftrightarrow 3) \big] \qquad (146)
\end{aligned}$$

The first term represents the nonresonant contribution, which will be investigated in detail in the following. The rest are the decomposition in the spin-isospin channels assuming that the K_3^+ is the spectator. The term $(2 \leftrightarrow 3)$ is the symmetrization of the amplitude. One should notice that the nonresonant contribution is naturally symmetrized, once it is a three-body diagram. The complete expression and derivation for the full production amplitude $\langle K_1^- K_2^+ K_3^+ | T^{(I,J)} | D \rangle$ is shown in Appendix H. The full production amplitude is obtained performing a coupled channel unitarization and its main ingredients are the kernels presented above.

As in the kernel, we are going to explain the main characteristic of the tree-level production amplitude for the ϕ and f_0 and the details about the nonresonant. The complete expressions can be found in Appendix F

7.3.1 $D^+ \to K^- K^+ K^+$ nonresonant amplitude

One of the biggest improvement of the MMM, compared to the Isobar model, is the nonresonant amplitude. The vast majority of the charmed meson decay models of the nonresonant amplitude is just a constant across the phase space. And this was no different in the previous Isobar results, where in Model 1, we used this constant parametrization. Compared to Models 2 and 3, the lack os phase variation on the high mass KK lead to a poor description of the data. In the MMM a proper three-body amplitude appears from the LO chiral lagrangian and it is identified as the nonresonant amplitude of this model.

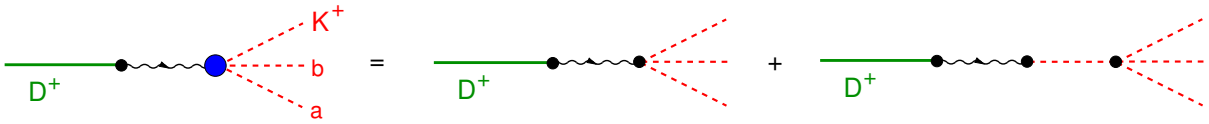

Figure 88: Tree-level nonresonant contact amplitudes. The coupling of the W boson in both right-hand side diagrams does not depends on a specific pair os K's. As consequence, these amplitudes are naturally symmetrized.

Individual contact contributions read

$$A^{\mu}_{(1)} \;=\; i\left[\frac{2\sqrt{2}}{3F_K}\right](2\,p_1 - p_2 - p_3)^{\mu}\;, \tag{147}$$

$$A^{\mu}_{(2)} \;=\; -i\left[\frac{2\sqrt{2}}{3F_K}\right]\frac{P^{\mu}}{P^2 - M_K^2}\left[p_1\cdot(p_2+p_3) - 2\,p_2\cdot p_3 + M_K^2\right]\;, \tag{148}$$

whereas their sum is

$$A^{\mu} \;=\; -i\left[\frac{2\sqrt{2}}{F_K}\right]\frac{1}{P^2 - M_K^2}\left\{\left[P^2\,(p_2+p_3)^{\mu} - P\cdot(p_2+p_3)P^{\mu}\right] + M_K^2\,p_1^{\mu}\right\}\;. \tag{149}$$

The corresponding decay amplitude reads

$$T_c \;=\; \left\{\left[\frac{G_F}{\sqrt{2}}\,\sin^2\theta_C\right]\sqrt{2}\,F_D\,\frac{M_K^2}{M_D^2 - M_K^2}\right\}\left\{\frac{\sqrt{2}}{F_K}\,\left[M_D^2 + M_K^2 - m_{23}^2\right]\right\}\;, \tag{150}$$

and an alternative form is

$$T_c \;=\; \left\{\left[\frac{G_F}{\sqrt{2}}\,\sin^2\theta_C\right]\sqrt{2}\,F_D\,\frac{M_K^2}{M_D^2 - M_K^2}\right\}\left\{\frac{\sqrt{2}}{F_K}\,\left[(m_{12}^2 - M_K^2) + (m_{13}^2 - M_K^2)\right]\right\} \tag{151}$$

Defining

$$C \;=\; \left\{\left[\frac{G_F}{\sqrt{2}}\,\sin^2\theta_C\right]\frac{2F_D}{F_K}\,\frac{M_K^2}{M_D^2 - M_K^2}\right\}\;, \tag{152}$$

one has

$$T_c \;=\; C\,\left\{\left[M_D^2 + M_K^2 - m_{23}^2\right]\right\}\;, \tag{153}$$

$$\;=\; C\,\left\{\left[(m_{12}^2 - M_K^2) + (m_{13}^2 - M_K^2)\right]\right\}\;. \tag{154}$$

Inspecting the equation above, since we are just dealing with tree-level amplitude for the nonresonant, no two-meson propagator appears. Consequently, the function is purely real and decrease as s_{23} increase. This changes the real part of the total amplitude in the high-mass $\bar{K}K$, without a phase variation. However, when summed with other amplitudes, changes the real/imaginary contribution of the total amplitude and could lead to a phase variation. The monte carlo simulation of the Isobar nonresonant and the MMM nonresonant are shown in the figure below.

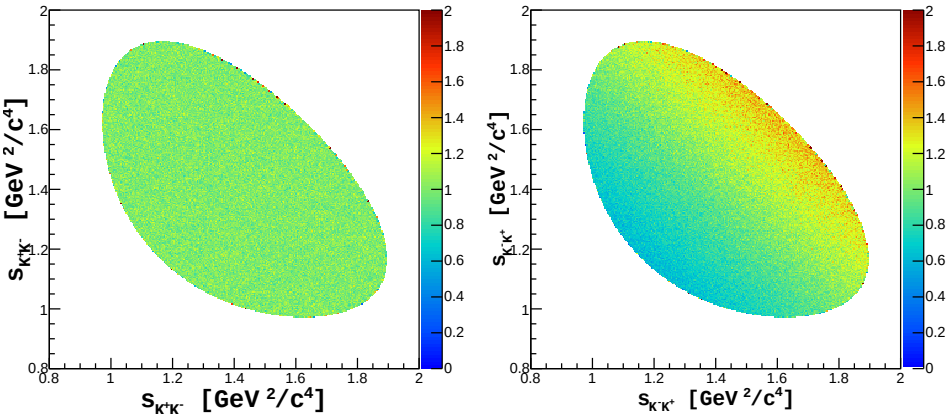

Figure 89: Dalitz plot with the MC simulation of: an uniform nonresonant amplitude (left); the nonresonant component of the Triple-M (right).

7.3.2 Tree level production subamplitudes.

In the evaluation of intermediate state contributions shown in diagrams (3A) and (3B) of Fig. 86, we need tree level contribution for the process $D \to a\, b\, K^+$, denoted by $T^{(J,I)}_{(0)}$, for spin J and isospin I. Using the constant C defined in Eq. 152, we have for the ϕ and f_0 channels:

$$[J, I = 1, 0] \to \langle\, V_8^{KK}\, K^+ |\, T^{(1,0)}_{(0)}\, |\, D\,\rangle = i\, Q\cdot(p_a - p_b)\; \Gamma^{(1,0)}_{(0)\,KK}\,, \tag{155}$$

$$\Gamma^{(1,0)}_{(0)\,KK} = C\left\{\left[\frac{3\,G_V^2}{F^2}\,\sin^2\theta\right]\,\frac{m_{12}^2}{D_\phi^{\pi\rho}(m_{12}^2)} - \frac{3}{2}\right\}, \tag{156}$$

$$\tag{157}$$

where Q is the D^+ momentum. This tree-level amplitude has two contributions, one from the direct production of the resonance and a constant term, which comes from the contact interaction. The bare pole of the resonance is inside the $D_\phi^{\pi\rho}$ function. The resummation of all diagrams with K-matrix approximation will include an imaginary part

to this amplitude, resulting in a width for the ϕ resonance.

$$[J, I = 0, 0] \to \langle\, S^{ab}\, K^{+} |\, T^{(0,0)}_{(0)} \,|\, D \,\rangle = \Gamma^{(0,0)}_{(0)\,a\,b}\,, \tag{158}$$

$$\Gamma^{(0,0)}_{(0)\,KK} = C \left\{ \left[\frac{16}{F^2}\right] \frac{[-\tilde{c}_d\, Q{\cdot}p_3 + \tilde{c}_m\, M_D^2]}{m_{12}^2 - m_{S1}^2} \left[\tilde{c}_d \left(m_{12}^2 - 2M_K^2\right) + 2\,\tilde{c}_m\, M_K^2\right] \right.$$

$$+ \left[\frac{1}{3\,F^2}\right] \frac{[-c_d\, Q{\cdot}p_3 + c_m\, M_D^2]}{m_{12}^2 - m_{So}^2} \left[c_d \left(m_{12}^2 - 2M_K^2\right) + 2\,c_m\, M_K^2\right]$$

$$\left. - \frac{3}{2} \left[M_D^2 - Q{\cdot}p_3\right] \right\}, \tag{159}$$

$$\tag{160}$$

Way more evolved, the bare amplitude for the f_0 already includes two poles. The singlet pole, related to the $\tilde{c}_d$ and $\tilde{c}_m$ parameters and the octet pole, with c_d and c_m. The last term in Eq. 210 is also consequence of a contact interaction that appears in this channel.

The unitarization process will resum all the possible diagrams, including all the possible loops. We are going to perform a coupled channel resummation. Besides the $\bar{K}K$ itself, the coupled channel will include the $\pi\pi$ channel for ρ, the $\pi\eta$ for the a_0 and, the more complicated one, $\pi\pi$, $\eta\eta$ for the f_0. The whole process is written is details in Appendix H.

In order to understand the problem in simple terms, we decided to take a minimal model, performing some approximations and compare it to the data. Once this minimal model is understood, corrections will be added to it.

7.4 Minimal Model

The main assumption of the minimal model accounts for the coupled channel contributions. These contributions lead to logarithmic functions, which are subleading functions.

Firstly, if we compare the diagrams (1A) and (2A) in Fig. 86. The former represents the non-resonant contribution and the latter a correction to this diagram with the inclusion of the unitarized $\bar{K}K$ scattering amplitude. This amplitude contains the rescattering for the $\bar{K}K$ system itself but also for other coupled channels. The function that accounts for the coupled channels has an opening threshold, where it is zero below this threshold. But even after the opening, the size of the coupled channel is subleading compared to the scattering $\bar{K}K \to \bar{K}K$ itself. Therefore, in diagrams (1A) and (2A), the rescattering for coupled channels are ignored. The same reasoning can be made for (1B) and (2B).

Secondly, for the diagrams (3A) and (3B) compared to (4,5 A) and (4,5 B), respectively. The resummation includes contributions on the numerator and on the denominator of the full production amplitude. The reasoning for the numerator is the same as before, coupled channels are ignored. However, for the denominator we kept only the imaginary part of the coupled channel contributions, this will contribute for the resonance width. For example, in the ρ production amplitude in Eq. 320, the term proportional to (1) $\Gamma^{(0,1)}_{(0)\,KK}$ is the only one kept. However, in Eq. 320, the terms $(1 - M_{11} - M_{22})$ are the only considered.

With these approximations, the amplitude for each channel can be written as follows

minimal model $J = 1$, $I = 1 \leftrightarrow \rho$ channel

The production amplitude reads

$$\begin{aligned}
\langle\, K_1^- K_2^+(K_3^+)|\, T^{(1,1)}\,|\, D\,\rangle &= -\,C\,\frac{1}{4}\left\{\frac{1}{D_\rho(m_{12}^2)}\,\left[\frac{G_V^2}{F^2}\,m_{12}^2 - \frac{1}{2}\,(m_{12}^2 - m_\rho^2)\right] + \frac{1}{2}\right\} \\
&\times\ (m_{13}^2 - m_{23}^2) \qquad (161)\\
D_\rho(m_{12}^2) &= (m_{12}^2 - m_\rho^2) + i\,m_\rho \Gamma_\rho(m_{12}^2) \qquad (162)\\
m_\rho\Gamma_\rho(m_{12}^2) &= \frac{1}{12\pi\,m_{12}}\left\{\frac{G_V^2}{F^4}\,m_{12}^2\,\left[2\,Q_{\pi\pi}^3 + Q_{KK}^3\right]\right. \\
&-\ \left.(m_{12}^2 - m_\rho^2)\,\left[P_{(\pi\pi|\pi\pi)}^{(1,1)}\,Q_{\pi\pi}^3 + P_{(KK|KK)}^{(1,1)}\,Q_{KK}^3\right]\right\} \qquad (163)
\end{aligned}$$

Where $Q_{ab} = \frac{1}{2}\sqrt{s - 2(M_a^2 + M_b^2) + (M_a^2 - M_b^2)/s}$.
In the minimal model, the ρ width contains the channels $\pi\pi \to \pi\pi$ and $\bar{K}K \to \bar{K}K$. In this expression one immediately see that the coupled channel $\pi\pi$ are only accounted in the width of the resonance. This opening of the channel will be represented in the plots as a 'cusp' in the lineshape. One should notice two terms in the curly brackets Eq. 170, the first is proportional to $1/D_\rho$, which is the propagator of the resonance an has a pole at $m_\rho^2 - im_\rho\Gamma_\rho$. The second term is just a $1/2$ factor and comes from a contact interaction. The ρ-channel amplitude will be highly suppressed. The terms $P^{(1,1)}$ are polynomial functions and its expressions are given in App. G.

minimal model $J = 1$, $I = 0 \leftrightarrow \phi$

The production amplitude reads

$$\begin{aligned}
\langle\, K_1^- K_2^+(K_3^+)|\, T^{(1,0)}\,|\, D\,\rangle &= -\,C\,\left\{\frac{1}{D_\phi(m_{12}^2)}\,\left[\frac{3\,G_V^2\,\sin^2\theta}{4\,F^2}\,m_{12}^2 - \frac{3}{8}\,D_\phi^{\pi\rho}(m_{12}^2)\right] + \frac{3}{8}\right\} \\
&\times\ (m_{13}^2 - m_{23}^2) \qquad (164)\\
D_\phi(m_{12}^2) &= (m_{12}^2 - m_\phi^2) + i\,m_\phi\,\Gamma_\phi(m_{12}^2) \qquad (165)\\
m_\phi\,\Gamma_\phi(m_{12}^2) &= \Gamma_{\pi\rho}\,\frac{m_{12}^3}{m_\phi^2}\,\frac{Q_{\pi\rho}^3}{\tilde{Q}_{\pi\rho}^3} \\
&+\ \frac{1}{12\pi\,m_{12}}\left[\frac{3\,G_V^2\,\sin^2\theta}{F^4}\,m_{12}^2 - (m_{12}^2 - m_\rho^2)\,P_{(KK|KK)}^{(1,0)}\right]\,Q_{KK}^3 \qquad (166)
\end{aligned}$$

The same ideas applies to the ϕ-channel. But, in this case, only the $\bar{K}K$ channel can couple to a ϕ. In contrast with the ρ-channel, the ϕ will be a significant contribution. Due its thin width, given in Eq. 166, the rest of the Dalitz plot is not populated by the ϕ.

minimal model $J = 0,\ I = 1 \leftrightarrow a_0$

The production amplitude reads

$$\begin{aligned}
&\langle\, K_1^- K_2^+(K_3^+)|\, T^{(0,1)}\,|\, D\,\rangle \\
&= C\,\left\{\frac{1}{D_{a_0}(m_{12}^2)}\,\left\{\left[\frac{1}{2\,F^2}\right]\,\left[c_d\,Q{\cdot}p_+ - c_m\,Q^2\right]\,\left[c_d\,(m_{12}^2{-}2\,M_K^2) + 2\,c_m\,M_K^2\right]\right.\right. \\
&\left.\left. + (m_{12}^2 - m_{a_0}^2)\,\left[\frac{1}{4}\,(Q^2 - Q{\cdot}p_+){-}\right]\right\} - \frac{1}{4}\,(Q^2 - Q{\cdot}p_+)\right\}
\end{aligned} \tag{167}$$

$$D_{a_0}(m_{12}^2) = (m_{12}^2 - m_{a_0}^2) + i\,m_{a_0}\,\Gamma_{a_0}(m_{12}^2) \tag{168}$$

$$\begin{aligned}
&m_{a_0}\Gamma_{a_0}(m_{12}^2) = \frac{1}{8\pi\,m_{12}}\,\left\{\left[\frac{4}{3\,F^4}\right]\,\left[c_d\,(m_{12}^2{-}M_\pi^2{-}M_8^2) + 2\,c_m\,M_\pi^2\right]^2\,Q_{\pi 8}\right. \\
&+ \left[\frac{2}{F^4}\right]\,\left[c_d\,(m_{12}^2{-}2\,M_K^2) + 2\,c_m\,M_K^2\right]^2\,Q_{KK} \\
&\left. + (m_{12}^2{-}m_{a_0}^2)\,\left[P_{(\pi 8|\pi 8)}^{(0,1)}\,Q_{\pi 8} + P_{(KK|KK)}^{(0,1)}\,Q_{KK}\right]\right\}.
\end{aligned} \tag{169}$$

Where Q^2 is the momentum of the D^+ and $Q{\cdot}p_+$ is the scalar product of the D^+ with the spectator kaon. Rather involved, the width of this amplitude includes more terms than the vectorial resonances. Member of the octet, the parameters related to the a_0 amplitudes are only the c_d and c_m.

minimal model $J = 0,\ I = 0 \leftrightarrow f_0$

The production amplitude reads

$$\begin{aligned}
&\langle\, K_1^- K_2^+(K_3^+)|\, T^{(0,0)}\,|\, D\,\rangle = C\,\left\{\frac{1}{D_{f_0}^2(m_{12}^2)}\right. \\
&\times\left[(m_{12}^2 - m_{So}^2)\,\left[\frac{8}{F^2}\right]\,\left[\tilde{c}_d\,Q{\cdot}p_+ - \tilde{c}_m\,Q^2\right]\,\left[\tilde{c}_d\,\left(m_{12}^2 - 2M_K^2\right) + 2\,\tilde{c}_m\,M_K^2\right]\right. \\
&+ (m_{12}^2 - m_{S1}^2)\,\left[\frac{1}{6\,F^2}\right]\,\left[c_d\,Q{\cdot}p_+ - c_m\,Q^2\right]\,\left[c_d\,\left(m_{12}^2 - 2M_K^2\right) + 2\,c_m\,M_K^2\right] \\
&\left.\left. + (m_{12}^2 - m_{S1}^2)\,(m_{12}^2 - m_{So}^2)\,\frac{3}{4}\,\left[Q^2 - Q{\cdot}p_+\right]\right] - \frac{3}{4}\,\left[Q^2 - Q{\cdot}p_+\right]\right\}
\end{aligned} \tag{170}$$

$$D^2_{f_0}(m^2_{12}) = (m^2_{12}-m^2_{S1})\,(m^2_{12}-m^2_{So}) + i\,D_{IM}(m^2_{12}) \tag{171}$$

$$\begin{aligned}
D_{IM}(m^2_{12}) &= \frac{1}{8\pi\, m_{12}}\left\{(m^2_{12}-m^2_{So})\left[\frac{1}{F^4}\right]\left\{6\left[\tilde{c}_d\, s-(\tilde{c}_d-\tilde{c}_m)\,2M^2_\pi\right]^2 Q_{\pi\pi}\right.\right.\\
&+ 8\left[\tilde{c}_d\, s-(\tilde{c}_d-\tilde{c}_m)\,2M^2_K\right]^2 Q_{KK} + 2\left[\tilde{c}_d\, s-(\tilde{c}_d-\tilde{c}_m)\,2M^2_8\right]^2 Q_{88}\Big\}\\
&+ (m^2_{12}-m^2_{S1})\left[\frac{1}{F^4}\right]\Big\{\left[c_d\, s-(c_d-c_m)\,2M^2_\pi\right]^2 Q_{\pi\pi}\\
&+ \frac{1}{3}\left[c_d\, s-(c_d-c_m)\,2M^2_K\right]^2 Q_{KK}\\
&+ \left.\frac{1}{3}\left[c_d\,(s-2M^2_8)+c_m\,(16M^2_K-10M^2_\pi)/3\right]^2 Q_{88}\right\}
\end{aligned} \tag{172}$$

$$- (m^2_{12}-m^2_{S1})\,(m^2_{12}-m^2_{So})\frac{1}{2}\left[P^{(0,0)}_{(\pi\pi|\pi\pi)}\,Q_{\pi\pi}+P^{(0,0)}_{(KK|KK)}\,Q_{KK}+P^{(0,0)}_{(88|88)}\,Q_{88}\right]\Big\}\ .$$

Way more complicated than the a_0, some points has to be stressed in this amplitude. First, the presence of a double-pole in $1/D^2_{f_0}$. This is a consequence of allowing the f_0 to be either a singlet or octet. Secondly, as in the a_0, the complexity in the width comes from the open channels. The scalars resonances can couple to more channels than the vectorial resonances, the f_0 couples to $\pi\pi$, $\bar{K}K$ and $\eta\eta$ (represented by 88).

Again, it is clear that coupled channel effects are only in the width of the resonance, *i.e.* in the imaginary part of the denominator. No effects of coupled channel are found in the numerator and in the real part of the denominator, which is the double-pole.

7.5 Preliminary fit results

Using the Minimal model, we are going to fit the data wtih the same procedure defined in Sec. 4. This result is very preliminary and there is still room for improvements.

The free parameters of this fit are the coupling constants c_d, c_m, $\tilde{c}_d$, $\tilde{c}_m$ and masses m_{S0}, m_{S1} and m_{a_0}. This problem allows multiple solutions, *i.e.* local minima. In order to avoid this problem, we attacked the problem in the following way. First, using the literature numbers, in App. A, we evaluated the quality of the fit. Then, we scan parameter by parameter looking for the global minimum. In this sequential process, whenever a parameter seems to be in the minimum, we fixed and moved to another parameter. After achieving a stable minimum, we gave this as input for a true minimization procedure. We kept fixed, for stability reasons, the octet masses, m_{a_0} and m_{So}, in the minimum found in these scans. The results for the parameters are shown in Table 30 and the plots in Figs. 90 and 91.

Altough the description of the data is satisfactory, $\chi^2/\text{ndof} = 859.01/494 = 1.74$, is not as good as the Isobar result. However, the outcome physical meaning is way more rich. Inspecting the χ^2 distribution plot in Fig. 91, the main difficulty lies on the ϕ region, suggesting that the interference between the ϕ and the $\mathcal{S}$-wave still needs improvement.

Table 30: Results of a preliminary fit to the minimal Multi-Meson Model

	c_d	c_m	$\tilde{c}_d$	$\tilde{c}_m$
fit	$(2.534 \pm 0.026) \times 10^{-2}$	$(5.01 \pm 0.14) \times 10^{-2}$	$(1.100 \pm 0.030) \times 10^{-2}$	$(5.257 \pm 0.091) \times 10^{-2}$
App. A	0.032	0.043	$0.032/\sqrt{3}$	$0.043/\sqrt{3}$

	m_{S0}	m_{S1}	m_{a_0}
fit	0.9274	1.3232 ± 0.0098	1.42791
PDG	-	-	0.980/1.474

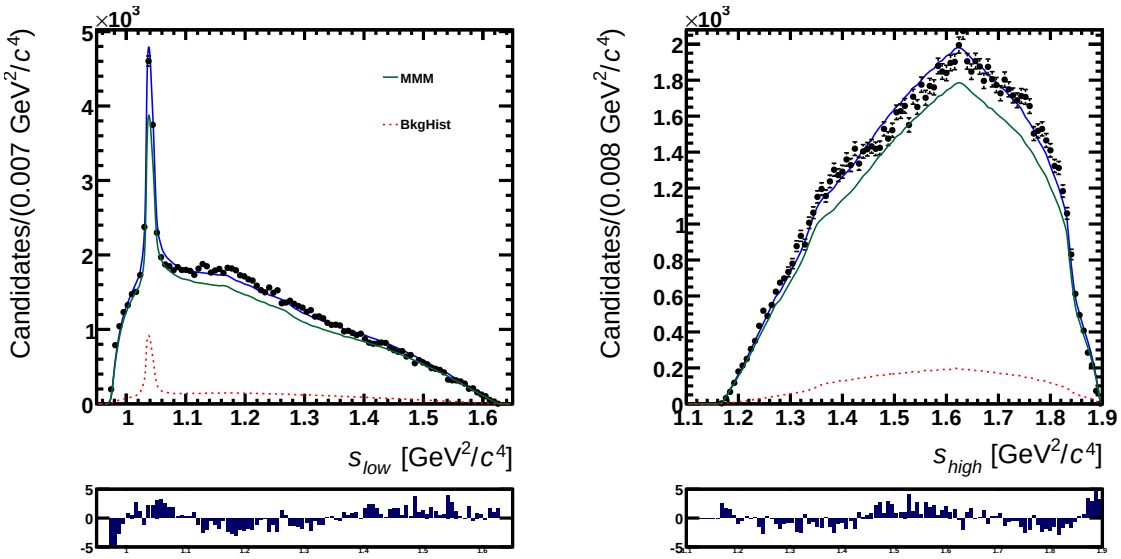

Figure 90: Projections of the data onto $s_{\rm hi}$ (left) and $s_{\rm lo}$ axes (right). The fit result (blue line) for minimal MMM is superimposed. The background contribution are also shown.

In order to understand each component in detail, a plot of the channels ρ, a_0 and f_0 are displayed in Fig. 92.

As expected, the ρ contribution is highly suppressed. The f_0 plays a significant role when compared to the a_0. The results for the f_0 octet and singlet masses suggest that this amplitude is a linear combination between a low and high mass pole. The ϕ resonance is very thin and its the main contribution to the $\mathcal{P}$-wave. The plots of the $\mathcal{P}$-wave, basically ϕ, and $\mathcal{S}$-wave are further shown.

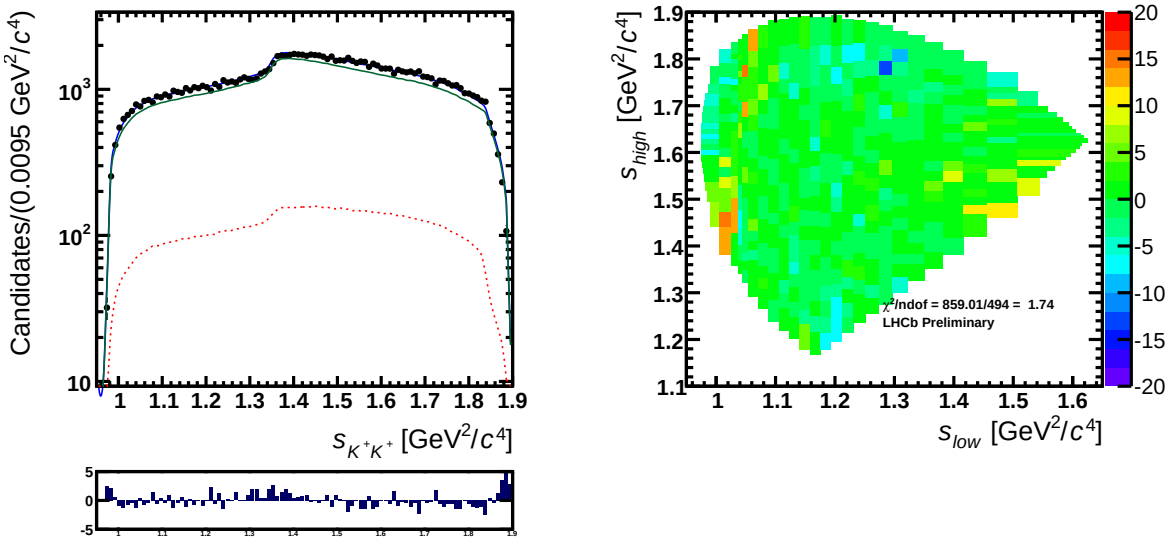

Figure 91: Left: projection of the data onto s_{23} axis, with the fit result for minimal MMM superimposed. Right: the distribution of the signed χ^2 over the Dalitz plot.

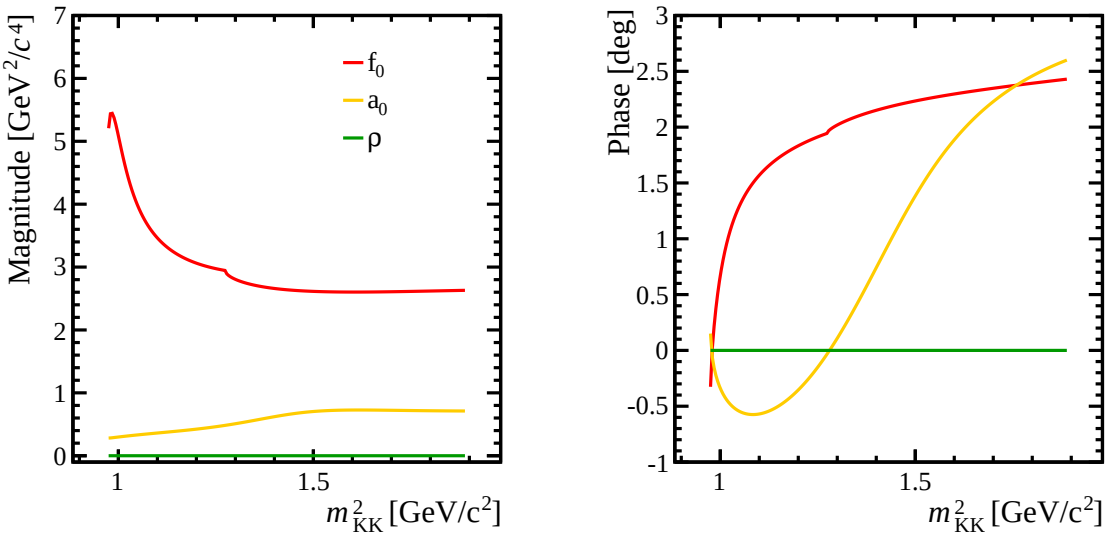

Figure 92: Left: Magnitude of the minimal production amplitude for each channel. Right: Phase part.

7.6 Triple-M summary

Although a reasonable description of the $D^+ \to K^-K^+K^+$ is obtained with the Multi-meson Model, the Isobar still gives a better χ^2/ndof. However, the results shown in this section are very preliminary and can be improved. The description of the $\mathcal{P}$-wave is very similar to the Isobar, where the ϕ is the only contribution. Here, we allowed the ρ-channel to contribute but it comes out to be highly suppressed in the fit. The $\mathcal{S}$-wave is composed of the f_0 octet/singlet, a_0 and the nonresonant amplitude. The latter does not have any free parameter but is an essential amplitude to the fit. The f_0 gives the major

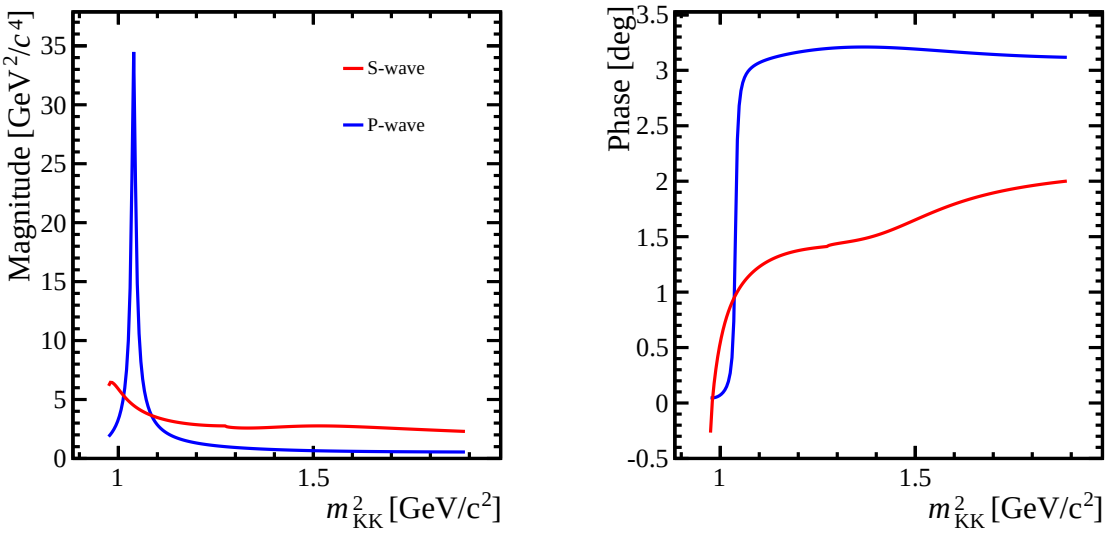

Figure 93: Magnitude (left) and phase variation (right) of the minimal production amplitude for each channel.

contribution the $\mathcal{S}$-wave and it is composed of two poles. The octet at high mass and the singlet at low mass, shown in Table 30

8 Conclusions

Charm physics: You haven't seen anything yet - the best things are still to come!

I.I. Bigi

In this thesis we have presented the first amplitude analysis of the $D^+ \to K^-K^+K^+$ doubly Cabibbo-suppressed decay. Our main focuses were to understand the resonant intermediate structures for this decay and to interpret the $\bar{K}K$ $\mathcal{S}$-wave. Previous studies of the $\mathcal{S}$-wave [56,57] showed that the main difficulties were the disentangling of the a_0/f_0 contribution and the high mass phase variation contribution. We presented the study not only of the $D^+ \to K^-K^+K^+$ decay using the **Isobar Model** but also with an alternative model called **Multi-meson model**.

The first model used to analyze the LHCb data was the Isobar Model. Defined as a sum of resonant intermediate contributions, we tested 6 models with different contributions. The data is well described by models with resonances at both edges of the K^-K^+ spectrum. The precise nature of these resonant amplitudes cannot be determined at this point.

The first three are the main results. The first model were composed by an f_0, ϕ and a nonresonant flat contribution, where the last is one of the shortcoming of the Isobar Model. Additionally, this last contribution, due the lack of high-mass phase variation, has shown to be a poor description of the data. The models 2 and 3, which are very similar, showed to be the best results, since with an inclusion of a high-mass resonance, $f_0(X)$ in model 2 and $a_0(1450)$ in model 3, they deal with this phase variation. This confirms that the $\mathcal{S}$-wave should be between models 2 and 3.

Despite the good description of the data, it is not possible to disentangle the high mass contributions and the f_0/a_0. Therefore, these results are an effective description of different contributions.The inclusion a spin 2 contribution does not gives significant fit fraction for the fit.

The magnitude and phase of the S-wave amplitude, as a function of the K^-K^+ mass, are shown in Fig. 94 for main results, models 1, 2 and 3. The $\mathcal{P}$-wave is rather stable in all models.

The alternative model shown were the Multi-meson model. The preliminary fit shows good agreement with the data but still needs improvement. With the assumption that the annihilation topology is the main contribution for the decay, the MMM is proposed as a description of the matrix element $\langle\, (KKK)^+|A^\mu|0\,\rangle$ based on Chiral Perturbation Theory with Resonances. Contributions to this matrix element come from a direct nonresonant amplitude, which, in contrast to the constant parametrization by Isobar model, has dynamical effects and it is a purely three-body amplitude.

The resonant amplitudes are decomposed in four spin-isospin channels $J = 0, 1$ and $I = 0, 1$, which allow the appearance of the explicit resonances ρ, ϕ, a_0 and f_0. This decomposition enables us to distinguish between the a_0 and f_0 contributions. On top of that, the coupling constants appear clearly in the amplitude, derived from the LO and NLO Lagrangian. In contrast, the connection between the decay amplitude and the SM Lagrangian is hidden in the c_k's parameters of the Isobar model. These are the major improvements of the MMM compared to the Isobar.

The drawback is the complexity of the amplitude functions, wherefore we start from a minimal version of the MMM, leading to a preliminary understanding of the decay.

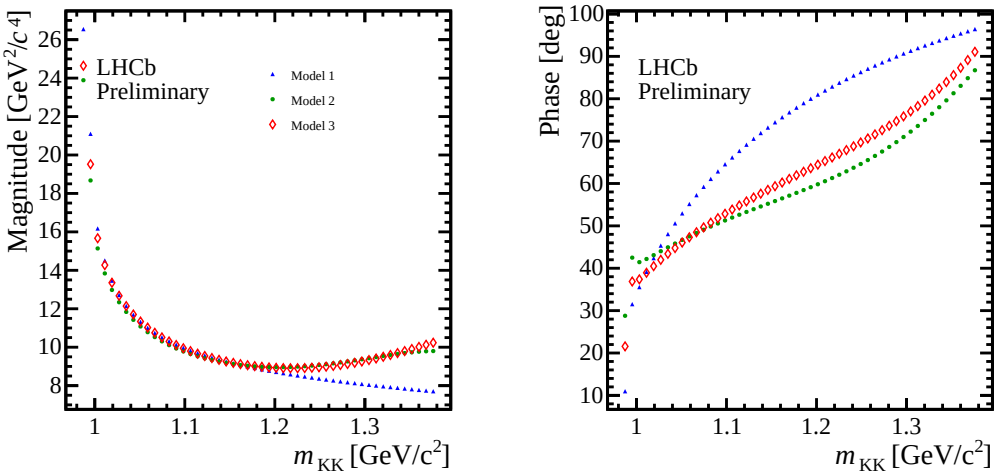

Figure 94: The magnitude and phase variation for models 1, 2 and 3.

However, even the complete model is not a full description of the $D^+ \to K^-K^+K^+$ decay since it does not contemplate the external W emission diagram. Nevertheless, the good agreement with the data shown with the MMM is a hint that this topology is actually suppressed. This is an ongoing work and more results are expected in the near future.

Acknowledgements

- Ao Alberto, por todos esses anos de orientação. Por toda sua paciência para me explicar todos os detalhes possíveis que podíamos enfrentar nesse problema. Por todas as nossas discussões e a quantidade imensurável de conhecimento que aprendi não só de física mas de como ser um pesquisador.

- À Carla, por acreditar em mim quando era apenas um calouro. Por todos esses anos de orientação incansável em todo nosso trabalho e na vida pessoal. Por ter sido uma das responsáveis por ter me 'tirado' da engenharia.

- À todo Charm Rio Group. Sandra e Érica por todo aprendizado durante esses anos na análise do $D^+ \to K^-K^+K^+$. À todas as 'crianças' do charm, Daniel, Danielle, Clarissa e um agradecimento especial ao meu grande amigo, my partner in crime, Josué Molina, por todas nossas discussões filosóficas e sua grande amizade.

- Ao Mané e à Pat, por esses últimos anos de trabalho no MMM, onde aprendi à olhar o mesmo problema de uma outra visão. Pela convivência que torna a pesquisa e o trabalho muito prazeroso.

- À todo pessoal da 514D e 515D, Guilherme, Alexandre, Gian Ricardo, Lfog e Felipe por todos os cafés, as discussões e a amizade.

- Ao Cnpq, pelo apoio financeiro.

- Aos meus amigos, "Happiness is only real when shared".

- Por último e mais importante, à minha familia. Minha mãe Heloisa, minha irmã Luli, meu pai José, meu tio Alexande e minha avó Izabel. Pessoas que pavimentaram o caminho para que eu pudesse seguir caminhando.

Appendix

A Numerical inputs for the Multi-Meson Model

Ideally, the theory predictions for all the constants appearing in the MMM should predict the data. $F = 0.093$
$c_d = 0.032, \quad c_m = 0.043, \quad \tilde{c}_d = 0.032/\sqrt{3} \quad \tilde{c}_m = 0.043\sqrt{3}$
$M_S = M_V = 1.0$
All the other values are extracted from the PDG.

B Further Checks

In this section we included some further checks which search for multiple minima and stability tests.

B.1 Multiple solution test

We look for multiple minima for the fits using models 2 , 3 and 5. The input parameters are sorted within wide enough ranges and the fit is performed a number of times. We then check if the fitted parameters are different.

For both Models 2 and 3, only one solution has been found, which matches respectively the solution found in Sec. 6.

Model 5 is essentially model 2 with the inclusion of a $f_2(1270)$. In the fit results, model 5 solution is clearly different from model 2 with a small contribution of the D-wave, so this is already some evidence of two different solutions.

Performing many fits, we show in Figure 95 the χ^2 distribution of those fits.

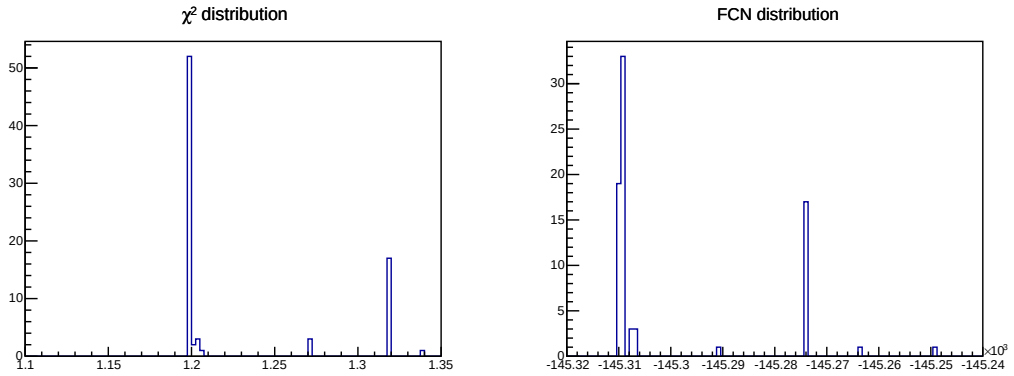

Figure 95: χ^2 distribution of Multiple solutions test for Model 5

In this plot, there are two minima, one for $\chi^2 \sim 1.2$ and another for $\chi^2 \sim 1.32$. By looking at each parameter it is possible to see that the former represent the Model 5 solution of Sec. 6 and the latter is the solution with the parameter $a_{f_2(1270)} = 0.047 \pm 0.12$, showing that this contribution is negligible, proving that is the same solution of Model 2.

B.2 Test for fit bias

A test is performed to check for any possible intrinsic bias due to the Dalitz fit procedure. A number of pseudoexperiments are ran where Fast Monte Carlo samples are generated based on the Model 3 result from Sec. 6 and then fitted using the same model and starting from random inputs. The samples have the same size of the original data sample and include also the effects due to acceptance and background. A Gaussian function is fit to the parameters distributions and the mean value and widths are shown in Table 31, together with the mean value of the uncertainty of each parameter. No biases are introduced in the fitting procedure.

Table 31: Magnitudes and phases outputs for the fit bias test using Model 3. The last column is the Gaussian width of the parameter distribution.

parameter	generated value	parameter mean	mean parameter error	parameter RMS
$a(a_0)$	3.41725	3.419 ± 0.007	0.063	0.060 ± 0.006
$\delta(a_0)$	44.629	44.19 ± 0.52	3.44	3.84 ± 0.42
$a(f_0)$	3.40375	3.399 ± 0.008	0.061	0.055 ± 0.007
$\delta(f_0)$	-71.753	-72.05 ± 0.20	1.34	1.44 ± 0.16

C Background subtracted and efficiency corrected $D^+ \to K^-K^+K^+$ Dalitz plot

The Dalitz plot of the $D^+ \to K^-K^+K^+$ decays is shown in Fig. 97, after background subtraction and efficiency correction.

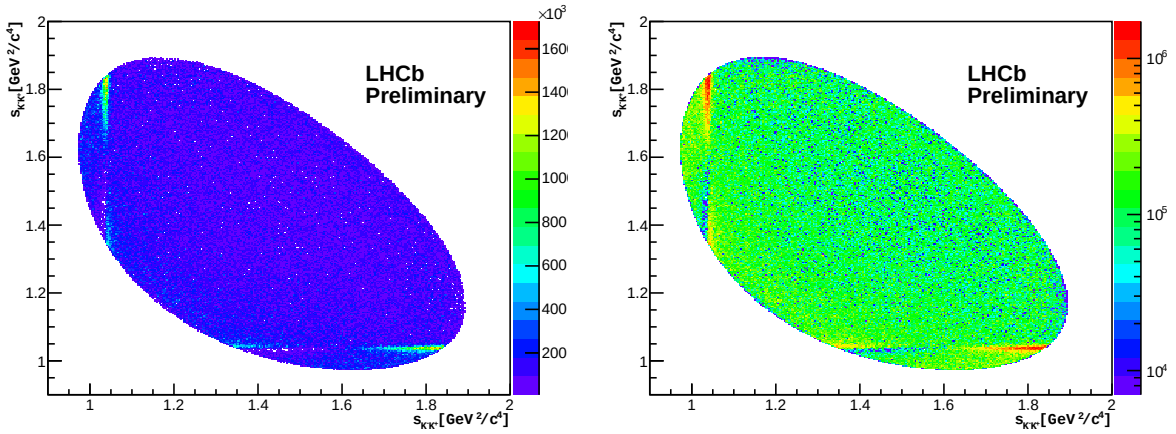

Figure 96: Background subtracted and efficiency corrected $D^+ \to K^-K^+K^+$ Dalitz plot. The left (right) plot is in linear (log) scale.

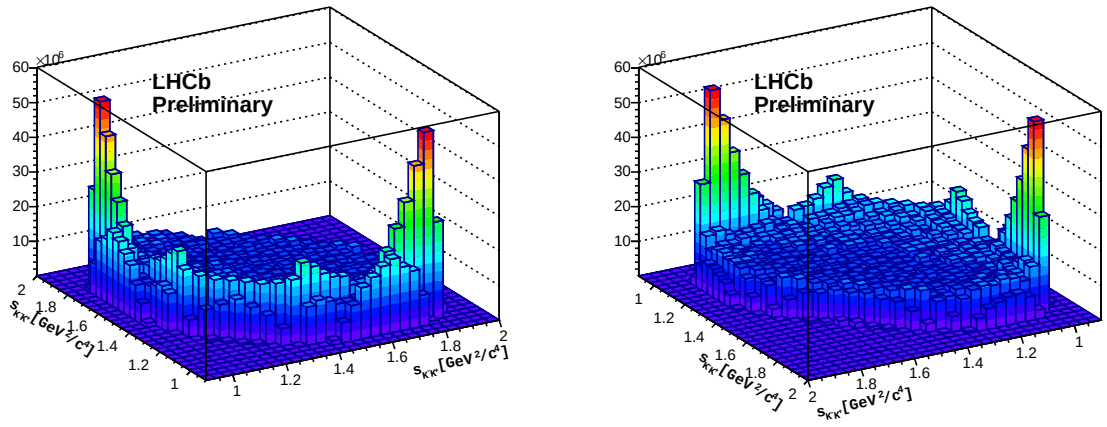

Figure 97: Two 3D views of the background subtracted and efficiency corrected $D^+ \to K^-K^+K^+$ Dalitz plot.

D two-meson propagators and functions Ω

Expressions presented here are conventional. They are displayed for the sake of completeness and rely on the the results of [1]. These integrals do not include symmetry factors, which are accounted for in the main text. One deals with both S and P waves and the corresponding two-meson propagators are associated with the integrals

$$\{I_{ab};\, I^{\mu\nu}_{ab}\} = \int \frac{d^4\ell}{(2\pi)^4} \frac{\{1;\, \ell^\mu\, \ell^\nu\}}{D_a\, D_b}, \tag{173}$$

$$D_a = (\ell + p/2)^2 - M_a^2\ , \qquad D_b = (\ell - p/2)^2 - M_b^2\ , \tag{174}$$

with $p^2 = s$. Both integrals I_{ab} and $I^{\mu\nu}_{ab}$ are evaluated using dimensional techniques [1]. For $s \geq (M_a + M_b)^2$, the function I_{ab} has the structure

$$I_{ab} \ = \ i\, \frac{1}{16\pi^2}\, \left[\Lambda_{ab} + i_{ab}\right] \tag{175}$$

where Λ_{ab} is a divergent function of the renormalization scale μ and of the number of dimensions n, which diverges in the limit $n \to 4$, whereas i is regular component, given by

$$i_{ab}(s) = 1 + \frac{m_a^2 + m_b^2}{m_a^2 - m_b^2}\, \ln\frac{m_a}{m_b} - \frac{m_a^2 - m_b^2}{s}\, \ln\frac{m_a}{m_b}$$

$$- \frac{\sqrt{\lambda}}{s}\, \ln\left[\frac{s - m_a^2 - m_b^2 + \sqrt{\lambda}}{2\, m_a\, m_b}\right] + i\,\pi\, \frac{\sqrt{\lambda}}{s}\ , \tag{176}$$

$$\lambda = s^2 - 2\, s\, (m_a^2 + m_b^2) + (m_a^2 - m_b^2)^2\ . \tag{177}$$

which, for $a = b$, reduces to

$$i_{aa}(s) = 2 - \frac{\sqrt{\lambda}}{s}\, \ln\left[\frac{s - 2\, m_a^2 + \sqrt{\lambda}}{2\, m_a^2}\right] + i\,\pi\, \frac{\sqrt{\lambda}}{s}\ . \tag{178}$$

The tensor integral is needed for $a = b$ only, and one has

$$I^{\mu\nu}_{aa} \ = \ i\, \frac{1}{16\pi^2}\, \left\{ \frac{p^\mu\, p^\nu}{s}\, \left[\Lambda^{pp}_{aa} + \frac{1}{12}\left[s - 4\, m_x^2\right]\ i_{aa}\right]\right.$$

$$\left. - \ g^{\mu\nu}\, \left[\Lambda^{g}_{aa} + \frac{1}{12}\left[s - 4\, m_a^2\right]\ i_{aa}\right]\right\}\ , \tag{179}$$

where Λ^{pp}_{aa} and Λ^{g}_{aa} are divergent quantities.

In the K-matrix approximation, one keeps only the imaginary parts of the loop integrals, which are contained in the function i and has

$$i_{ab} \ \to \ -\frac{1}{16\,\pi}\, \frac{\sqrt{\lambda}}{s}\ , \tag{180}$$

$$i^{\mu\nu}_{aa} \ \to \ \frac{1}{192\,\pi}\, \left[g^{\mu\nu} - \frac{p^\mu p^\nu}{s}\right]\, \frac{\lambda^{3/2}}{s^2}\ . \tag{181}$$

In the decay calculation, it is more covenient to use the functions $\bar{\Omega}$, defined by

$$i_{ab} \;\to\; -i\,\bar{\Omega}^S_{ab}\,, \tag{182}$$

$$i^{\mu\nu}_{aa} \;\to\; \frac{i}{4}\left[g^{\mu\nu} - \frac{p^\mu p^\nu}{s}\right]\bar{\Omega}^P_{aa}\,. \tag{183}$$

These results are related with CM momenta by

$$\bar{\Omega}^S_{ab} = -\frac{i}{8\pi}\,\frac{Q_{ab}}{\sqrt{s}}\,\theta(s-(M_a+M_b)^2)\,, \tag{184}$$

$$\bar{\Omega}^P_{aa} = -\frac{i}{6\pi}\,\frac{Q^3_{aa}}{\sqrt{s}}\,\theta(s-4\,M_a^2)\,, \tag{185}$$

$$Q_{ab} = \frac{1}{2}\,\sqrt{s-2\,(M_a^2+M_b^2)+(M_a^2-M_b^2)^2/s}\,. \tag{186}$$

E SU(3) intermediate states

In the treatment of intermediate states, it is convenient to work with Cartesian $SU(3)$ states $|a\,b\,\rangle$. We need just intermediate states with the same quantum numbers of the K^-K^+ system, which are given by

$$|V_3^{\pi\pi}\,\rangle \;=\; (1/\sqrt{2})\,|1\,2-2\,1\,\rangle, \tag{187}$$

$$|V_3^{KK}\,\rangle \;=\; (1/2)\,|4\,5-5\,4-6\,7+7\,6\,\rangle, \tag{188}$$

$$|V_8^{KK}\,\rangle \;=\; (1/2)\,|4\,5-5\,4+6\,7-7\,6\,\rangle, \tag{189}$$

$$|U_3^{\pi 8}\,\rangle \;=\; (1/\sqrt{2})\,|3\,8+8\,3\,\rangle, \tag{190}$$

$$|U_3^{KK}\,\rangle \;=\; (1/2)\,|4\,4+5\,5-6\,6-7\,7\,\rangle, \tag{191}$$

$$|S^{\pi\pi}\,\rangle \;=\; (1/\sqrt{3})\,|1\,1+2\,2+3\,3\,\rangle, \tag{192}$$

$$|S^{KK}\,\rangle \;=\; (1/2)\,|4\,4+5\,5+6\,6+7\,7\,\rangle, \tag{193}$$

$$|S^{88}\,\rangle \;=\; |8\,8\,\rangle. \tag{194}$$

The state $|K^-K^+\,\rangle$ includes a conventional phase an reads

$$|K^-K^+\,\rangle \;=\; -(1/2)\,|(4-i\,5)(4+i\,5)\,\rangle = -(1/2)\,|4\,4+5\,5\,\rangle - i\,(1/2)\,|4\,5-5\,4\,\rangle \tag{195}$$

and, therefore,

$$\langle\,K^-\,K^+| \;=\; (i/2)\,\langle\,V_3^{KK}+V_8^{KK}| - (1/2)\,\langle\,U_3^{KK}+S^{KK}|. \tag{196}$$

F tree production sub-amplitudes

In the evaluation of intermediate state contributions shown in diagrams of Fig.86, we need tree level contribution for the process $D \to a\,b\,K^+$, denoted by $T^{(J,I)}_{(0)}$, for spin J and isospin I. Using the constant C defined in Eq. 152, we have

$$[J, I = 1, 1] \to \langle\, V_3^{ab}\, K^+ |\, T^{(1,1)}_{(0)}\, |\, D\,\rangle = i\, Q{\cdot}(p_a - p_b)\; \Gamma^{(1,1)}_{(0)\,a\,b}\,, \tag{197}$$

$$\Gamma^{(1,1)}_{(0)\,\pi\pi} = C \left\{ \left[\frac{\sqrt{2}\, G_V^2}{F^2} \right] \frac{m_{12}^2}{m_{12}^2 - m_\rho^2} - \frac{1}{\sqrt{2}} \right\}, \tag{198}$$

$$\Gamma^{(1,1)}_{(0)\,KK} = C \left\{ \left[\frac{G_V^2}{F^2} \right] \frac{m_{12}^2}{m_{12}^2 - m_\rho^2} - \frac{1}{2} \right\} \tag{199}$$

$$\tag{200}$$

$$[J, I = 1, 0] \to \langle\, V_8^{KK}\, K^+ |\, T^{(1,0)}_{(0)}\, |\, D\,\rangle = i\, Q{\cdot}(p_a - p_b)\; \Gamma^{(1,0)}_{(0)\,KK}\,, \tag{201}$$

$$\Gamma^{(1,0)}_{(0)\,KK} = C \left\{ \left[\frac{3\, G_V^2}{F^2}\, \sin^2\theta \right] \frac{m_{12}^2}{D_\phi^{\pi\rho}(m_{12}^2)} - \frac{3}{2} \right\}, \tag{202}$$

$$\tag{203}$$

$$[J, I = 0, 1] \to \langle\, U_3^{ab}\, K^+ |\, T^{(0,1)}_{(0)}\, |\, D\,\rangle = \Gamma^{(0,1)}_{(0)\,a\,b}\,, \tag{204}$$

$$\Gamma^{(0,1)}_{(0)\,\pi 8} = C \left\{ \left[\frac{\sqrt{2}}{\sqrt{3}\, F^2} \right] \frac{[-c_d\, Q{\cdot}p_3 + c_m\, M_D^2]}{m_{12}^2 - m_{a_0}^2} \left[c_d\, \left(m_{12}^2 - M_\pi^2 - M_8^2 \right) + 2\, c_m\, M_\pi^2 \right] \right.$$
$$\left. - \frac{\sqrt{3}}{\sqrt{2}} \left[\frac{1}{3}\, M_D^2 - Q{\cdot}p_3 \right] \right\}, \tag{205}$$

$$\Gamma^{(0,1)}_{(0)\,KK} = C \left\{ \left[\frac{1}{F^2} \right] \frac{[-c_d\, Q{\cdot}p_3 + c_m\, M_D^2]}{m_{12}^2 - m_{a_0}^2} \left[c_d\, \left(m_{12}^2 - 2M_K^2 \right) + 2\, c_m\, M_K^2 \right] \right.$$
$$\left. - \frac{1}{2} \left[M_D^2 - Q{\cdot}p_3 \right] \right\}, \tag{206}$$

$$\tag{207}$$

$$[J, I = 0, 0] \to \langle\, S^{ab}\, K^{+} |\, T^{(0,0)}_{(0)}\, |\, D\,\rangle = \Gamma^{(0,0)}_{(0)\,a\,b}\,, \tag{208}$$

$$\Gamma^{(0,0)}_{(0)\,\pi\pi} = C \left\{ \left[\frac{8\sqrt{3}}{F^2}\right] \frac{[-\tilde{c}_d\, Q{\cdot}p_3 + \tilde{c}_m\, M_D^2]}{m_{12}^2 - m_{S1}^2} \left[\tilde{c}_d \left(m_{12}^2 - 2M_\pi^2\right) + 2\,\tilde{c}_m\, M_\pi^2\right] \right.$$

$$- \left[\frac{1}{\sqrt{3}\,F^2}\right] \frac{[-c_d\, Q{\cdot}p_3 + c_m\, M_D^2]}{m_{12}^2 - m_{So}^2} \left[c_d \left(m_{12}^2 - 2M_\pi^2\right) + 2\,c_m\, M_\pi^2\right]$$

$$\left. - \frac{\sqrt{3}}{2} \left[M_D^2 - Q{\cdot}p_3\right] \right\}, \tag{209}$$

$$\Gamma^{(0,0)}_{(0)\,KK} = C \left\{ \left[\frac{16}{F^2}\right] \frac{[-\tilde{c}_d\, Q{\cdot}p_3 + \tilde{c}_m\, M_D^2]}{m_{12}^2 - m_{S1}^2} \left[\tilde{c}_d \left(m_{12}^2 - 2M_K^2\right) + 2\,\tilde{c}_m\, M_K^2\right] \right.$$

$$+ \left[\frac{1}{3\,F^2}\right] \frac{[-c_d\, Q{\cdot}p_3 + c_m\, M_D^2]}{m_{12}^2 - m_{So}^2} \left[c_d \left(m_{12}^2 - 2M_K^2\right) + 2\,c_m\, M_K^2\right]$$

$$\left. - \frac{3}{2} \left[M_D^2 - Q{\cdot}p_3\right] \right\}, \tag{210}$$

$$\Gamma^{(0,0)}_{(0)\,88} = C \left\{ \left[\frac{8}{F^2}\right] \frac{[-\tilde{c}_d\, Q{\cdot}p_3 + \tilde{c}_m\, M_D^2]}{m_{12}^2 - m_{S1}^2} \left[\tilde{c}_d \left(m_{12}^2 - 2M_8^2\right) + 2\,\tilde{c}_m\, M_8^2\right] \right.$$

$$+ \left[\frac{1}{3\,F^2}\right] \frac{[-c_d\, Q{\cdot}p_3 + c_m\, M_D^2]}{m_{12}^2 - m_{So}^2} \left[c_d \left(m_{12}^2 - 2M_8^2\right) + c_m \left(-10M_\pi^2 + 16M_K^2\right)/3\right]$$

$$\left. - \frac{1}{2} \left[\frac{5}{3}\, M_D^2 - 3\, Q{\cdot}p_3\right] \right\}. \tag{211}$$

with

$$Q{\cdot}p_3 = \frac{1}{2} \left[M_D^2 + M_K^2 - m_{12}^2\right]\,. \tag{212}$$

G scattering kernels

The intermediate scattering amplitudes depend on interaction kernels in the four channels considered, associated with $J, I = 1, 0$. The kernel matrix elements for the reaction $c\,d \to a\,b$ are written as $\langle\, cd \,|\, \mathcal{K}^{J,I} \,|\, ab \,\rangle$, in terms of the states defined in App.E, and displayed below. All kernels are written as sums of NLO resonance contributions and chiral polynomials, involving both LO and NLO terms. The NLO polynomials are derived by assuming that the LECs are saturared by intermedate vector and scalar resonances, with masses M_V and M_S, respectively. The kernel matrix elements read

$$[J, I = 1, 1] \to \langle\, V_3^{ab} \,|\, \mathcal{K}^{(1,1)} \,|\, V_3^{cd} \,\rangle = (t-u)\; \mathcal{K}^{(1,1)}_{(ab|cd)} \tag{213}$$

$$\mathcal{K}^{(1,1)}_{(\pi\pi|\pi\pi)} = -2 \left[\frac{G_V^2}{F^4}\right] \frac{s}{s - m_\rho^2} + P^{(1,1)}_{(\pi\pi|\pi\pi)} \tag{214}$$

$$P^{(1,1)}_{(\pi\pi|\pi\pi)} = \left[\frac{1}{F^2}\right] + \left[\frac{G_V^2\, s}{F^4 M_V^2}\right] + \left[\frac{4}{F^4\, M_{S_1}^2}\right] \left[-\tilde{c}_d^{\,2}\, s + 4\, \tilde{c}_d\, \tilde{c}_m\, M_\pi^2\right]$$
$$+ \left[\frac{2}{3F^4\, M_{So}^2}\right] \left[-c_d^2\, s + 4\, c_d\, c_m\, M_\pi^2\right] \tag{215}$$

$$\mathcal{K}^{(1,1)}_{(\pi\pi|KK)} = -\sqrt{2} \left[\frac{G_V^2}{F^4}\right] \frac{s}{s - m_\rho^2} + P^{(1,1)}_{(\pi\pi|KK)} \tag{216}$$

$$P^{(1,1)}_{(\pi\pi|KK)} = \left[\frac{\sqrt{2}}{2\, F^2}\right] + \left[\frac{\sqrt{2}\, G_V^2\, s}{2\, F^4 M_V^2}\right] + \left[\frac{\sqrt{2}}{F^4\, M_{So}^2}\right] \left[-c_d^2\, s + 2\, c_d\, c_m\, (M_\pi^2 + M_K^2)\right] \tag{217}$$

$$\mathcal{K}^{(1,1)}_{(KK|KK)} = -\left[\frac{G_V^2}{F^4}\right] \frac{s}{s - m_\rho^2} + P^{(1,1)}_{(KK|KK)} \tag{218}$$

$$P^{(1,1)}_{(KK|KK)} = \left[\frac{1}{2\, F^2}\right] + \left[\frac{G_V^2\, s}{2\, F^4 M_V^2}\right] + \left[\frac{4}{F^4\, M_{S_1}^2}\right] \left[-\tilde{c}_d^{\,2}\, s + 4\, \tilde{c}_d\, \tilde{c}_m\, M_K^2\right]$$
$$- \left[\frac{1}{3F^4\, M_{So}^2}\right] \left[-c_d^2\, s + 4\, c_d\, c_m\, M_K^2\right] \tag{219}$$

$$[J, I = 1, 0] \to \langle\, V_8^{ab} \,|\, \mathcal{K}^{(1,0)} \,|\, V_8^{cd} \,\rangle = (t-u)\; \mathcal{K}^{(1,0)}_{(ab|cd)} \tag{220}$$

$$\mathcal{K}^{(1,0)}_{(KK|KK)} = -3 \left[\frac{G_V^2\, \sin^2\theta}{F^4}\right] \frac{s}{D_\phi^{\pi\rho}} + P^{(1,0)}_{(KK|KK)} \tag{221}$$

$$P^{(1,0)}_{(KK|KK)} = \left[\frac{3}{2\, F^2}\right] + \left[\frac{3\, G_V^2\, s}{2\, F^4 M_V^2}\right] + \left[\frac{4}{F^4\, M_{S_1}^2}\right] \left[-\tilde{c}_d^{\,2}\, s + 4\, \tilde{c}_d\, \tilde{c}_m\, M_K^2\right]$$
$$+ \left[\frac{5}{3F^4\, M_{So}^2}\right] \left[-c_d^2\, s + 4\, c_d\, c_m\, M_K^2\right] \tag{222}$$

$$[J, I = 0, 1] \to \langle\, U_3^{ab} \,|\, \mathcal{K}^{(0,1)} \,|\, U_3^{cd} \,\rangle = \mathcal{K}^{(0,1)}_{(ab|cd)} \tag{223}$$

$$\mathcal{K}^{(0,1)}_{(\pi 8|\pi 8)} = -\,\frac{1}{s - m_{a_0}^2}\,\left[\frac{4}{3\,F^4}\right]\,\left[c_d\,(s - M_\pi^2 - M_8^2) + c_m\,2M_\pi^2\right]^2 + P^{(0,1)}_{(\pi 8|\pi 8)} \tag{224}$$

$$P^{(0,1)}_{(\pi 8|\pi 8)} = \left[\frac{2M_\pi^2}{3F^2}\right] + \left[\frac{4}{F^4\,M_{S_1}^2}\right]\left\{\frac{2\,\tilde{c}_d^2}{3\,s^2}\,\left[s^2 - 2\,s\,(M_\pi^2 + M_8^2) + (M_\pi^2 - M_8^2)^2\right]^2\right.$$
$$+\,\frac{2\,\tilde{c}_d}{s}\,(\tilde{c}_d - \tilde{c}_m)\,(M_\pi^2 + M_8^2)\,\left[s^2 - 2\,s\,(M_\pi^2 + M_8^2) + (M_\pi^2 - M_8^2)^2\right]$$
$$\left.+\,(\tilde{c}_d - \tilde{c}_m)^2\,8\,M_\pi^2\,M_8^2\right\} \tag{225}$$

$$\mathcal{K}^{(0,1)}_{(\pi 8|KK)} = -\,\frac{1}{s - m_{a_0}^2}\,\left[\frac{2\sqrt{2}}{\sqrt{3}\,F^4}\right]\,\left[c_d\,(s - M_\pi^2 - M_8^2) + c_m\,2M_\pi^2\right]\,\left[c_d\,s - (c_d - c_m)\,2M_K^2\right]$$
$$+P^{(0,1)}_{(\pi 8|KK)} \tag{226}$$

$$P^{(0,1)}_{(\pi 8|KK)} = \left[\frac{(3s - 4M_K^2)}{\sqrt{6}\,F^2}\right] - \left[\frac{\sqrt{6}\,G_V^2}{3\,F^4\,M_V^2}\right]\left[2\,s^2 - \frac{5}{2}\,s\,(M_\pi^2 + 2M_K^2 + M_8^2)\right.$$
$$\left.+4\,(M_\pi^2 + M_8^2)\,M_K^2 + \frac{1}{2}\left(1 + \frac{2\,M_K^2}{s}\right)(M_\pi^2 - M_8^2)^2\right]$$
$$-\left[\frac{\sqrt{2}}{\sqrt{3}\,F^4\,M_{So}^2}\right]\,\left\{(2/3)\,c_d^2\,\left[\left[s - (M_\pi^2 + 2M_K^2 + M_8^2)\right]^2 + (M_\pi^2 - M_K^2)(M_K^2 - M_8^2)\right.\right.$$
$$-\,(M_\pi^2 - M_8^2)^2 M_K^2/s\Big] + c_d\,s\,\left[c_d\,(M_\pi^2 + 2M_K^2 + M_8^2) - c_m\,(-2\,M_\pi^2 + 6\,M_K^2)\right]$$
$$-\,c_d^2\,\left[(M_\pi^2 + M_K^2)^2 + (M_K^2 + M_8^2)^2\right]$$
$$+\,2\,c_d\,c_m\,\left[(M_\pi^2 + M_K^2)(2M_\pi^2 - 3M_K^3 - M_8^2) + (M_K^2 + M_8^2)(-M_\pi^2 + 3M_K^2)\right]$$
$$\left.+\,2\,c_m^2(M_\pi^2 + M_K^2)(-3M_\pi^2 + 5M_K^2)\right\}^{(4So)} \tag{227}$$

$$\mathcal{K}^{(0,1)}_{(KK|KK)} = -\frac{1}{s - m_{a_0}^2}\,\left[\frac{2}{F^4}\right]\,\left[c_d\,s - (c_d - c_m)\,2M_K^2\right]^2 + P^{(0,1)}_{(KK|KK)} \tag{228}$$

$$P^{(0,1)}_{(KK|KK)} = \left[\frac{s}{2F^2}\right] - \left[\frac{G_V^2}{3\,F^4\,M_V^2}\right]\,\left[2\,s^2 - 10\,s\,M_K^2 + 8\,M_K^4\right]$$
$$+\left[\frac{4}{F^4\,M_{S_1}^2}\right]\,\left[\frac{2}{3}\,\tilde{c}_d^2\,\left[s - 4\,M_K^2\right]^2 + 4\,\tilde{c}_d\,(\tilde{c}_d - \tilde{c}_m)\,s\,M_K^2 - 8\,(\tilde{c}_d^2 - \tilde{c}_m^2)\,M_K^4\right]$$
$$-\left[\frac{1}{3\,F^4\,M_{So}^2}\right]\,\left\{(2/3)\,c_d^2\,\left[s - 4\,M_K^2\right]^2 + 4\,c_d\,(c_d - c_m)\,s\,M_K^2 - 8(c_d^2 - c_m^2)\,M_K^4\right\} \tag{229}$$

$$[J, I = 0, 0] \to \langle\, S^{ab} \,|\, \mathcal{K}^{(0,0)} \,|\, S^{cd} \,\rangle = \mathcal{K}^{(0,0)}_{(ab|)} \tag{230}$$

$$\mathcal{K}^{(0,0)}_{(\pi\pi|\pi\pi)} = -\,\frac{1}{s - m^2_{S1}}\,\left[\frac{12}{F^4}\right]\,\left[\tilde{c}_d\, s - (\tilde{c}_d - \tilde{c}_m)\, 2M^2_\pi\right]^2$$

$$-\,\frac{1}{s - m^2_{So}}\,\left[\frac{2}{F^4}\right]\,\left[c_d\, s - (c_d - c_m)\, 2M^2_\pi\right]^2 + P^{(0,0)}_{(\pi\pi|\pi\pi)} \tag{231}$$

$$P^{(0,0)}_{(\pi\pi|\pi\pi)} = \left[\frac{2s - M^2_\pi}{F^2}\right] - \left[\frac{4\, G^2_V}{3\, F^4\, M^2_V}\right]\left[2\, s^2 - 10\, s\, M^2_\pi + 8\, M^4_\pi\right]$$

$$+\left[\frac{4}{F^4\, M^2_{S_1}}\right]\,\left[\frac{2}{3}\,\tilde{c}^2_d\,\left[s - 4\, M^2_\pi\right]^2 + 4\,\tilde{c}_d\,(\tilde{c}_d - \tilde{c}_m)\, s\, M^2_\pi - 8\,(\tilde{c}^2_d - \tilde{c}^2_m)\, M^4_\pi\right]$$

$$+\left[\frac{2}{3\, F^4\, M^2_{So}}\right]\,\left[\frac{2}{3}\,c^2_d\,\left[s - 4\, M^2_\pi\right]^2 + 4\, c_d\,(c_d - c_m)\, s\, M^2_\pi - 8(c^2_d - c^2_m)\, M^4_\pi\right] \tag{232}$$

$$\mathcal{K}^{(0,0)}_{(\pi\pi|KK)} = -\,\frac{1}{s - m^2_{S1}}\,\left[\frac{8\sqrt{3}}{F^4}\right]\,\left[\tilde{c}_d\, s - (\tilde{c}_d - \tilde{c}_m)\, 2M^2_\pi\right]\,\left[\tilde{c}_d\, s - (\tilde{c}_d - \tilde{c}_m)\, 2M^2_K\right]$$

$$+\frac{1}{s - m^2_{So}}\,\left[\frac{2}{\sqrt{3}\, F^4}\right]\,\left[c_d\, s - (c_d - c_m)\, 2M^2_\pi\right]\,\left[c_d\, s - (c_d - c_m)\, 2M^2_K\right]$$

$$+P^{(0,0)}_{(\pi\pi|KK)} \tag{233}$$

$$P^{(0,0)}_{(\pi\pi|KK)} = \left[\frac{\sqrt{3}\, s}{2F^2}\right] - \left[\frac{\sqrt{3}\, G^2_V}{3\, F^4\, M^2_V}\right]\left[2\, s^2 - 5\, s\,(M^2_\pi + M^2_K) + 8\, M^2_\pi\, M^2_K\right]$$

$$+\left[\frac{\sqrt{3}}{F^4\, M^2_{So}}\right]\,\left\{\frac{2}{3}\,c^2_d\,\left[\left[s - 2\,(M^2_\pi + M^2_K)\right]^2 - (M^2_\pi - M^2_K)^2\right]\right.$$

$$\left.+\,2\, c_d\,(c_d - c_m)\, s\,(M^2_\pi + M^2_K) - 2(c^2_d - c^2_m)\,(M^2_\pi + M^2_K)^2\right\} \tag{234}$$

$$\mathcal{K}^{(0,0)}_{(\pi\pi|88)} = -\,\frac{1}{s - m^2_{S1}}\,\left[\frac{4\sqrt{3}}{F^4}\right]\,\left[\tilde{c}_d\, s - (\tilde{c}_d - \tilde{c}_m)\, 2M^2_\pi\right]\,\left[\tilde{c}_d\, s - (\tilde{c}_d - \tilde{c}_m)\, 2M^2_8\right]$$

$$+\frac{1}{s - m^2_{So}}\,\left[\frac{2}{\sqrt{3}\, F^4}\right]\,\left[c_d\, s - (c_d - c_m)\, 2M^2_\pi\right]\,\left[c_d\,(s - 2M^2_8) + c_m\,(16M^2_K - 10M^2_\pi)/3\right]$$

$$+P^{(0,0)}_{(\pi\pi|88)} \tag{235}$$

$$P^{(0,0)}_{(\pi\pi|88)} = \left[\frac{\sqrt{3}\, M^2_\pi}{3F^2}\right] + \left[\frac{2}{\sqrt{3}\, F^4\, M^2_{So}}\right]\,\left\{(2/3)\, c^2_d\,\left[\left[s - 2\,(M^2_\pi + M^2_8)\right]^2 - (M^2_\pi - M^2_8)^2\right]\right.$$

$$\left.+\;\; 2\, c_d\, s\,\left[c_d\,(M^2_\pi + M^2_8) - 2\, c_m\, M^2_\pi\right] - 2\, c^2_d (M^2_\pi + M^2_8)^2 + 8\, c^2_m\, M^4_\pi\right\} \tag{236}$$

$$\mathcal{K}^{(0,0)}_{(KK|KK)} = -\,\frac{1}{s - m^2_{S1}}\,\left[\frac{16}{F^4}\right]\,\left[\tilde{c}_d\, s - (\tilde{c}_d - \tilde{c}_m)\, 2M^2_K\right]^2$$

$$-\frac{1}{s - m^2_{So}}\,\left[\frac{2}{3\, F^4}\right]\,\left[c_d\, s - (c_d - c_m)\, 2M^2_K\right]^2 + P^{(0,0)}_{(KK|KK)} \tag{237}$$

H full production amplitudes

The tree level production amplitudes for channel with spin J and isospin I, given in App.F, are written as

$$\begin{aligned}\langle\, X^{ab}\, K^+ |\, T^{(J,I)}_{(0)}\,|\, D\,\rangle &= i\, Q\cdot(p_a - p_b)\, \Gamma^{(1,I)}_{(0)\,a\,b} \quad \to (X = V_3, V_8) \\ &= \Gamma^{(0,I)}_{(0)\,a\,b} \quad \to (X = U_3, S) \end{aligned} \tag{243}$$

The full amplitudes are obtained by including all final state interactions indicated in Figs.86 and 87. The term involving a single meson-meson interaction reads

$$\begin{aligned}\langle\, X^{ab}\, K^+ |\, T^{(J,I)}_{(1)}\,|\, D\,\rangle &= i\, Q\cdot(p_a - p_b)\, \Gamma^{(1,I)}_{(1)\,a\,b} \quad \to (X = V_3, V_8) \\ &= \Gamma^{(0,I)}_{(1)\,a\,b} \quad \to (X = U_3, S) \end{aligned} \tag{244}$$

with

$$\Gamma^{(J,I)}_{(1)\,ab} = -\sum_{cd}\, \mathcal{K}^{(J,I)}_{cd|ab}\, \left[S\, \bar{\Omega}^J_{cd}\right]\, \Gamma^{(J,I)}_{(0)\,cd} \tag{245}$$

where the $\mathcal{K}^{(J,I)}_{cd|ab}$ are the scattering kernels displayed in App. G, $\bar{\Omega}^J_{cd}$ are the two-meson propagators given in App. D, and the symmetry factor $S = 1 \to c \neq d$ and $S = 1/2 \to c = d$.

The tree level amplitude is given by Eqs. 197-212. The one-loop contribution is obtained with the help of the result

$$\int \frac{d^4\ell}{(2\pi)^4}\, \frac{1}{[p_c^2 - M_x^2]\,[p_d^2 - M_x^2]} \;=\; -i\, \bar{\Omega}^P_{xx} \tag{246}$$

and reads

$$\langle\, S\,(K^+)\,|\, T^{(0,0)}_{(1)}\,|\, D\,\rangle = \left\{\Gamma^{(0,0)}_{(1)\,\pi\pi}\, \langle\, S^{\pi\pi}| + \Gamma^{(0,0)}_{(1)\,KK}\, \langle\, S^{KK}| + \Gamma^{(0,0)}_{(1)\,88}\, \langle\, S^{88}|\right\} \tag{247}$$

$$\Gamma^{(0,0)}_{(1)\,\pi\pi} = -\mathcal{K}^{(0,0)}_{\pi\pi|\pi\pi}\left[\frac{1}{2}\,\bar{\Omega}^S_{\pi\pi}\right]\, \Gamma^{(0,0)}_{(0)\,\pi\pi} - \mathcal{K}^{(0,0)}_{\pi\pi|KK}\left[\frac{1}{2}\,\bar{\Omega}^S_{KK}\right]\, \Gamma^{(0,0)}_{(0)\,KK} - \mathcal{K}^{(0,0)}_{\pi\pi|88}\left[\frac{1}{2}\,\bar{\Omega}^S_{88}\right]\, \Gamma^{(0,0)}_{(0)\,88} \tag{248}$$

$$\Gamma^{(0,0)}_{(1)\,\pi\pi} = -\mathcal{K}^{(0,0)}_{\pi\pi|KK}\left[\frac{1}{2}\,\bar{\Omega}^S_{\pi\pi}\right]\, \Gamma^{(0,0)}_{(0)\,\pi\pi} - \mathcal{K}^{(0,0)}_{KK|KK}\left[\frac{1}{2}\,\bar{\Omega}^S_{KK}\right]\, \Gamma^{(0,0)}_{(0)\,KK} - \mathcal{K}^{(0,0)}_{KK|88}\left[\frac{1}{2}\,\bar{\Omega}^S_{88}\right]\, \Gamma^{(0,0)}_{(0)\,88} \tag{249}$$

$$\Gamma^{(0,0)}_{(1)\,\pi\pi} = -\mathcal{K}^{(0,0)}_{\pi\pi|88}\left[\frac{1}{2}\,\bar{\Omega}^S_{\pi\pi}\right]\, \Gamma^{(0,0)}_{(0)\,\pi\pi} - \mathcal{K}^{(0,0)}_{KK|88}\left[\frac{1}{2}\,\bar{\Omega}^S_{KK}\right]\, \Gamma^{(0,0)}_{(0)\,KK} - \mathcal{K}^{(0,0)}_{88|88}\left[\frac{1}{2}\,\bar{\Omega}^S_{88}\right]\, \Gamma^{(0,0)}_{(0)\,88} \tag{250}$$

These results can be expressed in a matrix form, as

$$\Gamma^{(0,0)}_{(1)} = \begin{bmatrix}\Gamma^{(0,0)}_{(1)\,\pi\pi} \\ \Gamma^{(0,0)}_{(1)\,KK} \\ \Gamma^{(0,0)}_{(1)\,88}\end{bmatrix} = \begin{bmatrix}M_{11} & M_{12} & M_{13} \\ M_{21} & M_{22} & M_{23} \\ M_{31} & M_{32} & M_{33}\end{bmatrix}\, \begin{bmatrix}\Gamma^{(0,0)}_{(0)\,\pi\pi} \\ \Gamma^{(0,0)}_{(0)\,KK} \\ \Gamma^{(0,0)}_{(0)\,88}\end{bmatrix} = M^{(0,0)}\, \Gamma^{(0,0)}_{(0)} \tag{251}$$

with

$$M_{11} = -\mathcal{K}^{(0,0)}_{\pi\pi|\pi\pi}\left[(1/2)\,\bar{\Omega}^{S}_{\pi\pi}\right] \tag{252}$$

$$M_{12} = -\mathcal{K}^{(0,0)}_{\pi\pi|KK}\left[(1/2)\,\bar{\Omega}^{S}_{KK}\right] \tag{253}$$

$$M_{13} = -\mathcal{K}^{(0,0)}_{\pi\pi|88}\left[(1/2)\,\bar{\Omega}^{S}_{88}\right] \tag{254}$$

$$M_{21} = -\mathcal{K}^{(0,0)}_{\pi\pi|KK}\left[(1/2)\,\bar{\Omega}^{S}_{\pi\pi}\right] \tag{255}$$

$$M_{22} = -\mathcal{K}^{(0,0)}_{KK|KK}\left[(1/2)\,\bar{\Omega}^{S}_{KK}\right] \tag{256}$$

$$M_{23} = -\mathcal{K}^{(0,0)}_{KK|88}\left[(1/2)\,\bar{\Omega}^{S}_{88}\right] \tag{257}$$

$$M_{31} = -\mathcal{K}^{(0,0)}_{\pi\pi|88}\left[(1/2)\,\bar{\Omega}^{S}_{\pi\pi}\right] \tag{258}$$

$$M_{32} = -\mathcal{K}^{(0,0)}_{KK|88}\left[(1/2)\,\bar{\Omega}^{S}_{KK}\right] \tag{259}$$

$$M_{33} = -\mathcal{K}^{(0,0)}_{88|88}\left[(1/2)\,\bar{\Omega}^{S}_{88}\right] \tag{260}$$

Eq.(330) can be generalized to

$$\Gamma^{(0,0)}_{(n+1)} = M^{(0,0)}\;\Gamma^{(o,0)}_{(n)} = \left[M^{(0,0)}\right]^{n+1}\;\Gamma^{(0,0)}_{(0)} \tag{261}$$

and the full expansion in the number of loops is given by

$$\begin{aligned} S^{(0,0)}\,\Gamma^{(0,0)}_{(0)} &= \Gamma^{(0,0)}_{(0)} + \left[M^{(0,0)}\right]^{1}\;\Gamma^{(0,0)}_{(0)} + \left[M^{(1,1)}\right]^{2}\;\Gamma^{(0,0)}_{(0)} + \cdots \\ &= \left[1 + M^{(0,0)}\,S^{(0,0)}\right]\;\Gamma^{(0,0)}_{(0)} \end{aligned} \tag{262}$$

This yields

$$S^{(0,0)} = \left[1 + M^{(0,0)}\,S^{(0,0)}\right] \quad \rightarrow \quad \left[1 - M^{(0,0)}\right]S^{(0,0)} = 1 \tag{263}$$

and

$$S^{(0,0)} = \left[1 - M^{(0,0)}\right]^{-1} \tag{264}$$

$$= \frac{1}{\det(1-M)}$$

$$\times \begin{bmatrix} [(1-M_{22})(1-M_{33})-M_{23}M_{32}] & [M_{12}(1-M_{33})+M_{13}M_{32}] & [M_{13}(1-M_{22})+M_{12}M_{23}] \\ [M_{21}(1-M_{33})+M_{23}M_{31}] & [(1-M_{11})(1-M_{33})-M_{13}M_{31}] & [M_{23}(1-M_{11})+M_{13}M_{21}] \\ [M_{31}(1-M_{22})+M_{21}M_{32}] & [M_{32}(1-M_{11})+M_{12}M_{31}] & [(1-M_{11})(1-M_{22})-M_{12}M_{21}] \end{bmatrix}$$

with

$$\begin{aligned} \det(1-M) &= (1-M_{11})\,(1-M_{22})\,(1-M_{33}) \\ &-(1-M_{11})\,M_{23}\,M_{32} - (1-M_{22})\,M_{13}\,M_{31} - (1-M_{33})\,M_{12}\,M_{21} \\ &-M_{12}\,M_{23}\,M_{31} - M_{21}\,M_{32}\,M_{13} \end{aligned} \tag{265}$$

Calling $\bar{\Gamma}^{(0,0)} = S^{(0,0)}\,\Gamma^{(0,0)}_{(0)}$, one has

$$\begin{aligned}
\bar{\Gamma}^{(0,0)}_{\pi\pi} &= \frac{1}{\det(1-M)}\Big\{[(1-M_{22})(1-M_{33})-M_{23}M_{32}]\,\Gamma^{(0,0)}_{(0)\,\pi\pi} + [M_{12}(1-M_{33})+M_{13}M_{32}]\,\Gamma^{(0,0)}_{(0)\,KK} \\
&+ [M_{13}(1-M_{22})+M_{12}M_{23}]\,\Gamma^{(0,0)}_{(0)\,88}\Big\} \qquad (266)\\
\bar{\Gamma}^{(0,0)}_{KK} &= \frac{1}{\det(1-M)}\Big\{[M_{21}(1-M_{33})+M_{23}M_{31}]\,\Gamma^{(0,0)}_{(0)\,\pi\pi} + [(1-M_{11})(1-M_{33})-M_{13}M_{31}]\,\Gamma^{(0,0)}_{(0)\,KK} \\
&+ [M_{23}(1-M_{11})+M_{13}M_{21}]\,\Gamma^{(0,0)}_{(0)\,88}\Big\} \qquad (267)\\
\bar{\Gamma}^{(0,0)}_{88} &= \frac{1}{\det(1-M)}\Big\{[M_{31}(1-M_{22})+M_{21}M_{32}]\,\Gamma^{(0,0)}_{(0)\,\pi\pi} + [M_{32}(1-M_{11})+M_{12}M_{31}]\,\Gamma^{(0,0)}_{(0)\,KK} \\
&+ [(1-M_{11})(1-M_{22})-M_{12}M_{21}]\,\Gamma^{(0,0)}_{(0)\,88}\Big\} \qquad (268)
\end{aligned}$$

The full amplitude is then given by

$$\langle\, S(K_3^+)|\, T^{(0,0)}\,|\, D\,\rangle = \Big\{\bar{\Gamma}^{(0,0)}_{\pi\pi}\,\langle\, S^{\pi\pi}| + \bar{\Gamma}^{(0,0)}_{KK}\,\langle\, S^{KK}| + \bar{\Gamma}^{(0,0)}_{88}\,\langle\, S^{88}|\Big\} \qquad (269)$$

Using eq.(196), one has

$$\langle\, K_1^- K_2^+(K_3^+)|\, T^{(0.0)}\,|\, D\,\rangle = -\,\frac{1}{2}\,\bar{\Gamma}^{(0,0)}_{KK} \qquad (270)$$

In order to avoid double counting, one subtracts the contribution already included in the non-resonant term and finds

$$\langle\, K_1^- K_2^+(K_3^+)|\, T^{(0,0)}\,|\, D\,\rangle = -\,\frac{1}{2}\,\Big[\bar{\Gamma}^{(0,0)}_{KK} - \Gamma^{(0,0)}_{c|KK}\Big] \qquad (271)$$

The full production amplitude for the process $D^+ \to K^-\,K^+\,K^+$ is given by

$$\begin{aligned}
\langle\, K_1^- K_2^+ K_3^+|\, T\,|\, D\,\rangle &= \langle\, K_1^- K_2^+ K_3^+|\, T_c\,|\, D\,\rangle \\
&+ \big[\langle\, K_1^- K_2^+(K_3^+)|\, T^{(1,1)}\,|\, D\,\rangle + \langle\, K_1^- K_2^+(K_3^+)|\, T^{(1,0)}\,|\, D\,\rangle \\
&+ \langle\, K_1^- K_2^+(K_3^+)|\, T^{(0,1)}\,|\, D\,\rangle + \langle\, K_1^- K_2^+(K_3^+)|\, T^{(0,0)}\,|\, D\,\rangle \\
&+ (2 \leftrightarrow 3)\big] \qquad (272)
\end{aligned}$$

where the partial contributions are given by
$T_c \to$ eq.(153) , $T^{(1,1)} \to$ eq.(291) , $T^{(1,0)} \to$ eq.(305) , $T^{(1,1)} \to$ eq.(324) , $T^{(1,1)} \to$ eq.(350)
.

H.1 production amplitude $J = 1$, $I = 1$

The tree level amplitude is given by Eqs. 197-199. The one-loop contribution is obtained with the help of the result

$$\int \frac{d^4\ell}{(2\pi)^4} \, \frac{Q\cdot(p_c - p_d)\,(t-u)}{[p_c^2 - M_x^2]\,[p_d^2 - M_x^2]} \;=\; -i\,Q\cdot(p_a - p_b)\,\bar{\Omega}^P_{xx} \tag{273}$$

and reads

$$\langle\, V_3\,(K^+)\,|\,T^{(1,1)}_{(1)}\,|\,D\,\rangle = Q\cdot(p_a - p_b)\,\left\{ i\,\Gamma^{(1,1)}_{(1)\,\pi\pi}\,\langle\, V_3^{\pi\pi}| + i\,\Gamma^{(1,1)}_{(1)\,KK}\,\langle\, V_3^{KK}| \right\} \tag{274}$$

$$\Gamma^{(1,1)}_{(1)\,\pi\pi} = -\mathcal{K}^{(1,1)}_{\pi\pi|\pi\pi}\left[\frac{1}{2}\,\bar{\Omega}^P_{\pi\pi}\right]\Gamma^{(1,1)}_{(0)\,\pi\pi} - \mathcal{K}^{(1,1)}_{\pi\pi|KK}\left[\frac{1}{2}\,\bar{\Omega}^P_{KK}\right]\,\Gamma^{(1,1)}_{(0)\,KK} \tag{275}$$

$$\Gamma^{(1,1)}_{(1)\,KK} = -\mathcal{K}^{(1,1)}_{\pi\pi|KK}\left[\frac{1}{2}\,\bar{\Omega}^P_{\pi\pi}\right]\,\Gamma^{(1,1)}_{(0)\,\pi\pi} - \mathcal{K}^{(1,1)}_{KK|KK}\left[\frac{1}{2}\,\bar{\Omega}^P_{KK}\right]\,\Gamma^{(1,1)}_{(0)\,KK} \tag{276}$$

These results can be expressed in a matrix form, as

$$\Gamma^{(1,1)}_{(1)} = \begin{bmatrix} \Gamma^{(1,1)}_{(1)\,\pi\pi} \\ \Gamma^{(1,1)}_{(1)\,KK} \end{bmatrix} = \begin{bmatrix} M_{11} & M_{12} \\ M_{21} & M_{22} \end{bmatrix} \begin{bmatrix} \Gamma^{(1,1)}_{(0)\,\pi\pi} \\ \Gamma^{(1,1)}_{(0)\,KK} \end{bmatrix} = M^{(1,1)}\,\Gamma^{(1,1)}_{(0)} \tag{277}$$

with

$$M_{11} = -\mathcal{K}^{(1,1)}_{\pi\pi|\pi\pi}\left[\frac{1}{2}\,\bar{\Omega}^P_{\pi\pi}\right] \tag{278}$$

$$M_{12} = -\mathcal{K}^{(1,1)}_{\pi\pi|KK}\left[\frac{1}{2}\,\bar{\Omega}^P_{KK}\right] \tag{279}$$

$$M_{21} = -\mathcal{K}^{(1,1)}_{\pi\pi|KK}\left[\frac{1}{2}\,\bar{\Omega}^P_{\pi\pi}\right] \tag{280}$$

$$M_{22} = -\mathcal{K}^{(1,1)}_{KK|KK}\left[\frac{1}{2}\,\bar{\Omega}^P_{KK}\right] \tag{281}$$

Eq.(277) can be generalized to

$$\Gamma^{(1,1)}_{(n+1)} = M^{(1,1)}\,\Gamma^{(1,1)}_{(n)} = \left[M^{(1,1)}\right]^{n+1}\,\Gamma^{(1,1)}_{(0)} \tag{282}$$

and the full expansion in the number of loops is given by

$$\begin{aligned} S^{(1,1)}\,\Gamma^{(1,1)}_{(0)} \;&=\; \Gamma^{(1,1)}_{(0)} + \left[M^{(1,1)}\right]^1\,\Gamma^{(1,1)}_{(0)} + \left[M^{(1,1)}\right]^2\,\Gamma^{(1,1)}_{(0)} + \cdots \\ &=\; \left[1 + M^{(1,1)}\,S^{(1,1)}\right]\,\Gamma^{(1,1)}_{(0)} \end{aligned} \tag{283}$$

This yields

$$S^{(1,1)} = \left[1 + M^{(1,1)}\,S^{(1,1)}\right] \quad\rightarrow\quad \left[1 - M^{(1,1)}\right]S^{(1,1)} = 1 \tag{284}$$

and

$$
\begin{aligned}
S^{(1,1)} &= \left[1 - M^{(1,1)}\right]^{-1} \\
&= \frac{1}{(1-M_{11})\,(1-M_{22}) - M_{12}\,M_{21}} \begin{bmatrix} (1-M_{22}) & M_{12} \\ M_{21} & (1-M_{11}) \end{bmatrix}
\end{aligned} \tag{285}
$$

Calling $\bar{\Gamma}^{(1,1)} = S^{(1,1)}\,\Gamma^{(1,1)}_{(0)}$, one has

$$
\bar{\Gamma}^{(1,1)}_{\pi\pi} = \frac{m_{12}^2 - m_\rho^2}{D_\rho(m_{12}^2)} \left[(1-M_{22})\,\Gamma^{(1,1)}_{(0)\,\pi\pi} + M_{12}\,\Gamma^{(1,1)}_{(0)\,KK}\right] \tag{286}
$$

$$
\bar{\Gamma}^{(1,1)}_{KK} = \frac{m_{12}^2 - m_\rho^2}{D_\rho(m_{12}^2)} \left[M_{21}\,\Gamma^{(1,1)}_{(0)\,\pi\pi} + (1-M_{11})\,\Gamma^{(1,1)}_{(0)\,KK}\right] \tag{287}
$$

$$
D_\rho = (m_{12}^2 - m_\rho^2)\,\left[(1-M_{11})\,(1-M_{22}) - M_{12}\,M_{21}\right] \tag{288}
$$

The full amplitude is then given by

$$
\langle\, V_3(K_3^+)|\, T^{(1,1)}\,|\, D\,\rangle = Q\cdot(p_a - p_b)\,\left\{ i\,\bar{\Gamma}^{(1,1)}_{\pi\pi}\,\langle\, V_3^{\pi\pi}| + i\,\bar{\Gamma}^{(1,1)}_{KK}\,\langle\, V_3^{KK}|\right\} \tag{289}
$$

Using eq.(196) and $Q\cdot(p_a - p_b) = (m_{13}^2 - m_{23}^2)/2$, one has

$$
\langle\, K_1^- K_2^+(K_3^+)|\, T^{(1,1)}\,|\, D\,\rangle = -\,\frac{1}{4}\,\bar{\Gamma}^{(1,1)}_{KK}\,(m_{13}^2 - m_{23}^2) \tag{290}
$$

In order to avoid double counting, one subtracts the contribution already included in the non-resonant term and finds

$$
\langle\, K_1^- K_2^+(K_3^+)|\, T^{(1,1)}\,|\, D\,\rangle = -\,\frac{1}{4}\,\left[\bar{\Gamma}^{(1,1)}_{KK} - \Gamma^{(1,1)}_{c|KK}\right]\,(m_{13}^2 - m_{23}^2) \tag{291}
$$

H.2 production amplitude $J = 1,\ I = 0$

The tree level amplitude is given by Eqs. 201-202. The one-loop contribution is obtained with the help of the result

$$\int \frac{d^4\ell}{(2\pi)^4}\ \frac{Q\cdot(p_c-p_d)\ (t-u)}{[p_c^2-M_x^2]\ [p_d^2-M_x^2]}\ =\ -i\,Q\cdot(p_a-p_b)\ \bar{\Omega}^P_{xx} \tag{292}$$

and read

$$\langle\, V_8\,(K^+)\,|\,T^{(1,0)}_{(1)}\,|\,D\,\rangle = Q\cdot(p_a-p_b)\ \left\{ i\,\Gamma^{(1,0)}_{(1)\,KK}\,\langle\, V_8^{KK}|\right\} \tag{293}$$

$$\Gamma^{(1,0)}_{(1)\,KK} = -\mathcal{K}^{(1,0)}_{KK|KK}\left[\frac{1}{2}\,\bar{\Omega}^P_{KK}\right]\ \Gamma^{(1,0)}_{(0)\,KK} \tag{294}$$

These results can be reexpressed as

$$\Gamma^{(1,0)}_{(1)} = M\ \Gamma^{(1,0)}_{(0)} \tag{295}$$

with

$$M = -\mathcal{K}^{(1,0)}_{KK|KK}\left[\frac{1}{2}\,\bar{\Omega}^P_{KK}\right] \tag{296}$$

Eq.(295) can be generalized to

$$\Gamma^{(1,0)}_{(n+1)} = M\ \Gamma^{(1,0)}_{(n)} = [M]^{n+1}\ \Gamma^{(1,0)}_{(0)} \tag{297}$$

and the full expansion in the number of loops is given by

$$\begin{aligned} S^{(1,0)}\,\Gamma^{(1,0)}_{(0)} &= \Gamma^{(1,0)}_{(0)} + [M]^1\ \Gamma^{(1,0)}_{(0)} + [M]^2\ \Gamma^{(1,0)}_{(0)} + \cdots \\ &= \left[1 + M\,S^{(1,0)}\right]\ \Gamma^{(1,0)}_{(0)} \end{aligned} \tag{298}$$

This yields

$$S^{(1,0)} = \left[1 + M\,S^{(1,0)}\right] \quad\rightarrow\quad [1-M]\,S^{(1,0)} = 1 \tag{299}$$

and

$$S^{(1,0)}\ =\ \frac{1}{(1-M)} \tag{300}$$

Calling $\bar{\Gamma}^{(1,0)} = S^{(1,0)}\,\Gamma^{(1,0)}_{(0)}$, one has

$$\bar{\Gamma}^{(1,0)}_{KK} \;=\; \frac{m_{12}^2 - m_\phi^2}{D_\phi(m_{12}^2)}\,\Gamma^{(1,0)}_{(0)\,KK} \quad\to\quad \frac{D_\phi^{\pi\rho}}{D_\phi(m_{12}^2)}\,\Gamma^{(1,0)}_{(0)\,KK} \tag{301}$$

$$D_\phi \;=\; (m_{12}^2 - m_\rho^2)\,\left(1+\mathcal{K}^{(1,0)}_{KK|KK}\left[\frac{1}{2}\,\bar{\Omega}^P_{KK}\right]\right) \quad\to\quad D_\phi^{\pi\rho}\,\left\{1+\mathcal{K}^{(1,0)}_{KK|KK}\left[\frac{1}{2}\,\bar{\Omega}^P_{KK}\right]\right\} \tag{302}$$

The full amplitude is then given by

$$\langle\, V_8(K_3^+)|\, T^{(1,0)}\,|\, D\,\rangle = Q\cdot(p_a - p_b)\,\left\{i\,\bar{\Gamma}^{(1,0)}_{KK}\,\langle\, V_8^{KK}|\right\} \tag{303}$$

Using eq.(196) and $Q\cdot(p_a - p_b) = (m_{13}^2 - m_{23}^2)/2$, one has

$$\langle\, K_1^- K_2^+(K_3^+)|\, T^{(1,0)}\,|\, D\,\rangle = -\,\frac{1}{4}\,\bar{\Gamma}^{(1,0)}_{KK}\,(m_{13}^2 - m_{23}^2) \tag{304}$$

In order to avoid double counting, one subtracts the contribution already included in the non-resonant term and finds

$$\langle\, K_1^- K_2^+(K_3^+)|\, T^{(1,0)}\,|\, D\,\rangle = -\,\frac{1}{4}\,\left[\bar{\Gamma}^{(1,0)}_{KK} - \Gamma^{(1,0)}_{c|KK}\right]\,(m_{13}^2 - m_{23}^2) \tag{305}$$

H.3 production amplitude $J=0,\, I=1$

The tree level amplitude is given by Eqs. 204-206. The one-loop contribution is obtained with the help of the result

$$\int \frac{d^4\ell}{(2\pi)^4}\; \frac{1}{[p_c^2-M_x^2]\,[p_d^2-M_y^2]} \;=\; -i\,\bar{\Omega}^S_{xy} \tag{306}$$

and reads[T−32|12/4]

$$\langle\, U_3\,(K^+)\,|\,T^{(0,1)}_{(1)}\,|\,D\,\rangle = \Big\{\Gamma^{(0,1)}_{(1)\,\pi 8}\,\langle\, U_3^{\pi 8}| + \Gamma^{(0,1)}_{(1)\,KK}\,\langle\, U_3^{KK}|\Big\} \tag{307}$$

$$\Gamma^{(0,1)}_{(1)\,\pi 8} = -\mathcal{K}^{(0,1)}_{\pi 8|\pi 8}\left[\bar{\Omega}^S_{\pi 8}\right]\,\Gamma^{(0,1)}_{(0)\,\pi 8} - \mathcal{K}^{(0,1)}_{\pi 8|KK}\left[\frac{1}{2}\,\bar{\Omega}^S_{KK}\right]\,\Gamma^{(0,1)}_{(0)\,KK} \tag{308}$$

$$\Gamma^{(0,1)}_{(1)\,KK} = -\mathcal{K}^{(0,1)}_{\pi 8|KK}\left[\bar{\Omega}^S_{\pi 8}\right]\,\Gamma^{(0,1)}_{(0)\,\pi 8} - \mathcal{K}^{(0,1)}_{KK|KK}\left[\frac{1}{2}\,\bar{\Omega}^S_{KK}\right]\,\Gamma^{(0,1)}_{(0)\,KK} \tag{309}$$

These results can be expressed in a matrix form, as

$$\Gamma^{(0,1)}_{(1)} = \begin{bmatrix}\Gamma^{(0,1)}_{(1)\,\pi 8}\\ \Gamma^{(0,1)}_{(1)\,KK}\end{bmatrix} = \begin{bmatrix}M_{11} & M_{12}\\ M_{21} & M_{22}\end{bmatrix}\,\begin{bmatrix}\Gamma^{(0,1)}_{(0)\,\pi 8}\\ \Gamma^{(0,1)}_{(0)\,KK}\end{bmatrix} = M^{(0,1)}\,\Gamma^{(0,1)}_{(0)} \tag{310}$$

with

$$M_{11} = -\mathcal{K}^{(0,1)}_{\pi 8|\pi 8}\left[\bar{\Omega}^S_{\pi 8}\right] \tag{311}$$

$$M_{12} = -\mathcal{K}^{(0,1)}_{\pi 8|KK}\left[(1/2)\,\bar{\Omega}^S_{KK}\right] \tag{312}$$

$$M_{21} = -\mathcal{K}^{(0,1)}_{\pi 8|KK}\left[\bar{\Omega}^S_{\pi 8}\right] \tag{313}$$

$$M_{22} = -\mathcal{K}^{(0,1)}_{KK|KK}\left[(1/2)\,\bar{\Omega}^S_{KK}\right] \tag{314}$$

Eq.(310) can be generalized to

$$\Gamma^{(0,1)}_{(n+1)} = M^{(0,1)}\,\Gamma^{(0,1)}_{(n)} = \left[M^{(0,1)}\right]^{n+1}\,\Gamma^{(0,1)}_{(0)} \tag{315}$$

and the full expansion in the number of loops is given by

$$\begin{aligned} S^{(0,1)}\,\Gamma^{(0,1)}_{(0)} &= \Gamma^{(0,1)}_{(0)} + \left[M^{(0,1)}\right]^1\,\Gamma^{(0,1)}_{(0)} + \left[M^{(0,1)}\right]^2\,\Gamma^{(0,1)}_{(0)} + \cdots \\ &= \left[1 + M^{(0,1)}\,S^{(0,1)}\right]\,\Gamma^{(0,1)}_{(0)} \end{aligned} \tag{316}$$

This yields

$$S^{(0,1)} = \left[1 + M^{(0,1)}\,S^{(0,1)}\right] \quad\rightarrow\quad \left[1 - M^{(0,1)}\right]S^{(0,1)} = 1 \tag{317}$$

and

$$\begin{aligned} S^{(0,1)} &= \left[1 - M^{(0,1)}\right]^{-1} \\ &= \frac{1}{(1-M_{11})\,(1-M_{22}) - M_{12}\,M_{21}}\begin{bmatrix}(1-M_{22}) & M_{12}\\ M_{21} & (1-M_{11})\end{bmatrix} \end{aligned} \tag{318}$$

Calling $\bar{\Gamma}^{(0,1)} = S^{(0,1)}\, G^{(0,1)}_{(0)}$, one has

$$\bar{\Gamma}^{(0,1)}_{\pi 8} = \frac{(m_{12}^2 - m_{a_0}^2)}{D_{a_0}(m_{12}^2)} \Big[(1-M_{22})\, \Gamma^{(0,1)}_{(0)\,\pi 8} + M_{12}\, \Gamma^{(0,1)}_{(0)\,KK} \Big] \tag{319}$$

$$\bar{\Gamma}^{(0,1)}_{KK} = \frac{(m_{12}^2 - m_{a_0}^2)}{D_{a_0}(m_{12}^2)} \Big[M_{21}\, \Gamma^{(0,1)}_{(0)\,\pi 8} + (1-M_{11})\, \Gamma^{(0,1)}_{(0)\,KK} \Big] \tag{320}$$

$$D_{a_0} = (m_{12}^2 - m_{a_0}^2)\, [(1-M_{11})\,(1-M_{22}) - M_{12}\, M_{21}] \tag{321}$$

The full amplitude is then given by

$$\langle\, U_3(K_3^+)|\, T^{(0,1)}\, |\, D\,\rangle = \Big\{ \bar{\Gamma}^{(0,1)}_{\pi 8}\, \langle\, U_3^{\pi 8}| + \bar{\Gamma}^{(0,1)}_{KK}\, \langle\, U_3^{KK}| \Big\} \tag{322}$$

Using eq.(196), one has

$$\langle\, K_1^- K_2^+(K_3^+)|\, T^{(0,1)}\, |\, D\,\rangle = -\,\frac{1}{2}\, \bar{\Gamma}^{(0,1)}_{KK} \tag{323}$$

In order to avoid double counting, one subtracts the contribution already included in the non-resonant term and finds

$$\langle\, K_1^- K_2^+(K_3^+)|\, T^{(0,1)}\, |\, D\,\rangle = -\,\frac{1}{2}\, \Big[\bar{\Gamma}^{(0,1)}_{KK} - \Gamma^{(0,1)}_{c|KK} \Big] \tag{324}$$

H.4 production amplitude $J = 0,\ I = 0$

The tree level amplitude is given by Eqs. 208-212. The one-loop contribution is obtained with the help of the result

$$\int \frac{d^4\ell}{(2\pi)^4}\ \frac{1}{[p_c^2 - M_x^2]\,[p_d^2 - M_x^2]}\ =\ -i\,\bar{\Omega}^P_{xx} \tag{325}$$

and reads

$$\langle\, S\,(K^+)\,|\,T^{(0,0)}_{(1)}\,|\,D\,\rangle = \left\{\Gamma^{(0,0)}_{(1)\,\pi\pi}\,\langle\, S^{\pi\pi}|\,+\,\Gamma^{(0,0)}_{(1)\,KK}\,\langle\, S^{KK}|\,+\,\Gamma^{(0,0)}_{(1)\,88}\,\langle\, S^{88}|\right\} \tag{326}$$

$$\Gamma^{(0,0)}_{(1)\,\pi\pi} = -\mathcal{K}^{(0,0)}_{\pi\pi|\pi\pi}\left[\frac{1}{2}\,\bar{\Omega}^S_{\pi\pi}\right]\,\Gamma^{(0,0)}_{(0)\,\pi\pi} - \mathcal{K}^{(0,0)}_{\pi\pi|KK}\left[\frac{1}{2}\,\bar{\Omega}^S_{KK}\right]\,\Gamma^{(0,0)}_{(0)\,KK} - \mathcal{K}^{(0,0)}_{\pi\pi|88}\left[\frac{1}{2}\,\bar{\Omega}^S_{88}\right]\,\Gamma^{(0,0)}_{(0)\,88} \tag{327}$$

$$\Gamma^{(0,0)}_{(1)\,\pi\pi} = -\mathcal{K}^{(0,0)}_{\pi\pi|KK}\left[\frac{1}{2}\,\bar{\Omega}^S_{\pi\pi}\right]\,\Gamma^{(0,0)}_{(0)\,\pi\pi} - \mathcal{K}^{(0,0)}_{KK|KK}\left[\frac{1}{2}\,\bar{\Omega}^S_{KK}\right]\,\Gamma^{(0,0)}_{(0)\,KK} - \mathcal{K}^{(0,0)}_{KK|88}\left[\frac{1}{2}\,\bar{\Omega}^S_{88}\right]\,\Gamma^{(0,0)}_{(0)\,88} \tag{328}$$

$$\Gamma^{(0,0)}_{(1)\,\pi\pi} = -\mathcal{K}^{(0,0)}_{\pi\pi|88}\left[\frac{1}{2}\,\bar{\Omega}^S_{\pi\pi}\right]\,\Gamma^{(0,0)}_{(0)\,\pi\pi} - \mathcal{K}^{(0,0)}_{KK|88}\left[\frac{1}{2}\,\bar{\Omega}^S_{KK}\right]\,\Gamma^{(0,0)}_{(0)\,KK} - \mathcal{K}^{(0,0)}_{88|88}\left[\frac{1}{2}\,\bar{\Omega}^S_{88}\right]\,\Gamma^{(0,0)}_{(0)\,88} \tag{329}$$

These results can be expressed in a matrix form, as

$$\Gamma^{(0,0)}_{(1)} = \begin{bmatrix}\Gamma^{(0,0)}_{(1)\,\pi\pi}\\ \Gamma^{(0,0)}_{(1)\,KK}\\ \Gamma^{(0,0)}_{(1)\,88}\end{bmatrix} = \begin{bmatrix}M_{11} & M_{12} & M_{13}\\ M_{21} & M_{22} & M_{23}\\ M_{31} & M_{32} & M_{33}\end{bmatrix}\,\begin{bmatrix}\Gamma^{(0,0)}_{(0)\,\pi\pi}\\ \Gamma^{(0,0)}_{(0)\,KK}\\ \Gamma^{(0,0)}_{(0)\,88}\end{bmatrix} = M^{(0,0)}\,\Gamma^{(0,0)}_{(0)} \tag{330}$$

with

$$M_{11} = -\mathcal{K}^{(0,0)}_{\pi\pi|\pi\pi}\left[(1/2)\,\bar{\Omega}^S_{\pi\pi}\right] \tag{331}$$

$$M_{12} = -\mathcal{K}^{(0,0)}_{\pi\pi|KK}\left[(1/2)\,\bar{\Omega}^S_{KK}\right] \tag{332}$$

$$M_{13} = -\mathcal{K}^{(0,0)}_{\pi\pi|88}\left[(1/2)\,\bar{\Omega}^S_{88}\right] \tag{333}$$

$$M_{21} = -\mathcal{K}^{(0,0)}_{\pi\pi|KK}\left[(1/2)\,\bar{\Omega}^S_{\pi\pi}\right] \tag{334}$$

$$M_{22} = -\mathcal{K}^{(0,0)}_{KK|KK}\left[(1/2)\,\bar{\Omega}^S_{KK}\right] \tag{335}$$

$$M_{23} = -\mathcal{K}^{(0,0)}_{KK|88}\left[(1/2)\,\bar{\Omega}^S_{88}\right] \tag{336}$$

$$M_{31} = -\mathcal{K}^{(0,0)}_{\pi\pi|88}\left[(1/2)\,\bar{\Omega}^S_{\pi\pi}\right] \tag{337}$$

$$M_{32} = -\mathcal{K}^{(0,0)}_{KK|88}\left[(1/2)\,\bar{\Omega}^S_{KK}\right] \tag{338}$$

$$M_{33} = -\mathcal{K}^{(0,0)}_{88|88}\left[(1/2)\,\bar{\Omega}^S_{88}\right] \tag{339}$$

Eq.(330) can be generalized to

$$\Gamma^{(0,0)}_{(n+1)} = M^{(0,0)}\,\Gamma^{(o,0)}_{(n)} = \left[M^{(0,0)}\right]^{n+1}\,\Gamma^{(0,0)}_{(0)} \tag{340}$$

and the full expansion in the number of loops is given by

$$\begin{aligned} S^{(0,0)}\,\Gamma^{(0,0)}_{(0)} &= \Gamma^{(0,0)}_{(0)} + \left[M^{(0,0)}\right]^1\,\Gamma^{(0,0)}_{(0)} + \left[M^{(1,1)}\right]^2\,\Gamma^{(0,0)}_{(0)} + \cdots \\ &= \left[1 + M^{(0,0)}\,S^{(0,0)}\right]\,\Gamma^{(0,0)}_{(0)} \end{aligned} \tag{341}$$

This yields

$$S^{(0,0)} = \left[1 + M^{(0,0)}\,S^{(0,0)}\right] \quad \rightarrow \quad \left[1 - M^{(0,0)}\right] S^{(0,0)} = 1 \tag{342}$$

and

$$S^{(0,0)} = \left[1 - M^{(0,0)}\right]^{-1} \tag{343}$$

$$= \frac{1}{\det(1-M)}$$

$$\times \begin{bmatrix} [(1-M_{22})(1-M_{33})-M_{23}M_{32}] & [M_{12}(1-M_{33})+M_{13}M_{32}] & [M_{13}(1-M_{22})+M_{12}M_{23}] \\ [M_{21}(1-M_{33})+M_{23}M_{31}] & [(1-M_{11})(1-M_{33})-M_{13}M_{31}] & [M_{23}(1-M_{11})+M_{13}M_{21}] \\ [M_{31}(1-M_{22})+M_{21}M_{32}] & [M_{32}(1-M_{11})+M_{12}M_{31}] & [(1-M_{11})(1-M_{22})-M_{12}M_{21}] \end{bmatrix}$$

with

$$\begin{aligned} &\det(1-M) = (1-M_{11})\,(1-M_{22})\,(1-M_{33}) \\ &-(1-M_{11})\,M_{23}\,M_{32} - (1-M_{22})\,M_{13}\,M_{31} - (1-M_{33})\,M_{12}\,M_{21} \\ &-M_{12}\,M_{23}\,M_{31} - M_{21}\,M_{32}\,M_{13} \end{aligned} \tag{344}$$

Calling $\bar{\Gamma}^{(0,0)} = S^{(0,0)}\,\Gamma^{(0,0)}_{(0)}$, one has

$$\begin{aligned} \bar{\Gamma}^{(0,0)}_{\pi\pi} &= \frac{1}{\det(1-M)}\Big\{[(1-M_{22})(1-M_{33})-M_{23}M_{32}]\,\Gamma^{(0,0)}_{(0)\,\pi\pi} + [M_{12}(1-M_{33})+M_{13}M_{32}]\,\Gamma^{(0,0)}_{(0)\,KK} \\ &+ [M_{13}(1-M_{22})+M_{12}M_{23}]\,\Gamma^{(0,0)}_{(0)\,88}\Big\} \end{aligned} \tag{345}$$

$$\begin{aligned} \bar{\Gamma}^{(0,0)}_{KK} &= \frac{1}{\det(1-M)}\Big\{[M_{21}(1-M_{33})+M_{23}M_{31}]\,\Gamma^{(0,0)}_{(0)\,\pi\pi} + [(1-M_{11})(1-M_{33})-M_{13}M_{31}]\,\Gamma^{(0,0)}_{(0)\,KK} \\ &+ [M_{23}(1-M_{11})+M_{13}M_{21}]\,\Gamma^{(0,0)}_{(0)\,88}\Big\} \end{aligned} \tag{346}$$

$$\begin{aligned} \bar{\Gamma}^{(0,0)}_{88} &= \frac{1}{\det(1-M)}\Big\{[M_{31}(1-M_{22})+M_{21}M_{32}]\,\Gamma^{(0,0)}_{(0)\,\pi\pi} + [M_{32}(1-M_{11})+M_{12}M_{31}]\,\Gamma^{(0,0)}_{(0)\,KK} \\ &+ [(1-M_{11})(1-M_{22})-M_{12}M_{21}]\,\Gamma^{(0,0)}_{(0)\,88}\Big\} \end{aligned} \tag{347}$$

The full amplitude is then given by

$$\langle\, S(K_3^+)|\, T^{(0,0)}\,|\, D\,\rangle = \left\{\bar{\Gamma}^{(0,0)}_{\pi\pi}\,\langle\, S^{\pi\pi}| + \bar{\Gamma}^{(0,0)}_{KK}\,\langle\, S^{KK}| + \bar{\Gamma}^{(0,0)}_{88}\,\langle\, S^{88}|\right\} \tag{348}$$

Using eq.(196), one has

$$\langle\, K_1^- K_2^+(K_3^+)|\, T^{(0.0)}\,|\, D\,\rangle = -\,\frac{1}{2}\,\bar{\Gamma}^{(0,0)}_{KK} \tag{349}$$

In order to avoid double counting, one subtracts the contribution already included in the non-resonant term and finds

$$\langle\, K_1^- K_2^+(K_3^+)|\, T^{(0,0)}\,|\, D\,\rangle = -\,\frac{1}{2}\,\left[\bar{\Gamma}^{(0,0)}_{KK} - \Gamma^{(0,0)}_{c|KK}\right] \tag{350}$$

I Individual Resonances

This Appendix contains Monte Carlo simulations of the Dalitz Plot for each individual resonance contribution, obtained by the squared modulus of the corresponding amplitude.

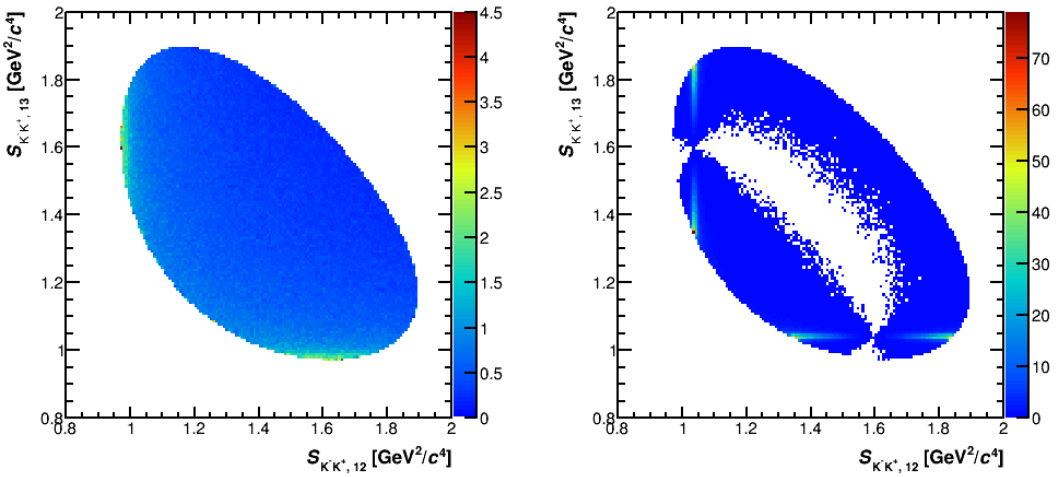

Figure 98: Dalitz Plot of the $f_0(980)$ resonance on the left and ϕ on the right.

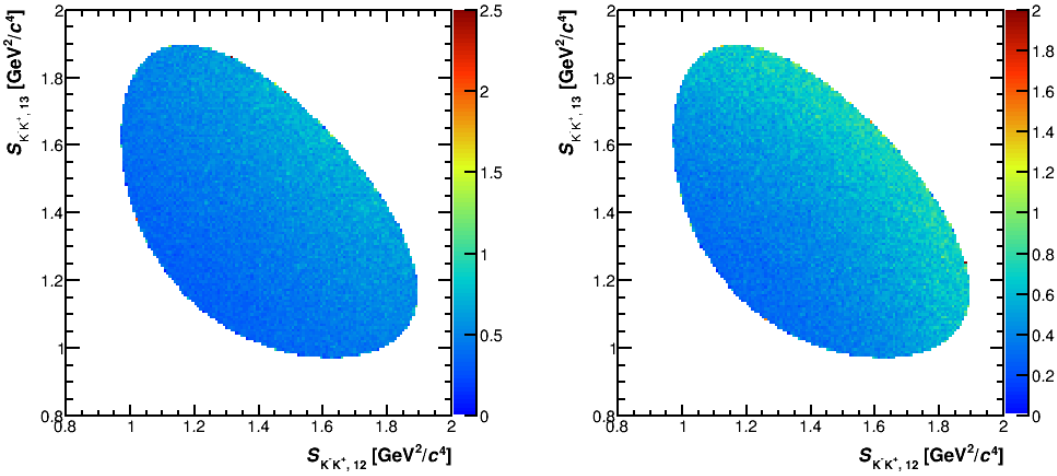

Figure 99: Dalitz Plot of the $f_0(1370)$ resonance from Model 2 on the left and $a_0(1450)$ on the right.

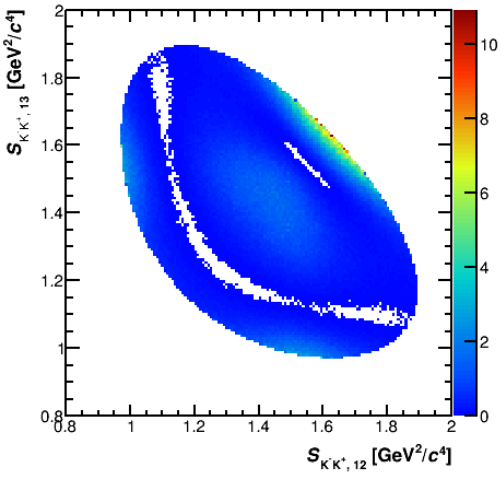

Figure 100: Dalitz Plot of the $f_2(1270)$ resonance

References

[1] J. Gasser and H. Leutwyler. Chiral Perturbation Theory to One Loop. *Annals Phys.*, 158:142, 1984.

[2] G. Ecker, J. Gasser, A. Pich, and E. de Rafael. The Role of Resonances in Chiral Perturbation Theory. *Nucl. Phys.*, B321:311–342, 1989.

[3] Rio Charm Group. Rio+. `https://github.com/danielsibemol/RioRep/tree/master/Rio`, 2016.

[4] T. P. Cheng and L. F. Li. *Gauge Theory of Elementary Particle Physics*. 1984.

[5] C. S. Wu, E. Ambler, R. W. Hayward, D. D. Hoppes, and R. P. Hudson. Experimental test of parity conservation in beta decay. *Phys. Rev.*, 105:1413–1415, Feb 1957.

[6] R. P. Feynman and Murray Gell-Mann. Theory of Fermi interaction. *Phys. Rev.*, 109:193–198, 1958.

[7] Julian S. Schwinger. A Theory of the Fundamental Interactions. *Annals Phys.*, 2:407–434, 1957.

[8] Sheldon Lee Glashow. *The Vector Meson in Elementary Particle Decay*. PhD thesis, Harvard U., 1959.

[9] S. L. Glashow. Partial Symmetries of Weak Interactions. *Nucl. Phys.*, 22:579–588, 1961.

[10] Steven Weinberg. A Model of Leptons. *Phys. Rev. Lett.*, 19:1264–1266, 1967.

[11] Abdus Salam. Weak and Electromagnetic Interactions. *Conf. Proc.*, C680519:367–377, 1968.

[12] Gerard 't Hooft. Gauge Theory and Renormalization. *NATO Sci. Ser. B*, 352:37–53, 1996.

[13] Y. Nir. Flavour Physics and CP Violation. In *Proceedings, 7th CERN–Latin-American School of High-Energy Physics (CLASHEP2013): Arequipa, Peru, March 6-19, 2013*, pages 123–156, 2015.

[14] M. Gell-Mann. The interpretation of the new particles as displaced charge multiplets. *Il Nuovo Cimento (1955-1965)*, 4(2):848–866, 1956.

[15] K. Nishijima. Charge Independence Theory of V Particles. *Progress of Theoretical Physics*, 13:285–304, March 1955.

[16] K. A. Olive et al. The Review of Particle Physics, Note on scan. *Chin. Phys. C*, 38:090001, 2015.

[17] Ling-Lie Chau. Quark Mixing in Weak Interactions. *Phys. Rept.*, 95:1–94, 1983.

[18] B. Kubis. Lectures at Hadron Physics Summer School 2016 (HPSS2016). 2016.

[19] Stefan Scherer and Matthias R. Schindler. A Chiral perturbation theory primer. 2005.

[20] Steven Weinberg. Phenomenological Lagrangians. *Physica*, A96:327–340, 1979.

[21] Ralph Assmann, Mike Lamont, and Steve Myers. A brief history of the lep collider. *Nuclear Physics B - Proceedings Supplements*, 109(2):17 – 31, 2002.

[22] Fabienne Marcastel. CERN's Accelerator Complex. La chaîne des accélérateurs du CERN. Oct 2013. General Photo.

[23] Roel Aaij et al. Prompt charm production in pp collisions at $\sqrt{s} = 7$ TeV. *Nucl. Phys. B*, 871(arXiv:1302.2864. LHCB-PAPER-2012-041. CERN-PH-EP-2013-009):1–20. 27 p, Feb 2013.

[24] Roel Aaij et al. Measurement of $\sigma(pp \to b\bar{b}X)$ at $\sqrt{s}$=7 TeV in the forward region. *Phys. Lett. B*, 694(arXiv:1009.2731. CERN-PH-EP-2010-029. LHCb-PAPER-2010-002):209–216. 16 p, Sep 2010. Comments: 11 pages, 5 figures, submitted to Physics Lett. B.

[25] LHC-B: A dedicated LHC collider beauty experiment for precision measurements of CP-violation. Letter of intent. 1995.

[26] Rolf Lindner. LHCb layout_2. LHCb schema_2. LHCb Collection., Feb 2008.

[27] A. Augusto Alves, Jr. et al. The LHCb Detector at the LHC. *JINST*, 3:S08005, 2008.

[28] LHCb collaboration. St material for publications. *http://lhcb.physik.uzh.ch/ST/public/material/index.php*.

[29] R. Fruhwirth. Application of Kalman filtering to track and vertex fitting. *Nucl. Instrum. Meth.*, A262:444–450, 1987.

[30] Roel Aaij et al. Measurement of the track reconstruction efficiency at LHCb. *JINST*, 10(02):P02007, 2015.

[31] M. Adinolfi et al. Performance of the LHCb RICH detector at the LHC. *Eur. Phys. J.*, C73:2431, 2013.

[32] R. Aaij et al. Prompt charm production in pp collisions at. *Nuclear Physics B*, 871(1):1 – 20, 2013.

[33] Michael E. Peskin and Daniel V. Schroeder. *An Introduction to quantum field theory*. 1995.

[34] R.H. Dalitz. Cxii. on the analysis of -meson data and the nature of the -meson. *The London, Edinburgh, and Dublin Philosophical Magazine and Journal of Science*, 44(357):1068–1080, 1953.

[35] David J. Herndon, Paul Söding, and Roger J. Cashmore. Generalized isobar model formalism. *Phys. Rev. D*, 11:3165–3182, Jun 1975.

[36] J. Blatt and J. Weisskopf. *Theoretical Nuclear Physics*. John Wiley and Sons, 1952.

[37] C. Zemach. Three-Pion Decays of Unstable Particles. *Phys. Rev. B*, 133:1201, 1964.

[38] S.M. Flatté. Coupled-channel analysis of the $\pi\eta$ and K$\bar{\text{K}}$$K$ systems near K$\bar{\text{K}}$$K$ threshold. *Physics Letters B*, 63:224, 1976.

[39] Jorge H. Alvarenga Nogueira et al. Summary of the 2015 LHCb workshop on multi-body decays of D and B mesons. 2016.

[40] M. Battaglieri et al. Analysis Tools for Next-Generation Hadron Spectroscopy Experiments. *Acta Phys. Polon.*, B46:257, 2015.

[41] Johannes Albrecht, V. V. Gligorov, G. Raven, and S. Tolk. Performance of the LHCb High Level Trigger in 2012. *J. Phys. Conf. Ser.*, 513:012001, 2014.

[42] Johannes Albrecht, V. V. Gligorov, G. Raven, and S. Tolk. Performance of the LHCb High Level Trigger in 2012. *J. Phys. Conf. Ser.*, 513:012001, 2014.

[43] Andreas Hocker et al. TMVA - Toolkit for Multivariate Data Analysis. *PoS*, ACAT:040, 2007.

[44] D. Craig, T. Gershon, T. Latham, and M. Whitehead. Dalitz plot analysis of $B_s^0 \to \bar{D}^0 K^- \pi^+$. *LHCb-ANA*, 2013-014, 2013.

[45] T. Latham et al. `Laura++` dalitz plot fitting package.

[46] E.M. Aitala et al. Study of the Decay $D_s^+ \to \pi^-\pi^+\pi^+$ and Measurement of f_0 Masses and Widths. *Phys. Rev. Lett*, 86:765, 2001.

[47] E.M. Aitala et al. Experimental Evidence for a Light and Broad Scalar Resonance in $D_s^+ \to \pi^-\pi^+\pi^+$ Decay. *Phys. Rev. Lett*, 86:770, 2001.

[48] J.M. Link et al. Dalitz plot analysis of $D^+_{(s)}$ and D^+ decay to $\pi^+\pi^-\pi^+$ using the K matrix formalism. *Phys.Lett. B*, 585:200, 2004.

[49] B. Aubert et al. Dalitz plot analysis of $D^+_s \to \pi^-\pi^+\pi^+$. *Phys. Rev. D*, 79:032003, 2009.

[50] A. Garmash et al. Evidence for Large Direct CP Violation in $B^\pm \to \rho(770)^0 K^\mp$ from Analysis of Three-Body Charmless $B^\pm \to K^\mp\pi^\pm\pi^\pm$ Decays . *Phys. Rev. Lett*, 96:251803, 2006.

[51] K. A. Olive et al. Review of Particle Physics. *Chin. Phys. C*, 38:090001, 2014.

[52] M. Ablikim et al. Resonances in $J/\psi \to \phi\pi\hat{} + \pi^-$ and $\phi K\hat{} + K^-$. *Phys.Lett. B*, 607:243, 2005.

[53] P. C. Magalhaes, M. R. Robilotta, K. S. F. F. Guimaraes, T. Frederico, W. de Paula, I. Bediaga, A. C. dos Reis, C. M. Maekawa, and G. R. S. Zarnauskas. Towards three-body unitarity in $D^+ \to K^-\pi^+\pi^+$. *Phys. Rev.*, D84:094001, 2011.

[54] P. C. Magalhães and M. R. Robilotta. $D^+ \to K^-\pi^+\pi^+$ - the weak vector current. *Phys. Rev.*, D92(9):094005, 2015.

[55] R. T. Aoude, P. C. Magalhães, A. C. dos Reis, and M. R. Robilotta. Multi-Meson Model applied to $D^+ \to K^+K^-K^+$. *PoS*, CHARM2016:086, 2016.

[56] Marina Artuso, Brian Meadows, and Alexey A. Petrov. Charm Meson Decays. *Ann. Rev. Nucl. Part. Sci.*, 58:249–291, 2008.

[57] B. et al Aubert. Amplitude analysis of the decay $D^0 \to K^-K^+\pi^0$. *Phys. Rev. D*, 76:011102, Jul 2007.